

M0004215TP

# **Investigation of the suitability of amorphous semiconductors as sensors for optical process tomography**

**ROBERT PETER JENNER**

A thesis submitted in partial fulfilment of the requirements of the  
University of Greenwich for the Degree of Doctor of Philosophy

July 2000



## ABSTRACT

In this work, the suitability of amorphous semiconductors as hard field optical sensors for application in optical process tomography (OPT) has been established. Two amorphous semiconductors were selected for the study, these being amorphous arsenic triselenide (a-As<sub>2</sub>Se<sub>3</sub>) and hydrogenated amorphous silicon (a-Si:H). The a-As<sub>2</sub>Se<sub>3</sub> device was a single layered structure of 60µm thickness fabricated upon a 2mm thick cylindrical aluminium substrate. The a-Si:H device was a multi-layered structure of 27.1µm overall thickness fabricated upon a 4mm thick cylindrical aluminium substrate. 20mm<sup>2</sup> samples were cut from the cylinders, their surface being left free for a xerographic investigation. For a tomographic investigation, semitransparent gold (Au) contacts were sputtered onto the surface of the devices to produce single contacts or contact arrays. The study comprised of the two fields of xerography and tomography. The xerographic study comprised of the measurement of such parameters as charge acceptance, dark decay, residual potential, and photoinduced discharge. The research project has concurred with other workers in that the dark discharge mechanism in a-As<sub>2</sub>Se<sub>3</sub> proceeds via a xerographic depletion discharge process, and a Poole-Frenkel type emission in a-Si:H.

The tomographic investigation involved the study of such parameters as detectivity, responsivity, steady state photocurrent, and photoinduced fatigue. Detectivity has found to be dependant upon the magnitude of applied electric field and level of incident irradiance. Irradiance in the order of 3.45mW/cm<sup>2</sup> to 9.57mW/cm<sup>2</sup> for a-As<sub>2</sub>Se<sub>3</sub> and 5.31mW/cm<sup>2</sup> to 28.32mW/cm<sup>2</sup> for a-Si:H was required in order to produce a clean and repeatable photogenerated current pulse over the range of electric fields specified (0.66x10<sup>5</sup> V/cm to 1.66x10<sup>5</sup> V/cm). The production of steady state current has found to be dependant upon the magnitude of electric field, the level of irradiance, and the illumination period. Irradiance of 319mW/cm<sup>2</sup> to 1.46W/cm<sup>2</sup> with an illumination period of 520ns was required to produce steady state photocurrent in a-As<sub>2</sub>Se<sub>3</sub>, and 693mW/cm<sup>2</sup> to 2.62W/cm<sup>2</sup> with an illumination period of 880ns for a-Si:H. A linear relationship between electric field and responsivity has been observed in both materials over a range of irradiance of 3.45mW/cm<sup>2</sup> to 9.57mW/cm<sup>2</sup>. Responsivity in the order of 87.86µA/W to 145.19µA/W for a-As<sub>2</sub>Se<sub>3</sub> and 14.19µA/W to 103.81µA/W for a-Si:H has been demonstrated. An investigation as to the effects of photoinduced fatigue in both a-As<sub>2</sub>Se<sub>3</sub> and a-Si:H has been carried out by the application of pulsed visible light of various flash repetition rate (FRR) under a constant high electric field over a 30 minute illumination period. It has been shown that the rate of fatigue is dependant upon the material, time, electric field, light intensity, and FRR. A maximum operating speed of 20Hz has been determined for a-As<sub>2</sub>Se<sub>3</sub> and 100Hz for a-Si:H. The maximum operating speed of 20Hz for a-As<sub>2</sub>Se<sub>3</sub> was deemed unsuitable for OPT application and the a-As<sub>2</sub>Se<sub>3</sub> material was eliminated from further tomographic investigation. Tomographic prototypes were employed to establish the a-Si:H devices ability to produce qualitative and quantitative data. The results of this investigation demonstrated that 1mm changes in water level and 0.5% changes in fluid colour could be accurately determined by the a-Si:H device at speeds required for OPT. The use of an a-Si:H device containing a Au contact array facilitated the imaging of the curvature of a pipeline and a phantom object contained within the pipeline. The results of the overall investigation have confirmed that the a-Si:H device is suitable for application as a hard field optical sensor for OPT.

## **ACKNOWLEDGEMENTS**

I am very grateful to my supervisor Dr S.M. Vaezi-Nejad for his help, guidance and financial support throughout the course of the research project. I am also grateful to my second supervisor Dr Charles May for his interest in this work.

I wish to thank the technical staff of the Medway School of Engineering, in particular Mr Ian Cakebread for their help and advice.

I wish to thank the Solid State Research group at Imperial College, London, for supplying the majority of the amorphous materials employed in this project. I particularly want to thank the head of the group Dr Juhasz for his help and advice.

Finally I wish to thank the head of the Medway School of Engineering Professor Alan Reed for his moral and additional financial support throughout the research project.

## **Author's Note**

All of the work contained within this thesis is the sole and original work of the author, except where otherwise stated by acknowledgement or reference.

**CONTENTS**

	Page
LIST OF FIGURES.	1
LIST OF TABLES.	7
CHAPTER 1: INTRODUCTION	8
CHAPTER 2: LITERATURE REVIEW	12
2.1    Medical tomography	12
2.2    Process tomography	19
2.2.1    Electrical impedance tomography	19
2.2.2    Ultrasonic tomography	21
2.2.3    Optical process tomography	23
2.3    Chapter summary	32
CHAPTER 3: AMORPHOUS SEMICONDUCTORS	34
3.1    Amorphous arsenic triselenide (a-As <sub>2</sub> Se <sub>3</sub> )	34
3.2    Hydrogenated amorphous silicon (a-Si:H)	36
3.3    Xerography	38
3.4    Charge acceptance	40
3.5    Dark decay	45
3.5.1    a-As <sub>2</sub> Se <sub>3</sub>	45
3.5.2    a-Si:H	56
3.6    Chapter summary	61
CHAPTER 4: EXPERIMENTAL APPARATUS AND PROCEDURES	62
4.1    Xerographic mode of operation	62
4.1.1    Sample preparation	62
4.1.2    Experimental procedures for the xerographic mode of operation	64
(i)    Dark decay	64
(ii)   Photoinduced discharge	66
4.1.3    Experimental apparatus in the xerographic mode	67
(i)    Light tight enclosure	67
(ii)   Timing/position sensor units	67
(iii)  Sample translation mechanism	68
(iv)  Measuring station	70

	Page
(v)    Scorotron charger	72
(vi)   Data acquisition	80
4.2    Electroded mode of operation	82
4.2.1  Sample preparation	89
4.2.2  Experimental procedures for electroded mode of operation	91
(i)    Steady state and detectivity	91
(ii)   Establishment of maximum operat -ing speed through photoinduced fatigue	92
(iii)  Establishment of quantitative data	93
(iv)  Establishment of qualitative data	95
(v)    Production of images	95
4.2.3  Xenon flash unit	96
(i)    Light source	97
(ii)   Discharge mechanisms	102
(iii)  Control signal generation	107
(iv)   Control of light intensity / duration	109
4.2.4  Light detection mechanism	113
4.3    Chapter summary	115
<b>CHAPTER 5: RESULTS OF XEROGRAPHIC INVESTIGATION</b>	<b>116</b>
5.1    Xerographic mode of operation	116
5.1.1  a-As <sub>2</sub> Se <sub>3</sub>	116
(i)    Charge acceptance	116
(ii)   Dark decay	118
(iii)  Photoinduced discharge	124
5.1.2  a-Si:H	127
(i)    Charge acceptance	127
(ii)   Dark decay	130
(iii)  Photoinduced discharge	133
5.2    Chapter summary	135

	Page
CHAPTER 6: RESULTS OF TOMOGRAPHIC INVESTIGATION	140
6.1    a-As <sub>2</sub> Se <sub>3</sub>	140
6.1.1    Detectivity	140
6.1.2    Production of steady state current	145
6.1.3    Establishment of maximum operating speed by the determination of the effects of photoinduced fatigue	147
6.2    a-Si:H	156
6.2.1    Detectivity	156
6.2.2    Production of steady state current	157
6.2.3    Establishment of maximum operating speed by the determination of the effects of photoinduced fatigue	161
6.2.4    Establishment of pipeline limits	168
6.2.5    Establishment of quantitative data	172
6.2.6    Establishment of qualitative data	177
6.2.7    Production of basic images	180
(i)    Curvature of the pipeline	180
(ii)   Phantom object	183
6.3    Chapter summary	187
CHAPTER 7: DISCUSSION OF EXPERIMENTAL RESULTS	190
7.1    Xerographic investigation	190
7.1.1    Charge acceptance	190
(i)    a-As <sub>2</sub> Se <sub>3</sub>	190
(ii)   a-Si:H	190
7.1.1    Dark decay	191
(i)    a-As <sub>2</sub> Se <sub>3</sub>	191
(ii)   a-Si:H	192
7.2    Tomographic investigation	192
7.2.1    Detectivity	192
(i)    a-As <sub>2</sub> Se <sub>3</sub>	192
(ii)   a-Si:H	193
7.2.2    Production of steady state current	196

	Page
(i)    a-As <sub>2</sub> Se <sub>3</sub>	196
(ii)   a-Si:H	197
7.2.3  Establishment of maximum operating speed by the determination of the effects of photoinduced fatigue	198
(i)    a-As <sub>2</sub> Se <sub>3</sub>	198
(ii)   a-Si:H	208
7.2.4  Establishment of quantitative data	213
7.2.5  Establishment of qualitative data	216
7.2.6  Production of images	217
(i)    Curvature of the pipeline	217
(ii)   Phantom object	218
<b>CHAPTER 8: CONCLUSIONS AND SUGGESTIONS</b>	<b>220</b>
<b>FOR FURTHER WORK</b>	
8.1    a-As <sub>2</sub> Se <sub>3</sub>	220
8.1.1  Xerographic investigation	220
8.1.2  Tomographic investigation	220
8.2    a-Si:H	221
8.2.1  Xerographic investigation	221
8.2.2  Tomographic investigation	221
8.3    Suggestions for further work	224
8.3.1  Effects of pulsed illumination	224
8.3.2  Light source	224
8.3.3  Effects of elevated temperature	225
8.3.4  Tomographic rig	225
8.3.5  Device design	225
<b>REFERENCES</b>	<b>227</b>
<b>APPENDICES</b>	<b>234</b>
1      Core MATLAB program	234
2      Turbo C control program listing	236
3      Establishment of optimum probe to sample surface spacing and electrostatic voltmeter calibration.	251

		Page
4	MATLAB analysis programs	255
	(i) a-As <sub>2</sub> Se <sub>3</sub>	255
	(ii) a-Si:H	257
5	MATLAB program for the production of 3D images	259
6	Published paper	261

**LIST OF FIGURES**

Figure		Page
3.1	Surface charge density vs. surface potential for depletive and capacitive charging.	44
3.2	Xerographic depletion discharge process.	47
3.3	Determination of depletion time.	53
4.1	Basic block diagram for xerographic mode of operation.	63
4.2	Sample geometry.	63
4.3	Sample translation mechanism.	71
4.4	Basic timing diagram for sample translation mechanism.	71
4.5	Transparent probe arrangement.	73
4.6	Basic corona charger.	75
4.7	Basic point to plane corona charger.	75
4.8	Basic scorotron.	75
4.9	Effect of coronode to sample surface spacing on corona onset voltage.	79
4.10	Control grid functionality on a typical a-Si:H sample.	79
4.11	Cross section through scorotron charger.	81
4.12	Internal mechanism of scorotron charger.	81
4.13	Basic flow diagram for the acquisition of charge decay data.	83
4.14	Block diagram for the electroded mode of operation.	85
4.15	Basic electrical circuit arrangement for electroded experimentation.	88
4.16	Mask arrangements for samples under electroded mode of operation.	88
4.17	Positioning of peak photocurrent to exploit maximum sensitivity between full and empty pipelines.	94

Figure	Page
4.18 Positioning and geometry of phantom object .	94
4.19 Basic block diagram of xenon flash unit.	98
4.20 Internal mechanism of L2441 xenon discharge lamp.	100
4.21 Light flux distribution.	100
4.22 Timing diagram for the initiation of a single light pulse.	104
4.23 Basic block diagram of SCR firing mechanism.	106
4.24 Effect of changing illumination period on recorded light intensity.	108
4.25 Effect of changing the illumination period on the production of photocurrent.	108
4.26 Effect of varying discharge capacitance on input energy whilst maintaining constant input voltage.	110
4.27 Control of light pulse duration.	110
4.28 Effect on input energy whilst varying the input voltage whilst maintaining constant discharge capacitance.	112
4.29 Control of light pulse intensity whilst maintaining pulse duration.	112
4.30 Sketch of main discharge capacitor mechanism.	114
4.31 Light detection circuit.	114
5.1 Acceptance potential for a-As <sub>2</sub> Se <sub>3</sub> sample.	117
5.2 Surface charge density vs. surface potential for a-As <sub>2</sub> Se <sub>3</sub> .	117
5.3 Dark discharge curves for a-As <sub>2</sub> Se <sub>3</sub> .	120
5.4 Dark current density vs. time.	121
5.5 Double log plot for a-As <sub>2</sub> Se <sub>3</sub> showing depletion time.	121
5.6 Comparison of experimental data and Abkowitz model.	125
5.7 Abkowitz models showing effects of thermal generation and surface injection.	125

Figure	Page
5.8 Photoinduced and dark discharge curves for a-As <sub>2</sub> Se <sub>3</sub> .	128
5.9 Comparison of photoinduced discharge curves over varying electric field.	128
5.10 Photoinduced discharge curves due to varying light intensity.	129
5.11 Magnification of photoinduced discharge curves.	129
5.12 Dark discharge curve showing charge acceptance for a-Si:H.	131
5.13 Surface charge density vs. surface potential for a-Si:H.	131
5.14 Dark discharge curves for a-Si:H.	132
5.15 Dark discharge rate vs. time for a-Si:H.	134
5.16 Double log plot of dark discharge rate for a-Si:H.	134
5.17 Determination of experimental Poole-Frenkel coefficient.	137
5.18 Comparison of Dark discharge curves and photoinduced discharge curves for a-Si:H.	138
5.19 Photoinduced discharge curves due to varying levels of electric field.	138
5.20 Photoinduced discharge curves due to 15% changes in light intensity.	139
6.1 Typical photogenerated current pulses in a-As <sub>2</sub> Se <sub>3</sub> due to varying levels of irradiance at $E= 0.66 \times 10^5$ V/cm.	142
6.2 Typical photogenerated current pulses in a-As <sub>2</sub> Se <sub>3</sub> due to varying levels of irradiance at $E= 1 \times 10^5$ V/cm.	142
6.3 Typical photogenerated current pulses in a-As <sub>2</sub> Se <sub>3</sub> due to varying levels of irradiance at $E= 1.33 \times 10^5$ V/cm.	143
6.4 Linear relationship between responsivity and electric field in a-As <sub>2</sub> Se <sub>3</sub> .	144
6.5 Typical steady state conditions for a-As <sub>2</sub> Se <sub>3</sub> .	144
6.6 Increased sensitivity to changes in irradiance by positioning of peak photocurrent.	148

Figure	Page
6.7 Calculation period of dark current.	149
6.8 Effect of increasing flash repetition rate from 20Hz to 100Hz in a-As <sub>2</sub> Se <sub>3</sub> .	149
6.9 Dark current due to varying flash repetition rates in a-As <sub>2</sub> Se <sub>3</sub> .	151
6.10 Effect of altering the electric field and irradiance upon photoinduced fatigue in a-As <sub>2</sub> Se <sub>3</sub> .	151
6.11 Dark current over a range of electric field in a-As <sub>2</sub> Se <sub>3</sub> .	153
6.12 Effect of altering the electric field and irradiance on the rate of photoinduced fatigue in a-As <sub>2</sub> Se <sub>3</sub> .	153
6.13 Dark currents over a range of applied electric field in a-As <sub>2</sub> Se <sub>3</sub> .	154
6.14 Normalised signal response over a range of applied electric field in a-As <sub>2</sub> Se <sub>3</sub> .	154
6.15 Mean signal response for full and empty pipelines in a-As <sub>2</sub> Se <sub>3</sub> .	155
6.16 Maximum separation between full and empty pipelines in a-As <sub>2</sub> Se <sub>3</sub> .	155
6.17 Typical photogenerated current pulses in a-Si:H due to varying levels of irradiance at $E= 0.66 \times 10^5$ V/cm.	158
6.18 Typical photogenerated current pulses in a-Si:H due to varying levels of irradiance at $E= 1 \times 10^5$ V/cm.	158
6.19 Typical photogenerated current pulses in a-Si:H due to varying levels of irradiance at $E= 1.33 \times 10^5$ V/cm.	159
6.20 Linear relationship between responsivity and electric field in a-Si:H.	160
6.21 Typical steady state photocurrent for a-Si:H.	160
6.22 Effect of increasing flash repetition rate from 20 Hz to 100Hz in a-Si:H.	162
6.23 Effect of varying flash repetition rate on mean signal response in a-Si:H.	164
6.24 Average dark currents over a range of flash repetition rates in a-Si:H.	164

Figure	Page
6.25 Increase in average dark current due to an increase in flash repetition rate in a-Si:H.	165
6.26 Normalised relaxation curves due to varying rates of flash repetition rate in a-Si:H.	165
6.27 Normalised relaxation curves due to varying rates of flash repetition rate over last 1ms of experiment in a-Si:H.	166
6.28 Signal response due to varying levels of applied electric field in a-Si:H.	166
6.29 Average dark currents over a range of applied electric field in a-Si:H.	169
6.30 Maximum separation between full and empty pipelines in a-Si:H.	169
6.31 Maximum separation between full and empty pipelines over multiple test runs in a-Si:H.	170
6.32 Definitive pipeline limits for full and empty pipelines for a-Si:H.	173
6.33 Average dark currents for full and empty pipelines in a-Si:H.	173
6.34 Signal response due to varying levels of water for a-Si:H.	174
6.35 Signal response due to a columnised light beam in a-Si:H.	176
6.36 Signal response due to varying levels of additive concentration for a-Si:H.	178
6.37 Signal response due to 0.5% changes in additive concentration for a-Si:H.	181
6.38 Au contact positioning for contact array.	182
6.39 Mean signal response for contact array.	182
6.40 3D representation of the bottom curvature of the pipeline using a sixteen contact array.	184
6.41 Mean signal response due to insertion of phantom object.	185
6.42 3D representation of the mean signal response due to the phantom object.	188
7.1 Dependence of minimum irradiance upon applied electric field.	194
7.2 Dependence of maximum irradiance upon applied electric field.	194

Figure		Page
7.3	Increase in responsivity due to increased electric field.	199
7.4	Typical relaxation time from the steady state for a-As <sub>2</sub> Se <sub>3</sub> .	199
7.5	Normalised relaxation curves due to varying flash repetition rate.	202
7.6	Sketch of regions of sensitivity through pipeline.	215
7.7	Sketch of simplified light paths through pipeline.	215
7.8	Effect of altering distance of light source from sample surface.	219

**LIST OF TABLES**

Table		Page
5.1	Range of electric fields employed in the xerographic investigation.	120
5.2	Summary of dark decay analysis data for a-As <sub>2</sub> Se <sub>3</sub> .	126
5.3	Required surface potentials for maintenance of electric field in a-Si:H.	132
5.4	Results of dark decay analysis in a-Si:H.	137
6.1	Summary of detectivity experimentation showing minimum light conditions for the current system for a-As <sub>2</sub> Se <sub>3</sub> .	143
6.2	Summary of steady state experimentation showing maximum light conditions for the current system for a-As <sub>2</sub> Se <sub>3</sub> .	148
6.3	Summary of detectivity experimentation showing minimum light conditions for the current system for a-Si:H.	159
6.4	Summary of steady state experimentation showing maximum light conditions for the current system for a-Si:H.	162
6.5	Test data for establishment of pipeline limits for a-Si:H.	170
6.6	Definitive pipeline limits for full and empty pipelines for a-Si:H.	170
6.7	Summary of quantitative data for a-Si:H.	174
6.8	Summary of qualitative data for a-Si:H.	178
6.9	Summary of qualitative data due to 0.5% changes in fluid mix for a-Si:H.	181
6.10	Mean signal response for contact array for 3D representation of the bottom curvature of the pipeline for a-Si:H.	184
6.11	Mean signal response for contact array for 3D representation of the phantom object for a-Si:H.	188

## CHAPTER 1

### INTRODUCTION

The research presented within this thesis was concerned with investigating the suitability of amorphous semiconductors, primarily amorphous arsenic triselenide ( $a\text{-As}_2\text{Se}_3$ ) and hydrogenated amorphous silicon ( $a\text{-Si:H}$ ) as hard field sensors for optical process tomography (OPT) applications. Both  $a\text{-As}_2\text{Se}_3$  and  $a\text{-Si:H}$  underwent extensive research in the early 1980's to the early 1990's for application in the xerographic industries. Amorphous semiconductors possess the highly desirable quality in that they can be made into very large area devices due to the fact that they are not bound by the same constraints as crystalline materials. This fact allows great flexibility in amorphous semiconductor device design.

OPT is a relatively new technology which began to develop mainly in the mid 1980's, and arose due to the development of high speed, low cost parallel computing systems as well as major advances in digital electronics and measurement transducers. Tomography itself is not a new process and can be dated back to the x-ray experiments carried out by Röntgen in 1896. The term tomography is from the Greek 'τομοζ' which means to slice. There are two main applications for tomography, these being the fields of medical tomography and industrial process tomography. Similar tomographic methods can be applied to both medical tomography and industrial process tomography, however, the aims of medical tomography differ greatly to those of industrial process tomography. Although the research presented within this thesis was primarily concerned with OPT, references are made to medical tomography systems where appropriate due to their close relation to OPT systems in the methodology, technology, application, or sensing materials employed. It will be shown that tomographic imaging systems developed for medical investigations are finding application in industrial process tomography.

Industrial process tomography can be used to image or monitor processes within pipelines, vessels, separator tanks, reactors, and indeed any system where access is restricted. The aim of process tomography is to obtain quantitative and qualitative data about the medium under test and not necessarily to produce high resolution images. In

most industrial applications, visual inspection of the process by a trained engineer would yield little applicable information of the process except in the case of a gross malfunction (Beck *et al*, 1999). This statement serves to highlight the difference between process tomography and medical tomography in which visual inspection of very high resolution images by trained personnel is required. This issue is discussed further in chapter 2.

Process tomography aims to allow the operator to accurately analyse the internal characteristics of media under test with a view to improving the design of equipment and processes for handling media, thus improving efficiency, safety, and operational costs. Industry is under considerable pressure to manage resources more efficiently and responsibly in order to meet governmental concerns over environmental issues and also customer demand for increased product quality. Thus there is an ever increasing demand from the manufacturing industries to gain new knowledge of how industrial processes behave. This increased knowledge of process behaviour is best undertaken by advances in tomographic imaging systems (Williams and Beck, 1996).

A typical tomography system contains both hardware and software. The hardware aspect of the system will contain sensing elements and signal generation/detection electronics. The software aspect of the system is used to issue/receive control signals, for signal reconstruction/interpretation, and also for image display. In order for detailed analysis of the media under test to be achieved, the system should ideally be non-invasive and non-intrusive, i.e. the system should not require that the walls of the vessel under test are ruptured (by the insertion of probes for example) and that the system does not interfere with the medium under test. Optical tomography systems fulfil these requirements as will be demonstrated in this thesis.

One of the most important aspects of a tomographic imaging system is the type of sensor that is used. The basis of any measurement system is to exploit differences or contrast in the properties of the media being examined. There are many types of sensors available for tomography and the most commonly used are based upon transmission, diffraction, or electrical phenomena.

The following properties are highly desirable from a potential sensor material for tomographic purposes. The sensor should;

- Allow good spatial resolution.
- Have good sensitivity.
- Have fast speed of response.
- Be compact.
- Be chemically and mechanically stable and durable.
- Require minimal maintenance.
- Require minimal calibration.
- Be non-invasive.
- Be non-intrusive.
- Be portable.
- Be safe.
- Be reliable.
- Allow flexibility in system design.

I believe the amorphous semiconductor sensors investigated by OPT techniques in the current research, can help to fulfil most of these requirements and offer many advantages when compared to crystalline semiconductor sensors and other tomographic techniques.

Chapter two reviews past and current tomographic imaging systems in the fields of both medical radiology and OPT as well as serving to distinguish between the aims of medical tomography and industrial process tomography. The review further serves to demonstrate that whilst medical radiology systems are becoming ever more complex, a clear trend in industrial process tomography towards conceptually simple, flexible, but effective tomographic imaging systems is emerging and that optical techniques are at the forefront of this trend.

Chapter three provides a discussion of amorphous semiconductors and the properties they possess that we believe make them suitable for application as hard field sensors for OPT. Chapter 4 details the experimental apparatus developed for this research in

order to allow the investigation of the amorphous semiconductors under xerographic and OPT conditions to be undertaken. Chapter 5 summarises the results of a xerographic investigation carried out upon the materials under test in order to validate material and sample integrity. Xerographic experiments were performed upon the free surface of the materials to establish their electrical characteristics. Analysis of the experimental data obtained, was then compared to previously published works using known theories in order to assess the behaviour of the samples and justify their selection for the current research.

Chapter 6 summarises the results of experiments conducted on electroded samples and compares the characteristics of the a-As<sub>2</sub>Se<sub>3</sub> and a-Si:H materials under OPT conditions with a view to establishing their suitability for OPT applications. Chapter 7 discusses the experimental results and highlights the strengths and weakness of the materials under test for application in OPT. Finally chapter 8 draws a final conclusion and offers suggestion for further works.

## CHAPTER 2

### LITERATURE REVIEW

The literature review has been divided into two sections. The first details medical radiology systems that employ amorphous semiconductors as the sensing elements. Although these systems fall outside of the definition of 'optical' tomography which is described shortly, the materials employed as the sensors, the methodology, and the potential application of such systems in industrial process tomography justify their inclusion in the literature review. The second section of the literature review details optical tomography systems that demonstrate the current trend towards conceptually simple, low cost, safe, effective imaging systems. A brief discussion of other commonly applied process tomography techniques is also included. Relevant literature appropriate to the development of the experimental apparatus are discussed in chapter 4.

#### 2.1 Medical tomography

Medical tomography frequently employs penetrative radiation such as x-rays and gamma rays, and also ultrasonic and electromagnetic techniques (amongst many others) to produce very high quality two or three dimensional images of the human body. The images produced by medical tomographic imaging systems are interpreted manually by highly trained medical personnel who visually inspect the tomographic images for signs of disease or abnormalities. Thus, one of the main objectives of medical tomography systems is to produce the highest quality images possible to aid this visual inspection. The process of 'optically' imaging the body involves passing light from a radiation source, through the body to a detector or detectors placed on the other side of the body. Visible light (400nm to 720nm) can not easily pass through biological tissue and so 'optical' medical tomography systems normally employ ultraviolet, near infrared, x-ray and gamma radiation as the radiation source.

Fletcher (1996), states that in the strictest sense, optical tomographic imaging systems use visible light as the illumination source. This statement would suggest that medical imaging systems that use the radiation sources described above cannot be termed true optical tomographic systems. This statement cannot be deemed to be correct for all medical 'optical' imaging systems however. Beuthan *et al* (1996) described the

tomographic imaging of a rat brain which utilised light with a peak wavelength of 685nm as the illumination source. Light was passed from a laser diode through a rat brain to a crystalline silicon avalanche PIN photodiode located on the other side of the rat brain. Beuthan *et al* describe an optical 'window' in the region of 600nm to 1100nm in which light can penetrate biological tissue. As this 'window' incorporated an element of visible light (600nm-720nm) the medical imaging system could correctly be described as an 'optical' tomographic system. However, Honlet (1998) argues that x-rays can be physically seen and therefore should also be termed as 'optical' imaging systems. For purposes of clarity in this thesis, the term 'optical' is only applied to tomographic imaging systems which utilise visible light as the radiation source.

The most widely used technique of imaging large parts of the body is that of x-ray imaging which is termed radiography. In radiography, x-rays are passed through the section of the body to be imaged to an x-ray detector located on the other side of the body. The image is then most commonly developed onto film for analysis by medical practitioners. The use of film to display the image can be a very time consuming and costly process and extensive research has been undertaken as to how this process could be made more efficient for many years. The current 'state of the art' medical x-ray systems have done away with film development altogether and have replaced this process with digital images which are stored and displayed upon a computer. Such systems have the advantage that the images are available to the medical practitioner almost simultaneously, there are no developing costs, the images can be stored on computer disc, and can be transferred to other medical establishments or departments by using computer networks.

The current 'state of the art' digital x-ray systems commonly employ amorphous semiconductors as the sensing elements. Although interest in using amorphous semiconductors as sensing mechanisms for x-ray systems started around the 1970's, it is only very recently that such systems have begun to become a reality and are being commercially produced. Although these systems are not strictly speaking 'optical' tomography systems because they use penetrating x-ray as the radiation source, the sensing materials employed and the methodology of such systems can be very similar to OPT, and indeed, as will be shown, are finding application in process tomography.

### Zhao and Rowlands 1992

One of the earlier attempts at a digital x-ray imaging system was described by Zhao and Rowlands in 1992. The system developed by Zhao and Rowlands employed an amorphous selenium (a-Se) flat panel as an x-ray detector for radiology. The emerging x-rays were applied to the a-Se flat panel array directly. Amorphous selenium has the highly desirable property of being able to convert energy from x-ray photons to electrical charge directly (Kasap *et al*, 2000). The a-Se was deposited on a glass substrate to a thickness of up to 500µm together with an array of thin film field effect transistors (FET). The a-Se panel was divided up into greater than  $3 \times 10^6$  pixels, each pixel containing an a-Se photo-conductor and a FET. When x-rays were incident upon the surface of the a-Se panel, electron hole pairs were released within the photoconductive layer which were then directed to the surface of the a-Se panel. Each pixel contained an electrode which collected the induced charge and the collected charge was applied to a storage capacitor. The storage capacitor was in turn connected to the FET. When the induced latent image was to be read, each row of pixels were addressed sequentially by a gate control pulse, thus each FET in a row was turned on at the same time which meant that the system was essentially self scanning. The detected charge for each column of pixels was then amplified, multiplexed and digitised to form the digital data set that was used to form the image.

### Neitzel *et al* 1994

The system described by Neitzel *et al* employed the use of a a-Se alloy drum as a direct x-ray detector for chest radiography. The a-Se was deposited on a metallic substrate (which was large enough to cover the entire thoracic region) to a thickness of 500µm. Arsenic (0.5%) was added to the a-Se to improve the thermal stability of the device. A 1µm layer of organic polymer was then applied to the surface of the a-Se as an atmospheric protection mechanism. In order to produce an image, the vertically mounted drum was rotated at a speed of 60rpm and a surface charge of positive polarity was applied by the use of a corona charger. While the surface charge was being established by the corona charger, a negative potential of 1500V was applied to the metallic substrate in order to produce an electric field within the a-Se layer. The rotation of the charged drum was then stopped and the patient was positioned in front of the drum. X-rays were then passed through the patient to the surface of the drum

where a latent image was formed on the a-Se layer of the drum by the conversion of the energy created by the incident x-ray photons being converted to electrical charge. The drum was then accelerated to 300rpm and an array of 36 readout probes were used to sense the charge on the surface of the drum. The sensor array was then moved around the drum at distance of one pixel (0.2mm). This process was continued for 15 seconds until the entire surface of the drum had been scanned. The detected charge data was finally amplified, digitised and displayed upon a computer screen for analysis.

#### Graeve *et al* 1995

The system developed by Graeve *et al* employed a-Si:H photodiode arrays as an x-ray detector for medical tomography. Hydrogenated amorphous silicon differs from a-Se and high purity crystalline silicon in that it cannot convert energy from x-ray photons to electrical charge directly (Yaffe and Rowlands, 1997). A scintillator device was therefore required to convert the x-ray radiation to visible light. The sensor described, contained a 256x256 pixel array with each pixel containing a photodiode and four switching diodes. The diodes were fabricated using plasma enhanced chemical vapour deposition techniques (PECVD). The sensor employed X-Y addressing of the rows and columns by the use of electrodes. The switching diodes were incorporated into the pixels to allow individual addressing. The whole structure was manufactured upon a glass substrate. When an image capture was required, the emerging x-rays were converted to visible light by a commercially available scintillator. The a-Si:H photodiode array then collected the visible light photons. The collected photons then activated the relevant photodiodes contained within the pixels and an analogue signal was produced. As with the system described by Zhao and Rowlands (1992), the sensor array was scanned sequentially column by column. The resulting analogue voltages were then amplified, digitised and displayed upon a computer screen for analysis.

#### Apte *et al* 1998

The system described by Apte *et al* was developed for medical imaging with possible application in non-destructive testing (NDT) and high speed document scanning. The developed system employed a single flat panel of 29.2 x 40.6 cm<sup>2</sup> area and was claimed to be the largest hydrogenated amorphous silicon flat panel 2D digital radiography system in the world. The a-Si:H panel was specifically designed for

imaging of the thoracic region. The panel consisted of greater than 7 million pixels, with each pixel containing a photodiode and transistor. The principle of operation of this system is essentially the same as the systems described above with sequential addressing of each of the pixels, the major difference is the size of the panel produced. Apte *et al* claimed that the only future improvements likely to take place in digital radiography would be in the efficiency of scintillator devices and improvements in pixel design and not in developing new materials as the sensing elements. The statement that improvements in material technology cannot be made was deemed to be incorrect as Popov *et al* (1998) for example, attempted to devise a digital x-ray imaging system that utilised a-Si:H as the sensing material which did not require a scintillator to convert the x-ray radiation to visible light.

#### Popov *et al* 1998

The system described by Popov *et al* utilised hydrogenated amorphous silicon nitride (a-SiN:H) as a direct x-ray detector. The a-SiN:H film was deposited upon a 2 inch square glass substrate in an 100x100 array of thin film diodes (TFD) each of 200x200 $\mu\text{m}$  dimensions. The system described required no switching electronics and no x-ray conversion layer. The a-SiN:H material was used to detect the emerging x-rays and also to generate an electrical signal (as with a-Se). The active area of the prototype was divided up into pixels as with the other systems described previously, i.e. constructed into rows and columns. In the system described, 'islands' of a-SiN:H were built up at the row/column intersections upon the glass substrate. The TFD's were then fabricated onto these a-SiN:H islands. Row addressing was achieved by row control buses manufactured by etching, whereas column control buses were manufactured by deposition. As there were no controlling electronics in the pixels, the TFD's occupied the entire pixel thus giving a better resolution than systems which require controlling electronics to be present. Although this type of arrangement is in its infancy, it shows great promise in improving current 'state of the art' digital radiography systems. For example, if a-SiN:H could be employed in the system described by Apte *et al*, the scintillator could be removed and the resolution of the system could be improved due to the active area in each pixel being 100% of the available area.

Anderson *et al* 1998

The system described by Anderson *et al* utilised a-Si:H as the detection unit with the system being primarily designed for use in medical radiography. Amorphous silicon was deposited onto a glass substrate which measured 8 x 10 inches. The active data acquisition area of the panel was 1536 x 1920 127 $\mu$ m pixels, and each of these pixels again contained a photodiode and a thin film transistor (TFT). When light was incident upon the a-Si:H flat panel, a charge proportional to the light intensity was induced within the photodiode. The charge was detected by charge amplifiers, each charge amplifier being connected to a data line. As with other systems discussed previously each row of photodiodes was addressed sequentially and the detected charge was transferred, digitised and image displayed upon PC screen. The a-Si:H photodiodes used in the system can detect light in the range 400nm-720nm i.e. visible light and Anderson *et al* state that the system developed for medical radiology also had possible application in NTD. If the system were to be used for medical radiology, a scintillator layer would be required to convert the penetrative x-rays to visible light as discussed previously. This would also be true for NDT applications where penetrative x-ray systems were permitted. Possible applications of the system in NDT were stated as the 2D imaging of electronic modules, printed circuit boards (PCB's), and weld/crack inspection. All of the stated applications relied upon the use of penetrative x-ray.

The medical digital radiology systems described above have many desirable features such as very high resolution, high speed, and portability of the flat panels, nevertheless they also have properties that could make them unsuitable for process tomography. Industrial process tomography demands low cost, low maintenance, fast, safe, reliable tomographic imaging systems. The medical digital x-rays systems described are very complex, high cost systems which can only image in 2 dimensions. Additional problems for use of such systems in industrial process tomography are that of operator safety and array reliability. X-rays are hazardous radiation and as such, any tomographic system employing such radiation would require additional safety features and operator training increasing the cost of the system. Also, the effects of long term radiation exposure on the amorphous semiconductor arrays is not fully understood (Boudry and Antonuk, 1996).

There are many industrial process applications where digital radiology systems could be applied, examples include crack, flaw, and corrosion detection in processes where access to the media under test is not possible or difficult. Digital x-rays systems can also have applications in the food industries for the detection of foreign objects within food stuffs (Graves *et al*, 1998). Lopushansky *et al* (1998) describe a digital radiology system designed specifically for industrial process imaging applications. The design of the radiology system serves to highlight the difference in aims of medical tomography and process tomography.

#### Lopushansky *et al* 1998

The digital radiography system developed by Lopushansky *et al* was designed to image corrosion and cracks on pipelines which were covered in insulation and weather protection making them inaccessible to visual inspection. The system was a scanner based design with a radiation source and a linear array of a-Si:H photodiodes incorporating a scintillator device. A motor system moved the radiation source and sensor array along the section of pipeline to be imaged. As mentioned previously, the aims of process tomography differ from medical tomography in that the focus is on obtaining quantitative and qualitative data rather than high quality images. As such, the sensor array deployed in the system described by Lopushansky *et al* was a simple 128 linear array of photodiodes. Although the detector array greatly differed from the complex medical radiology sensing arrays, the principle of operation is the same. The x-rays from the radiation source were passed through the pipeline under test and the emerging x-rays were converted to visible light by a scintillator. The visible light was then detected by the photodiode array.

The medical radiology system described by Anderson *et al* (1998) was stated as having application in crack and weld inspection in industrial pipelines. The array developed by Anderson *et al* employed an array containing approximately 3 million pixels. The system described by Lopushansky *et al* (1998) which was specifically designed for crack and weld inspection of industrial pipelines employed a sensor array containing just 128 pixels. The difference in complexity of the two systems for identical application in process tomography serves to highlight the difference in the technological requirements of medical and process tomography. All of the medical imaging systems described have possible application in OPT if visible light were to be

employed as the illumination source. However, the complexity, cost, and constructional problems of using flat panel devices could make such systems unattractive for many OPT applications.

## 2.2 Process tomography

There are many tomographic techniques employed in process tomography, including optical, x-ray, gamma-ray, microwave, acoustics, ultrasonics, electrical impedance, positron emission, nuclear magnetic resonance imaging, velocimetry techniques, and neutron transmission amongst many others. Each of the tomographic techniques described have strengths and weaknesses and no particular technique is suitable for all tomographic applications. In the field of medical tomography, research is being clearly focused upon very high resolution digital radiology systems where image quality is all important. However, in the field of process tomography, current research is focusing on developing simple, low cost, portable but effective tomographic techniques. The most common tomographic techniques being developed for this purpose include electrical impedance tomography, ultrasonic tomography, and ever increasingly, optical tomography (Williams and Beck, 1995). A brief discussion of electrical impedance tomography and ultrasonic tomography is presented below which is followed by a review of optical process tomography systems.

### 2.2.1 Electrical impedance tomography

The most common tomographic systems that utilise the measurement of electrical properties as the sensing mechanism are capacitive and resistive tomographic systems which can be classified (along with the lesser employed inductive tomography) under the description of electrical impedance tomography (EIT). The most common applications for such systems include, liquid mixing and multiphase flow, powder mixing transport and conveying, reactor studies, thermal mapping, ground water monitoring and soil remediation (Chaouki *et al*, 1997). A brief discussion of the two main types of EIT systems i.e., capacitive and resistive follows.

#### A) Capacitive tomography

Electrical capacitive tomography (ECT) is a technique applied to obtain information about the distribution of the contents of closed pipes or vessels by measuring variations in the dielectric properties of the media inside the vessel. Typical

information that can be acquired by ECT systems include volume fraction and velocity measurements of multiphase flows. The sensing electrodes in ECT systems can be mounted either inside or outside of the vessel. If the vessel under test is metallic, then the sensing electrodes are normally located in the wall of the vessel. This however makes the system intrusive which is an undesirable feature in process tomography. If the vessel under test is an insulator such as plastic then the sensing electrodes are normally mounted on the outside of the vessel. Capacitance sensors consist of electrode pairs which are located on opposite sections of the process to be monitored. Voltage is usually applied to the electrode pairs in sequence and an electrical charge measured as current is determined. The reader is referred to Huang *et al* 1991, Xie *et al* 1991, and Beck *et al* 1993 for a comprehensive discussion of ECT system design.

#### B) Electrical resistive tomography

Electrical resistive tomography (ERT) involves sensing changes in electrical resistivity between liquid/liquid or liquid/solid mixtures in vessels. ERT is suited for the imaging or monitoring of vessels containing conductive media such as aqueous phases. Electrically conducting electrodes are inserted into the wall of the vessel under test so that electrical contact with the media can be established. The electrodes themselves are normally manufactured from materials such as brass, stainless steel and silver alloys. The electrodes have to be made from a material that is more conductive than the media under test to avoid the problems of contact impedance. The reader is referred to Dickin *et al* 1993 for a discussion of typical ERT system design.

EIT systems in general are quite fast with image capture of approximately 100 frames per second when compared to systems that employ ionising radiation (0.1 to 10 frames per second), however, OPT systems can produce image capture at around 1000 frames per second (Williams and Beck, 1995). Advantages of EIT systems are that they are relatively low cost, conceptually fairly simple, safe, and can provide both qualitative and quantitative data and have found applications in both process tomography and medical tomography. ECT has found particular application in the imaging and monitoring of low conductivity materials such as oil, dry powders, and plastics, and also in the field of flame and combustion imaging. A disadvantage of EIT systems is that they require a large number of electrodes if good resolution is to be achieved. A

large number of electrodes in such systems can lead to very complex reconstruction algorithms which require extra processing time. This additional processing time slows down the rate at which the media can be imaged and so real time imaging is difficult. This is a particular problem in ECT as the electrodes employed have to be physically large to be able to give enough capacitive charge, and the enforced layout of such electrodes leads to poor spatial resolution in the centre of the captured image. EIT systems have a spatial resolution of approximately 5% of the vessel diameter (Dickin *et al*, 1993) compared to approximately 1% for ionising radiation and optical techniques (Beck *et al*, 1999).

The electrodes used in EIT applications are soft field sensors, this means that the sensitivity of the measuring system is altered by the medium under test. This is due to electric field equipotentials being distorted by variations in the electrical properties of said media which can lead to distortion of the resulting image. This is a particular problem in multi-module systems which require image registration. Dual module systems contain two or more sensing elements employing differing detection principles or materials. The resulting two images have to be aligned to form the finished image. Because of distortion on the image caused by variations in the electrical properties of the media, this alignment or image registration can be very difficult. ERT systems also suffer from the problem of the sensing electrodes being invasive i.e. probes are required to be inserted into the walls of the vessel containing the process. This is a particular problem in the food processing industries as potentially poisonous contaminants can build up upon the probes leading to problems in keeping the process sterile (Williams *et al*, 1995). Tomography systems that employ invasive electrodes are also unsuitable for application where the process is abrasive as damage to the electrodes can seriously inhibit the system performance. EIT system can often suffer from poor resolution and constructional problems due to the large physical size of the electrodes employed.

### 2.2.2 Ultrasonic tomography

Ultrasonic tomography reconstitutes the morphology of an object by using the contrasting property, the refractive index, or the ratio of the ultrasonic velocities locally in the test object (Chaouki *et al* 1997). Ultrasound systems are most commonly used in medical imaging where they have been used to image unborn foetuses, and

kidney/gall stones. Ultrasound has the property of being able to not only detect and image an object, but can also give accurate information as to the object location. Applications of ultrasonic systems in process tomography include imaging multiphase flows, liquid-gas boundaries, and for flaw, crack, and corrosion detection. Ultrasonic systems are particularly suited for flaw and crack detection as ultrasonic attenuation's are influenced by voids, cracks and other defects within the medium under test (Forsyth *et al*, 1994). Ultrasonic systems are not widely used in process tomography to date due to the complexity and cost of such systems. Medical ultrasonic scanners, although costly, are intended for a very limited number of applications and so do not need to be portable. In process tomography there are a vast variety of processes that an ultrasonic scanner could be applied to, but as their process is liable to be unique to a particular plant, custom made scanners would have to be commissioned. This would extend the cost of an already high cost imaging system. However, in keeping with the current demands by industry for simple and effective tomography systems, cost effective ultrasonic scanners are now being developed which utilise a fairly simple source/detection unit. Lines, (1998) described such a system.

#### Lines 1998

Ultrasonic systems unlike any of the other systems described in this thesis, contain single transmitter/detector units, i.e. the unit both emits and detects the ultrasonic waves. The system developed by Lines used an array of piezo-polymer detectors to image weld defects. The system was a hand held system which had interchangeable array heads which meant that the system could be used for a wide range of applications without the need for custom commissioned sensing arrays. The array comprised of 128 linear elements of piezo-polymer which is a highly damped material. The piezo-electric polymer is less sensitive than piezo-ceramics which are much more commonly used, but the piezo-polymer had the highly desirable feature that it could be relatively easily 'customised' to fit a wide variety of applications. The array was moved over the whole surface of the weld to be tested in a linear fashion, and this type of arrangement can be termed 'paintbrush' or longitudinal array scanning. Ultrasonic waves in the frequency range 2MHz – 5MHz were emitted from the array unit which was passed over the scan area. The piezo-polymer array then detected the returning waves and the data was stored. The reader is referred to Lin and Hoyle (1995) for a review of ultrasonic sensor arrangements.

Disadvantages of ultrasonic systems are that they are limited to the speed of sound and so are relatively slow (typically 1 to 10 frames per second) when compared to optical or EIT systems. An interesting and important feature of the system developed by Lines is that resolution and sensitivity were deliberately sacrificed for flexibility in the size and shape in the array design in order to improve customisation and therefore portability and application of such systems.

### 2.2.3 Optical process tomography

As previously mentioned, optical tomography can be defined as imaging systems that employ visible light as a radiation source. The light is usually passed through a medium under test to a detector or detectors placed on the other side of the vessel containing said media. This statement is not strictly correct, as charge coupled devices (CCD) can be used to image not only visible light passed through the media by an emitter, but can be used to image naturally radiating visible light (from flames for example) and so such systems can be termed optical tomography systems even though visible light is not necessarily passed through the media under test.

Optical tomography is best suited for the imaging/detection of particles, pastes, foams, liquid mixing and multi-phase flow. OPT is particularly suited to multiphase flow as the wavelength of the emitted light can be selected to be invisible to the carrier phase of the flow. If for example air was being used to convey a powder through a pipeline, the emitted light would only be attenuated by the flowing powder and not by the carrier phase. In this manner an accurate model of the powder flow can be derived. If the process contained a carrier gas and more than one powder, multi-mode systems in which differing sensors and emitters can be employed could be used to differentiate between the various powders. In such systems two light sources and detectors would be used, the first emitter/detector array would be chosen to be sensitive to one of the powders and insensitive to the other powder and the carrier phase. The second emitter/detector array would be chosen to be sensitive to the other powder. In this way both powders could be imaged individually and at the same time.

The advantages of OPT systems are that the technique is non-invasive, non-intrusive, conceptually simple, safe, high speed, and because light is used rather than electrical properties no interference from electrical noise is encountered; additionally the small

wavelengths used can give high spatial resolution, the response times of the system are minimal, a wide variety of detectors/emitters are commercially available, and the propagation of light through the media under test can be functionally described. The main disadvantages of OPT systems are twofold.

Firstly, OPT requires that a transparent 'window' (often referred to as a sight glass) is incorporated in the vessel containing the media in order for the light to be able to pass through the vessel and media to a detector. This has implications as to the portability of OPT systems. OPT is not therefore ideally suited to portable NDT apparatus as a section of transparent material would have to be inserted into the vessel wall before testing could commence. For example, if the flow of a material in a pipeline were to be imaged or monitored, a section of pipeline would have to be removed in order for a transparent window to be inserted. Depending on the process this may not be possible. If the insertion of a transparent window were possible, the process would have to be taken off-line while the window was inserted and the imaging system set. This would be a very time consuming and therefore costly exercise and is not a desirable procedure in process tomography. If possible, transparent windows should be incorporated into a process at the design stage to allow optical access for optical tomography. Even if optical access were not possible in a process, OPT can still be a valuable tool as the process could be modelled in a laboratory situation where OPT could be employed.

Secondly, in OPT light cannot pass through very dense or opaque media. This is not a problem in object detection, but is obviously a major problem if it is required that the tomography system be able to 'see' inside the object. OPT still has many uses in systems that have dense or opaque processes. For example, an OPT systems could be used to monitor the height of an opaque liquid or solid layer in a separator tanks. If a linear array of detectors were to be placed up the side of the separator tank in increments that related to the liquid height, light could be passed through the separator to the detector array. Light would be detected where there was no opaque liquid or solid, and no light detected where there was opaque liquid or solid. In this manner the height of the opaque material could easily be established. OPT has also been used in the food processing industries as contaminant detectors. Such a system was described by Withers in 1996.

Withers 1996.

The system described by Withers was developed in order that the monitoring of contaminate film build up within food process pipelines be achieved without the need for intrusive or invasive electrodes. This was achieved by employing an optical tomography system that utilised visible light as the illumination source. In the system described by Withers optical windows were inserted into the process pipelines at strategic positions so that optical access could be achieved. As the foodstuff flowed through the pipelines, fouling occurred due to contaminate films building up inside the pipelines, this was obviously a contamination risk and a serious problem when dealing with food. In order to be able to monitor the build up of the contaminate films, a visible light source was positioned on one side of the pipeline and a detector on the other side of the pipeline. The tomographic system was calibrated when no contaminate was present. A certain photogenerated current was then induced in the detector by the light incident on the detector surface. This current was then converted to a voltage, digitised, and stored into memory as a datum value, i.e. all other voltages were compared to this value which denoted a contaminate free pipeline. The process was then allowed to flow and contaminate films started to form on the transparent windows over a period of time.

The process was continuously monitored by the tomographic system, and as the film began to form, the light passed from the light source to the detector was attenuated by the contaminate film and the intensity of the light reaching the detector was reduced. The attenuated light that fell upon the detector surface produced a smaller magnitude of photogenerated current and therefore voltage due to the effects of attenuation. The rate of attenuation was proportional to the thickness of the deposited contaminate film, i.e. the thicker the film the greater the rate of attenuation. As the process continued, a comprehensive range of voltages were detected and stored in memory. The differences in detected light intensities and the associated voltages were used to produce quantitative data that related to the thickness of the contaminate layer. When the contaminate layer became so thick that the visible light could not pass through it, the plant operatives took the process off-line for cleaning. From the data gathered from this process, the intensity of the light source could be chosen to be able to pass through a predetermined thickness of contaminate film.

### Gregory and Hertz 1989

The system developed by Gregory and Hertz used a HeNe laser with a peak wavelength of 685nm as the illumination source and a commercially available array of crystalline silicon photodiodes to image laminar flows of methane and oxygen flowing through a pipeline. The system described utilised a rectangular and circular nozzle to produce a steady state laminar flow of gas through the section of pipeline. As the system was in the steady state, each projection of the process was achieved by altering the rotation of the nozzles between each projection. In order to perform an image capture, light from the laser was passed through a spherical and cylindrical lens arrangement to a concave mirror. The lens arrangement was used to produce a fan beam of light. The concave mirror was angled in such a way as to direct the light through the process to a polarizer and onto another concave mirror. The emerging light was then passed to the photodiode array which was located remotely from the process by the second mirror. A current was then induced in the photodiode array which was converted to a voltage, digitised and then stored.

The system described by Gregory and Hertz scanned the photodiode array 50 times for each projection, each scan taking 16.6ms. Six projections were taken of the process under test which meant that an image capture without processing time would take approximately 1 second. One second is the slowest image capture rate that is generally considered to be acceptable for process tomography (Williams and Beck 1995) and therefore the system described was slow. Other disadvantages of such a system is that it contained very complex optical lens and mirror arrangements which would make the system unsuitable for industrial process tomography where fast, simple and efficient systems are required. The cost of the lens arrangement and also the maintenance and installation of the lens system would also make such a system unsuitable.

An additional problem that could make the system described unsuitable for OPT as with many other developed systems, is that it employed a high intensity laser as the illumination source. Lasers are high cost, complex devices that can be difficult to set up and can pose a serious risk to operator safety. Gregory and Hertz employed neutral density filters to reduce the intensity of the light to reduce the risk to operator safety. However, the use of neutral density filters again increased the cost and complexity of

the system. A further problem with the system was stated by the authors themselves. The crystalline silicon array used to detect the light was an intensified photodiode array which was not required for the application at hand but was the only commercially available device that fitted the physical requirements of the system. This statement highlights the need for sensing materials that can be easily customised for individual process tomography applications.

#### Dugdale *et al* 1991

The system described by Dugdale *et al* was developed to produce three dimensional images of crude oil flowing in a pipeline. The system described used light of 950nm wavelength to which crude oil is semitransparent. Although the system used infrared light as the illumination source, the system design described could utilise visible light for other process tomography applications. Dugdale *et al* attempted to develop a low cost, reliable, fast, accurate tomographic system using commonly available discrete components in order to satisfy the demands of the process industries. The infrared light was supplied via light emitting diodes (LED's) and detected by crystalline silicon PIN photodiodes arranged in arrays around a transparent section of pipeline. The emitter detector pairs were arranged in a parallel fashion with each emitter detector pair forming a view and eight views forming a projection. Eight projections were utilised giving a total of 64 views. In order to capture an image, the first LED and detector in a projection were activated, the remaining LED/detector pairs remained inactive. The LED was pulsed with a current of 1A for a period of several  $\mu$ s and the resulting infrared light was passed to a pinhole. The LED was pulsed for a brief period in order to prevent destruction of the LED device by the high input current. The normally destructive input current was applied to the LED in order to obtain maximum light intensity from the device.

The pinhole was used to collimate the emitted light into a beam of 5mm diameter. The collimated beam was then passed through the flowing process to the corresponding detector placed on the other side of the pipeline. A photogenerated current was induced in the detector which was converted to a voltage, digitised and stored. The LED/detector pair was deactivated and the next view in the projection was activated. This process continued until all 64 views had been activated. The LED/detector pairs

were activated and deactivated in this fashion to ensure that the detector only received light from its corresponding LED emitter. This parallel projection technique allowed image reconstruction algorithms developed for medical x-ray imaging to be used. The system used the differences in voltages caused by the attenuation of the light as it passed through the process to provide the data set required to image the process. The use of transputer networks allowed the process to be imaged in real time.

The system described suffered from several problems. Firstly, the system employed discrete photodiodes as the detector mechanism, thus the dimensions of the detector array and therefore the resolution of the system was limited by the physical dimensions of the photodiodes. The physical size of the photodiodes limited the number of beams that could be used in the system, and for the system described, the light beams had to be placed 13mm apart. The second problem with the system is also related to the size of the photodiodes employed. The active area of the photodiodes were  $4\text{mm}^2$ , thus Dugdale *et al* used a light beam of 5mm diameter in order to completely illuminate the active area of the photodiode, this has been done in order to produce maximum photogenerated current from the photodiodes with the light intensity available from the LED's.

The resolution of the system could be improved by using photodiodes with a smaller active area and packaging, thus increasing the number of photodiodes that could be put into the array. However, the smaller active area of the photodiode would result in less photogenerated current for the same value of light intensity. A possible way to compensate for a smaller photodiode active area would be to increase the intensity of the light beam. Dugdale *et al* proposed that laser diodes could be used for this purpose. However, this would greatly increase the cost and complexity of the system. The system described by Dugdale *et al* again highlighted the problem of having to rely upon commercially available components as the sensing mechanism. Lack of customisation in the sensor array was again a limiting factor in the system design and therefore performance.

Green *et al* 1998

The system developed by Green *et al* was designed to image particulate flowing through a pipeline. Air was used as a carrier phase. Green *et al* acknowledged the problems of poor resolution in previous OPT systems that employed LED's or laser diodes as the illumination source and discrete photodiodes as the detection mechanism due to the physical size of the components. Green *et al* also acknowledged the construction constraints and increased cost imposed by employing said devices.

The system developed by Green *et al* utilised two projections containing 16 views in each projection. In order to improve system resolution, simplify systems design and reduce construction costs, Green *et al* employed a single visible light source (halogen) which was used to supply light to optical fibre light guides. The optical fibre light guides were 1mm in diameter which was a significant reduction in size on LED's or laser diodes, thus more sensors could be placed around the pipeline. Optical fibre light guides were also positioned on the other side of the pipeline to collect the light and convey it to photodiodes where a current was induced, converted to a voltage, digitised and stored for analysis.

The system described by Green *et al* has several advantages over previous systems such as described by Dugdale *et al*. Firstly a single visible light source was used to supply light to all fibre optic light guides in the system. This was achieved by using a parabolic reflector to convert the light emission from the source to parallel rays of light and then passing the light to the light guides without the need for complex and expensive lens arrangements. Secondly the use of fibre optic light guides allowed more sensors to be placed around the pipeline thus increasing the resolution of the system. Thirdly the use of small diameter fibre optic light guides allowed great flexibility in the positioning of the emitter/sensor pairs thus reducing system complexity and constructional problems. Finally, the use of fibre optic light guides to convey the collected light to photodiodes meant that the photodiodes could be positioned remotely to the pipeline thus allowing greater choice in light detection mechanism.

However, the use of 1mm diameter fibre optic light guides did not result in the system being able to resolve 1mm areas of the pipeline. The fibre optic light guides had a

metal block inserted at the end of the fibre optic to columnise the light beam. This light beam however still 'fanned out' as it exited from the collimator and produced a 4mm diameter light beam. A 1mm gap was left between the light beam to prevent divergence of the beams. This meant that the optical fibre light guides had to be placed 5mm apart if interference between the light beams were to be avoided. Although the 5mm resolvable area produced by the system developed by Green *et al* was a significant improvement upon the system developed by Dugdale *et al* (13mm between beams) the resolution of the system may prove insufficient for many applications.

The system developed by Green *et al* was designed to produce parallel light beams in order that reconstruction algorithms developed for x-ray imaging systems could be employed. A way to improve system resolution would be to use fan or cone beam projection and apply the light directly to a sensor array. This however, would lead back to the constructional problems of using commercially available photodiodes. Charge coupled devices have been used to try to overcome this problem.

#### Thomas *et al* 1998

The system developed by Thomas *et al* utilised OPT to image the structure of cellular foams and employed a CCD camera as the detector. The foam in question was a mixture of water and detergent and was created in a Perspex vessel by air being passed through the mixture. The bubble size was of the order of several millimetres. Visible light from a diffuse source was applied to one side of the Perspex vessel. A CCD camera was then used to detect the emerging light. The CCD camera was set at an angle of 60° to the process to reduce the problems of reflection (Darton *et al* 1995). The CCD array in the camera contained approximately 19,000 pixels. The system described by Thomas *et al* was a coaxial tomography system in which the process was revolved around the emitter/detection mechanism. Approximately 25s were required to construct an image of the foam contained within the vessel. Although valid for laboratory experimentation, the time required to reconstruct the image was clearly unacceptable for industrial OPT applications. The system was slow because of the fact that only a single CCD camera was employed. The physical size and cost of the CCD camera prohibited the use of multiple cameras and therefore projections, and which

would also lead to constructional problems. Additionally, the number of pixels in the array led to complex reconstruction algorithms which also slowed the system down.

Any real improvements in systems such as the one described by Thomas *et al* are going to come from the material and device employed as the detector. CCD's most commonly employ crystalline silicon as the photoconductive material. The CCD devices are based upon the same principle of operation as the flat panel digital radiography systems described earlier. The majority of CCD's contain a silicon wafer that is divided up into individual sensing elements (pixels). Each pixel converts optical energy into electrical charge. When the pixel array is scanned, the induced charge is amplified, digitised and stored. CCD's are configured in two main formats these being area scan and line scan devices. In an area scan device, the pixel array is scanned synchronously and a two dimensional image is displayed. In a line scan device, the pixels are configured in a single row array. This row array is scanned from end to end. If relative motion is introduced between the sensor array and the object, a two dimensional image can be produced in which one dimension represents the distance moved between the start of each scan (Fletcher, 1996).

A major limiting factor in the production of CCD's is that they most commonly utilise crystalline semiconductors and therefore cannot be made into array's bigger than around  $5\text{cm}^2$ . Amorphous semiconductors on the other hand, can be made into very large area devices due to their non-crystalline structure. It is possible to 'tile' silicon wafers to make a larger area device but this leads to a loss of resolution along the join lines. Because of their small dimensions when compared to the flat panel devices described earlier, CCD cameras rely upon a lens arrangement to focus the image onto the pixel array. Depending upon the quality of the lens, the process of enlarging or reducing the image can also lead to poor resolution. CCD systems also suffer from shading and blooming problems. Shading occurs when there is a mismatch in the sensitivity of the sensing elements i.e. for the same incident light falling upon two separate pixels, one pixel may generate more current than the other pixel. Blooming occurs when an individual pixel has received more light than it can record and the induced charge spills over into the next pixel or pixels causing distortion of the image. Reflection from shiny surfaces is a major cause of blooming in CCD devices. Charge

injection devices (CID) are currently being developed in an attempt to channel away excess charge from the pixel array.

CCD device's also suffer from image 'lag'. Image lag occurs to the time required to dispel the induced charges from the sensor array. Before another image can be captured, all of the induced charge has to be removed. If any charge were to remain in the sensors array when another image capture was in progress, the residual charge would produce errors in the captured image. It is therefore important that the materials used in the sensor array have fast charging times, can retain the charge for the required amount of time for charge transfer to be completed, and that the residual charge retention of the device be as low as possible in order that any remaining charge can be removed as quickly as possible.

### 2.3 Chapter summary

The literature review has sought to demonstrate that great interest in amorphous semiconductors as sensors for tomographic imaging is currently being shown. The advantages of amorphous semiconductors such as increased sensitivity to radiation, ease of manufacture into large area devices at relatively low cost, and great flexibility in sensor design, has led to ever wider use of amorphous semiconductors particularly in the field of medical radiology.

However, the literature review has also sought to differentiate between the aims and objectives of medical tomography and industrial process tomography. It has been shown that current trends in industrial process tomography are moving away from expensive and complex imaging systems towards the conceptually simple. The motivation behind this trend has been to reduce system purchase cost, maintenance costs, operator training, and risk to operator safety whilst improving system portability and allowing greater flexibility in system design. Improvements in tomographic system design will help provide the process industries with an enhanced understanding of process dynamics leading to more reliable, cost effective, and environmentally friendly processing plants.

It has been shown that commercially available discrete components have been commonly employed in current tomographic system design in attempt to meet the

industries requirements. However, it has also been demonstrated that lack of choice in the selection of components in conjunction with their physical size can place restrictions on the design of any potential imaging system thus limiting system resolution. Because of the nature of amorphous materials they can be manufactured at low cost onto a large number of substrates and into very large area devices. This allows great flexibility in the size and shape of the device. The method of placing gold contacts onto the surface of the amorphous semiconductor devices as employed in the current research, facilitates great flexibility in the customisation of sensor arrays for tomographic application, thus lifting the restrictions that can be imposed by discrete devices. The a-As<sub>2</sub>Se<sub>3</sub> and a-Si:H materials employed in the research also have the benefits of being sensitive to the entire visible spectrum, are mechanically and chemically stable, and can be operated at high temperature. I therefore believe that amorphous semiconductors employed as optical sensors can contribute to the advancement of process tomographic imaging systems, thus helping to meet the current requirements of the process industries.

## **CHAPTER 3**

### **AMORPHOUS SEMICONDUCTORS**

The term amorphous can be defined as ‘shapeless’, disorganised’, or ‘random’. Amorphous materials can be insulators, semiconductors, or superconductors in which periodicity is absent (Mott and Davis, 1979 and Elliot, 1992) i.e. they are not bonded by the same rigid constraints that crystalline materials are. Amorphous semiconductors possess the following advantages over crystalline materials that I believe make them particularly suitable for application in OPT.

The a-As<sub>2</sub>Se<sub>3</sub> and a-Si:H materials employed in the current research were non-commercial xerographic drums manufactured by various research organisations which were donated to this research. In order to justify the use of the a-As<sub>2</sub>Se<sub>3</sub> and a-Si:H samples available to the current research project, the integrity of the samples had to be established. This sample validation process was achieved by the means of a xerographic investigation. As mentioned previously, both a-As<sub>2</sub>Se<sub>3</sub> and a-Si:H were the subject of intense investigation during the mid 1980’s to early 1990’s for application in the xerographic industries. Since then, organic materials have dominated the xerographic industry. As such, many works relating to the xerographic properties and physical behaviour of the a-As<sub>2</sub>Se<sub>3</sub> and a-Si:H materials were published during this time period. The current research therefore, sought to perform xerographic investigation upon the a-As<sub>2</sub>Se<sub>3</sub> and a-Si:H devices and compare both the experimental results and analytical results to previous published work. If a good agreement in experimental results and physical phenomena presented in prior published works could be demonstrated, validation of the integrity of the samples could be confirmed. The results of the xerographic investigation are detailed in chapter five. A brief description of the a-As<sub>2</sub>Se<sub>3</sub> and a-Si:H materials follows. A discussion of the xerographic measurements and relevant models employed in the current investigation is then presented.

#### **3.1 Amorphous arsenic triselenide**

Amorphous selenium (a-Se) is a chalcogenide glass that was first investigated for use in the xerographic industries in the early 1950’s and has commonly been used in the xerographic industries since then. Amorphous selenium is a highly sensitive material

which is particularly sensitive to the blue region of the visible spectrum. This could be seen as a disadvantage in xerographic and tomographic imaging systems as it could limit the type of light source that can be employed in the imaging system. Optical filters could be used to produce light of the required wavelength, but this would increase the complexity and cost of the imaging system. A requirement of xerographic photoreceptors (as with OPT sensors) is that they are sensitive to the entire visible region of the electromagnetic spectrum. The sensitivity of a-Se in the red region can be improved by the addition of tellurium (Te) to the a-Se film. The addition of arsenic (As) to the a-Se film can also improve stability and increase the sensitivity of the film in the red region of the visible spectrum.

Amorphous selenium (a-Se) also suffers from the additional problems of structural instability which could make it unsuitable for tomographic imaging systems. Amorphous selenium can crystallise at temperatures above 100°C which will mean that the a-Se film will become very highly conductive and any applied electrostatic charge will dissipate almost as quickly as it is deposited. The introduction of As not only increases the sensitivity of the a-Se film, it can also retard the crystallisation rate if the quantity of As is sufficient. Selenium alloys comprising of 40% As and 60% a-Se are termed a-As<sub>2</sub>Se<sub>3</sub> and are sensitive to the entire visible spectrum and are more mechanically and chemically durable than a-Se alloys containing much smaller (less than 1%) amounts of As. The addition of 40% As to the a-Se results in crystallisation now occurring at a much higher temperature of approximately 300°C (Kasap 1991), thus a-As<sub>2</sub>Se<sub>3</sub> has the potential to be employed in extreme processing conditions.

In a-As<sub>2</sub>Se<sub>3</sub> films, only the holes are mobile within the film. The addition of 40% As to the a-Se also has an effect upon the drift mobility of the holes within the film. The As acts as a shallow hole trap that can result in a build up of residual potential when the film is subjected to a charge of positive polarity or exposed to highly absorbed visible light. The build up of residual potential is an undesirable feature that could cause poor image resolution in xerographic and tomographic imaging systems. In order to reduce or eliminate the build up of hole trapping due to the addition of As to the a-Se film, chlorine (Cl) in the order of 10-50ppm is added to the a-As<sub>2</sub>Se<sub>3</sub> film (Pai 1997). The addition of Cl improves the hole mobility within the a-As<sub>2</sub>Se<sub>3</sub> film which compensates for the hole trapping caused by the addition of As, thus the build

up of residual potential is averted. However, the addition of Cl to the a-As<sub>2</sub>Se<sub>3</sub> film can have a disadvantage. If excess Cl is added to the a-As<sub>2</sub>Se<sub>3</sub> film, once the Cl has compensated for the hole trapping caused by the addition of As, it has no effect upon the hole mobility. The excess Cl does however affect the dark decay of the a-As<sub>2</sub>Se<sub>3</sub> film. As the thermal generation rate of a-Se is low, the a-As<sub>2</sub>Se<sub>3</sub> films can easily be charged to high surface potentials, thus the effect of excess Cl on the dark decay is not of critical importance.

A potential problem of employing a-As<sub>2</sub>Se<sub>3</sub> as an image sensor for OPT applications is that it is a glass and therefore inflexible, brittle, and therefore prone to damage. The rigid and delicate nature of a-As<sub>2</sub>Se<sub>3</sub> could prove troublesome in the design of a versatile sensor array. Amorphous selenium has a mechanical hardness (Vickers) of 30-50 kg/mm<sup>2</sup>. The addition of As to the a-Se film also has an effect on the mechanical hardness of the a-Se film, a-As<sub>2</sub>Se<sub>3</sub> has a mechanical hardness (Vickers) of 150-200 kg/mm<sup>2</sup>. The hardness of the sensors material is an important consideration as if the surfaces of the sensors were to become scratched, the optoelectronic responses of the materials would deteriorate and the sensor become useless. The mechanical hardness of the materials is an important factor as to the materials scratch resistance.

### 3.2 Hydrogenated amorphous silicon

Amorphous silicon (a-Si) is an extrinsic semiconductor that can be used as a photoreceptor. Amorphous silicon was traditionally fabricated by the thermal evaporation of the material followed by condensation onto a cooled substrate. The high boiling point of the silicon meant that electron beam evaporation had to be employed which resulted in the a-Si having an electrical resistivity of approximately 10<sup>3</sup> Ω/cm. The low electrical resistivity of the a-Si made it unsuitable for xerography as only low levels of electrostatic charge could be applied to the film surface which were insufficient for xerographic applications. The problem of the low resistivity of a-Si was overcome in the mid 1960's by the addition of hydrogen to the a-Si. The production of hydrogenated amorphous silicon (a-Si:H) was achieved by the glow discharge dissociation of silane gas (SiH<sub>4</sub>). The a-Si:H films had an electrical resistivity of 10<sup>9</sup> Ω/cm (Mort 1991), and as such allowed greater surface charges to be

deposited upon them. However, the range of application with this new value of resistance was still limited, thus research focused on how to improve the resistivity of the a-Si:H films.

The properties of a-Si and a-Si:H are critically dependent upon the density of localised states in the band gap. Such localised states arise from the inherent disorder and the presence of electrically active impurities (Mott and Davis 1979). The dominant state in a-Si is due to dangling bonds which are broken silicon bonds. Hydrogen can be added to the a-Si in order to effectively remove the dangling bonds and their localised states. The hydrogen does this by attaching to the dangling bonds which produces a lower concentration of gap states which increases the bandgap of the material. The a-Si:H sample used in the current research was doped with boron (B) by the manufacturers to make the material P type and to further improve the resistivity of the a-Si:H material. The position of the Fermi level relative to the conduction band denotes the number of free carriers within the film. In the undoped a-Si:H, the Fermi level is close to the conduction band which results in a greater number of free carriers within the film. The addition of boron to the a-Si:H at around 10ppm (Mort 1991), moves the Fermi level back towards the midpoint of the bandgap. This results in a decrease in the number of free carriers in the film and a resulting increase in the electrical resistivity of the film to approximately  $10^{13} \Omega/\text{cm}$ . The higher value of resistivity makes the a-Si:H material much more suitable for xerographic and tomographic processes as the increased resistivity allows greater surface charges to be placed upon the surface of the film.

Hydrogenated amorphous silicon is sensitive to the entire visible region of the electromagnetic spectrum, can be operated at temperatures of up to  $250^{\circ}\text{C}$  (Kasap 1991) and has a mechanical hardness (Vickers) of approximately  $1500 \text{ kg/mm}^2$  (Bauer and Paasche 1987). Hydrogenated amorphous silicon absorbs visible light more efficiently than crystalline silicon (c-Si) due to its superior absorption coefficient (Guba 2000). Hydrogenated amorphous silicon has an absorption edge at a higher energy than c-Si. This property is due to the loss of momentum conservation in the disordered structure and ensures that visible light is absorbed within approximately  $1\mu\text{m}$  of the film surface as opposed to hundreds of  $\mu\text{m}$  for c-Si (Palma 2000). This

property leads to lower manufacturing costs for a-Si:H devices as opposed to c-Si devices.

### 3.3 Xerography

Electrophotography or xerography is from the Greek terms xeros (dry), and graphos (write) and was invented in 1938 by C.F. Carlson. Xerography describes the formation of images produced by the creation of electrostatic charge patterns which are made visible to the human eye by the addition of charged pigment particles. Although imaging by the use of charge patterns can be traced back to Lichtenberg in 1778, Carlson was the first person to create a latent image on the surface of a charged photoconducting insulator by the use of selective photodischarge. Carlson went on to develop an automatic copying machine in 1942. In recent years the xerographic industry has had an annual income of over £60 billion (Borsenburger and Wiess 1998). A material is deemed suitable for use as a xerographic photoreceptor if the following requirements can be met.

#### 1. Good charge acceptance.

The material employed in the xerographic system must be capable of accepting high levels of surface charge deposited by corona charging. Levels of surface charge considered to be acceptable for xerographic applications are between  $0.5 \times 10^{-7}$  and  $1.5 \times 10^{-7} \text{ C/cm}^2$  (Schaffert 1975).

#### 2. Slow rate of dark decay.

The charge applied to the surface must be retained by the material long enough for the xerographic process to be completed. Thus the rate at which the applied charge dissipates in the dark must be as slow as possible.

#### 3. Rapid photoinduced discharge (PID).

For formation of a latent image upon the surface of a charged photoreceptor, the applied charge must be selectively photodischarged in order to form the charge pattern. Thus in order to obtain good contrast between the charged and uncharged areas, the material should dispel charge quickly and efficiently when exposed to visible light. Additionally, once the charge pattern has been formed and transferred to another medium, any remaining charge must be removed from the surface of the

material before the charging process can be repeated. The remaining charge is usually removed by flooding the surface of the material with visible light. The efficiency at which this charge can be removed dictates the speed of operation of any imaging system.

#### 4. Low residual potential.

If the charged material is left to decay over time in the dark or is discharged by illumination, the charge may not be completely dispelled and a small charge may remain. The remaining charge after dark decay or PID has taken place is termed the residual potential. In xerographic imaging systems it is desirable that the residual potential be as small as possible. Residual potential is problematic as it may build up with repeated imaging cycles. This means that the resolution of any measuring system will decrease with an increase in residual potential. In xerographic systems the build up in residual potential can also lead to poor contrast between charged and discharge areas in the latent image.

#### 5. Repeatability during repetitive imaging cycles.

Depending upon the application of an imaging system, the system may be required to produce images over multiple cycles, thus it is essential that the charge acceptance, partially charged areas, and the residual potential be maintainable, i.e. that they are reproducible over repetitive cycles. Photoreceptors are said to be fatigued when the electrical properties, and therefore imaging qualities deteriorate over a period of time due to repetitive use. The effects of fatigue usually wear off if the photoreceptor is allowed to rest in the dark. However, in xerographic systems such as laser printers and photocopiers, high image capture rates are required which need to be maintained for extended periods of time. In such systems fatigue can be very problematic. The speed of operation of a given system will be determined not only by the charge retention and PID rates, but also by the time required for the photoreceptor to regain its electrical properties after a xerographic has been performed. If the repetition rate of the process is faster than the time required by the photoreceptor to recover its electrical properties then the photoreceptor will suffer from fatigue and will lose its ability to produce images. Thus the rate at which a photoreceptor material fatigues is an important consideration when selecting a material for the image sensor.

The xerographic investigation reported here, aimed to provide an insight as to the charge acceptance, dark decay, and PID characteristics of the a-As<sub>2</sub>Se<sub>3</sub> and a-Si:H materials. An experimental apparatus was developed to facilitate this xerographic investigation and is detailed in chapter four along with experimental procedures employed. A discussion of the main topics of the xerographic investigation follows.

### 3.4 Charge acceptance.

The charge acceptance of a photoreceptor is the maximum amount of electrostatic charge that can be applied upon the surface of the photoreceptor under test. When ions are deposited onto the surface of the photoreceptor by corona charging, charges of the opposite polarity to that of the coronode will be induced in the substrate electrode. As the corona charging of the sample continues, the two charge distributions will reach an equilibrium point. At this point of equilibrium, no more electrostatic charge can be placed upon the surface of the photoreceptor as the charge leaks away as quickly as it is applied. The surface potential detected at this point of equilibrium is termed the acceptance potential ( $V_a$ ). The surface potential detected at the equilibrium point is related to the surface charge density ( $\delta$ ) by the following equation (Pai and Springett 1993, and Borsenburger and Wiess 1993) which treats the photoreceptor sample as a capacitor with the bulk layer regarded as a dielectric.

$$V_a = \left( \frac{\delta}{C} \right) = \left( \frac{eL}{\epsilon_o \epsilon_r} \right) \delta \quad (3.1)$$

Where  $V_a$  is the acceptance potential (V).

$e$  is the basic electron charge (C).

$\epsilon_o$  is the permittivity of free space (F/cm).

$\epsilon_r$  is the dielectric constant of the amorphous semiconductor layer.

$L$  is the thickness of the amorphous semiconductor layer (cm).

$\delta$  is the surface charge density (C/cm<sup>2</sup> eV).

$C$  is the geometric capacitance of the amorphous semiconductor layer (F).

Rearranging (3.1) in terms of  $\delta$  gives

$$\delta = \frac{V_a \epsilon_o \epsilon_r}{eL} \quad (3.2)$$

Thus the surface charge density can be calculated from the experimentally determined acceptance potential, film thickness, and the materials dielectric constant. The amount of charge that can be placed and retained upon the photoreceptor surface is due to the number of charge carriers generated or injected into the film. There are three main sources of charge carrier injection.

(i) Injection of free charge carriers at the photoreceptor surface.

The free surface of the photoreceptor acts as a blocking layer. This blocking layer prevents charge from being injected into the bulk of the photoreceptor layer. However, blocking layers are not wholly effective and charge carriers can be injected into the film which can dominate the dark decay of the material in the early stages of the dark decay process. The phenomena of surface injection is discussed in more detail later.

(ii) Thermally released carriers within the bulk of the photoreceptor layer

Early models of dark decay such as proposed by Schaffert 1975, neglected the contribution of thermally released charge carriers in the bulk layer at room temperature, with the charge carriers being solely injected from the photoreceptor sample substrate. Thus models as described by Schaffert considered the charging process to be purely capacitive. Subsequent research based upon the work of Amick 1959, has shown that thermally released carriers in the bulk of the layer significantly contribute to the charging process and show in fact, that the charging process is both capacitive and depletive. Pai 1998, described this charging process using a model that assumes the photoreceptor layer has a uniformly distributed number of hole trapping centres throughout the film, and that these trapping centres can be thermally ionised. The hole trapping centres are assumed to be negatively charged when ionised, and neutral when occupied. The model further assumes that the injection of charge carriers from the photoreceptor surface is negligible.

Thermal generation creates a free hole and a localised negatively charged trapping centre within the bulk layer. When the positive corona charging of the photoreceptor sample commences, any free holes within the bulk of the photoreceptor layer will be swept out of the film. As the charging process removes free holes from the bulk layer only the negatively charged localised trapping centres remain. As the corona charging process continues, the positive charges being placed upon the surface of the

photoreceptor are effectively neutralised by the negatively charged trapping centres. This process is termed depletion charging, i.e., the empty negatively charged trapping centres are being filled with the positive charge carriers and the induced surface charge is being depleted. The region in the bulk layer that contains the trapping centres is termed the depletion zone and is initially located just below the surface of the photoreceptor surface layer. As the corona charging process continues, the surface charge density ( $\delta$ ) increases and the trapping centres continue to be filled by the positive charge carriers. As more and more trapping centres start to fill up with charge carriers the depletion zone begins to expand. When the surface charge density is such that all of the trapping centres have been filled, the depletion of the negatively charged trapping centres is complete and the depletion zone extends all the way to the photoreceptor substrate. Once the depletion zone reaches the substrate of the photoreceptor, the charging process is purely capacitive, with the grounded substrate regarded as one electrode of the capacitor and the coronode of the corona charger, the other electrode. Figure 3.1 shows the two charging mechanisms. The graph was compiled using test data gathered from a dark decay curve for a sample of the a-Si:H material. The surface voltage at corona charging cessation ( $V_o$ ) was 449.34V and the stated relative permittivity ( $\epsilon_r$ ) for the material was taken as  $10^\dagger$ .

The surface charge density at the acceptance potential was  $9.16 \times 10^{11}$  (C/cm<sup>2</sup>). The number of trapping centres ( $N_b$ ) were chosen as 0,  $2.5 \times 10^{14}$ , and  $1 \times 10^{15}$  in order to demonstrate the charging process. Equations 3.3 and 3.4 (Borsenburger and Wiess, 1993) were used to calculate the charge data for the cases of  $\delta < (N_b \times L)$  and  $\delta > (N_b \times L)$  respectively.

For  $\delta < (N_b \times L)$

$$V = \frac{e\delta^2}{2\epsilon_0\epsilon_r N_b} \text{ Volts} \quad (3.3)$$

For  $\delta > (N_b \times L)$

$$V = \left( \frac{eL}{\epsilon_0\epsilon_r} \right) \left( \delta - \left( \frac{N_b L}{2} \right) \right) \text{ Volts} \quad (3.4)$$

<sup>†</sup> The relative permittivity of the a-Si:H material was determined and supplied to us by Imperial College who were the manufacturing and donating organisation of the a-Si:H materials employed in this research.

From Figure 3.1 it can be seen that for  $N_b=1 \times 10^{15}$  ( $\delta < N_b \times L$ ) the charging curve is non-linear indicating depletion charging. The charge curve can be seen to rise slowly and non-linearly indicating the filling of the trapping centres by the free carriers in the bulk of the photoreceptor film. Series  $N_b=2.5 \times 10^{14}$  assumes that charging has proceeded, and as such, the number of trapping centres has reduced due to free carriers filling the empty traps thus the depletion zone has widened. It can now be seen that the charge curve again shows non-linearity for surface charge densities of less than  $7 \times 10^{11}$  (C/cm<sup>2</sup>) eV but is starting to show linearity at surface charge densities of greater than  $7 \times 10^{11}$  (C/cm<sup>2</sup>) eV. This indicates that as the number of trapping centres has been further reduced and the depletion zone has widened even further towards the photoreceptor substrate and the charging is becoming more capacitive. Finally series  $N_b=0$  shows capacitive charging. The response is completely linear which means that all of the trapping centres have been filled and the depletion zone has extended all of the way to the photoreceptor substrate.

In order that a photoreceptor can be charged to a high, and therefore useful surface potential, the photoreceptor material must exhibit very high electrical resistivity. Although the current research project is not concerned with xerography itself, the electrical resistivity of the photoreceptor material is an important factor when considering the conductivity of the material. The conductivity of the material is of great importance for tomography. For most optical tomography systems, light is passed through a vessel and medium to a optical detector/detectors located on the other side of the vessel. The light incident upon the surface of the photoreceptor gives rise to a photocurrent within the photoreceptor layer which is normally converted to a voltage and digitised.

The analysis of the dark decay curves gives information as to the dark resistivity ( $\rho$ ) in  $\Omega/\text{cm}$  and the current density ( $j$ ) in  $\text{A}/\text{cm}^2$  of the photoreceptor materials. According to Schaffert 1975 and Vaezi-Nejad 1984, the dark resistivity in a-Se based materials can be determined from the slope of a  $\ln V$  vs  $t$  plot of the dark decay curve experimental data which is in the form

$$\rho = - \left( \frac{1}{\epsilon_0 \epsilon_r} \right) \left( \frac{d}{dt} \ln V \right)^{-1} \quad (3.5)$$

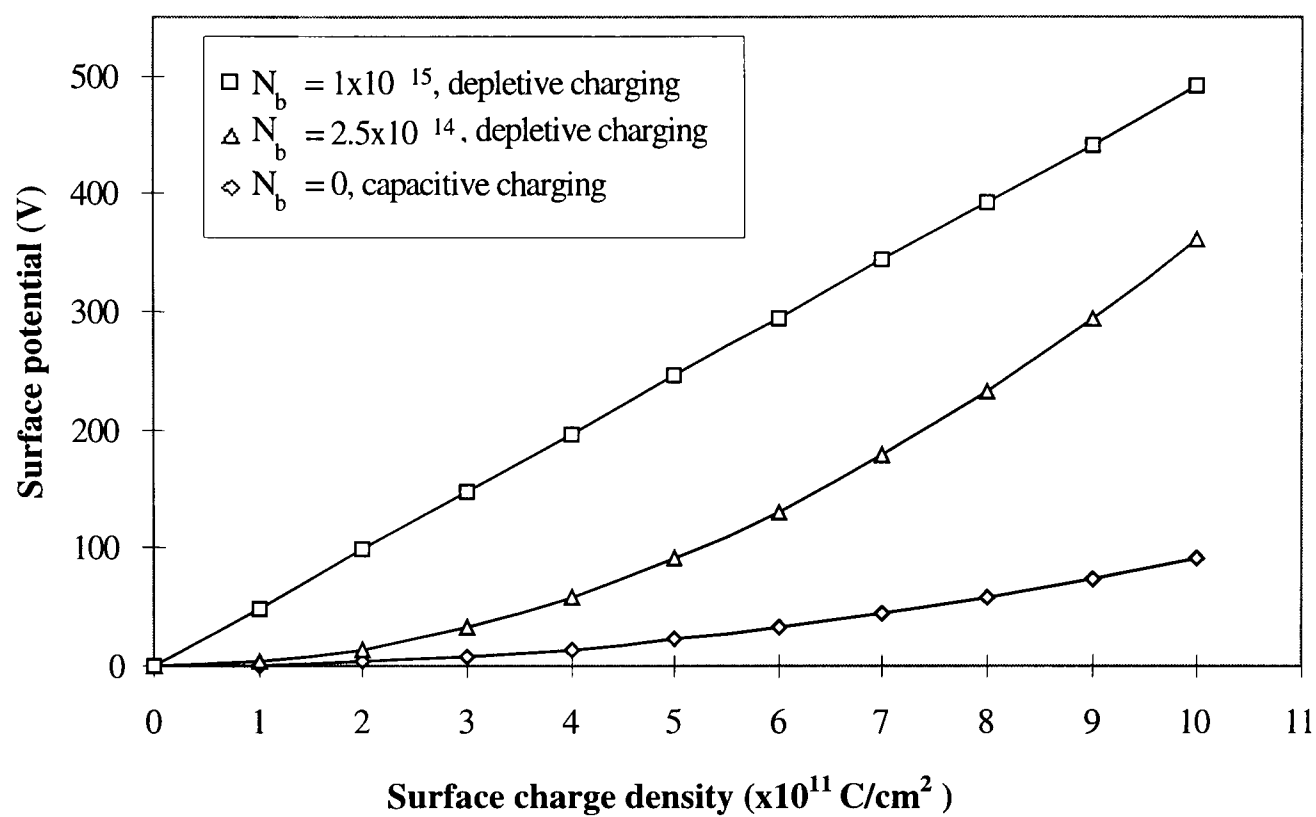


**Figure 3.1** Graph showing surface charge density vs surface potential for depletion and capacitive charging.

The slope of the dark decay curve is negative, thus the minus sign in Equation 3.5 can be ignored for computational purposes. The current density of the film ( $j$ ) in  $A/cm^2$  can also be determined from the experimental dark decay curve data by determining the slope of a  $V$  vs  $t$  plot. The current flowing through the photoreceptor film is therefore proportional to the slope of the  $V$  vs  $t$  plot which is in the form

$$j = \left( \frac{\epsilon_r}{L} \frac{dV}{dt} \right) \epsilon_0 \quad (3.6)$$

### 3.5 Dark decay.

#### 3.5.1 Amorphous arsenic triselenide

Once corona charging of the photoreceptor sample has ceased ( $t=0$ ), all of the trapping centres in the bulk of the layer are full and the depletion zone extends all of the way down to the photoreceptor substrate and the device can be thought of as a capacitor. As the bulk of the photoreceptor layer is not a perfect insulator, the applied surface charge will leak away in a dark environment over time. The electrostatic charge placed upon its surface will start to decay due to dark currents flowing in the film. Major contributors to the dark decay include the thermal generation of charge carriers in the bulk of the film (assuming that the substrate is non-injecting), and the injection of charge carriers from the surface. The dark discharge of  $a\text{-As}_2\text{Se}_3$  is thought to occur due to xerographic depletion discharge (XDD). The XDD process involves the thermal generation of mobile charge carriers (of the same sign as the surface charge) which become mobile within the bulk layer of the photoreceptor. As corona charging ceases, the thermally generated charge carriers are released from the trapping centres previously described, and are swept out of the bulk layer by an internal electric field leaving behind a deeply trapped space charge of the opposite sign to the thermally generated charge carrier. This negatively charged space region builds up as time proceeds causing the applied surface charge to decay. In the XDD mechanism, the rate of dark discharge is limited by the rate at which the negative space charge region builds up in the bulk of the layer. The XDD process is as follows and is shown graphically in figure 3.2.

A) Initially during the dark decay process, the density of negative space charges ( $\rho$ ) is less than the surface charge density ( $\delta$ ) i.e.  $\delta > \rho L$  at  $t=0$ . The depth at which the applied electric field is equal to 0 ( $X(Z_0)$  measured from the top surface of the photoreceptor) is equal to the thickness of the film i.e.  $X(Z_0) = L$ . This means that  $X(Z_0)$  extends all of the way down to the substrate and all of the trapping centres within the bulk layer are charged. In this condition, the bulk of the photoreceptor could be considered a perfect insulator and no loss of surface charge would occur therefore  $X(Z_0)$  would be independent of time.

B) However, at  $t > 0$  the thermal generation of charge carriers in the bulk layer and the injection of charge carriers from the surface of the photoreceptor will lead to dark currents which will induce dark decay of the applied electrostatic charge. As time proceeds, charge will be lost from the bulk layer due to the continued thermal generation of charge carriers. This means that the applied electric field will start to deplete, leaving behind the increasing spatially uniform space charge region at the grounded substrate. Under these conditions the electric field ( $E$ ) falls linearly with distance from the top surface of the photoreceptor.

C) As time continues to proceed, a point is reached where the surface charge density is equal to the space charge density ( $\rho$ ), i.e.  $\rho L = \delta$ . The point in time that this phenomena occurs is termed the depletion time ( $t_d$ ). The depletion time marks the point at which  $X(Z_0)$  is at the grounded substrate of the photoreceptor, and also marks a change in the dark discharge mechanism. For times greater than the depletion time, the applied electric field will be at a distance  $X(Z_0) < L$  from the surface of the photoreceptor, i.e. the distance at which the applied electric field is equal to 0, moves away from the grounded substrate and approaches the photoreceptor surface. This creates a neutral region that extends from  $X(Z_0)$  down to  $L$ . This means that holes generated within the  $X(Z_0)$  to the photoreceptor surface region which move into the neutral region from  $X(Z_0)$  to  $L$  will not be swept out of the bulk layer.

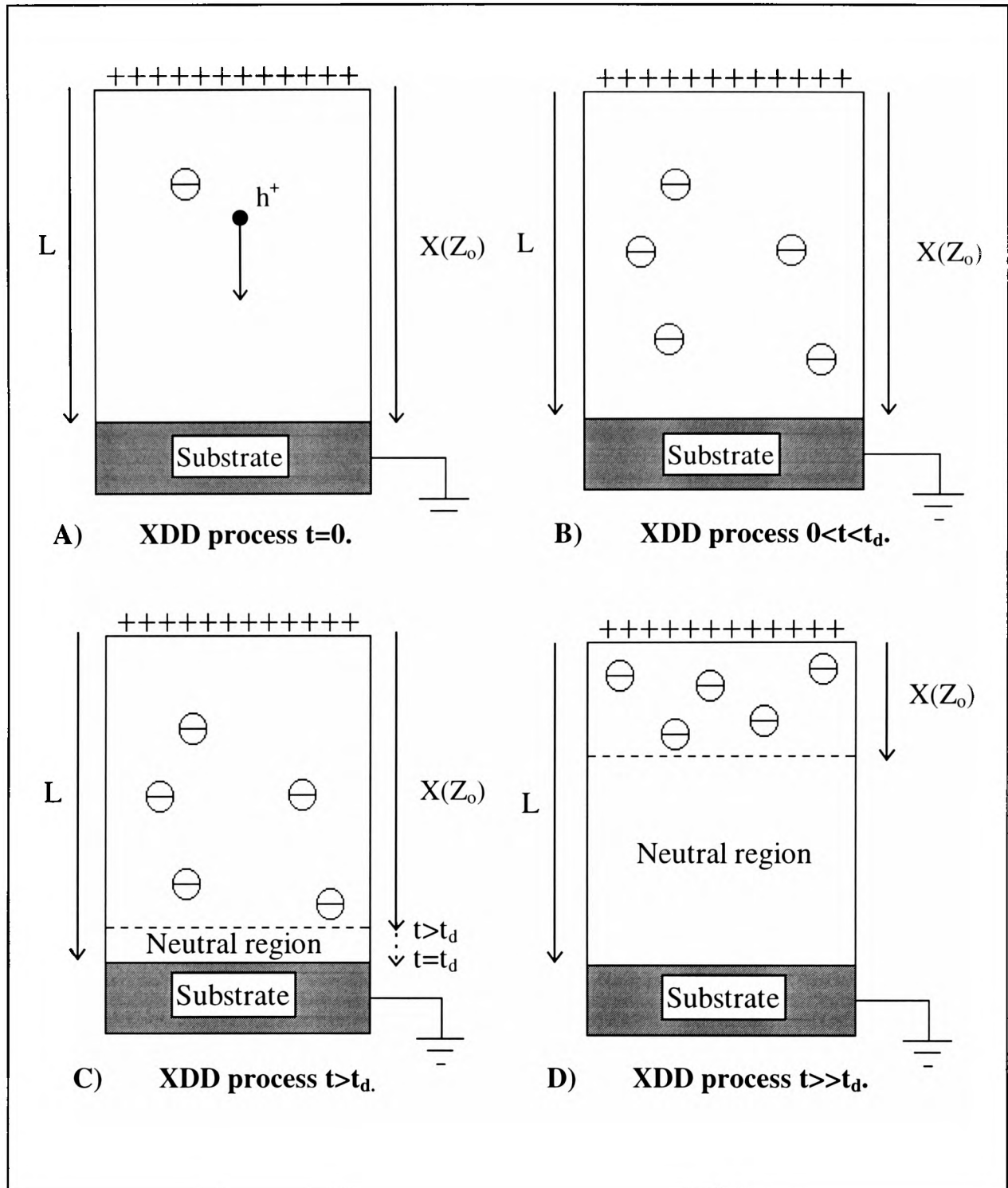


**Figure 3.2** Xerographic depletion discharge process. (Adapted from Kasap, 1991).

D) As time proceeds past  $t_d$ ,  $X(Z_o)$  becomes

$$X(Z_o) = \frac{\delta}{\rho} \text{ when } < L \quad (3.7)$$

This means that the surface charge density is being depleted by the space charge density within the bulk layer. As the holes are no longer being swept out of the bulk layer, the surface charge is being neutralised by the generated holes. When  $X(Z_o)$  is equal to 0, the bulk layer has been completely depleted of charge and has regained its space charge neutrality. Thus the dark discharge can be divided into two time zones these being when  $t < t_d$  and when  $t > t_d$ . At  $t \ll t_d$  the discharge process can be considered to be capacitive, and at  $t > t_d$  it is depletive. The discharge observed from  $t > 0$  to  $t < t_d$  is due to surface injection, i.e. surface generated current is injected into the bulk layer and thermal generation of charge carriers in the bulk. It is an essential requirement when performing dark decay experimentation, that the two surfaces of the photoreceptor do not inject charge into the bulk of the photoreceptor layer. This is so that the measured dark decay curve is due to the thermal generation and sweep out of charge carriers in the bulk of the layer and not due to any other source. However, even with the use of thin blocking layers between the substrate and the photoconductor, a fraction of the surface charge is injected into the bulk of the photoreceptor, and this current ( $J_s$ ) can dominate the dark decay in the  $t < t_d$  time period in a-As<sub>2</sub>Se<sub>3</sub> (Melnik 1980).

#### (i) Models of XDD

Early attempts to developed models to explain the dark discharge of a-Se and a-As<sub>2</sub>Se<sub>3</sub> were carried out by investigators such as Ing and Neyhart 1972, Kiess 1972, and Schien 1974. These early investigators attempted to deconvolute the dark currents flowing in the photoreceptor bulk by observing the dark decay curves for a series of samples of varying thickness over a range of charging voltages. However, these early models have had doubt cast as to their validity by latter researchers. In fact it is now known that the results were affected by incompletely resolved test data, specifically that the experimental data was not resolved past  $t_d$ .

The first a-As<sub>2</sub>Se<sub>3</sub> specific XDD model was proposed by Montrimas *et al* in 1972, and was an attempt to explain the dark discharge mechanism in this material. The XDD

model was developed further by Melnyk in 1980, and then by Abkowitz *et al* in 1985 (hereon after referred to as the Abkowitz model). Abkowitz *et al* developed a XDD model in which the dark discharge mechanism in a-As<sub>2</sub>Se<sub>3</sub> could be resolved. The model describes two time zones ( $t < t_d$  and  $t > t_d$  previously described) in which the rate of dark discharge is shown to behave differently, i.e. a minimum of two discharge mechanisms effect the dark decay. A limitation of the Abkowitz model is the assumption that the depletion time  $t_d$  is independent of the electric field. Kasap *et al* 1987 and Kasap 1989, (hereon after referred to as the Kasap model) developed the Abkowitz model further to demonstrate that the depletion time was in fact field dependent and was related to the initially deposited surface potential.

#### Abkowitz *et al*, 1985

The Abkowitz model was specifically developed to overcome the limitations of earlier models which neglected the effect of significant trapping due to the thermal generation of charge carriers and the simultaneous formation of a space charge region in the bulk layer of the photoreceptor. The XDD model is so termed as the discharge process relies upon the removal of one sign of charge carrier from the bulk layer. The XDD model also relies upon the fact that only one sign of the thermally generated charge carriers is mobile throughout the bulk layer.

The Abkowitz model describes an analytical process which allows the establishment of the two major contributors, i.e. current injected from the surface of the photoreceptor ( $J_s$ ) and current thermally generated in the bulk of the photoreceptor ( $G_B$ ) to the dark discharge to be distinguished without the need for the deconvolution procedure previously described. Abkowitz states that the instantaneous surface potential can be determined by integrating the applied electric field  $E(z)$  from the top surface of the photoreceptor to the depth at which  $X(Z_0)$  resides. This process yielded:

$$V = \frac{1}{\epsilon_r \epsilon_0} \int_0^{Z_0} dz E(z) \quad (3.8)$$

Where

- V is the surface potential (V).
- $Z_0$  is the depth at which the electric field in the bulk layer = 0.
- $\epsilon_0$  is the permittivity of free space (F/cm).

$\epsilon_r$  is the relative permittivity.

$E(z)$  is the electric field at  $z$  (V/cm).

Equation 3.8 yields

$$V = \frac{1}{\epsilon_r \epsilon_0} \int_0^{Z_0} dz \left[ \delta - \int_0^z dz \rho(z) \right] \quad (3.9)$$

Where

$\delta$  is the surface charge density (C/cm<sup>2</sup> eV).

$\rho$  is the space charge density.

When the dimension  $Z_0 < L$  ( $t > t_d$ ),  $Z_0$  and  $\delta$  are related by

$$\delta = \int_0^{Z_0} \rho(z) dz \quad (3.10)$$

Abkowitz goes on to state that if the XDD mechanism proceeds by a spatial uniform process, equations 3.8 and 3.9 simplify giving the instantaneous surface voltage as

$$V = \frac{\delta Z_0}{\epsilon_0 \epsilon_r} - \frac{\rho Z_0^2}{2 \epsilon_0 \epsilon_r} \quad (3.11)$$

The depletion time marks the boundary between the two time zones, and occurs when the charge in the bulk of the layer equals the charge remaining upon the surface of the photoreceptor, i.e.

$$\rho L = \delta \quad \text{at } t = t_d \quad (3.12)$$

In the depletion process from  $0 < t < t_d$ , the depletion is due to surface injection and the thermal generation of charge carriers in the bulk layer. However, at  $t < t_d$  although the surface charge density is decreasing with time, the volume of the bulk has not reduced as at  $t < t_d$  it is the counter charges at the grounded substrate that are being neutralised; the dimension  $X(Z_0)$  does not change, i.e.  $X(Z_0)$  is still =  $L$ . At  $t > t_d$  the depleted volume of the bulk layer does reduce and the dimension  $X(Z_0)$  moves towards  $E=0$ , i.e. the top surface of the photoreceptor. As  $t < t_d$  and  $t > t_d$  have different discharge

mechanisms separated by  $t=t_d$ , the point at which  $t=t_d$  should clearly show a change in the dark discharge rate when plotted against the decay time.

The Abkowitz model assumes that initially there is no surface charge loss due to surface injection on the dark discharge rate in the time zone  $t < t_d$ . This means that the dark discharge would be entirely due to the thermal generation of charge carriers in the bulk of the layer and the counter charges at the substrate being neutralised.

Thus in time zone 1  $\left(\frac{d\delta}{dt}=0\right)$  giving

$$V = \frac{\delta L}{\epsilon_0 \epsilon_r} - \frac{\rho L^2}{2\epsilon_0 \epsilon_r} \quad (3.13)$$

Which yields

$$\frac{dV}{dt} = -\frac{L^2}{2\epsilon_0 \epsilon_r} \frac{d\rho}{dt} \quad (3.14)$$

In time zone 2,  $t > t_d$

$$V = \frac{\delta^2}{2\epsilon_0 \epsilon_r \rho} \quad (3.15)$$

Which yields

$$\frac{dV}{dt} = -\frac{\delta^2}{2\epsilon_0 \epsilon_r \rho^2} \frac{d\rho}{dt} \quad (3.16)$$

Abkowitz states that when  $t=0$ ,  $V$  must equal the initial voltage deposited on the photoreceptor surface ( $V_0$ ). Also at  $t=0$ ,  $V_0$  must equal the surface charge density multiplied by the thickness of the film, divided by the permittivity of the sample, thus

$$V_{t=0} = \frac{\delta L}{\epsilon_0 \epsilon_r} \quad (3.17)$$

At  $t=t_d$   $\rho L = \delta$  thus

$$V = \frac{\delta L}{2\epsilon_0 \epsilon_r} = \frac{V_0}{2} \quad (3.18)$$

This means that if there were no contribution to the dark discharge due to surface injection,  $V(t_d)$  should be half  $V_0$ . Thus the contribution of surface injection on the dark discharge rate in the time zone  $t < t_d$  can be determined from experimental dark decay data. It has been shown that without the contribution of surface injection to the dark discharge,  $V(t_d)$  should be  $1/2 V_0$ . By plotting  $\ln dV/dt$  vs  $t$  logarithmically, the change in the dark discharge rate between the two time zones can clearly be seen. Thus by extrapolating the two responses at their intercept the depletion time can be established as is demonstrated in figure 3.3.

With the developed experimental apparatus, the dark discharge curves are digitally sampled and stored automatically when a test run is performed. By the application of linear regression to the  $\ln dV/dt$  vs  $t$  experimental data,  $t_d$  and  $V(t_d)$  can be established by the use of a look-up table containing the interpolated experimental data set. As the theoretical value of  $V_0/2$  does not include the contribution from surface charge injection, it follows that the measured value of  $V(t_d)$  should be smaller in magnitude than  $V_0/2$ , i.e. the measured value of  $V(t_d)$  contains contributions from the thermal generation of charge carriers in the bulk and from surface injection. Thus the difference between the theoretical value of  $V_0/2$  and the measured value of  $V(t_d)$  must equal the contribution to the dark discharge due to surface injection.

Kasap (1987) experimentally confirmed this theory. Ideally the experiment should be performed upon a sample with no contribution from surface injection and then on a sample with surface injection so that the previous theory could be confirmed. Kasap achieved this by charging an electroded sample to a very low potential at around 10V and monitoring the dark discharge. The purpose of this being that the dark decay would be so rapid that the contribution from surface injection would be negligible. A measurement of  $t_d$  and  $V(t_d)$  were then taken. The same electroded sample was then recharged to a much higher potential of approximately 500V which would result in a much longer dark decay and so contain surface injection. The measurements of  $t_d$  and  $V(t_d)$  were again undertaken and the two data sets compared. It was shown that the measured value of  $V(t_d)$  had indeed decayed beyond the theoretical value  $V_0/2$ , thus the contribution to the dark discharge by surface injection could be determined.

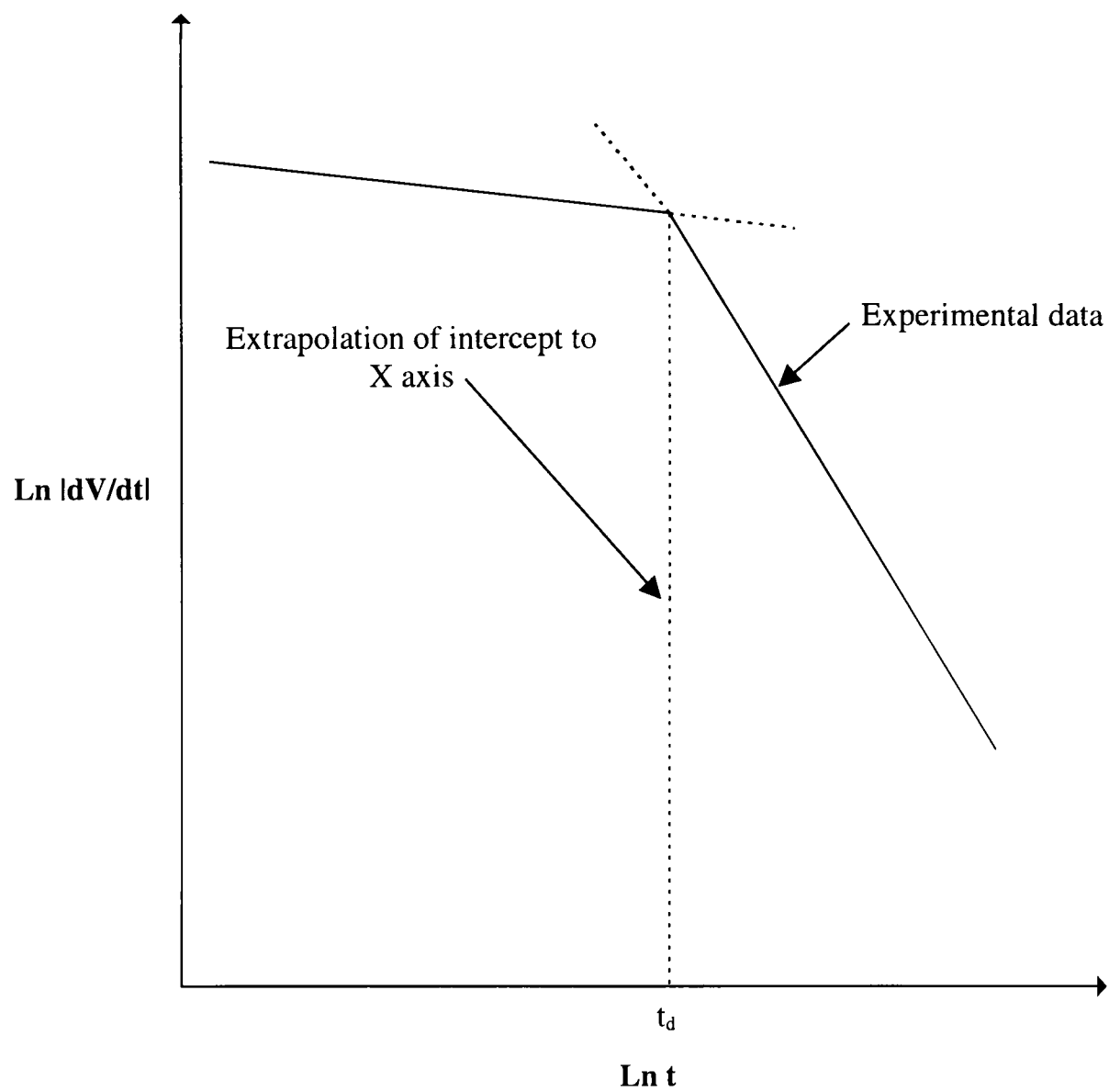


**Figure 3.3** Determination of depletion time.

Abkowitz (1985) states that the space charge density for a first order process from a distribution of energies can be expressed by the power law approximation

$$\rho(t) = at^p \quad (3.19)$$

Where  $a$  and  $p$  are constants with  $p$  being equal to or less than 1. The exponent  $p$ , is inversely proportional to a width parameter ( $W$ ) of the energy distribution of the form

$$p = \frac{kT}{W} \quad (3.20)$$

Where

$k$  is Boltzmann's constant.

$T$  is the absolute temperature.

As Abkowitz states that the depleted charge density can be described by power law time dependence, equations 3.14 and 3.16 can be expressed in the following manner

For  $t < t_d$

$$\frac{dV}{dt} = -\frac{L^2}{2\epsilon_r \epsilon_o} a p t^{p-1} \quad (3.21)$$

For  $t > t_d$

$$\frac{dV}{dt} = -\frac{\epsilon_r \epsilon_o}{2a} \left( \frac{V_o}{L} \right)^2 p t^{-p-1} \quad (3.22)$$

Abkowitz goes on to state that a plot of  $\ln |dV/dt|$  vs  $\ln t$  should have the following distinctive characteristics if the dark discharge proceeds by XDD.

1. There should be an abrupt change in  $|dV/dt|$  at  $t=t_d$  (time required for the bulk to generate a charge equal to the remaining surface charge).
2. The sum of the slopes of the two linear regions of the time zones  $t < t_d$  and  $t > t_d$  should equal -2.
3. At  $t_d$

$$\delta = L a t_d^p \quad (3.23)$$

or

$$t_d = \left( \frac{\delta}{aL} \right)^{\frac{1}{p}} = \left( \frac{2V_d \epsilon_r \epsilon_o}{aL^2} \right)^{\frac{1}{p}} \quad (3.24)$$

Where  $V_d$  is the voltage at the depletion time (V)

### Kasap 1987

A limitation of the Abkowitz model is the assumption that the bulk thermal generation process is independent of the electric field. Kasap went on to develop the models developed by Melnyk (1980) and Abkowitz *et al* (1985) further to demonstrate that the bulk thermal generation process is in fact field dependent. Kasap's model is based upon the principle that the thermal generation of charge carriers from localised states in the bulk of the layer is due to a Poole-Frenkel lowering of a Coulomb potential. The model assumes that the distribution of localised states is exponential in energy and the field dependence of the process can be determined from

$$\rho(t, E) \approx at^p \exp \left[ p \left( \frac{E}{E_{PF}} \right)^{\frac{1}{2}} \right] \quad (3.25)$$

Where  $E_{PF} = \left( \frac{kT}{\beta_{PF}} \right)^2$  ( $\beta_{PF}$  = Theoretical Poole-Frenkel coefficient)

Kasap's model states that the depletion time is related to the amount of surface potential initially placed upon the surface of the sample  $V_o(t=0)$ . This essentially means that at low electric fields when  $V_o < V_{PF}$ , a plot of  $\ln t_d$  vs  $\ln V_o$  has a slope of  $\frac{1}{p}$  which agrees with equation 3.21 as developed by Abkowitz. The Poole-Frenkel voltage ( $V_{PF}$ ) can be calculated from

$$V_{PF} = E_{PF} L = \left( \frac{kT}{\beta} \right)^2 L \quad (3.26)$$

As  $V_o$  increases beyond the Poole-Frenkel voltage, the depletion time is given by...

$$t_d \approx V^{\frac{1}{2p}} \quad (3.27)$$

When  $V_0 \gg V_{PF}$  no further increase in the depletion time occurs and  $t_d$  becomes constant.

### 3.5.2 Hydrogenated amorphous silicon

The exact nature of the dark decay mechanism in a-Si:H is unclear and is still open to debate. Baxendale *et al* (1990) state that three main conflicting theories on the dark discharge mechanism in a-Si:H exist. These are;

1. Dark discharge due to xerographic depletion discharge.
2. Dark discharge due to band to band thermal carrier excitation and sweep out of both species from midgap states in the intrinsic region.
3. Dark discharge due to the thermal emission and sweep out of both species from deep localised states in the intrinsic region.

#### Nakayama *et al*, 1987

Nakayama *et al* successfully applied XDD theory to a-Si:H:F and a-SiC:H in 1987. As with the Abkowitz model described previously, the model developed by Nakayama *et al* obeyed a power time dependence of the form

For  $t < t_d$

$$\frac{dV}{dt} \approx t^{-\left(\frac{1-T}{T_0}\right)} \quad (3.28)$$

Where

T is the absolute temperature (K).

$T_0$  is the absolute temperature (K) at which the applied electric field is equal to 0.

For  $t > t_d$

$$\frac{dV}{dt} \approx t^{-\left(\frac{1+T}{T_0}\right)} \quad (3.29)$$

The model proposed by Nakayama *et al* considers the Poole-Frenkel effect as described in the Kasap XDD model developed for a-As<sub>2</sub>Se<sub>3</sub>. In order to observe the Poole-Frenkel effect, Nakayama *et al* set the Poole-Frenkel coefficient ( $\beta$ ) to zero. A simulated double log plot of  $\ln(dV/dt)$  vs  $t$  was produced for varying values of  $V_0$ . The responses were found to have a very clear 'kink' at  $t_d$  and the slopes of the responses

were found to be  $-(1-T)/T_0$  for  $t < t_d$  and  $-(1+T)/T_0$  for  $t > t_d$ . Nakayama *et al* report that the responses in the  $t < t_d$  time zone fell exactly on the same line ( $\beta = 0$ ) regardless of the value of  $V_0$ . Nakayama *et al* go on to state that  $V(t_d)$  and  $V_0/2$  were the same regardless of the value of  $V_0$ . The process was then repeated with the theoretical Poole-Frenkel coefficient ( $2.4 \times 10^{-4} \text{ V/cm}^{1/2} \text{ eV}$ ). For this case, the simulated responses for the varying values of  $V_0$  were found not to fall along the same line in the  $t < t_d$  time zone, but fell more steeply with an increase in  $V_0$ . This resulted in the  $V(t_d)$  value being of lesser magnitude than  $V_0/2$ . Thus the introduction of the Poole-Frenkel coefficient had resulted in a dependence of  $V(t_d)$  upon  $V_0$ . From the  $\ln|dV/dt|$  vs  $\ln t$  plot shown by Nakayama *et al* for the various values of  $V_0$  (230V, 125V, and 75V) the depletion time was not easily determined because the responses were 'rounded' in the  $t_d$  region. The rounding of the response worsened for higher values of  $V_0$ . Nakayama *et al* treated the rounded responses at  $t > t_d$  as a straight line with a slope given by  $(1+T)/T_0$ .

#### Kakinuma and Wantanabe 1987

Kakinuma and Wantanabe (hereafter referred to as KW) studied the dark discharge in a-Si:H photoreceptors over various charging voltages at ambient temperature. The range of electric fields investigated were from 0V/cm to  $1.6 \times 10^5 \text{ V/cm}$ . KW state that no clear change in the dark discharge  $\ln|dV/dt|$  vs  $\ln t$  plot for the range of electric field studied could be determined. This was in contrast to a previous study by KW relating to a-Se films. Thus KW state that that they could find no clear change in the discharge mechanism in the a-Si:H material over the range of electric fields stated above. In order to gain insight into whether the material exhibited a Poole-Frenkel or Schottky dependence on the electric field, KW plotted  $L^{-1} \ln|dV/dt|$  as a function of the square root of the applied electric field. The result of this process produced straight lines which were indicative of a Poole-Frenkel or Schottky dependence.

KW argue that if this type of dependence is assumed then

$$\left| \frac{dV}{dt} \right| = \frac{I_0}{C} \exp\left( \frac{\beta \sqrt{(E-\phi)}}{kT} \right) \quad (3.30)$$

Where

- $I_0$  is a prefactor ( $I_0 \approx L$ ).
- $C$  is the geometric capacitance of the film.
- $\phi$  is the barrier height for charge emission.
- $\beta$  is the Poole-Frenkel ( $\beta_{PF}$ ) or Schottky ( $\beta_S$ ) coefficient which are given by:

$$\beta_{PF} = \sqrt{\frac{q^3}{\pi \epsilon_r \epsilon_0}} \quad (3.31)$$

Or

$$\beta_S = \sqrt{\frac{q^3}{4\pi \epsilon_r \epsilon_0}} \quad (3.32)$$

KW state that as  $\beta_{PF}$  and  $\beta_S$  differ by a factor of 2, by examining the slope of a  $L^{-1} \ln \ln V/dt$  vs  $\sqrt{E}$  plot, the permittivity of the sample can be calculated and applied to equations 3.31 and 3.32 and compared to the true value of permittivity for the material<sup>‡</sup>. Whichever of the two values of  $\epsilon_r$  yielded by equations 3.31 and 3.32 were closest to the true value of  $\epsilon_r$ , then dictated the discharge mechanism.

KW also investigated the effects of temperature on the dark discharge mechanism. KW state that the barrier height for charge emission ( $\phi$ ) could be found experimentally by measuring the temperature dependencies of  $\ln V/dt$ . KW state that when  $\ln \ln V/dt$  vs  $\frac{1}{T}$  is plotted, the barrier height can be determined from the slope of the response. From the results of this process, KW concluded that the dark discharge rate was greatly affected by temperature and that at elevated temperatures the dark discharge rate had increased. As with a-As<sub>2</sub>Se<sub>3</sub>, the dark discharge was due to dark current or currents flowing within the photoreceptor layer upon cessation of corona charging.

<sup>‡</sup> Based on supplied manufacturers data.

Again as with a-As<sub>2</sub>Se<sub>3</sub>, three main sources of current were identified as contributing to the dark discharge, i.e. the injection of current from the surface, the injection of current from the metal substrate, and the thermal generation of charge carriers within the bulk of the layer. KW state that when the dark current flowing in the film is due to thermal generation only the dark current density can be given by

$$\left| \frac{dV}{dt} \right| = \frac{q}{2\epsilon_r \epsilon_0} GL^2 \quad (3.33)$$

Where

G is the bulk generation rate (which is assumed to be uniform throughout the photoreceptor film).

By considering the contribution of current injected from the surface, KW calculated the dark current density in the film due to surface injection ( $J_s$ ) from;

$$\frac{1}{L} \left| \frac{dV}{dt} \right| = \frac{J_s + \frac{1}{2}qGL}{\epsilon_r \epsilon_0} \quad (3.34)$$

KW found that  $J_s$  increases with applied electric field and is therefore field dependent. KW concluded that the dominant dark discharge mechanism in a-Si:H is due to a Poole-Frenkel type bulk emission and that the photoreceptor is space charge free at all times.

#### Baxendale *et al*, 1990.

Baxendale *et al* attempted to elucidate the dark discharge mechanism in a-Si:H in 1990 by re-examining the works of Nakayama *et al* and Kakinuma and Wantanabe by the use of xerographic measurements. Baxendale *et al* examined the electric field and temperature variation of the dark discharge by charging the samples (27.1 $\mu$ m) to low and high values of  $V_0$  (92V and 737V respectively, and at a temperature range of  $\approx 17^\circ\text{C}$  to  $\approx 35^\circ\text{C}$ ) and plotting  $\ln|dV/dt|$  vs  $\ln t$ . No evidence of the normal features of a XDD mechanism was reported in agreement with KW. Baxendale *et al* went on to report that a plot of  $\ln|dV/dt|$  vs  $\ln V$  did reveal some interesting features not reported by KW. At the low charging regime  $V_0 < 250\text{V}$ , the rate of change of the surface

potential showed an increase with  $V_0$  with a constant value of  $V$ . In the charging regime  $V_0 > 250V$ , an initial period of rapid decay was reported that then decayed along a common featureless region. In order to examine this region more closely, these workers applied the analysis of KW but made the following assumptions.

1. The photoreceptor is space charge free at all times.
2. The dark discharge proceeds by the emission of mobile electrons and holes.
3. The applied electric field ( $E$ ) can be defined as

$$E = \frac{V}{L_2} \quad (\text{V/cm}) \quad (3.35)$$

Where  $L_2$  is the intrinsic layer thickness.

The dark current density was thus calculated from

$$J = \left( \frac{\epsilon_2}{L_2} \right) \left| \frac{dV}{dt} \right| \quad (3.36)$$

Where  $\epsilon_2$  is the dielectric constant for the intrinsic region.

If the dark current density is controlled by a thermal generation process only which involves a Poole-Frenkel or Schottky barrier lowering, then according to Baxendale *et al*, the dark current density is given by

$$J = J_0 \exp \left( \frac{\frac{1}{\beta E^2} - \phi}{kT} \right) \quad (3.37)$$

Baxendale *et al* applied equations 3.35 and 3.36 to high initial field decay curves over the range of temperatures previously stated and plotted the results on  $\ln|dV/dt|$  vs  $V^{1/2}$  axes. In agreement with KW linear plots were obtained. Following the analysis of KW, Baxendale *et al* concurred that the dark discharge was due to a Poole-Frenkel type emission of mobile holes and electrons within the intrinsic region.

### 3.6 Chapter summary

In this chapter I have sought to demonstrate the qualities that I believe make a-As<sub>2</sub>Se<sub>3</sub> and a-Si:H suitable for possible application in OPT. I have described the physical composition of the materials and stated qualities such as sensitivity to the visible spectrum, dark resistivity, and mechanical and chemical durability.

I have stated that both a-As<sub>2</sub>Se<sub>3</sub> and a-Si:H have been commonly employed in the xerographic industries due to their ability to be made into large area devices, their sensitivity to visible light, their high dark resistivity, high charge acceptance, slow dark decay and low levels of residual potential. I believe that many of these qualities would also make these materials suitable for application in OPT. A discussion of these qualities and their relevance to OPT has been included. A discussion of the physical behaviour, particularly the discharge mechanisms of the two materials has been included and relevant published mathematical models which describe the discharge mechanisms have been presented and employed in a xerographic investigation.

## **CHAPTER 4**

### **EXPERIMENTAL APPARATUS AND PROCEDURES**

The experimental apparatus developed for the research project are based on two desirable modes of operation, these being the xerographic and electroded modes. Both modes of operation required the use of high voltages and as such for safety purposes, a high voltage laboratory had to be designed and constructed to house the experimental apparatus. All experimental apparatus, with the exception of measuring apparatus, is located within a caged enclosure which conforms to all current health and safety regulations relating to working with high voltages.

In this chapter a detailed description of the developed experimental apparatus is given along with accompanying data showing apparatus functionality. The chapter has been divided into two sections which detail experimental measurements, procedures, and developed apparatus for the xerographic and electroded modes of operation.

#### 4.1 Xerographic mode of operation

In the xerographic mode of operation, an investigation of electrical properties such as dark decay, photoinduced discharge (PID), photoconductivity, and residual potential by electrostatic charging was carried out. A block diagram of the experimental apparatus developed for the project is given in Figure 4.1. With the exception of the personal computer, electrostatic voltmeter, and standard laboratory equipment, all hardware and software were designed and developed during the course of the study. The experimental apparatus was automated in order to provide operator safety, and also a fast, efficient, and reliable means of gathering and storing experimental data.

##### 4.1.1 Sample preparation

The samples employed in this study belong to drums which are commonly found in photocopying apparatus. The xerographic drums used in the study were donated to the research project by various academic institutions and industrial organisations.

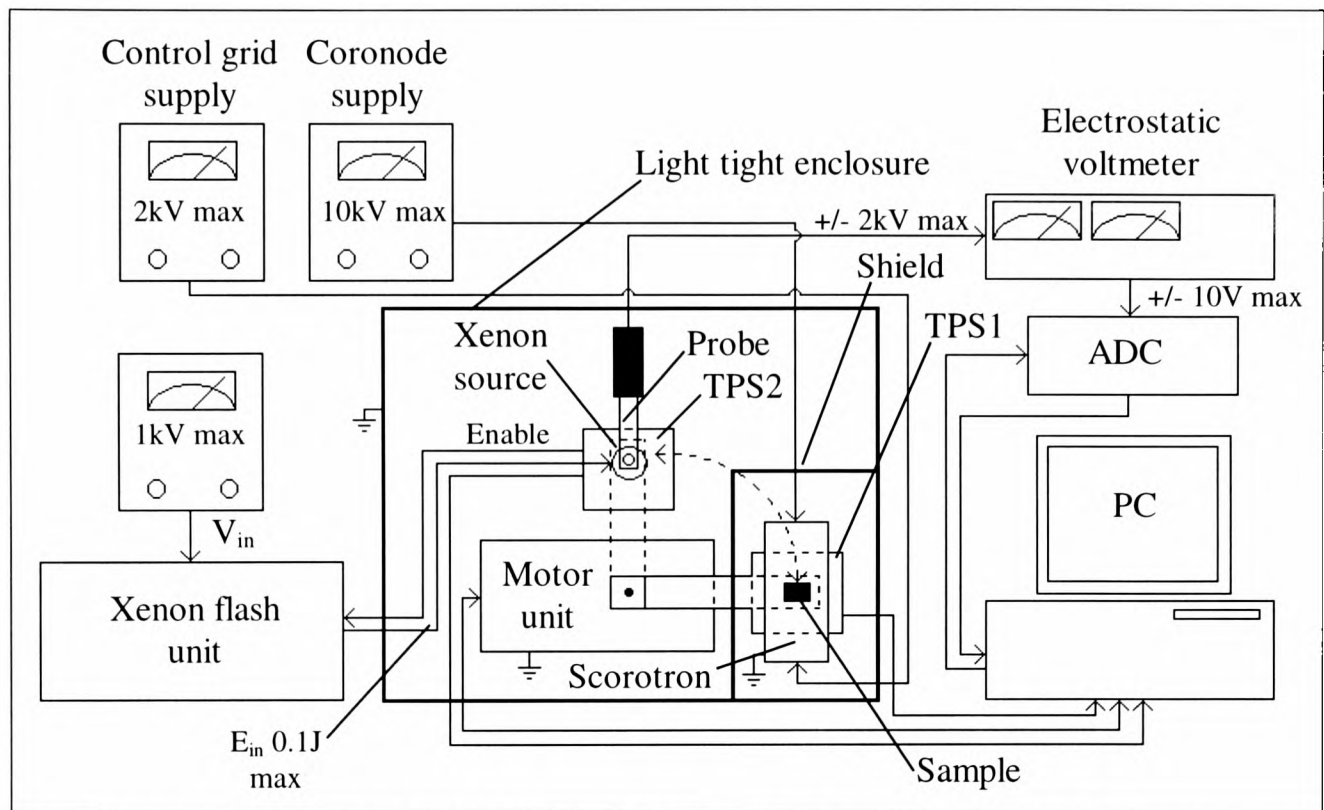


**Figure 4.1 Basic block diagram for xerographic mode of operation**

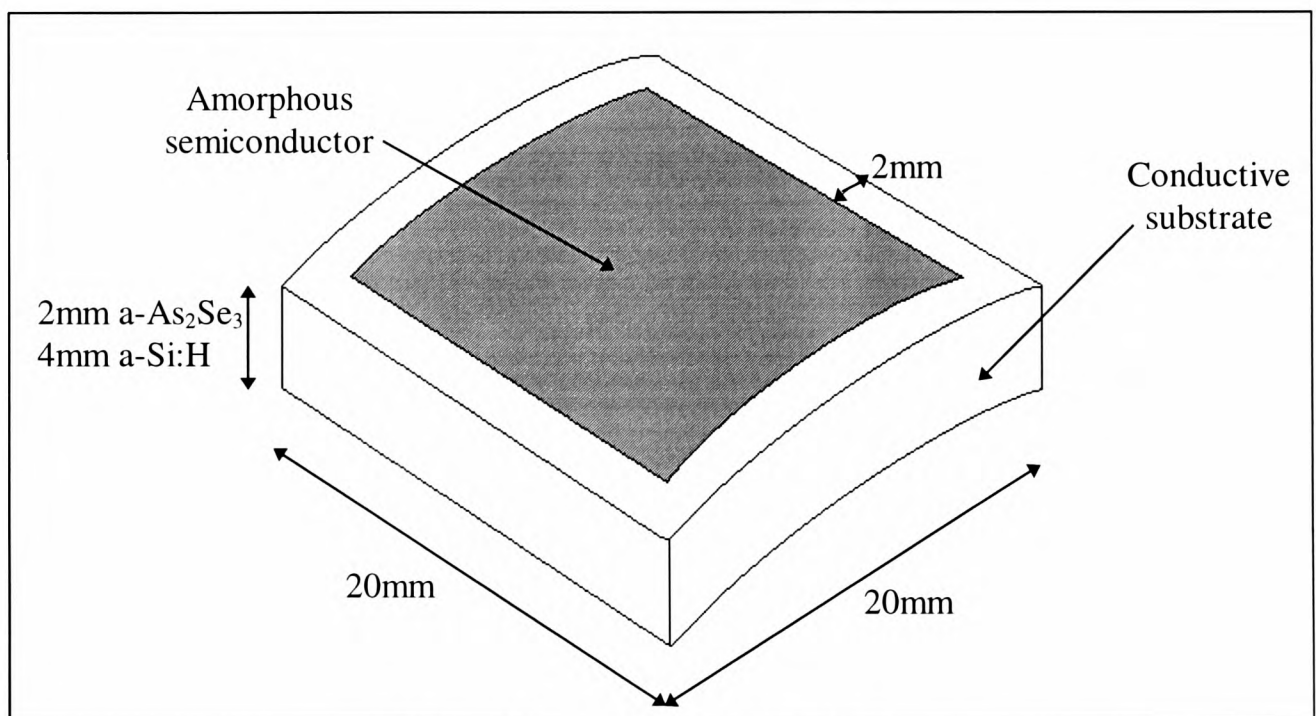


**Figure 4.2 Sample geometry**

The samples were 20mm<sup>2</sup> and were cut from the middle of the drums in order to attempt to obtain uniformity of the amorphous semiconductor film. A 2mm strip of semiconductor material was mechanically removed by hand from each edge of the sample in order to allow electrical access to the aluminium substrate as can be seen in figure 4.2. The samples were cut from the drums by the use of a fine fret saw. An exposed section of the conductive substrate of the drum was attached to a large flat metal base by the use of a metal G clamp in order to keep heat generated by the sawing action to a minimum thus reducing the risk of crystallisation of the amorphous semiconductor material. A lint free cloth was positioned between the flat metal base and the drum, with exception of the G clamp attachment point, in order to prevent possible scratching of the amorphous semiconductor material during the sawing process. The amorphous semiconductor material was removed from the cut samples by the use of a sharp scalpel blade. The sample surface was cleaned by the use of a clean lint free cloth to ensure removal of any contaminants before experimentation proceeded.

#### 4.1.2 Experimental procedures for the xerographic mode of operation

##### (i) Dark decay

Charge acceptance measurements were performed to establish the maximum electrostatic charge that could be placed upon the surface of the material under test. In order to perform a charge acceptance test, the prepared sample was inserted into a grounded, purpose built sample holder and fixed into position by the use of a malleable insulating material. Electrically conductive paint was then applied between the sample substrate and the sample holder in order to keep the substrate at the system ground. The sample was then positioned under a scorotron charger and a timing/position sensor unit. As the charge acceptance was an unknown quantity, a potential limiting grid contained within the scorotron charging unit was set to 2kV in order to prevent possible damage to the measuring probe which had a maximum voltage rating of 2kV. The purpose of the potential limiting grid was to allow control over the amount of charge placed upon the sample surface and also to aid the even distribution of the applied charge. The potential of the coronode contained within the scorotron unit was then set to the minimum potential required to produce corona onset.

The system was then energised and a core MATLAB program was invoked on the personal computer. The core MATLAB program listing can be seen in appendix 4A. Control of the experimental apparatus was then obtained by a Turbo C program which was activated by the core MATLAB program when experimentation was to be performed. The Turbo C program listing can be seen in appendix 4B. A position sensor was used to generate a sample position signal when the sample was correctly located under the scorotron unit. A position graphic was then displayed upon the PC screen. The desired sampling rate for the charge decay data was then entered into the PC and the control program was initiated.

The surface of the sample was then charged by the application of a positive potential to the coronode for a period of 1 second. Past authors such as Chan (1983) passed the sample linearly back and forth under a corona device in order to obtain uniformity of surface charge. However, due to the curvature of the samples employed in the current study, uniformity of surface charge would be difficult to achieve by this technique. Additionally, the process of agitating the sample under the scorotron charger would increase the time that the sample was positioned under the corona discharge which could lead to possible fatigue of the sample due to extended corona discharge. The transparent probe used to monitor the potential placed upon the sample surface, could only resolve an area of approximately 5mm due to the size of the aperture in the probe housing and a brass shroud employed to reduce the effects of stray capacitive coupling as detailed in section 4.1.2(iv). This meant that uniformity of applied surface charge was required only in the resolvable area of the measuring probe and not over the entire sample surface.

In order to attempt uniformity in the resolvable area of the probe, the sample was positioned at the scorotron charger in such a way that the centre of the sample (i.e. the peak of the curvature) was positioned in direct alignment with the coronode. The potential limiting grid was comprised of five parallel wires positioned between the coronode and the sample surface with the central grid wire in alignment with the centre of the sample. In this manner it was envisaged that the greatest level of charge uniformity could be achieved along the peak of the sample curvature. When the charged sample had been relocated to the transparent probe it was again positioned so the centre of the sample was in alignment with the aperture of the probe.

Once charged, the sample was then moved automatically to a measuring station located 90mm away from the scorotron unit. As the sample moved away from the scorotron unit, a timing function was started. Upon arrival at the measuring station, the sample was positioned underneath a transparent probe and a second timing/position sensor unit. At this time, the timing function was stopped and a position graphic was displayed upon the PC screen. A control signal was then sent to the PC and the data collection process was initiated. The analogue output from the transparent probe was converted to digital format and inputted to the PC. The surface potential applied to the sample surface was continuously displayed upon the PC screen. When the surface potential reached the residual potential, the operator issued a control signal which terminated the data collection process and the sample was returned automatically to the scorotron unit. The collected data were then stored in a file on the hard disk of the PC and the data automatically loaded into the core MATLAB program for analysis. The sample was then allowed to rest in the dark for a suitable period before experimentation proceeded. The coronode voltage was then increased and the procedure described above was repeated. This process continued until the acceptance potential had been reached.

For experimentation that required a known potential to be applied to the sample surface, the potential limiting grid was set to the desired potential prior to the commencement of experimentation. The coronode potential was set to an appropriate level determined from data obtained during charge acceptance measurements.

(ii) Photoinduced discharge

In order to monitor the decay of the applied surface charge under illumination, a control signal was automatically sent when the charged sample arrived at the second timing/position sensor unit. Upon receipt of the signal, the xenon flash unit issued a single pulse of light which was directed through the transparent probe and on to the sample surface. The resulting charge decay was then monitored as described in section 4.1.2(i).

### 4.1.3 Experimental apparatus in the xerographic mode

#### (i) Light tight enclosure

All experimentation in both the xerographic and electroded modes of operation were conducted in a purpose built light tight enclosure. The light tight enclosure was made from 4mm thick aluminium sheet which was held at the system ground. All conductive components within the light tight enclosure were also held at the system ground in order to prevent the build up of unwanted electrostatic charge which could interfere with the charge measurement process. An internal shield was built into the light tight enclosure which completely surrounded the scorotron charger in order to prevent corona generated noise from entering the measuring system. A slot was cut in the side of the shield to allow the sample to be moved from the scorotron charger to the measuring station. The light tight enclosure was designed so that the xerographic and tomographic measuring systems could be easily interchanged.

#### (ii) Timing/position sensor units

As experimentation was performed within a light tight enclosure, it was not possible for the operator to see the current location of the sample. Position sensors were included in the system in order to inform the operator of the samples current location. The position sensors employed were HOA2001-1 optical sensors with on board logic. The HOA2001-1 contained an infrared transmitter and receiver mounted in a slotted housing. The HOA2001-1 gave a logic high signal when the light beam was intact and a logic low signal upon interruption of the light beam.

A position sensor was located at the scorotron charger and also at the measuring station. A mechanical device was located underneath the arm that carried the sample and was used to interrupt the light beams of the timing/position sensor units. Initially the sample was positioned under the scorotron charger and the light beam of timing/position sensor 1 (TPS1) was interrupted. An inverted output was taken to the PC via centronics cable and the parallel port, and a position graphic was displayed upon the PC screen notifying the operator that the sample was in the correct position under the scorotron charger. When the charged sample was moved away from TPS1, the light beam was re-established and the position graphic was removed from the PC screen.

The time required for the sample to reach the measuring station upon cessation of corona charging had to be established for reasons that are stated in 4.2.3(iii). As the sample moved away from TPS1 and the light beam was re-established, a timer start signal was sent to the PC which started a timing function within the control software. Upon arrival at TPS2 located at the measuring station, the mechanical device underneath the sample support arm interrupted the light beam and a timer stop signal was issued. The sample translation time was then automatically displayed upon the PC screen. Additionally, when the light beam of TPS2 was interrupted, a signal was sent to the PC and a position graphic was displayed upon the PC screen to inform the operator that the sample was correctly positioned beneath the transparent probe. For PID experiments TPS2 also issued a signal (enable) to the xenon flash unit to produce a single pulse of light.

The timing/position sensor units were mounted on the lids of conductive boxes which were attached to the base of the light tight enclosure. The control/signal generation electronics were contained within the conductive boxes. Mechanical stops were located at the back of the HOA2001-1 devices to prevent the sample from travelling through the device. The sample was held in position beneath the scorotron charger by energising the coils of a stepper motor employed in the sample translation mechanism. The sample was held in position at the measuring station by purposely 'jamming' the coils of the stepper motor to prevent mechanical bounce when the sample arrived at the measuring station.

### (iii) Sample translation mechanism

The charged sample had to be moved away from the scorotron charger in order to prevent corona generated noise from entering the measuring station. Upon cessation of corona charging, the charge applied to the sample surface would start to decay. This had the result that the surface charge detected by the transparent probe was not the true value of applied charge, but was the amount of charge remaining after the sample had been moved to the measuring station. Thus it was necessary to move the charged sample to the measuring station in a short a time as possible. Past researchers have accomplished the sample translation by hand (Chan, 1983) and by linear systems driven by DC motors (Baxendale, 1989 and Kaura and Srivastava, 1987). Chan described moving the sample charged sample linearly from a charging station to a

measuring station 55mm away in a time of 0.5s. As the sample translation was performed by hand, the sample translation time would vary from experiment to experiment and as such, this type of system was considered to be unsuitable. Additionally, this type of system did not conform to health and safety regulations relating to working with high voltages. The system developed by Kaura and Srivastava utilised a linear DC motor controlled system and a sample translation time of approximately 1s was stated for a 80mm movement. Baxendale also employed DC motors in a linear sample translation mechanism, and stated a translation time of 800ms for a 70mm movement. A possible disadvantage of using DC motors as the sample translation mechanism was that computer interrupts may be required to establish the sample translation time.

In the current system, a special 90° stepper motor was used as the sample translation mechanism which moved the sample a distance of 90mm from the scrotron charger in approximately 420ms. The motor employed in the sample translation mechanism was an Astrosyn 18PD B003 permanent magnet type stepping motor with a holding torque of 380g/cm. The sample translation time was established by recording the current time from the internal clock of the PC using the 'gettime' function with Turbo C when the charged sample moved away from TPS1. Upon arrival of the sample at TPS2 the current clock time of the PC was again recorded and the start time was automatically subtracted from the stop time to establish the sample translation time. The internal clock of the PC was accurate to 1/100th of a second, thus the sample translation time was accurate to +/- 10ms.

The timing/position sensor units were positioned at 90° to one another in the light tight enclosure and the stepper motor system was located at the origin of the timing/position sensor units. The length of the arm that carried the sample was calculated to move the sample a distance of 90mm in a single step. As the stepper motor system could convey the sample to the measuring station in a single step, no time delays between motor coil excitations were required and only a single computer instruction was issued. This meant that the controlling software was free to establish the sample translation time without the need for interrupts. A basic diagram showing the sample translation mechanism positioned at the charging station is shown in figure 4.3. A basic timing diagram for the sample translation mechanism is shown in figure

4.4. The reader is referred to Chubb and Malinverni (1993), Stark (1990), and Yatuszuka *et al* (1994) for alternate sample translation mechanisms.

(iv) Measuring station

The measuring station was comprised of a timing/position sensor previously described, a transparent probe, analogue to digital conversion circuitry, an electrostatic voltmeter, and a personal computer as is shown in figure 4.1.

The transparent probe used for charge measurement was a Monroe model 1009T. The model 1009T was a non-contact probe which utilised a tuning fork arrangement to drive the output of the probe to the surface potential under test up to a maximum of +/-2kV. The model 1009T differed from standard electrostatic probes in that it had a small circular aperture in the probe housing to allow light to be passed through the probe housing to the sample surface for PID experiments. The probe was mounted parallel to the sample surface and was held in position by a purpose built bracketing system made from insulating material. The bracketing system contained three flexible joints so that the probe could be accurately positioned above the sample surface. The bracketing system was attached to a vertical vernier scale so that the height of the probe could be accurately set and reproduced.

In terms of accuracy in surface potential measurement, it was essential that the probe aperture measured the charge applied to the surface of the sample without the contribution of charge from other sources. For both dark decay and PID experiments, the charge measurement could be affected by undesired capacitive coupling to surfaces in close relation to the probe aperture. This is especially true of transparent probes as the small dimension of the probe housing when compared to traditional probes could allow the ingress of unwanted capacitive coupling into the probe aperture. Charge measurement for PID can also be affected by fringing errors which occur between illuminated and un-illuminated areas of the charged sample surface. In order to reduce possible errors due to capacitive coupling or fringing errors, a 5cm<sup>2</sup> brass shroud was manufactured and attached to the underside of the probe housing by the use of electrically conductive paint. This provided electrical connection to the grounded probe housing and also allowed the shroud to be temporarily attached to the delicate probe without damage.

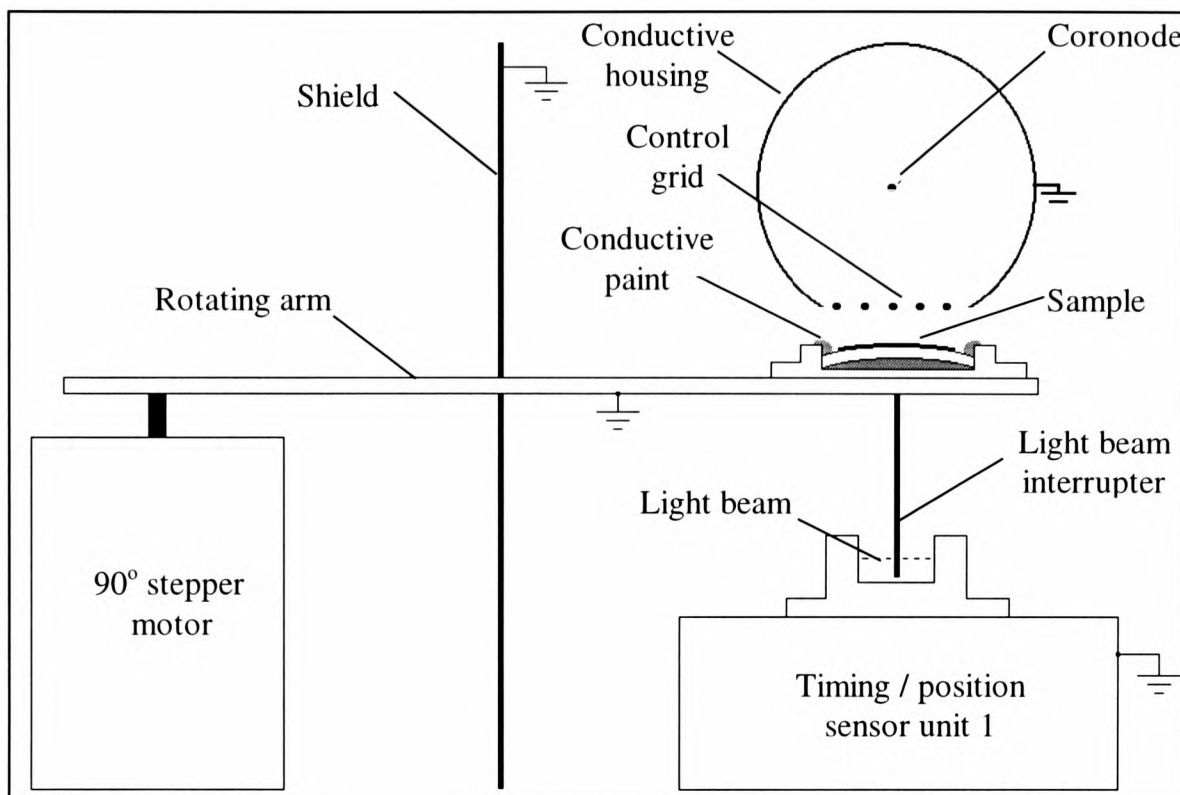


**Figure 4.3 Sample translation mechanism**

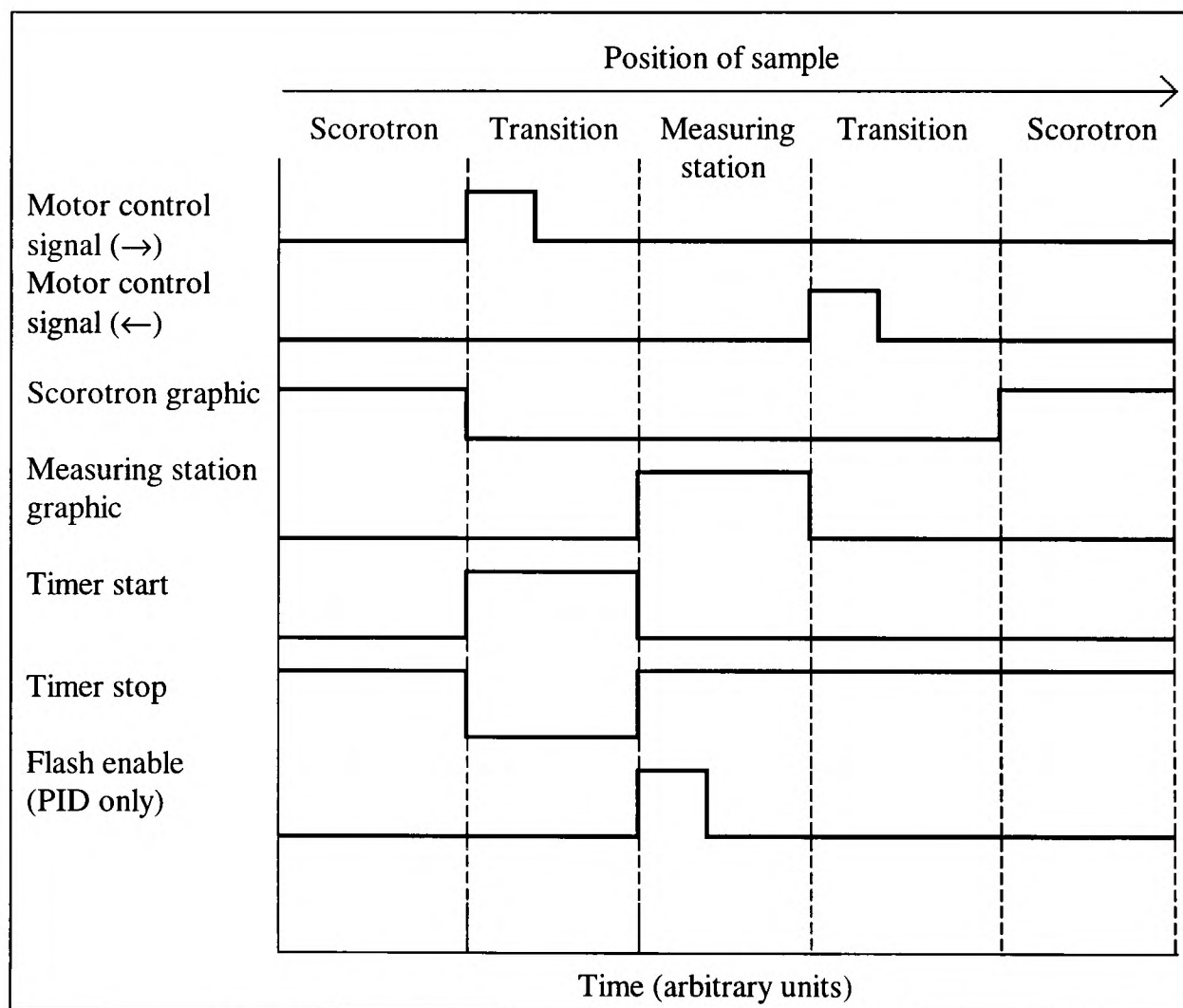


**Figure 4.4 Basic timing diagram for sample translation mechanism**

The use of a shroud effectively extended the dimensions of the probe housing around the sensitive aperture and unwanted stray charge coupled to the shroud and not the probe aperture. The transparent probe arrangement is shown in figure 4.5.

The analogue output from the transparent probe was taken to the input of a Monroe model 144 electrostatic voltmeter in order that the measured surface potential be determined. The model 144 measured the surface potential under test by a field nulling technique and the manufacturers claim a response time of <7.5ms and accuracy of 0.1%, for a 3mm probe to sample surface spacing (PSSS). The model 144 provided an analogue output that was equal to the measured charge at potentials of up to +/- 10V, and an output that was 1/200th of the input for potentials above +/-10V (2kV maximum input). The output of the model 144 was then digitised and inputted to the PC via an 8255A interface card. The establishment of the optimum PSSS and the calibration of the electrostatic voltmeter are detailed in appendix 4C.

(v) Scorotron charger

The purpose of the scorotron charger was to apply electrostatic charge in known or unknown quantities to the surface of the sample under test. The most effective way of applying the electrostatic charge to the sample surface was to spray the surface with ions produced from corona discharge. When a potential of several thousand volts is maintained between a conductive substrate and a coronode positioned close to the sample surface, corona emission from the coronode ionises air molecules which are drawn to the sample surface. Two main types of corona charge are commonly used in xerography, these being a wire (or point) to plane corona charger and the scorotron charger.

Hagihara and Okuda (1995) described a detachable corona charger which was of the basic wire type. The corona charger developed by Hagihara and Okuda was designed to apply electrostatic charge for latent image formation upon photoreceptor drums. The corona charger contained a single coronode strung in a tubular conductive housing as can be seen in figure 4.6. This type of corona charger can lead to poor homogeneity, overcharging of the sample, and difficulties in applying predetermined levels of electrostatic charge due to the lack of a potential limiting grid.

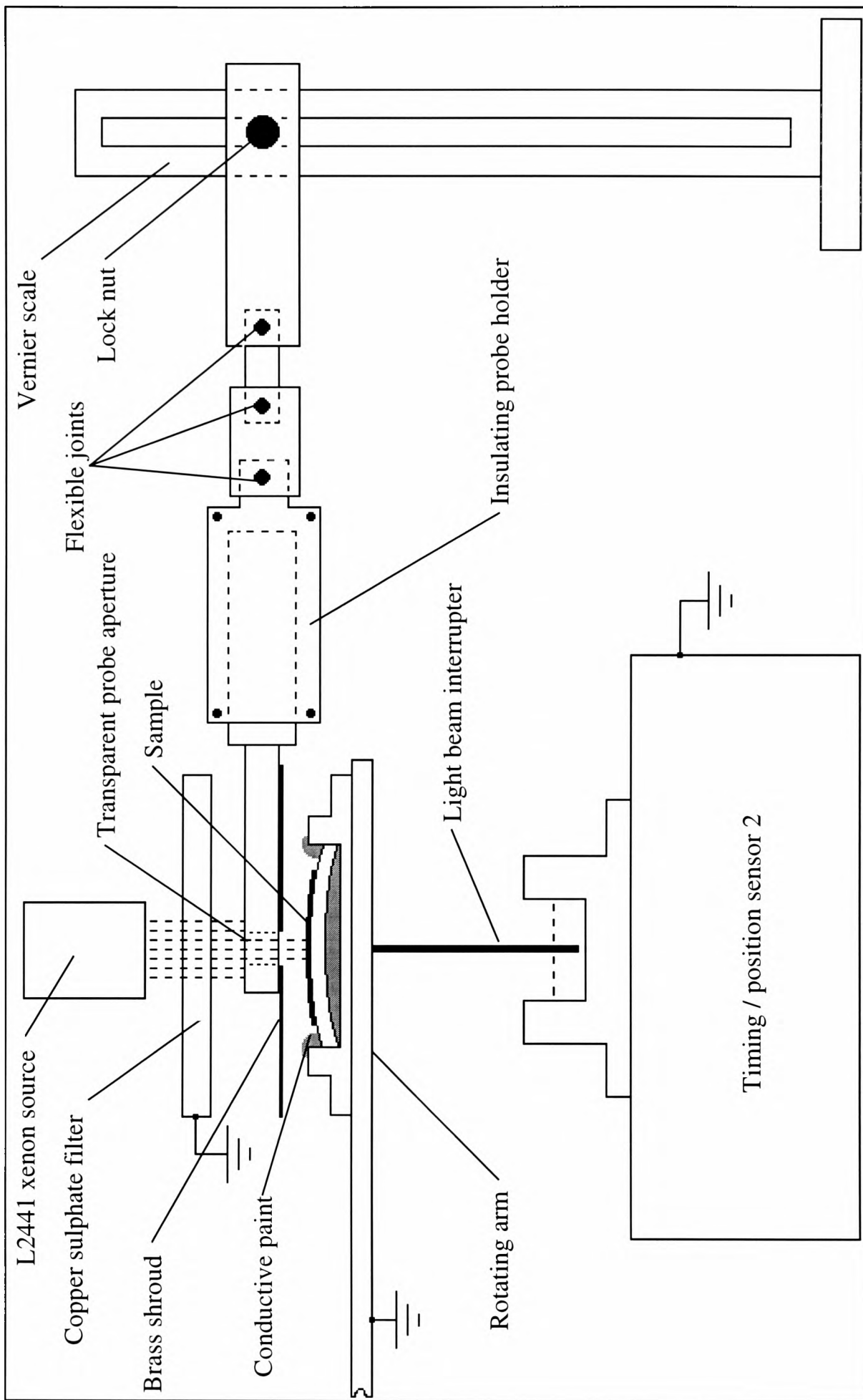
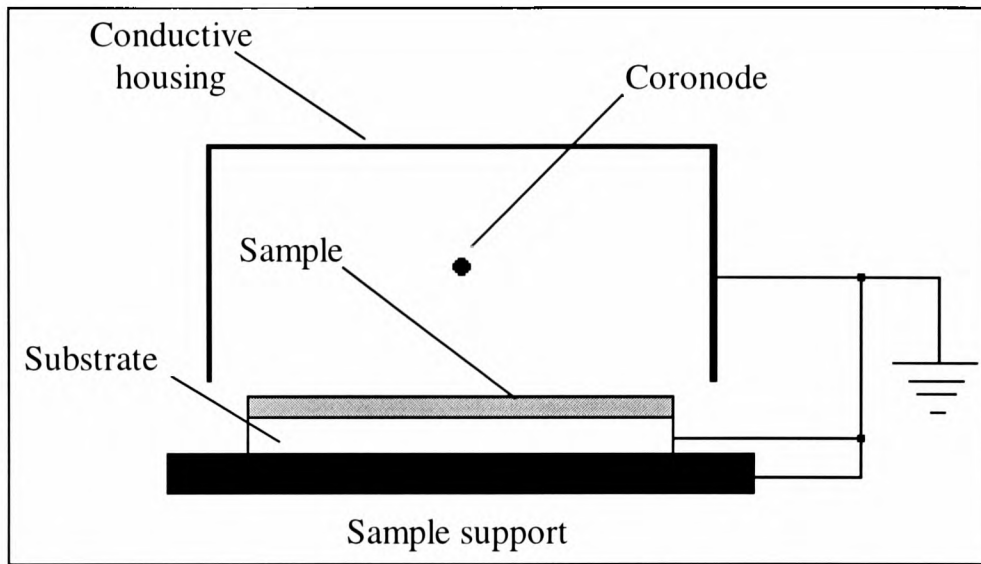


Figure 4.5 Transparent probe arrangement

Stark (1990) described a point to plane corona charger of the type shown in figure 4.7. Stark attempted to improve the homogeneity of a basic corona charger by utilising a fine (less than 100 $\mu$ m) needle point as the coronode without incorporating a potential limiting grid. Stark observed that good homogeneity was achieved in a 100mm diameter circular area radiating from the coronode. Although Stark demonstrated that the use of a needle point as the coronode could produce good homogeneity, the risk of overcharging of the sample and the problem of accurately applying predetermined levels of charge remained.

Gundlach and Bergen (1984) described a miniature scorotron charging device for xerography of the type shown in figure 4.8. The charging device incorporated a control screen attached to the bottom of the conductive housing so that the screen was in close relation to the material to which electrostatic charge was to be placed. The scorotron designed by Gundlach and Bergen incorporated a much smaller control grid and coronode to sample surface spacing (1.5mm and 5mm respectively) than stated in prior art (typically 12mm for each) in order to reduce the coronode voltage required to produce corona onset. Figure 4.9 shows the effect of increasing the coronode to sample surface spacing on the required corona onset voltage for a 50 $\mu$ m and 100 $\mu$ m coronode.

The reduction in required corona onset voltage had implications upon the type of control grid that could be employed. Gundlach and Bergen reported that fine mesh control screens provided excellent homogeneity and control of surface charge but could restrict the application of charge to the sample surface due to the low porosity of the mesh. This had the result that higher corona onset voltages were required which could lead to the problem of electrical arcing. Mesh control grids of a more open weave were reported as allowing more surface charge to be applied to the sample surface but at a reduction in control of the surface charge.



**Figure 4.6 Basic corona charger**

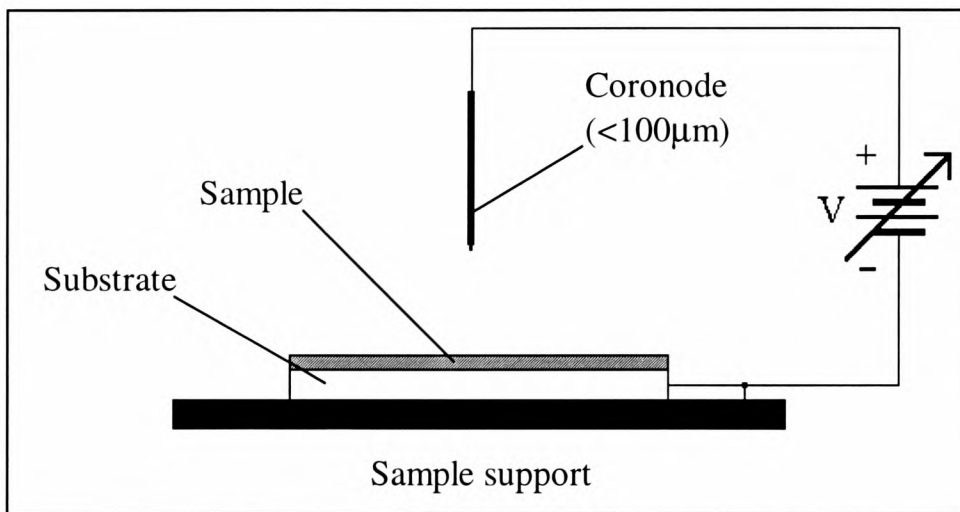


**Figure 4.7 Basic point to plane corona charger**

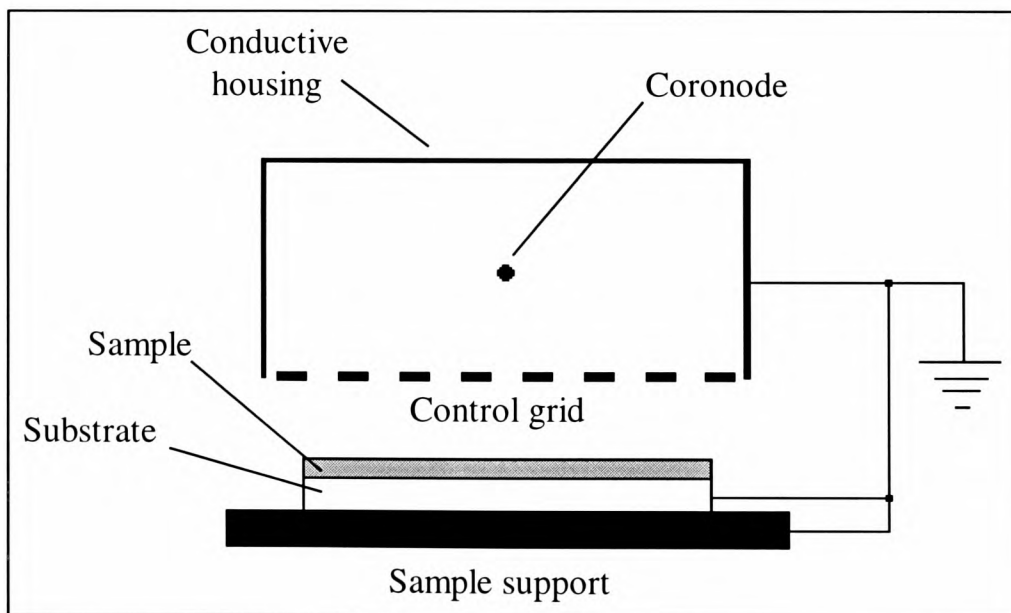


**Figure 4.8 Basic scorotron**

Pillai *et al* (1983) describe a multiple coronode scorotron that utilised parallel wires as the control grid. Parallel wires had been employed in place of a mesh in order to reduce the probability of electrical arcing. The possible loss of homogeneity and control over the applied surface charge that the use of parallel wires introduced was overcome by the use of three coronodes. However, this arrangement greatly increased the complexity of the device.

The scorotron charger designed for the research project embodied elements of the scorotron chargers discussed above. The scorotron contained a single 100 $\mu$ m tungsten coronode strung in the centre of a circular 1.5mm thick copper housing. A 20mm diameter charging window was cut from the underside of the housing to allow charging of the sample surface to take place. The 20mm<sup>2</sup> sample was positioned beneath the charging window and approximated the ‘missing’ section of the circular housing. A circular housing was chosen for the scorotron in order that an existing mathematical model for the design of corona chargers could be employed. Cobine (1958) stated that the corona characteristics of wires could be determined from data on coaxial cylinders (two concentric conductors separated by an insulator where the wire is considered to be the inner cylinder).

The electric gradient ( $E_c$ ) at the surface of a wire necessary to produce the onset of corona emission according to Cobine, was given by the following.

$$E_c = 31m\delta \left[ 1 + \frac{0.308}{\sqrt{\delta a}} \right] \text{ kV/cm} \quad (4.1)$$

Where

- a is the radius of the coronode (cm).
- m is a dimensionless irregularity factor which relates to the type of coronode employed in the charger and the manner by which corona emission proceeds along said coronode. Cobine states that for polished single strand coronodes as employed in the developed scorotron, m is unity.
- $\delta$  is the relative air density factor.

For air,  $\delta$  is

$$\delta = \frac{3.92b}{273 + t} \quad (4.2)$$

Where  $b$  is the air pressure in mercury (cm)

$t$  is the temperature ( $^{\circ}\text{C}$ )

For normal room temperature and air pressure both  $\delta$  and  $m$  are unity, thus equation 4.1 becomes

$$E_c = 31 \cdot \left( 1 + \frac{0.308}{\sqrt{a}} \right) \text{kV/cm} \quad (4.3)$$

The critical voltage ( $V_o$ ) at which corona onset is observed for Cobine's coaxial cylinder model was given by

$$V_o = E_c a \cdot \ln \left( \frac{R}{a} \right) \text{kV} \quad (4.4)$$

Where  $R$  is the radius (cm) of the outer cylinder (distance from coronode to sample surface) Thus combining equations 4.3 and 4.4 we get for normal air temperature and pressure

$$V_o = 31a \cdot \ln \left( \frac{R}{a} \right) \cdot \left( 1 + \frac{0.308}{\sqrt{a}} \right) \text{kV} \quad (4.5)$$

Equation 4.5 was used to compile the data for figure 4.9 which shows how the coronode to sample surface spacing effected the voltage required to produce corona onset. Assuming a  $50\mu\text{m}$  coronode and a coronode to sample surface spacing of 1.5cm, equation 4.5 yielded a corona onset voltage of 3.549kV which is in good agreement with Schaffert (1975) who states corona onset for a 2 mils ( $50.8\mu\text{m}$ ) coronode in a 1.5cm housing would be approximately 3.45kV.

The scorotron designed for this project employed a single  $100\mu\text{m}$  coronode in a 2.5cm diameter housing with a control grid made up of five  $100\mu\text{m}$  parallel wires located at the charging window. The coronode to control grid spacing was 1cm and the control

grid to sample surface spacing was 2.5mm giving a total coronode to sample surface spacing (R) of 1.25cm. The scorotron geometry resulted in a corona onset voltage of approximately 4.58kV.

A thicker coronode was employed in the scorotron to make the scorotron more experimentally robust, and also because of experimental difficulties with handling wire of such a small diameter. This resulted in the need for a higher coronode voltage to produce corona onset as can be seen in figure 4.9 which increased the risk of electrical arcing. In order to remedy this, a control grid of parallel wires was used in place of a fine wire mesh. This procedure could reduce the risk of electrical arcing but could also lead to a loss of functionality of the control grid. Rushing (1996) described a procedure for accurate reproduction of applied charge by the use of a look-up table.

Rushing stated that the relationship between the surface potential and the control grid voltage can be affected by variable emission from the coronode, the varying charge acceptance of the sample under test, wear, contamination, corrosion, and variable environmental conditions. To this end, Rushing compiled a table of grid voltage vs. measured charge data which could be updated, in order that desired surface charges could easily be reproduced. Due to the possible loss of functionality in the present scorotron due to the use of a parallel wire control grid, the technique developed by Rushing was adopted. Figure 4.10 demonstrates the functionality of the control grid. It was observed that the potential applied to the sample surface could be controlled and was accurate to within approximately 12V or less of the control grid voltage over the 300V to 600V range stated. The construction details of the scorotron charger are shown in figures 4.11 and 4.12. The reader is referred to Vaezi-Nejad and Juhasz (1989) for further review of corona charger design.

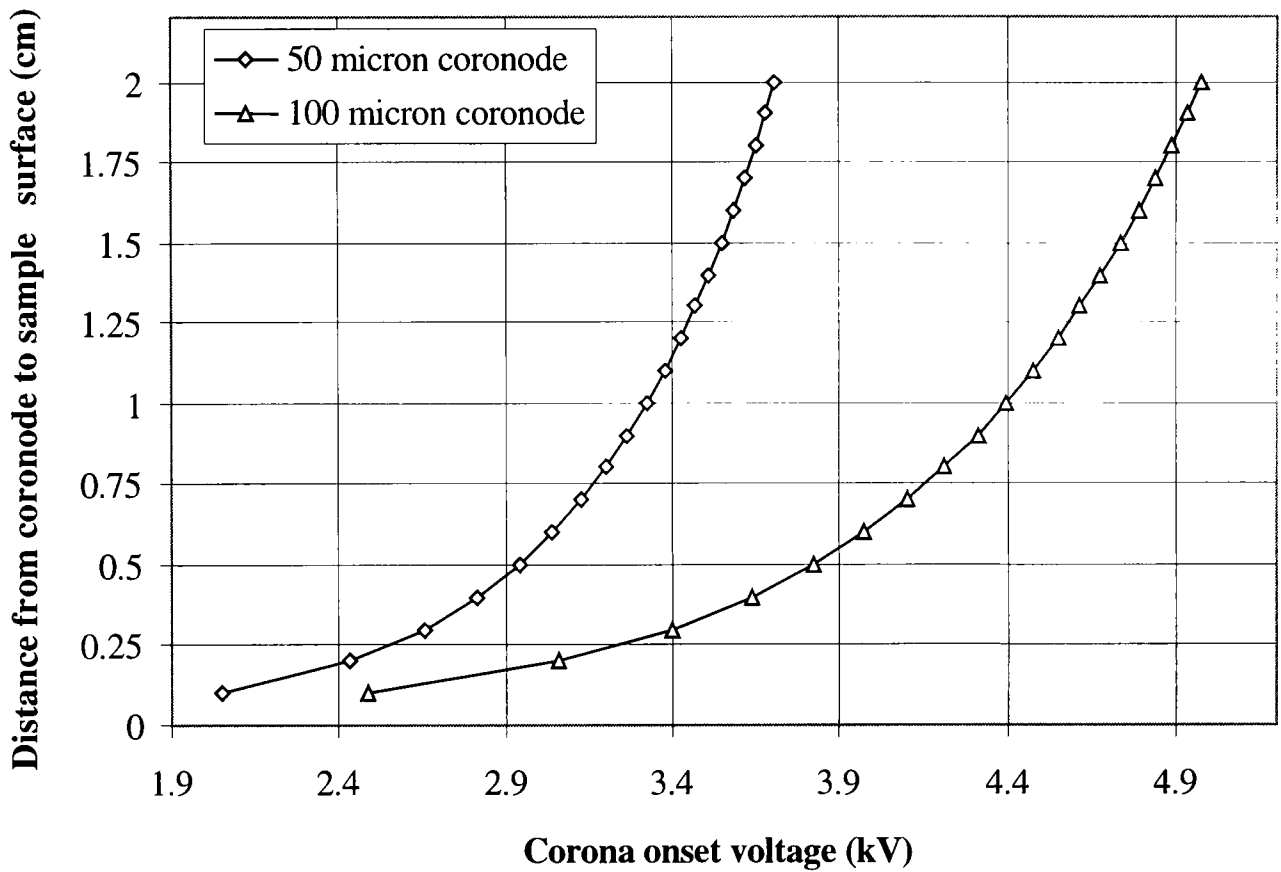


**Figure 4.9** Effect of coronode to sample surface spacing on corona onset voltage ( $R = 1.5\text{cm}$ ).

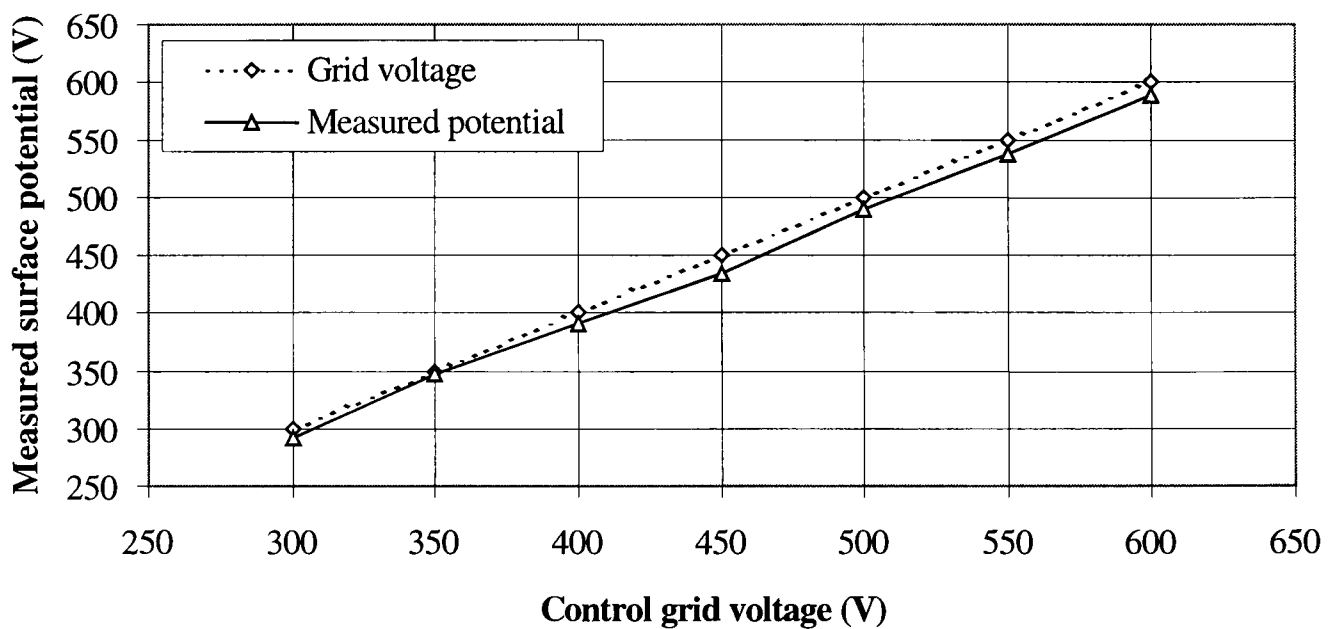


**Figure 4.10** Graph showing control grid functionality on a typical a-Si:H sample (coronode voltage 7kV)

(vi) Data acquisition and file management software

Control and data acquisition for the experimental apparatus was achieved by a combination of MATLAB and Turbo C programming. MATLAB was used to provide a main user interface, file management system, and to perform data analysis. Turbo C was used for control of the experimental apparatus and data acquisition purposes.

When experimentation was to be performed, the core MATLAB program was invoked and the operator was presented with a file management menu system. If dark decay or PID was to be performed, the 'create new file' option was selected and MATLAB gave up control to the Turbo C program. The user was then prompted for whether the surface potential was positive or negative, the sampling rate (ms), and the time the sample was to remain at the charging station. The time delay at the charging station was to allow charging of the sample surface before the sample was moved to the measuring station.

Once the required information was correctly entered, the control program was activated and the charged sample was moved to the measuring station once the time charging time delay had timed out. As the sample moved away from the charging station TPS1 issued a timer start signal and the current CPU time was recorded. The control program then continuously scanned for a position signal from TPS2 located at the measuring station. Once found, a timer stop signal was sent to the PC and the current CPU time was again recorded. The sample translation time was then automatically calculated and displayed upon the PC screen. At this time, the controlling C program opened a file called 'test' upon the hard drive of the PC. The position signal from TPS2 was also used to start a data acquisition process and the sampled data was written to the 'test' file on the PC hard drive.

Data acquisition and digital conversion was achieved by the use of a Burr Brown ADS7806 Low Power 12 Bit Sampling CMOS analogue to digital converter (ADC). The ADS7806 could convert to full 12 bit accuracy in a maximum of 25 $\mu$ s. Laser trimmed scaling resistors were configured to give a +/- 10V parallel output which resulted in a resolution of 4.88mV.

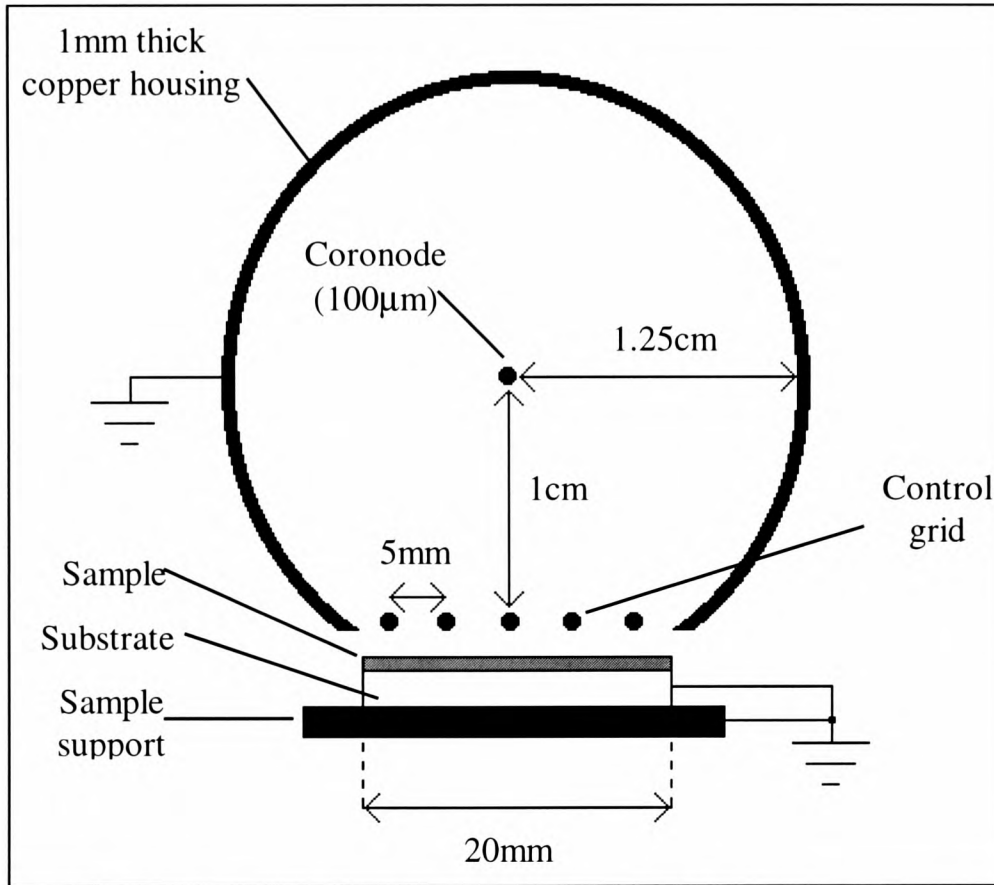


**Figure 4.11** Cross section through scorotron charger

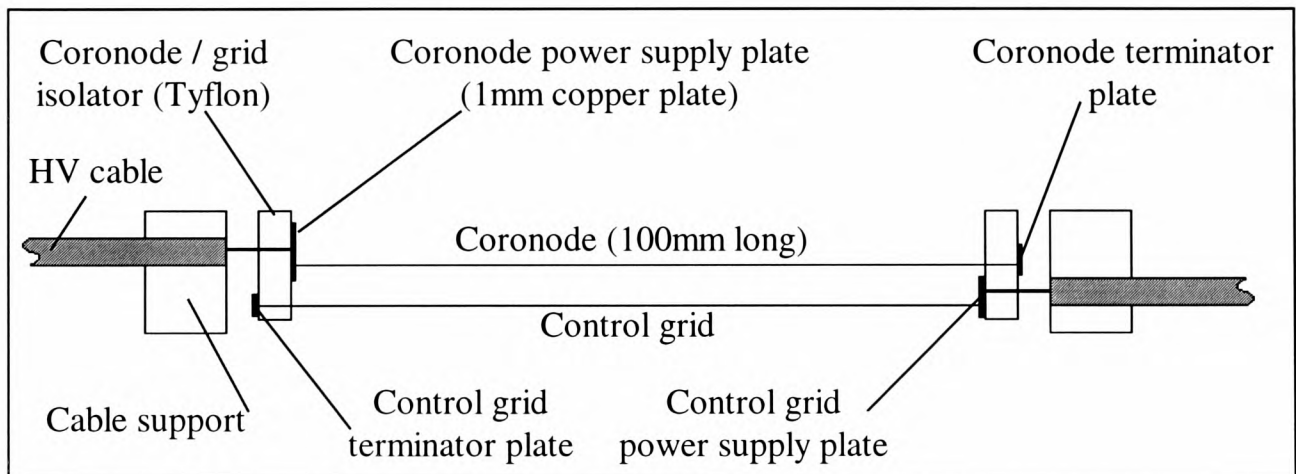


**Figure 4.12** Internal mechanism of scorotron charger

The output from the Monroe electrostatic voltmeter was 1/200th of its input, thus the output from the Monroe had to be multiplied to establish the correct potential. This meant that the data acquisition system was accurate to  $4.88281\text{mV} \times 200 = 0.9765\text{V}$ . The data acquisition system was again controlled by the Turbo C program and the resulting data was inputted to the PC via an 8255A interface board.

Upon storage of each sample of the charge decay data, the data acquisition system scanned for a termination signal which was sent by the user when the potential upon the sample surface had reached its residual potential. Upon receipt of this signal, the C program terminated data acquisition and closed the 'test' file on the hard drive. The Turbo C program then gave control back to the core MATLAB program. Figure 4.13 shows a basic flow diagram for the collection of positive charge decay data. When control was given back to the core MATLAB program, the user was prompted to save the file. The data file contained a two column array of time vs. surface voltage data and the current time, date, and run number was automatically added to the file for reference purposes and was the file was saved as a .mat file. Once the file had been saved, a plot of the time vs. surface potential data was automatically generated and the user then had the option of loading subprograms which were specifically written for the analysis of the discharge mechanisms of a-As<sub>2</sub>Se<sub>3</sub> and a-Si:H. The MATLAB program listings for the analysis of the discharge mechanisms for both materials can be seen in appendix 4D.

#### 4.2 Electroded mode of operation

In the electroded mode of operation, an investigation of the photoconductivity, sensitivity, photoinduced fatigue, and speed of response of the a-As<sub>2</sub>Se<sub>3</sub> and a-Si:H materials was carried out under optical process tomography (OPT) conditions. All tomographic experimentation was carried out in the same light tight enclosure used for xerographic experimentation. A block diagram of the experimental apparatus for the electroded mode of operation is shown in figure 4.14.

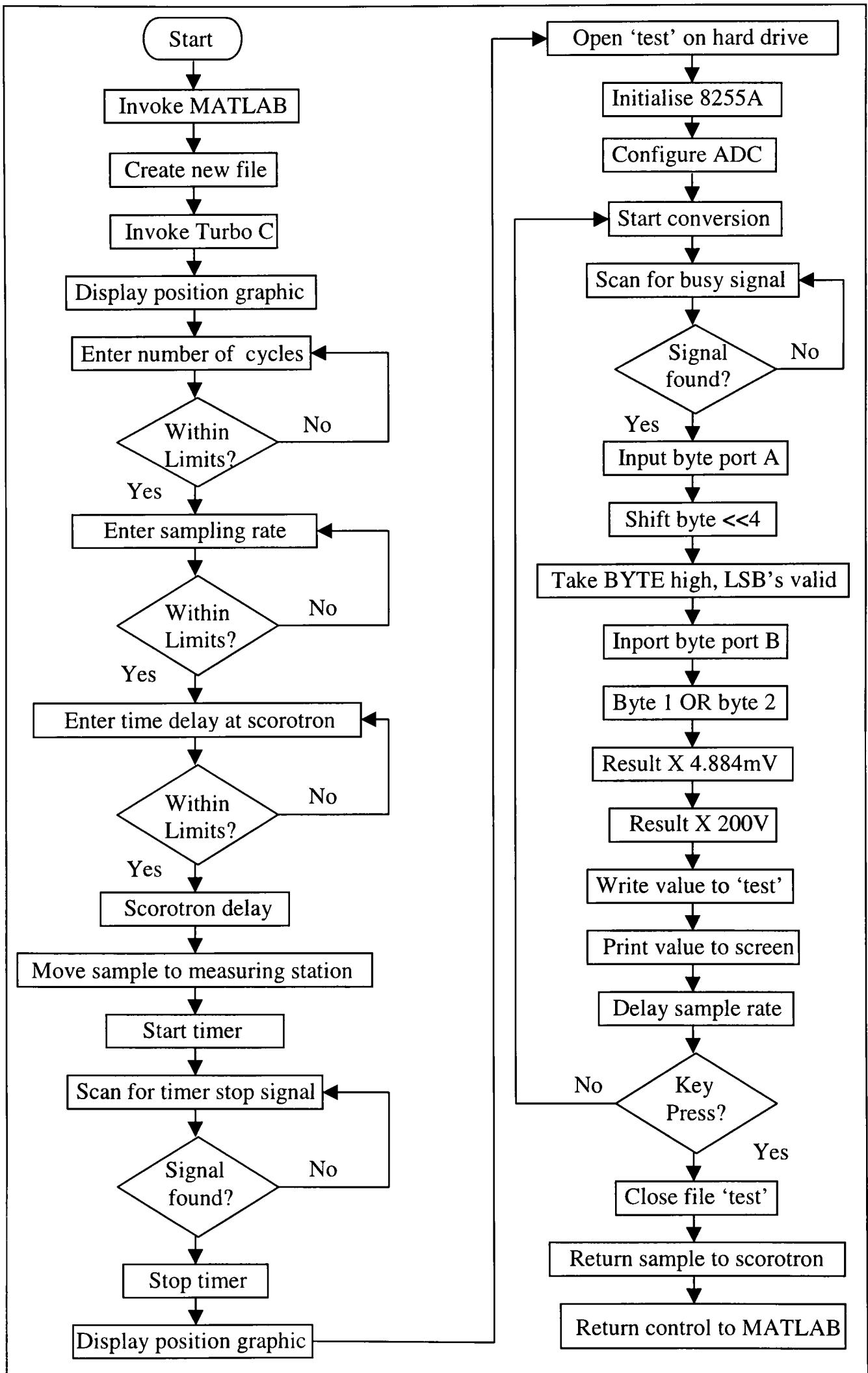
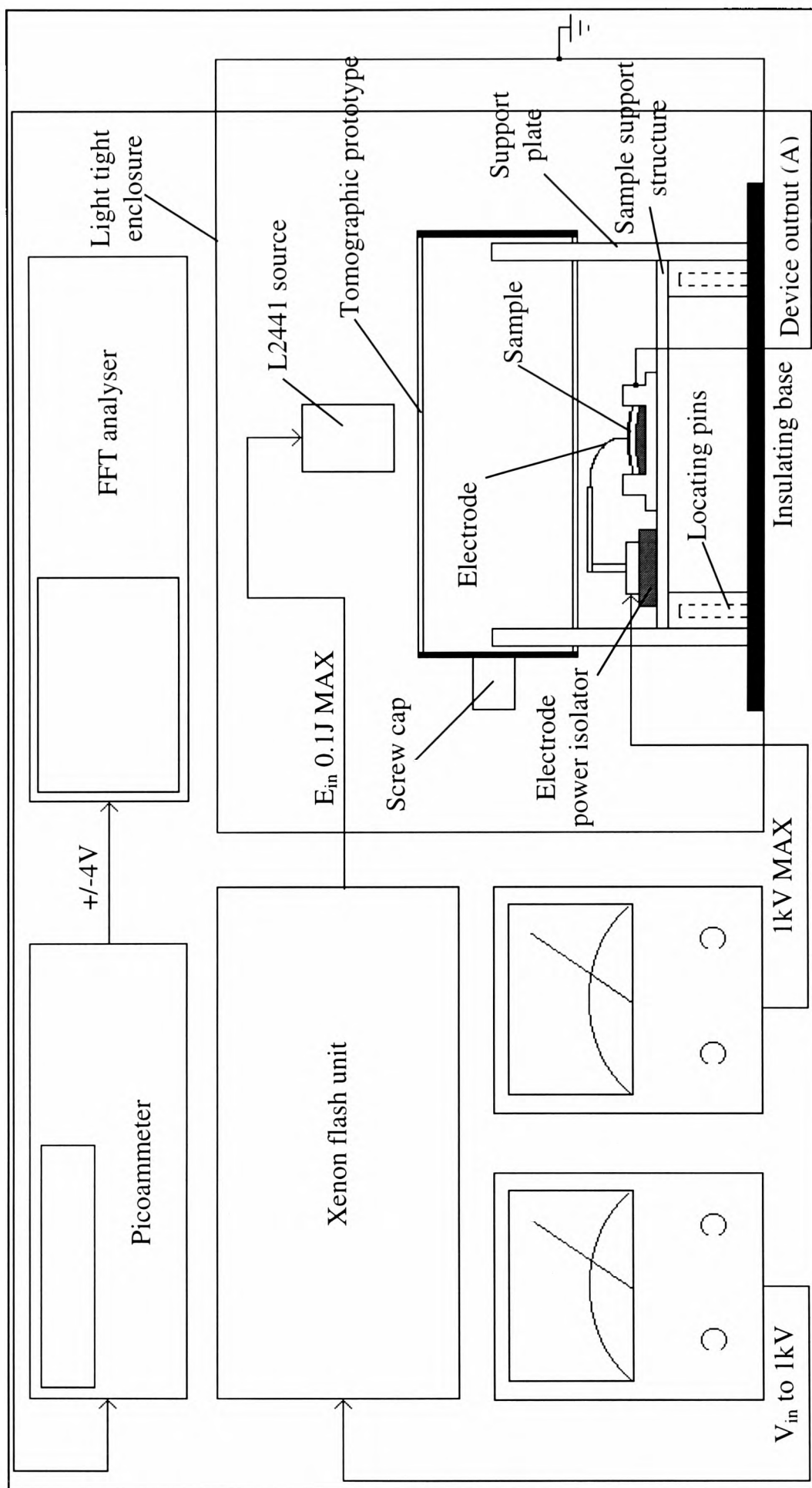


Figure 4.13 Basic flow diagram for the acquisition of charge decay data

The tomographic experimental apparatus was designed so that it was interchangeable with the measuring station previously described. Prior to the commencement of experimentation, the sample was placed in a purpose built holder which in turn sat on a sample support structure. A base made from insulating material was fixed to the floor of the light tight enclosure and locating holes were positioned around the base perimeter. Matching locating pins on the sample support structure ensured that the sample always returned to the exact position if the sample needed to be removed from the system. The sample holder was machined from conductive material which had a recess into which the sample was placed. Electrically conductive paint was then applied from the conductive sample holder to the exposed portion of the sample substrate. A low noise shielded cable was then attached to the sample holder which formed the device output.

A 100 $\mu\text{m}$  electrode was then attached to a power supply terminal which was located on the sample holder. An insulating device was used to isolate the power supply from the sample holder. The other end of the electrode was then attached to the desired gold contact by the use of electrically conductive paint. A support plate was attached to each end of the sample support structure which held a tomographic prototype in position directly over the sample. The tomographic prototypes comprised of transparent acrylic pipe which were sealed at both ends. A screw cap was located at one end of the pipe to allow the insertion of various media. The support plates suspended the pipe in such a fashion that the centre of the pipe was in direct alignment with the centre of the sample. The support plates were interchangeable so that pipelines of various dimension could be employed in the system. The samples were illuminated by the xenon light source which was positioned directly above the tomographic prototype in direct alignment with the centre of the pipeline and sample. The height of the light source could be adjusted for various pipeline dimensions. When experimentation was to be performed, the selected Au contact was switched to the system ground and the xenon source was pulsed at 100Hz for 15 minutes in order to bring the xenon gas up to maximum working temperature. Hamamatsu Photonics (1996) state that the intensity of the light is dependant upon the input energy to the source, the distance between the source electrodes, and the pressure of the xenon gas.



**Figure 4.14** Block diagram for electroded mode of operation.

The xenon source was run at the manufacturers recommendation of 100Hz for 15 minutes to ensure that the gas temperature and therefore pressure, was at its maximum and thus the light intensity was at its peak and most stable. This procedure was performed prior to every tomographic experiment.

After the light source warm up period, power was supplied to the electrode and therefore gold contact via a Brandenburg model 2475R stabilised HV supply. The model 2475R could supply potentials of up to  $\pm 1$  kV in graduated increments with lockable fine adjustment control. This allowed the potentials applied to the electrode to be accurately set and reproduced. A limiting resistor was inserted between the model 2475R and the electrode in order to limit the current applied to the sample. The potential applied to the electrode was monitored by a Solartron 7510 digital voltmeter (DVM) which had an accuracy of 0.001%. Figure 4.15 shows basic electrical circuit for the electroded experimentation.

The research project utilised varying magnitudes of photocurrent generated by pulses of visible light to generate qualitative and quantitative data. It was therefore essential that the current detected by the picoammeter employed to measure the photocurrent was as close to the actual current flowing in the circuit under test as was possible and was not influenced by the measurement system. Typical sources of errors in low current measurement include shunt resistance, triboelectric, piezoelectric, and electrochemical effects. Shunt resistance can occur due to the series cable that was connected to the picoammeter. Normal ammeters usually use a precision series resistor to determine a volt drop and hence the current flowing in the circuit. However, a voltage burden is introduced in such meters in the order of 200mV to 2V (Keithley Instruments, 1984). For normal current measurements this value is within acceptable ranges and so can be ignored, for low current measurements this voltage burden is unacceptable. The model 485 picoammeter employed in the research project was a negative feedback ammeter which meant that the input was fed to a high gain amplifier configured with negative feedback which is then connected to a standard voltage measuring circuit. The voltage burden was thus equal to the detected voltage drop divided by the gain of the amplifier and is reduced to approximately 100 $\mu$ V. The greatly reduced voltage burden reduces the amount of shunt resistance in the input

cable and so reduces measurement errors. The cable chosen as the input cable, was  $50\Omega$  coaxial shielded cable with the shield being taken to the system ground. Additionally the model 485 could accommodate up to  $10\text{nF}$  input capacitance which meant that extremely long input cables could be employed without introducing oscillations or instability into the measuring system.

Current errors due to triboelectric effects are due to friction between a conductor and its associated insulator. Friction causes free electrons to rub off of the conductor and cause a charge imbalance creating current flow. The magnitude of current due to the triboelectric effect is typically in the order of  $10\text{nA}$  for standard cable to  $0.01\text{pA}$  for low noise cable (Keithley Instruments, 1984). Thus it was concluded that the low noise cable employed in the system should not make a significant contribution to the measured current especially in the measurement of photogenerated current which has been found to be in the order of several  $\mu\text{A}$  in magnitude for the contact geometry's and electric fields employed in the current study.

Current generated due to the piezoelectric effect can be created when mechanical stress is applied to some types of insulating materials commonly employed in electrical cable connection or fixing mechanisms. Typical magnitudes of piezoelectric generated currents are in the order of  $0.01\text{nA}$  to  $0.01\text{pA}$  (Keithley Instruments, 1984) and as such current errors due to the piezoelectric effect were not considered to be problematic in the experimentation. However, as a precaution, the input cable to the picoammeter was connected to the conductive sample holder by a crimp tag which was bolted to the sample holder. No other connections, terminals, or fixing mechanisms were employed along the input cable length in order to keep any current due to the piezoelectric effect to a minimum. Another possible source of current error in low signal measurement was due to electrochemical effects. This is normally caused by contaminants creating weak batteries between two conductors which can generate current of a few  $\text{nA}$ .

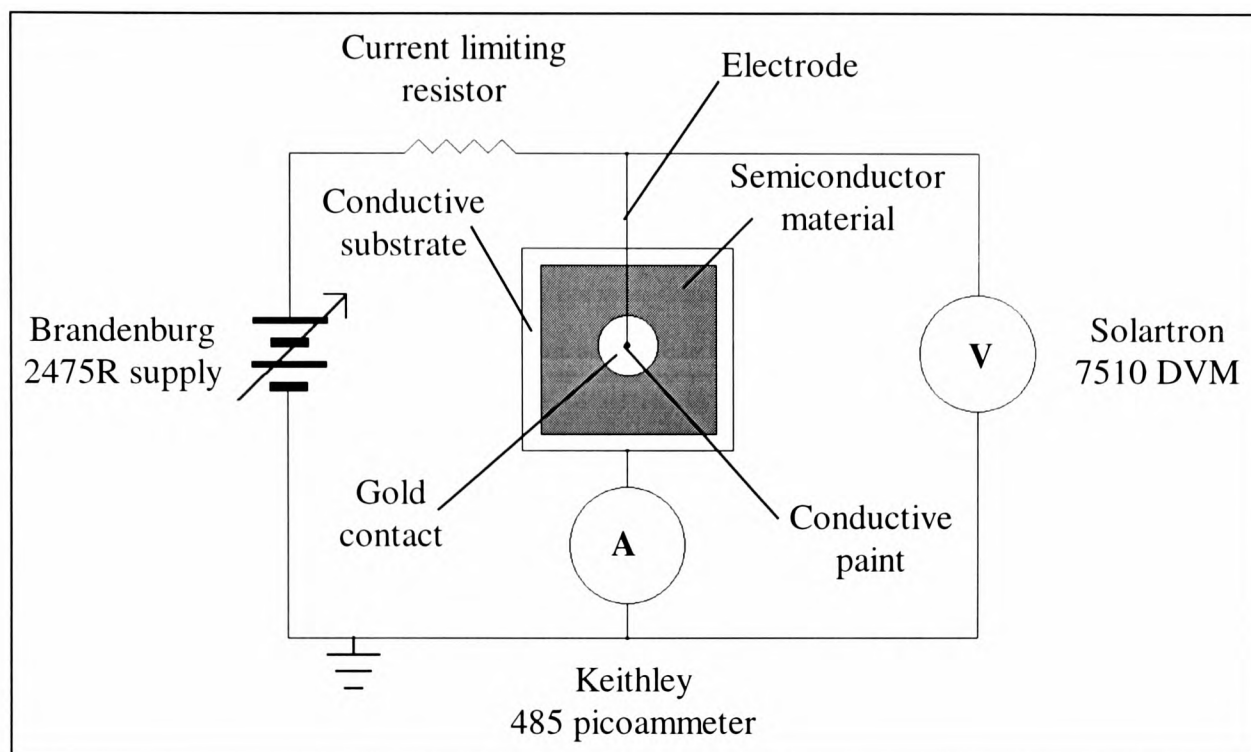


**Figure 4.15 Basic electrical circuit arrangement for electroded experimentation**

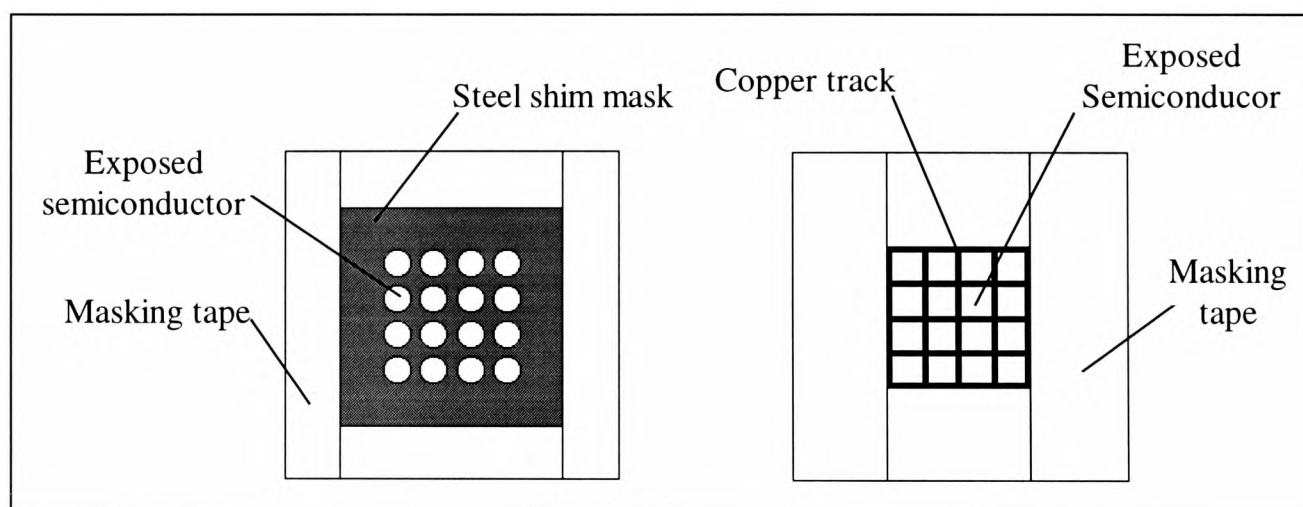


**Figure 4.16 Mask arrangements for samples under electroded mode of operation.**

The sample holder, sample support unit and shielded cable connections were regularly cleaned with methanol in order to prevent current due to electrochemical effects. Additionally, the model 485 is a negative feedback device and as such the input is guarded which eliminates any leakage current caused by high resistance paths between low current conductors and voltage sources.

The model 485 converted the input current to a voltage and gave an inverted analogue output in the range  $\pm 4V$ . This output was taken to a 100MHz Ono Sokki CF-4220 personal FFT analyser where it was converted to digital format. The CF-4220 was operated in the time domain where the time dependence of the current was monitored. If single events were to be captured, the CF-4220 was set to single shot mode and was triggered by an issued light pulse. The event was captured and manually stored to 3.5 inch disc. For experiments where the electrical properties of the samples over extended periods of time were to be monitored, a repetitive trigger within the CF-4220 was employed. The trigger was activated by repetitive light pulses and the time dependence data was continually updated for every trigger event. In this case, the time dependence data was stored by the CF-4220 automatically at a user defined frequency. The data was then transferred to PC for analysis using MATLAB and Excel.

Upon cessation of experimentation in the case of a sample containing a single contact, the contact was switched to the system ground and left for a suitable period before further experimentation was undertaken. In the case of a sample containing multiple contacts, upon cessation of experimentation the electrode was removed from the current contact and attached to the next contact in the array. The electrically conductive paint was allowed to dry for 15 minutes and then the contact was switched to the system ground. The sample was then allowed to rest for a suitable period before experimentation proceeded.

#### 4.2.1 Sample preparation

The samples used for the electroded mode of operation were of the same geometry as for the xerographic mode of operation but had semitransparent gold contacts sputtered onto their surface. Each of the gold contacts represented a single 'pixel' of information for OPT measurements. As with previous experiments in the xerographic mode, a 2mm strip of semiconductor material was removed from the samples in order

to allow electrical contact with the conductive substrate. Circular and square contacts of various size (2.5mm to 7mm) were formed in various configuration by the use of masks.

For the circular contacts, the masks were manufactured from 0.2mm thick steel shim. The shim was cut to be 6cm<sup>2</sup> and was sandwiched between two pieces of 6cm<sup>2</sup>, 1mm thick sheet steel, and was spot welded together along the outer edges. This was done in order to keep the shim taught and flat thus preventing tearing of the shim during machining. A milling machine with a drill attachment was then used to drill holes through the shim device in the desired configuration by the use of an X-Y table. The spot welds were then cut from the shim device and the shim removed and cut to size. The shim mask was then carefully cleaned with methanol and placed upon the surface of the sample where it was fixed in place by the use of masking tape. The use of masking tape to fix the masks resulted in additional time required to pump down the sputter coater as it introduced moisture into the vacuum chamber. However, the advantages of the tape in being able to accurately place and hold the mask in position outweighed this problem.

For square contacts, the masks were formed from self-adhesive copper track which was cut into 1mm wide strips and arranged into the desired configuration. Any area of exposed semiconductor material that was not required to be coated was covered with masking tape. The mask arrangements for the circular and square contacts are shown in figure 4.16.

The gold contacts were sputtered onto the surface of the prepared samples by the use of an Edwards S1050B sputter coater. The vacuum chamber was pumped down to  $7 \times 10^{-1}$  atm and then flushed through with Argon gas until the chamber pressure was  $3.3 \times 10^{-1}$  atm. Sputtering was then performed in three, two minute coats at 1kV/35mA. The coating time was limited to 2 minutes in order to reduce the possibility of crystallisation of the materials due to radiant heating (Johansen *et al*, 1998). A 10 minute period, under vacuum, was left between each coat. All samples used in the study were positioned in the vacuum chamber at the same time, well within the target area in order to achieve uniformity of film thickness.

#### 4.2.2 Experimental procedures for the electroded mode of operation.

##### (i) Steady state and detectivity experimentation

All experimentation to determine the light conditions and electric fields required for detectivity and steady state experiments in both the a-As<sub>2</sub>Se<sub>3</sub> and a-Si:H materials, was performed on samples containing a single 3mm diameter Au contact. The samples were located in the sample support structure previously described in direct alignment with a L2441 xenon light source which is described presently. The distance between the sample surface and the underside of the light source was set at a distance of 65mm.

The bulk of the tomographic experimentation employed a tomographic prototype that was comprised of a 50mm external diameter section of pipeline. 5mm were left between the underside of the light source and the prototype to allow removal of the prototype without disturbing the light source. 10mm were left between the underside of the prototype and the sample surface in order to accommodate the attachment of the electrode to the Au contact. The position of the light source was set with the tomographic prototype in-situ above the sample surface and was fixed into position. The light source then remained in this position for the majority of the tomographic investigations as is discussed shortly. Once the light source had been fixed into the correct position, the tomographic prototype was removed and the experimentation into determining the light levels required for detectivity and steady state experiments commenced.

The establishment of the detectivity and steady state conditions, i.e. the minimum and maximum light conditions for the given material was undertaken in the following manner. In the case of detectivity experiments, single light pulses of predetermined intensity and duration were issued from the light source and the resulting photogenerated current pulses recorded by a FFT analyser. The intensity and duration of the issued light pulse was altered until the smallest signal that was noise free and found to be repeatable was established. This process was repeated over the range of electric fields stated previously and the values of light intensity and duration that produced the smallest clean and repeatable signal set the minimum light conditions for the material under test.

In the establishment of steady state conditions, the photogenerated current due to single light pulses was again recorded using the FFT analyser. The intensity and duration of the issued light pulse was altered until steady state photogenerated current had been achieved. This process was again repeated over the range of electric field described previously. The light conditions required to produce steady state photocurrent then set the maximum light conditions for the material under test.

Further details of the experimental techniques employed in the determination of the detectivity and steady state conditions of the materials are discussed in the relevant sections in chapter 6.

(ii) Establishment of maximum operating speed due to the study of the effects of photoinduced fatigue

The investigation into the possible effects of photoinduced fatigue in the a-As<sub>2</sub>Se<sub>3</sub> and a-Si:H materials was carried out in the following manner. All experimentation was performed on single 3mm diameter Au contacts. Asymmetrical light pulse trains of up to 100Hz frequency were applied to the sample surface either directly or via a tomographic prototype for a half hour period. The resulting photogenerated current pulses were continuously monitored by the FFT analyser and a current pulses was automatically recorded every 15s. At the end of the test run, the peak magnitudes of the photogenerated current pulses were plotted vs time and any deterioration in the peak magnitude of the current pulses over the 30 minute test period could be determined.

This process was repeated under varying levels of flash repetition rate and electric field. The flash repetition rate at which no deterioration in the peak magnitude of the current pulses could was observable set the maximum operational speed of the material under test. Further discussion of the experimental techniques employed in the investigation of photoinduced fatigue are discussed in the relevant sections of chapter 6.

(iii) Establishment of quantitative data.

An initial investigation was carried out to determine if the a-As<sub>2</sub>Se<sub>3</sub> and a-Si:H materials were sensitive enough to distinguish between a pipeline full of water and an empty pipeline. This was done to ascertain the materials suitability for possible application in the imaging/detection of air bubble or plug flow. This was achieved by applying light pulse trains of up to 100Hz to the sample surface via a tomographic prototype. The resulting photogenerated current pulses were then sampled and recorded every 15 seconds for a 30 minute test period for both the full and empty pipelines and the average peak photocurrents were then compared.

The investigation then concentrated on developing experimental techniques that would produce maximum separation and therefore resolution between the full and empty pipelines. Maximum separation between the full and empty pipelines was achieved by accurately controlling the intensity and duration of the light pulses to position the peak of the resulting photogenerated current pulse for the full pipeline just under the steady state condition as can be seen in figure 4.17. It was found that if the photocurrent was approaching the steady state condition, the separation between the full and empty pipelines was negligible as the reduction in incident light intensity due to the effect of the empty pipeline was insufficient to move the peak photocurrent away from the steady state. By positioning the peak photocurrent for the pipeline full of water just below the slowly increasing response as the photocurrent neared the steady state condition, it was found that a much larger separation could be achieved.

Figure 4.17 demonstrates that the separation between the full and empty pipelines if the intensity and duration of the light pulses is sufficient to allow the photocurrent to approach the steady state was approximately 22nA. The separation between the full and empty pipelines when the light intensity and duration were set to position the peak photocurrent just below the steady state, was approximately 1.352μA. Thus the positioning of the peak photocurrent led to a 61 fold increase in separation between the responses for the full and empty pipelines, thus increasing the available resolution of the system for the collection of quantitative and qualitative data.

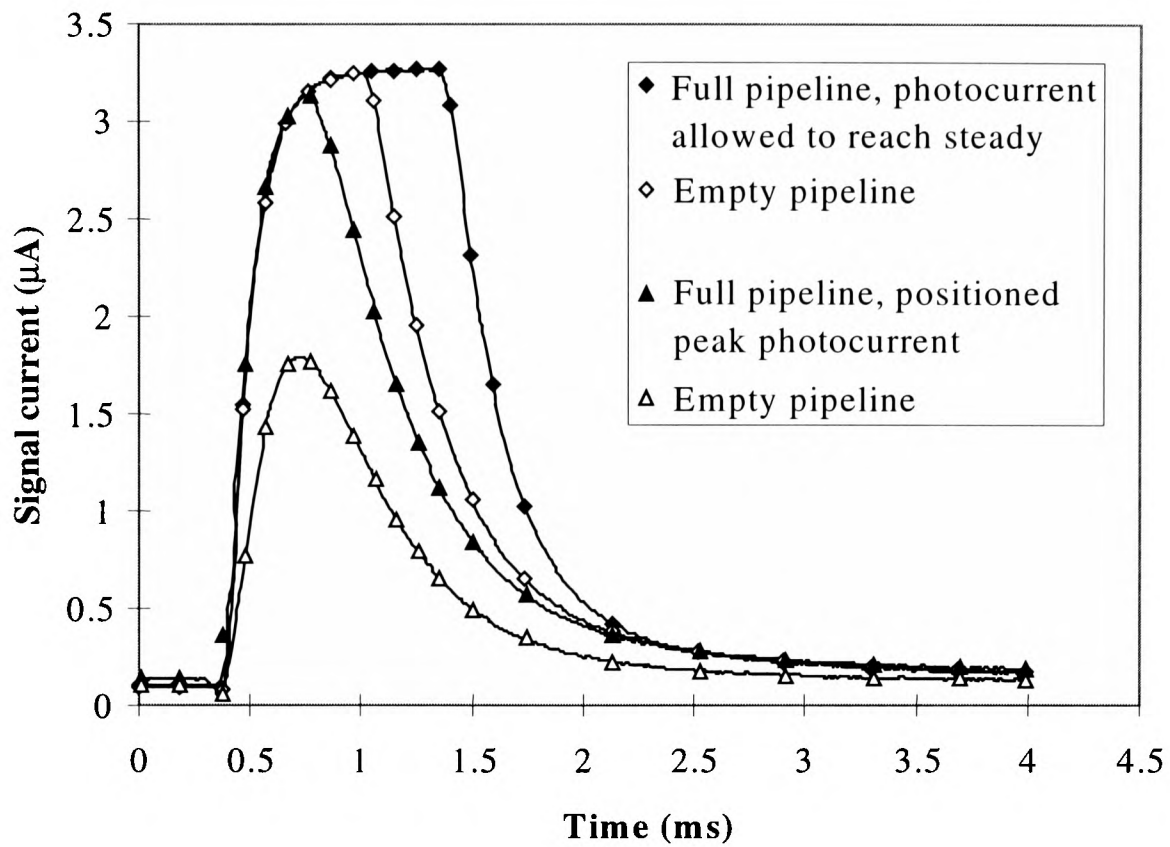


**Figure 4.17** Positioning of peak photocurrent to exploit maximum sensitivity between the full and empty pipelines. a-Si:H sample used  $E=1.66 \times 10^5$  V/cm.

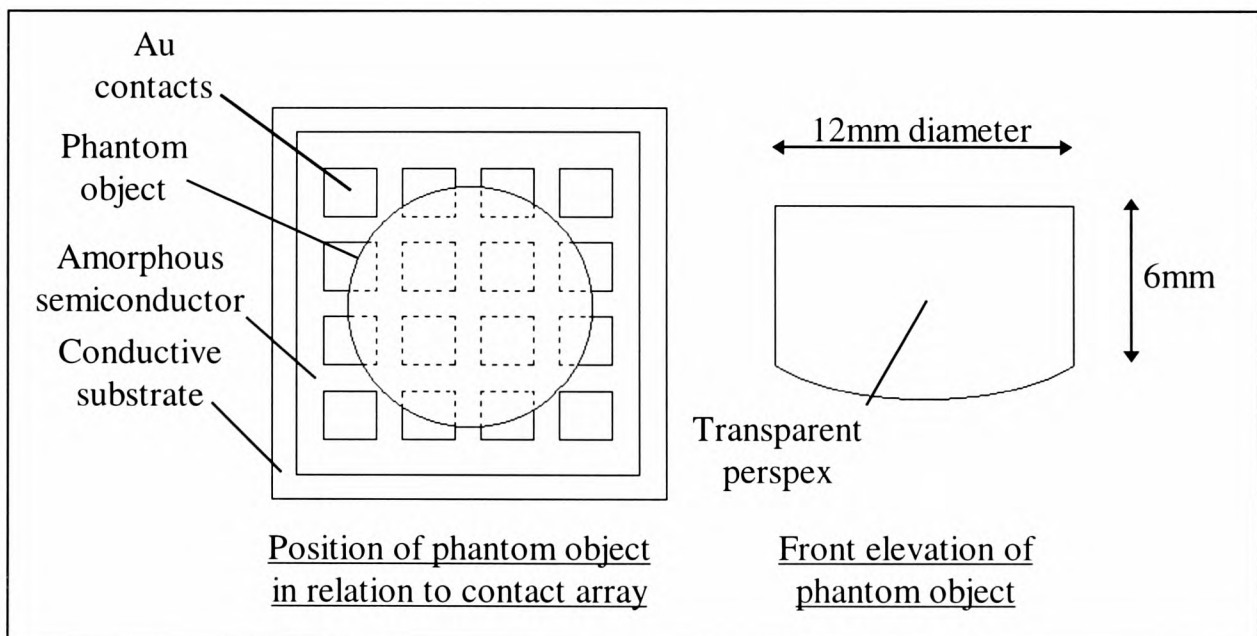


**Figure 4.18** Positioning and geometry of phantom object

Once the maximum separation between the full and empty pipelines had been established, the investigation focused on determining if the a-As<sub>2</sub>Se<sub>3</sub> and a-Si:H materials could distinguish between predetermined levels of water contained within the pipeline. Water was added to the tomographic prototype, and the water level checked by the use of a vertical scale. For reproducibility of results, multiple test runs were performed at each water level, as the exact water level would have been difficult to reproduce at a latter date. The water level was altered in smaller increments until the smallest detectable change had been established. The photogenerated current pulses were again recorded every 15 seconds for a 30 minute period. Further discussion of the experimental techniques employed in the collection of quantitative data is discussed further in the relevant section in chapter 4.

(iv) Establishment of qualitative data

An investigation was carried out to see if the a-As<sub>2</sub>Se<sub>3</sub> and a-Si:H materials could accurately detect changes in fluid colour within the pipeline. The aim of these series of experiments was to determine if the materials could find possible application in the quality control or batch monitoring of fluids flowing within a pipeline. A water based coloured concentrate was added to water by volume to produce a fluid mix. The initial investigation concerned altering the fluid concentration by 10%, and recording the photocurrent over the 30 minute test period. The percentage change in fluid concentration was reduced until the changes in fluid colour could no longer be accurately distinguished. Again, for reproducibility of results multiple test runs were performed at each fluid mix.

(v) Production of images

The aim of these series of experiments was to see if basic images could be produced from a sample containing an array of gold contacts. For imaging purposes, a sample containing sixteen 2.5mm<sup>2</sup> Au contacts was employed. The initial investigation was concerned with trying to establish if the contact array could determine the curvature of the bottom of the empty pipeline. In order to do this, the electrode was connected to the first contact in the array and the photogenerated current pulses were recorded over a 15 minute test period. This process was repeated three times for each contact in the array. The electrode was then attached to the next contact in the array and the test re-

run. This procedure was followed until the photogenerated current pulses from all 16 contacts had been recorded.

The investigation then moved on to try to produce a surface plot of a phantom object located at the bottom of the pipeline. Figure 4.18 shows the phantom object geometry and its position relative to the contact array. The phantom object was a 12mm diameter, 6mm deep Perspex pellet which was filed flat on its top surface. The bottom surface was shaped into a slight curvature that matched the internal curvature of the pipeline. The surfaces of the phantom object were then polished by the use of a polishing cloth and Perspex polish to remove file marks and regain transparency of the Perspex. The phantom object was then attached to the bottom of the pipeline with a clear adhesive.

The phantom object was designed in such a manner that when it was in-situ in the tomographic prototype and correctly positioned above the contact array, 4 contacts within the array were uncovered, 8 were partially covered and 4 were fully covered. This was done to produce contrasting levels of photocurrent due to the phantom object and the pipeline in order to produce a basic image of the phantom object and its relation to the pipeline.

The measurement procedure for the collection of data from the contact array described above was followed until the photocurrent pulses from all 16 contacts in the array over the 15 minute test period had been recorded. A mechanical device located on the tomographic prototype containing the phantom object used in conjunction with a datum marker, ensured that the phantom object was returned to the same position when the power electrode needed to be attached to the next contact in the array. Images from the collected data were formed using MATLAB.

#### 4.2.3 Xenon flash unit

The light source developed for use in both the electroded and xerographic modes of operation was a xenon flash light source. The light source was designed to allow the intensity, duration, and flash repetition rate (FRR) to be easily controlled. The xenon source was located directly above the transparent probe in the xerographic mode of operation, and directly above the tomographic prototype in the electroded mode of

operation. The controlling and driving circuitry for the xenon source was located outside of the light tight enclosure in order to allow easy operator access. The light source was controlled by a control box which was located outside of the high voltage cage in order that the light source could be controlled remotely.

For the xerographic mode of operation, the light source was used to discharge applied electrostatic charge for PID experimentation. For PID experiments a single pulse of light was issued automatically as the charged sample arrived at the measuring station. Upon arrival of the sample at the measuring station, the light beam of TPS2 was interrupted and an 'enable' signal was sent to the xenon flash unit which issued the light pulse. For the electroded mode of operation, both single and repetitive light pulses were required. As the sample in the electroded mode was static and did not have electrostatic charge upon its surface, the application of the light pulses was achieved manually by the use of a function generator which was located outside of the high voltage cage. Figure 4.19 shows a block diagram of the developed xenon flash unit.

(i) Light source

The light source used in the flash unit was a super quiet model L2441 xenon discharge lamp, with a spectral distribution of 240 - 2000nm and a maximum FRR of 100Hz. The L2441 is 22mm in diameter and has a fused window through which the light is emitted. The window material for the L2441 is borosilicate glass which is especially manufactured for visible light (400 - 700nm) applications, and which greatly reduces the emission of far ultraviolet and ultraviolet (125 - 400nm) light and near, infrared, and far infrared (700nm - 5 $\mu$ m) light from the source. The internal mechanism of the L2441 can be seen in figure 4.20.

Traditional xenon discharge lamps have been known to suffer from instability due to variation of the cathode, anode, and trigger probe characteristics contained within the discharge lamp. The variation in the operating characteristics resulted from erosion of the cathode over extended operating times which resulted in the arc gap between the cathode and anode increasing which effected the intensity of the light (Hamamatsu, 1995).



Tomographic experimentation performed in the electroded mode of operation, exploited variance in light incident upon the sample surface to establish quantitative or qualitative data. Thus it was of vital importance that the light source be as stable as possible so that the variation in incident light could be attributed to the media contained within the tomographic prototype and not fluctuation in the light source itself.

The L2441 is a super quiet xenon flash lamp. This means that a specially designed cathode with very high durability is employed within the discharge lamp. The cathode within the L2441 should not erode during the lifetime of the lamp (approximately  $1.2 \times 10^9$  flashes) and produces a maximum output fluctuation of 3.5%. The stability of the L2441 was not only dependant upon the type of cathode employed, but was also influenced by the FRR and the stability of the power supply and therefore input energy supplied to the discharge lamp.

The intensity of the light from the L2441 is nearly proportional to the input energy supplied (Hamamatsu, 1995). The input energy was applied to the L2441 source by charging and then discharging high voltage capacitors into a trigger socket and the L2441 source. The power supply for the main discharge capacitors ( $C_m$ ) was a Brandenburg model 2475R stabilised HV supply. The model 2475R was used to supply voltages up to 1kV with a maximum output ripple of  $\pm 5$ mV for all voltage settings. The investigation utilised voltages of 400V to 1kV for the charging of the discharge capacitors which resulted in a stability of  $\pm 0.00125\%$  ( $V_{in}=400$ V) to  $\pm 0.0005\%$  ( $V_{in}=1$ kV) of the main power supply. High quality low impedance polypropylene capacitors were employed as  $C_m$  in order to further improve stability of the light source.

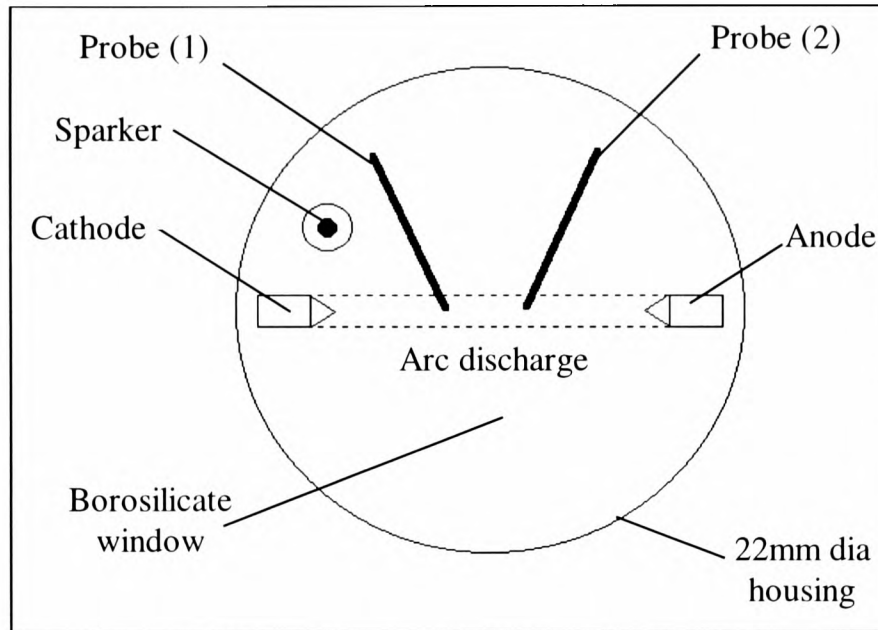


**Figure 4.20 Internal mechanism of L2441 xenon discharge lamp.**

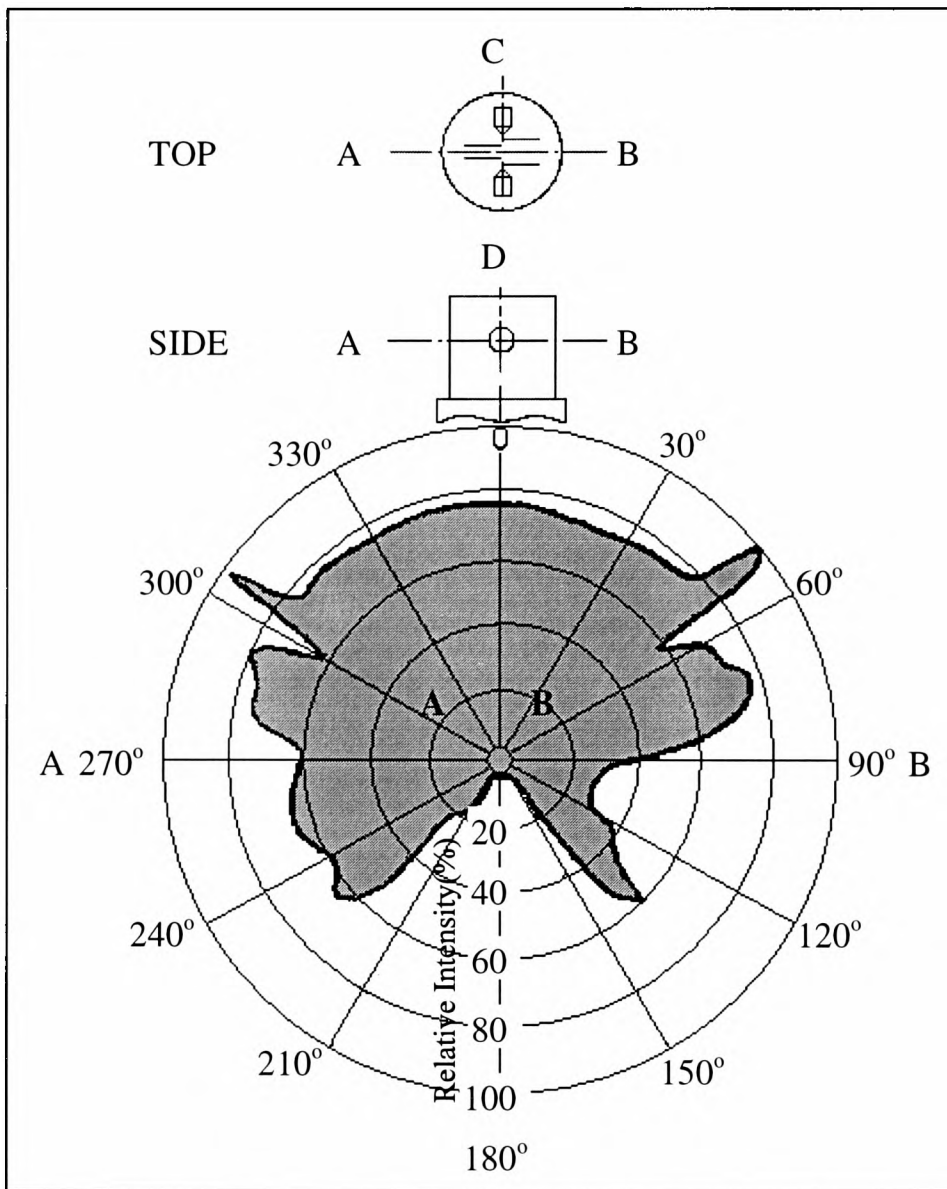


**Figure 4.21 Light flux distribution (From Hamamatsu, 1996).**

Manufacturers data stated that the stability of the light was effected by the FRR, and that the higher the FRR the more unstable the light source became. Williams and Beck (1995) state that the minimum operating speed required for real time OPT applications is 100Hz. Conveniently, the maximum operating speed of the L2441 xenon source coincides with this requirement. For tomographic experimentation, the light source was set to the maximum FRR that the materials could accommodate (up to 100Hz) in order that maximum instability be introduced into the light source and therefore the collected data. In this manner, the suitability of the a-As<sub>2</sub>Se<sub>3</sub> and a-Si:H materials for the production of quantitative and qualitative data at speeds required for OPT applications could be established.

The L2441 has an arc size (distance from anode to cathode) of 1.5mm which is one of the shortest arc sizes currently available and is capable of delivering light pulses of less than 1 $\mu$ s duration. The small arc size results in superior intensity over larger arc sizes as it reduces the volume and duration of the emitted light. The light is emitted through the borosilicate window which is located in the top of the L2441. The light flux is distributed at an angle of +/- 45° from the emission point as can be seen in figure 4.21. Figure 4.21 shows the light flux distribution of the L2441 when orientated in the AB direction. It could be seen that the greatest area of uniform light flux distribution was between 300 and 60°. A scale drawing of the L2441 was produced and it was found that the largest diameter single gold contact that could be inserted into the area of greatest light flux distribution was a 7mm dia contact. This set the maximum size of single contact that could be employed if uniform light distribution was to be achieved.

Figure 4.21 demonstrates that the largest area of uniform light flux distribution is offset from the centre of the light source. Accordingly, the light source was orientated in the AB direction and was positioned so that the largest area of light flux distribution aligned with the centre of the sample under test. This alignment was achieved manually by the use of a set square, and once set, the position of the light source was not altered for any reason until the investigation into the materials suitability for OPT had been established. The bulk of the experimentation in the electroded mode of operation was concerned with establishing the electrical properties of the a-As<sub>2</sub>Se<sub>3</sub> and

a-Si:H materials and as such only single contacts were employed. The single contacts were positioned in the centre of the samples which meant that the contacts were positioned within the area of uniform light flux distribution. Samples with sixteen  $2.5\text{mm}^2$  contacts were employed in the imaging of the curvature of the bottom of an empty section of pipeline and also in the imaging of a phantom object located on the bottom of a section of pipeline. A 1mm gap was left between contacts which gave a total active area of  $13\text{mm}^2$  for the array. From scaled drawings of the L2441 light flux distribution based on manufacturers data, the largest array that could be fitted into the area of uniform distribution was found to be approximately  $12.4 \times 9.91\text{mm}$ . This resulted in a shortfall of 0.6mm in the X direction of the array and 3.09mm in the Y direction. As the contacts were  $2.5\text{mm}^2$ , the 3.09mm shortfall meant that the last row of contacts in the array were outside of the area of uniform light flux distribution. In order to minimise and evenly distribute this shortfall in the Y direction, the light source was shifted 1.5mm backwards in the Y direction so that the first and last rows of contacts in the area were partially within the area of evenly distributed light flux. The realignment of the light source was undertaken only after the investigation of the electrical properties of the materials under test had been completed.

(ii) Discharge mechanisms.

A pulse of light was initiated by discharging a trigger capacitor ( $C_t$ ) into the E2442 trigger module.  $C_t$  was a single  $0.47\mu\text{F}$  HV ceramic capacitor charged to 160V which delivered approximately 0.6mJ of energy ( $E=1/2CV^2$ ) to the E2442 trigger module upon discharge. The E2442 in turn then applied a 5-7kV voltage spike to a sparker contained within the L2441. The sparker provided an electrical arc across the anode and cathode which allowed the main discharge capacitors ( $C_m$ ) to discharge into the L2441. The current from the discharge by  $C_m$  then ionised the xenon gas producing the flash of light.

The developed light source provided asynchronous light pulses, and a HV C122M silicon controlled rectifier (SCR) firing mechanism was employed to control the charging and discharge periods of  $C_m$ . The illumination period ( $C_m$  discharge period) was denoted by  $t_{\text{ill}}$  and the dark period ( $C_m$  charging period) was denoted by  $t_{\text{dark}}$ . The conduction of the SCR could be controlled by the application of voltage to the gate of

the device. To keep the SCR in the 'off' condition ( $t_{\text{dark}}$ ), the cathode of the device was kept at -5V. When the SCR was required to be fired into the 'on' condition ( $t_{\text{ill}}$ ) thus allowing  $C_t$  and therefore  $C_m$  to discharge, +1.5V was applied to the gate of the device. The time that the SCR was in the 'on' condition dictated the time that  $C_m$  was allowed to discharge. The timing diagram for the initiation of a single pulse of light is shown in figure 4.22.

The SCR conduction conditions were controlled by the use of a UA474CN differential amplifier and SN74121N monostable multivibrators. For the 'off' condition of the SCR, the offset null on the differential amplifier was set so that the output of the amplifier which was taken to the gate of the device, was held at -5V when no signal was applied. This ensured that the gate voltage was negative with respect to the cathode which was held at the system ground and the SCR was efficiently turned off. When the SCR was required to turn on, the enable signal from TPS2 was fed via a HCPL2200 optocoupler to the input of the first monostable multivibrator (MM1). An optocoupler was used to prevent misfiring of the SCR and therefore the L2441 source due to transient effects. The output of MM1 was taken to both the input of the second monostable multivibrator (MM2) and the non-inverting input of the differential amplifier. The output of MM1 was high for a period of 40ns upon the receipt of the enable signal. MM2 was configured as a negative edge triggered device, and was triggered into the high condition by the falling edge of the output from MM1.

The output from MM2 was taken to the inverting input of the differential amplifier which when high, swung the output of the differential amplifier to the positive supply rail and the SCR was fired 'on'. The time that the output of MM2 was high was set by an RC circuit. A voltage divider circuit was used to limit the voltage applied to the gate of the SCR to +1.5V. When the output of MM2 timed out, the output of the differential amplifier and therefore the gate of the SCR returned to -5V and the device turned off. Figure 4.23 shows the basic SCR firing mechanism. The accurate control of  $t_{\text{ill}}$  and  $t_{\text{dark}}$  was an important consideration when tomographic experimentation was to be performed. The investigation into possible effects due to photoinduced fatigue of the materials under test, required that the response of the samples be monitored over varying rates of flash repetition and light intensity/duration.

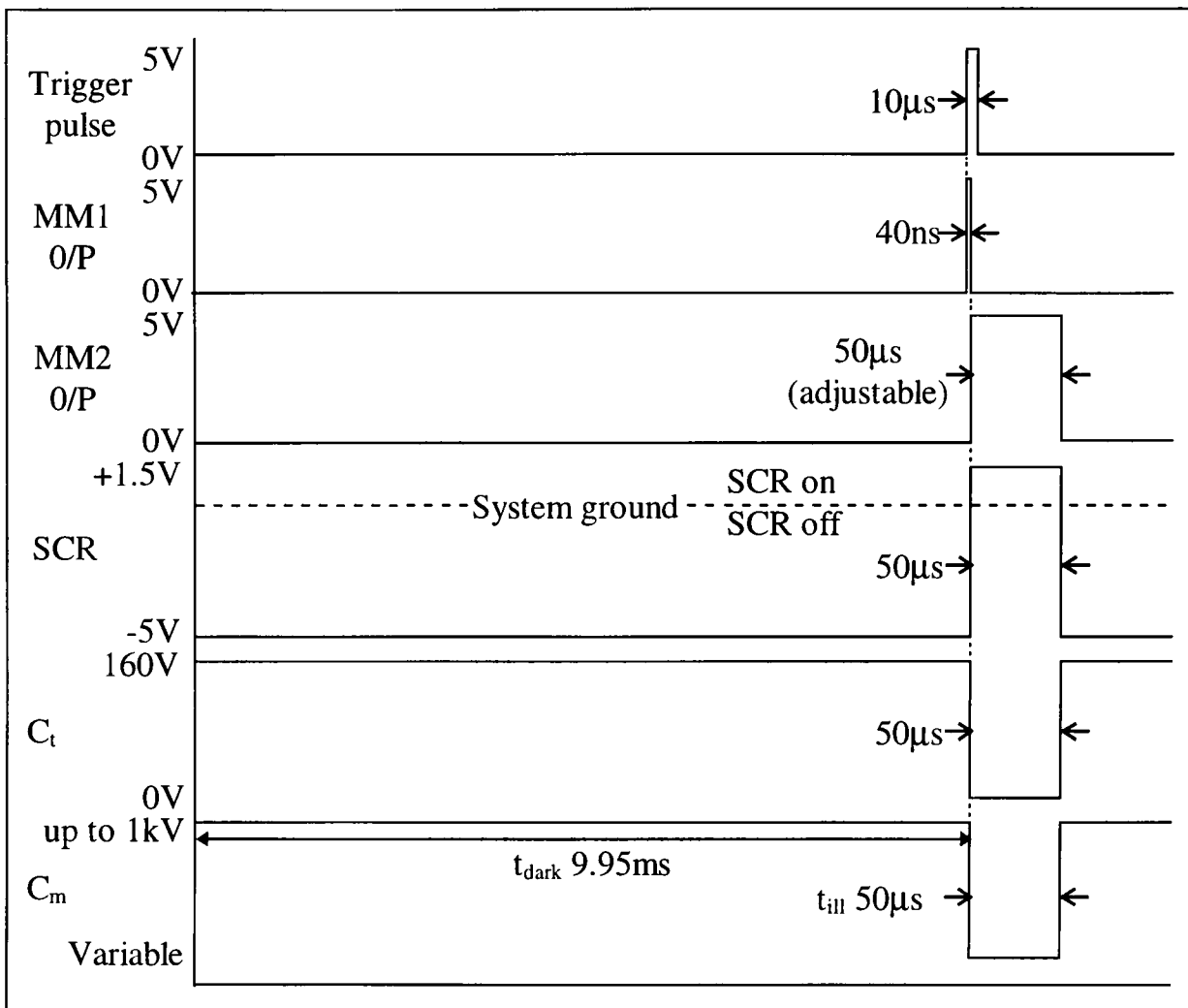


**Figure 4.22** Timing diagram for the initiation of a single light pulse. The time that the SCR is fired on or off and the charge/discharge times of C<sub>t</sub> and C<sub>m</sub> are dependant upon the adjustment of MM2. The potential to which C<sub>m</sub> will discharge is also dependant upon the adjustment of MM2.

In this manner the maximum operating parameters of the materials could be established. It was therefore of vital importance that the variance in incident light falling upon the sample surface be caused by the tomographic prototype and media and not because of limitations of the xenon flash unit.

The intensity of the light pulses issued could degrade due to incorrect capacitor charging at high FRR's if the time constants of the xenon flash unit were not accurately set. The time allowable for the charging and discharging of  $C_m$  was dependant upon the FRR. If for example the FRR was 20Hz, 50ms per light pulse could be allowed for charging/discharging purposes. If the FRR was 100Hz, 10ms per light pulse could be allowed for charging/discharging purposes.

The intensity of the emitted light pulses could also degrade at higher FRR's if larger values of input energy were required. The HV power supply used to charge  $C_m$  had a relatively low output current of 3.5mA which was limited by the manufacture for safety reasons. Higher values of input energy would draw more current from the power supply. If at high FRR's the power supply could not supply sufficient current,  $C_m$  would be prevented from becoming fully charged and the intensity of the light pulses would diminish as a result.

Nakamura *et al* (1977) described a electronic discharge flash device that terminated the capacitor discharge long before it was fully discharged. The cut off mechanism described by Nakamura *et al* was incorporated to allow faster FRR rates due to the greatly reduced time required for capacitor discharge. As the peak discharge energy occurred at the onset of discharge, the remaining charge did not contribute to the production of the light pulse and was deemed redundant. In the xenon flash unit developed for the current investigation, the SCR firing mechanism was used to prevent full capacitor discharge in order to allow maximum capacitor charge time ( $t_{\text{dark}}$ ). This was achieved by setting  $t_{\text{ill}}$  to the minimum required for efficient capacitor discharge. This resulted in a asynchronous light pulse with  $t_{\text{ill}}$  at 50 $\mu$ s and  $t_{\text{dark}}$  at 9.95ms.

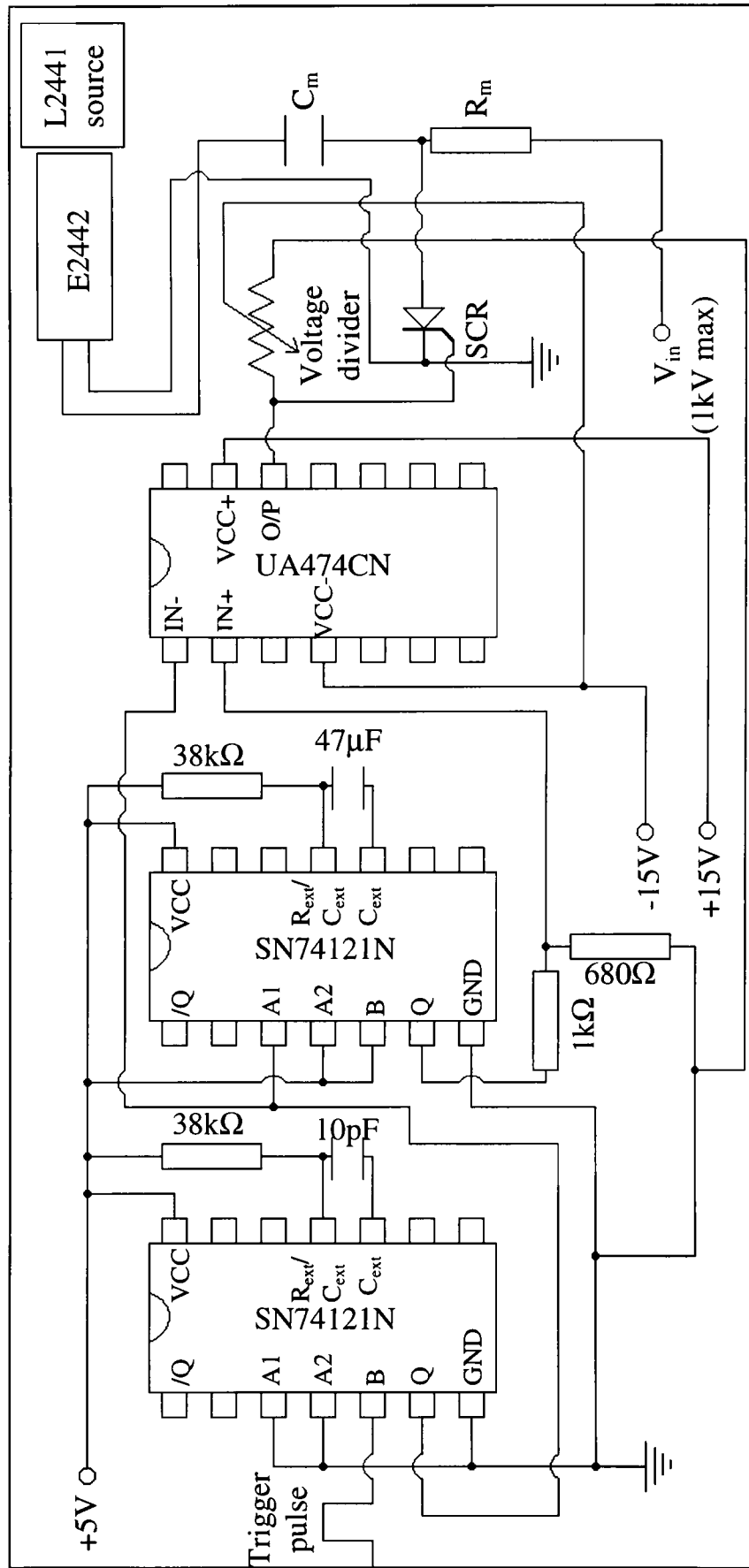


Figure 4.23 Basic block diagram of SCR firing mechanism

The effect of varying the illumination period and therefore the available capacitor charge time can be seen in figure 4.24. The two light pulses shown were recorded by the use of a fast PIN photodiode as described in section 4.2.4. The light pulses were produced by setting  $C_m$  at 54nF and the input voltage ( $V_{in}$ ) to  $C_m$  at 1kV and varying  $t_{ill}$  by adjustment of the timing function of MM2 on the SCR firing mechanism. With  $t_{ill}$  at 1.5ms and  $t_{dark}$  at 8.5ms, a peak detected voltage of 3.33V was observed. With  $t_{ill}$  at 50 $\mu$ s and  $t_{dark}$  at 9.95ms a peak detected voltage of 3.71V was observed giving a difference in light intensity of 0.38V. Figure 4.25 shows the effect of this change in light intensity of the production of photocurrent. It was observed that the longer capacitor charge time associated with  $t_{ill} = 50\mu$ s produced more photocurrent than with the longer illumination period which demonstrated that the timing parameters of the xenon flash unit could indeed inhibit the production of photocurrent if incorrect.

In order to ensure that the light intensity and therefore photocurrent did not degrade due to timing constraints within the xenon flash unit, the timing constraints were set using the maximum FRR of 100Hz and maximum input energy of 0.1J. In this manner the xenon flash unit was able to produce constant light intensity at a given value of input energy (0.1J max) for any FRR up to 100Hz. This procedure ensured that any variance in photocurrent used for OPT measurements was solely due to the tomographic prototype and media under test and not due to limitations of the light source.

### (iii) Control signal generation

In the xerographic mode of operation single light pulses were issued upon receipt of an enable signal. The enable signal was a logic signal that was generated upon the interruption of the light beam of TPS2 by the arrival of the charged sample. The enable signal was active high, and electronic latching mechanisms were employed to prevent erroneous enable signal generation. A frequency generator circuit contained within the xenon flash unit was configured to continuously produce a logic pulse train of 100kHz frequency with 10% duty cycle which was applied to the input of a pulse selector mechanism. Upon receipt of the enable signal, the pulse selector mechanism was activated and a single pulse from the pulse train was allowed through to the output of the pulse selector mechanism.

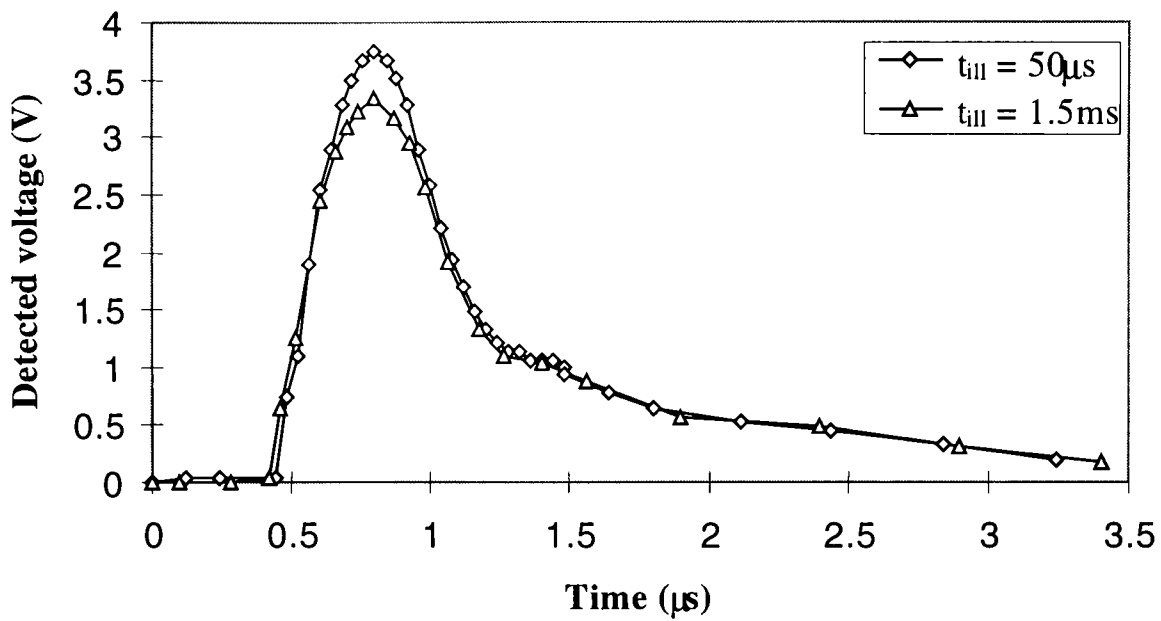


**Figure 4.24** Effect of changing the illumination period on recorded light intensity

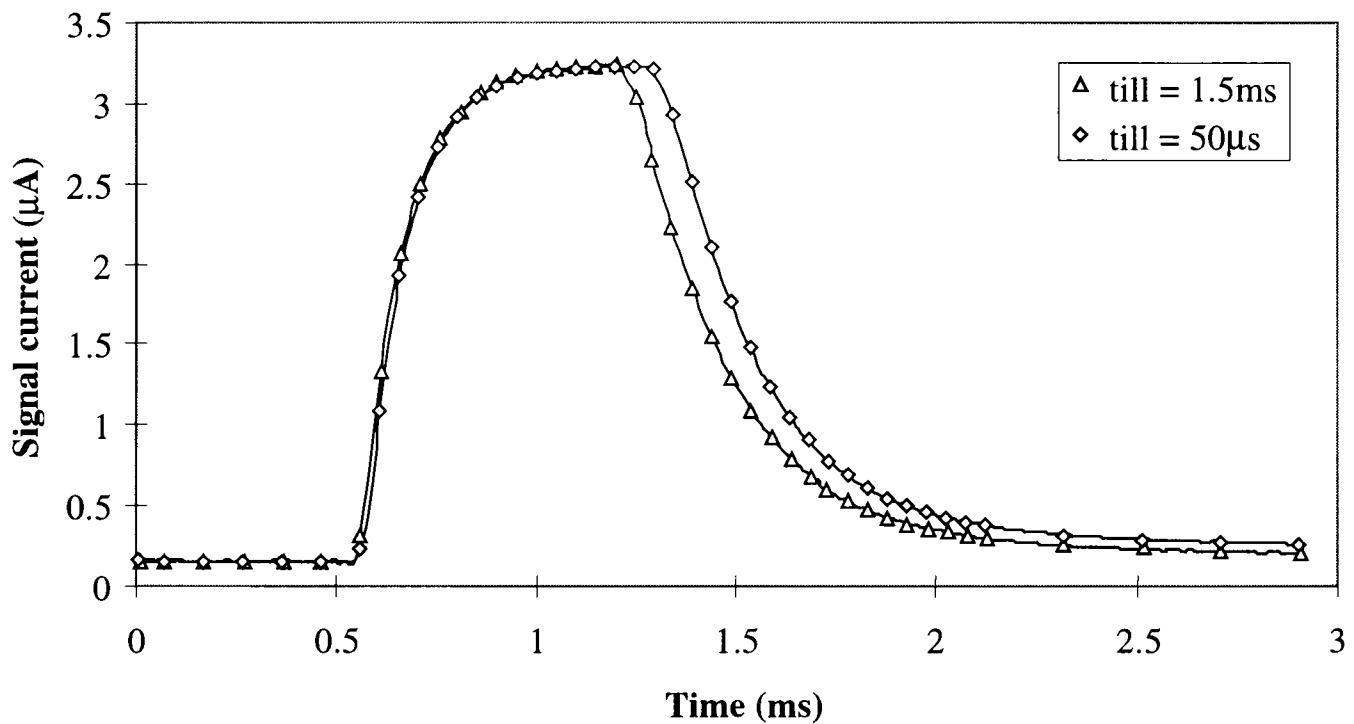


**Figure 4.25** Effect of changing the illumination period on the production of photocurrent in a-As<sub>2</sub>Se<sub>3</sub>.  $E=1.33 \times 10^5$  V/cm,  $C_m=54$ nF,  $V_{in}=1$ kV).

This output was in turn taken to the input of a HCPL2200 optocoupler contained within the xenon flash unit. The xenon flash unit was located outside of the light tight enclosure, and the optocoupler was used to electrically isolate the xenon flash timing and discharge mechanisms from the control and signal generation electronics contained within the light tight enclosure. This was done to eliminate false firing of the light source due to electrical noise. The output of the HCPL2200 was then taken to the input of the SCR firing mechanism where the timing parameters of the  $t_{\text{ill}}$  and  $t_{\text{dark}}$  were set. The enable signal was reset upon departure of the sample from TPS2, and the electronic latching mechanisms were reset as the sample arrived back at TPS1.

For experimentation in the electroded mode, single and repetitive light pulses were required. As the electric field across the samples was continuously applied via an electrode connected to the gold contact on the sample surface, there was no time requirement on issuing the light pulse(s) and so this was accomplished manually. The pulse train required to produce the desired FRR was supplied via a function generator and control box located remotely to the HV cage. The output of the pulse train was taken directly to the input of the HCPL2200 optocoupler circuit. A control box was constructed in order for the operator to allow pulse trains or single pulses though to the xenon flash unit. The control box was also used to apply the electric field to the sample under test or switch the contact to the system ground.

(iv) Control of light intensity and duration.

The intensity and duration of the emitted light was dependant upon the arc size of the light source, the discharge capacitance ( $C_m$ ), the impedance of the leads between  $C_m$  and the light source, and the input voltage to the discharge capacitor ( $V_{\text{in}}$ ). The developed xenon flash unit utilised variation in  $C_m$  and  $V_{\text{in}}$  to change the intensity and duration of the light pulse. The size of  $C_m$  effected the duration of the light due to resulting increased discharge time. However, it was not possible to vary  $C_m$  and maintain the desired input energy ( $E_{\text{in}}$ ) without also altering  $V_{\text{in}}$  as were are bound by the following relationship.

$$E_{\text{in}} = \frac{C_m V_{\text{in}}^2}{2} \text{ (J)} \quad (4.6)$$

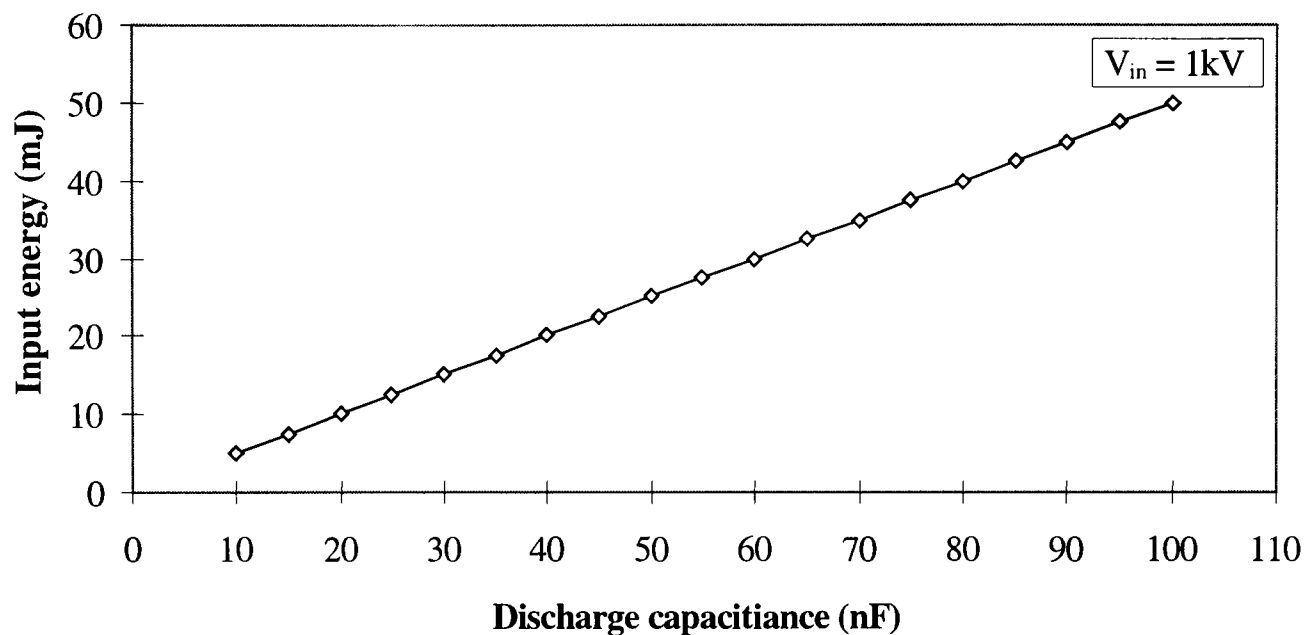


**Figure 4.26** Effect of varying discharge capacitance on input energy whilst maintaining constant input voltage.

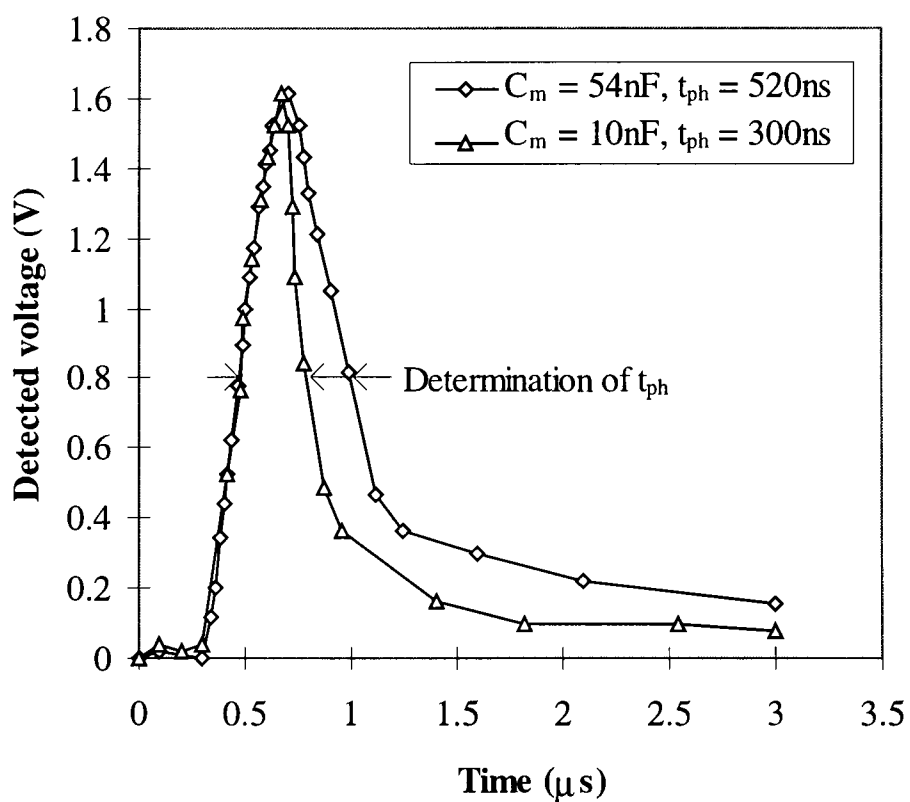


**Figure 4.27** Control of light pulse duration.

Figure 4.26 demonstrates that if the duration of the light pulse were to be increased by changing  $C_m$ ,  $V_{in}$  would have to be adjusted to maintain the desired input energy. The maintenance of  $E_{in}$  when  $C_m$  was varied, was achieved by recording the light pulse due to the original value of  $C_m$  on a digital storage oscilloscope by the use of a fast PIN photodiode described in section 4.2.4.  $C_m$  was then set to its new value and the resulting light pulse was again displayed upon the oscilloscope.  $V_{in}$  was adjusted until the intensity of the light pulses matched the recorded light pulse. Figure 4.27 shows the control of the light pulse duration by the use of the experimental technique described. All light pulse duration times quoted in this thesis are half times, i.e. the duration of the pulse between half peak points and are denoted by  $t_{ph}$ .

Control of the intensity of the light pulse when constant pulse duration was required, was achieved by employing a fixed value of capacitance and altering  $V_{in}$ . Figure 4.28 demonstrated that the input energy and therefore the light intensity could be increased by an associated increase in input voltage. However, figure 4.28 also demonstrated that it was not possible to have maximum light intensity and very short light pulses at the same time. In theory, if a 10nF  $C_m$  was required to supply maximum input energy (0.1J) to the light source,  $V_{in}$  would be required to be in the order of approximately 4.5kV. However, the maximum voltage rating for the L2441 xenon source was 1kV, and 1.5kV for the HV capacitors that formed  $C_m$ . This meant that for  $C_m = 10\text{nF}$  the maximum input energy at 1kV would be 5mJ, which was 1/20th of the maximum input energy. If higher light intensities were required, a larger value of  $C_m$  would have to be employed which would result in a longer pulse duration due to the increased discharge time. For the developed xenon flash unit, the largest value of  $C_m$  that could be employed whilst maintaining maximum input energy at  $V_{in} = 1\text{kV}$  was 0.2 $\mu\text{F}$ . Figure 4.29 shows the control of the light pulse intensity whilst maintaining light pulse duration.

Xenon discharge bulbs are commonly employed in xerographic time of flight (XTOF) experiments due to the very short light pulse duration's obtainable. In such systems the main discharge capacitor is commonly soldered directly to the light source in order to keep the impedance of the leads between the discharge capacitor and the light source

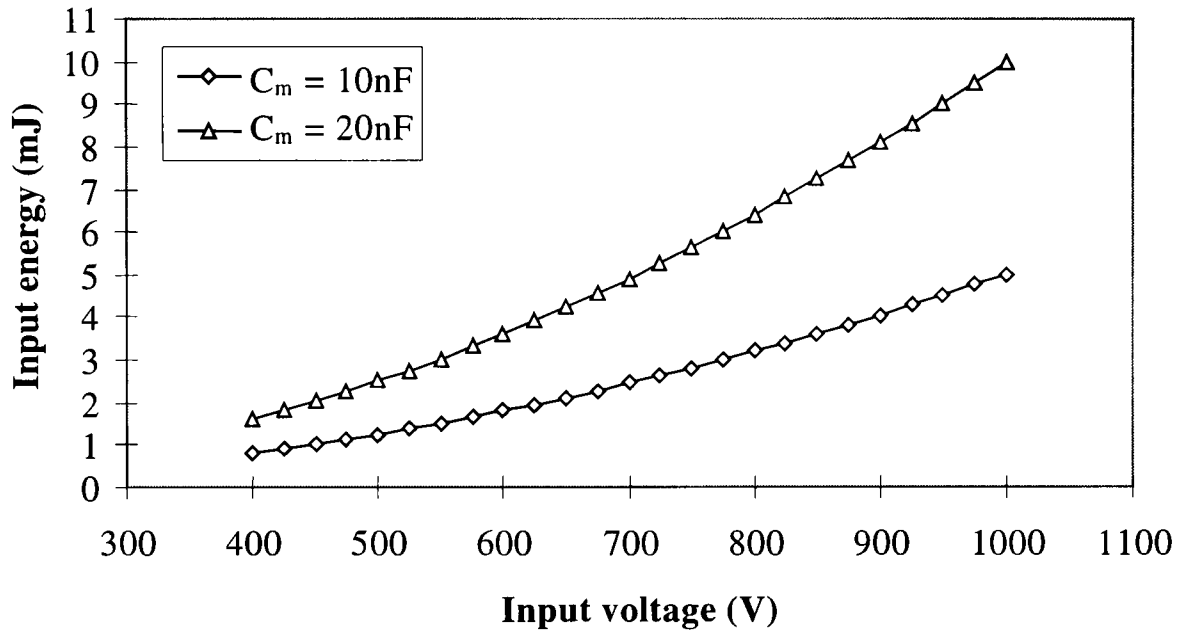


**Figure 4.28** Effect on input energy of varying the input voltage whilst maintaining constant discharge capacitance.

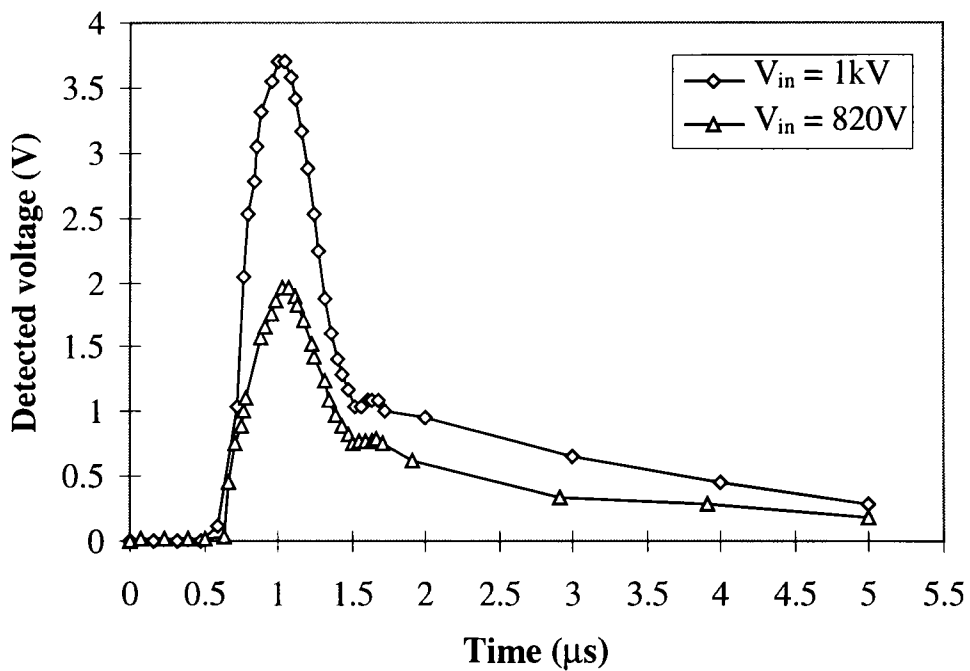


**Figure 4.29** Control of light intensity whilst maintaining pulse duration.

to a minimum. However, this practice would result in a fixed pulse duration. In order to change the pulse duration the existing capacitor would have to be de-soldered and a new capacitor soldered to the light source.

The light source in the current investigation was accurately positioned at a set distance and orientation above the sample. In order ensure repeatability of results it was important not to disturb the light source throughout the course of the investigation. In accordance with this requirement,  $C_m$  was incorporated into the xenon flash unit which was located outside of the light tight enclosure.  $C_m$  was comprised of high voltage, low impedance polypropylene capacitors connected to give the desired value of discharge capacitance. The capacitors were mounted on printed circuit boards (PCB) which could be simply inserted into the xenon flash unit by the use of a purpose built support/connection mechanism which can be seen in figure 4.30. This system had the disadvantage in that it introduced impedance due to the length of the cable from  $C_m$  to the light source thus increasing the shortest light pulse that would be possible from the unit. However, the system had the advantage in that the desired value of discharge capacitance could be efficiently set without disrupting to the light source. The reader is referred to Jenner and Vaezi-Nejad (1999) for further details of the developed xenon flash unit.

#### 4.2.4 Light detection mechanism

The intensity and duration of the issued light pulses were recorded by the use of a Hamamatsu S1722-02 fast PIN photodiode and a Fluke PM388OA 100MHz storage oscilloscope. The S1722-02 was configured as a high speed light detector as shown in figure 4.31. The photodiode was contained within in a replica of the sample support structure shown in figure 4.14. The photodiode was positioned at the same height as the sample surface, and locating pins on the bottom of the sample support structure replica ensured the photodiode was in the same alignment with the light source. When a light pulse was to be recorded, the sample support structure was removed from the light tight enclosure and the replica structure was inserted. The desired light intensity and duration were then set and the resulting light pulse recorded by the storage oscilloscope. The replica structure was then removed and the sample replaced into the system at which point tomographic experimentation commenced.

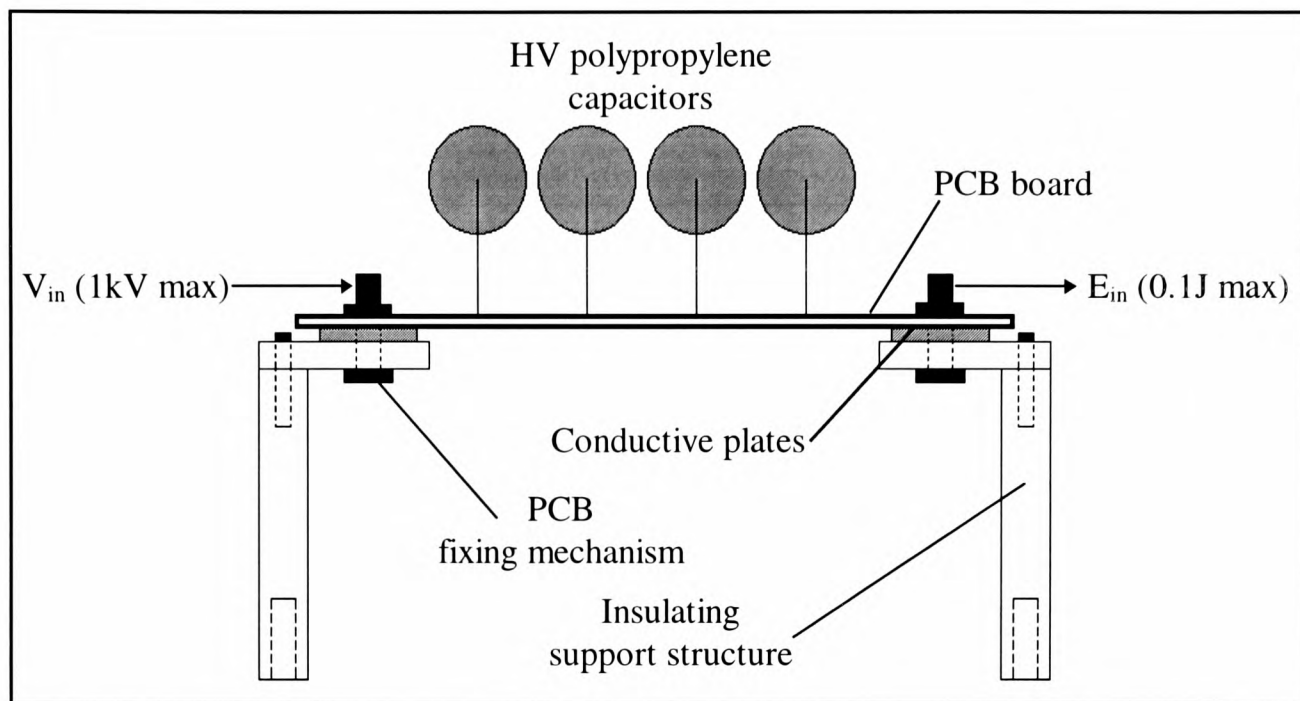


**Figure 4.30 Sketch of main discharge capacitor ( $C_m$ ) mechanism.**

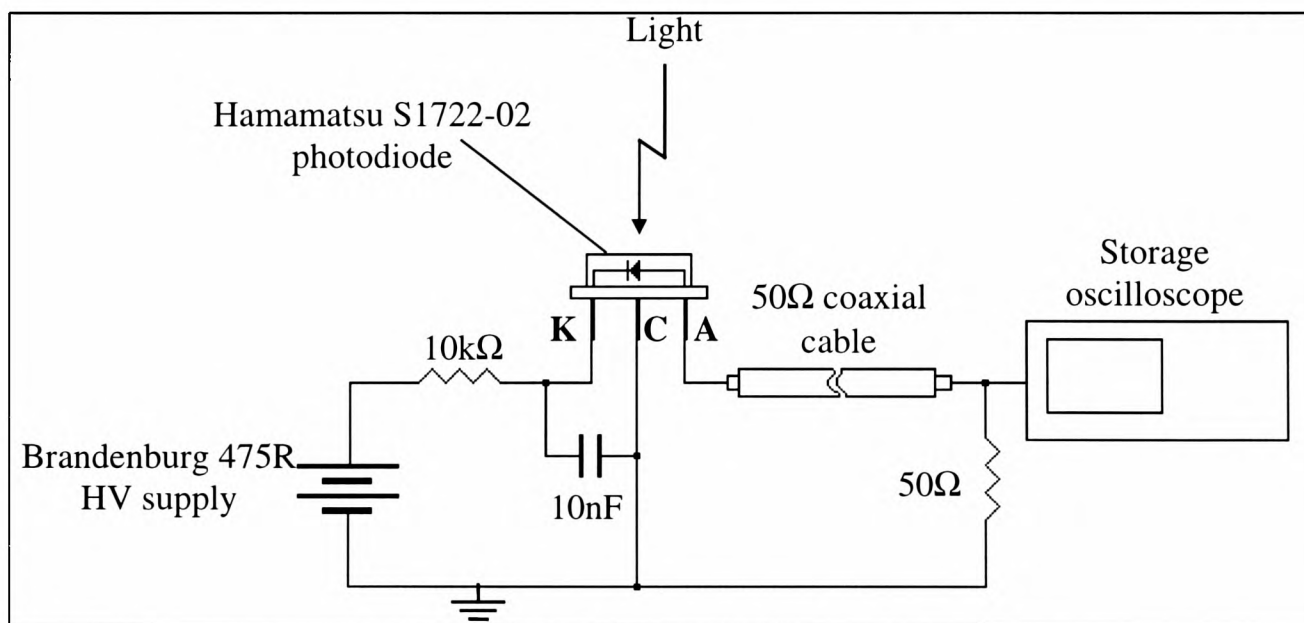


**Figure 4.31 Light detection circuit.**

### 4.3 Chapter summary

The development of an experimental apparatus that allows both xerographic and tomographic investigations to be carried out has been described. A laboratory has been specifically designed and modified for the experimental apparatus. A light tight enclosure has been designed and constructed to house both the xerographic and tomographic apparatus.

#### 4.3.1 Xerographic apparatus

An automated experimental apparatus has been developed to allow the study of such parameters as charge acceptance, dark decay, residual potential and photoinduced discharge to be carried out safely and efficiently. A scorotron device has been designed and constructed that allows predetermined levels of surface potential to be applied to the sample under test. An automatic sample translation mechanism incorporating position and timing sensors has been developed to move the charged sample from the scorotron charge to a measuring station. A measuring station has been developed which comprises of a transparent probe, sampling electronics, conversion electronics and an electrostatic voltmeter in order to accurately and efficiently monitor and record the charge decay data. Controlling software has been written in the Turbo C language. MATLAB programs have been written to allow the discharge characteristics of the a-As<sub>2</sub>Se<sub>3</sub> and a-Si:H materials to be determined. The experimental procedures for all xerographic measurements taken have been described.

#### 4.3.2 Tomographic apparatus

A tomographic apparatus has been developed that allows the insertion of tomographic prototypes containing various media to be inserted between a light source and sensor. The apparatus allows the insertion of various dimension of tomographic prototype. A developed versatile xenon flash unit that is operated remotely to provide light pulses of user defined intensity, duration and repetition rate has been described. The developed xenon flash unit is capable of supplying light for parallel projection, fan beam projection, and cone beam projection. A sample support structure has been described which allows the sample and tomographic prototypes to be accurately positioned within the tomographic apparatus. A fast light detection mechanism has been designed and constructed to measure the intensity and duration of the issued light pulses.

## CHAPTER 5

### RESULTS OF XEROGRAPHIC INVESTIGATION

This chapter is concerned with presenting the results of the xerographic investigation carried out during the course of the current study. The chapter is divided into two main sections which deal with the results obtained from the a-As<sub>2</sub>Se<sub>3</sub> and a-Si:H materials separately.

#### 5.1 Xerographic mode of operation.

The aim of the xerographic investigation was to study the electrical properties of the a-As<sub>2</sub>Se<sub>3</sub> and a-Si:H materials with a view to establishing their suitability for further investigation as sensors for OPT applications. The investigation involved studying the acceptance potential, dark decay, PID, and residual potentials of the materials. The discharge mechanisms of the materials were also investigated by applying existing theoretical models for the a-As<sub>2</sub>Se<sub>3</sub> and a-Si:H materials to the gathered experimental data as detailed in chapter three. In this manner, if good agreement with the existing models were achieved, the quality of the materials available to the research project could be confirmed and resulting experimental data which indicated the materials suitability for OPT applications could be relied upon.

##### 5.1.1 Amorphous arsenic triselenide

###### (i) Charge acceptance

The charge acceptance of the a-As<sub>2</sub>Se<sub>3</sub> samples was established by setting the control grid contained within the scorotron charger to the maximum 2kV and charging the surface of the sample for a 1s period and monitoring the resulting dark decay. This procedure was repeated under various levels of coronode voltage until the optimum charge that could be placed upon the sample surface had been established. Figure 5.1 show the charge acceptance and dark decay curve (DDC) for the a-As<sub>2</sub>Se<sub>3</sub> material. The charge acceptance ( $V_a$ ) for the a-As<sub>2</sub>Se<sub>3</sub> material was found to be in the order of 1078.42V. Schaffert (1975) stated that a good photoreceptor should be capable of sustaining surface charge densities of between  $0.5 \times 10^{-7}$  and  $1.5 \times 10^{-7}$  C/cm<sup>2</sup>.

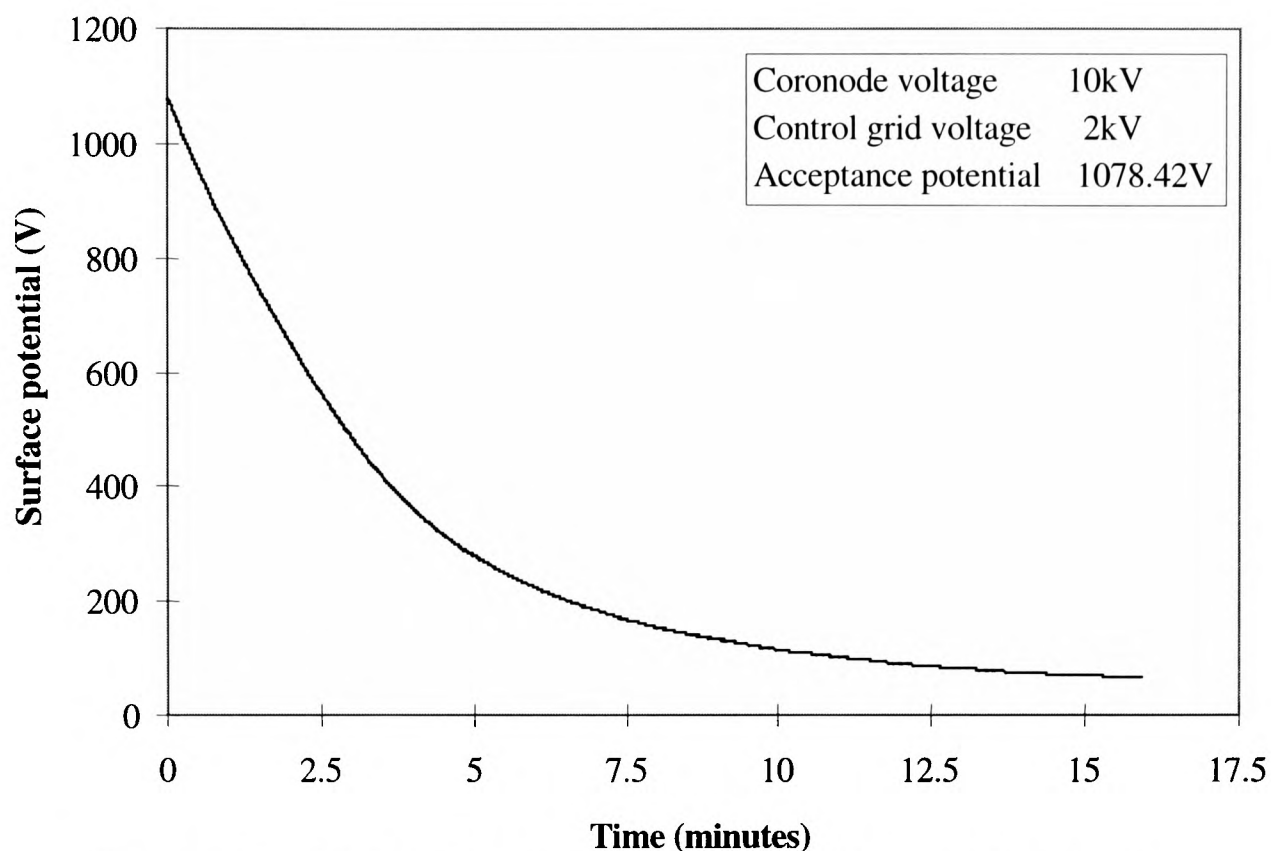


**Figure 5.1 DDC showing acceptance potential for a-As<sub>2</sub>Se<sub>3</sub> sample.**

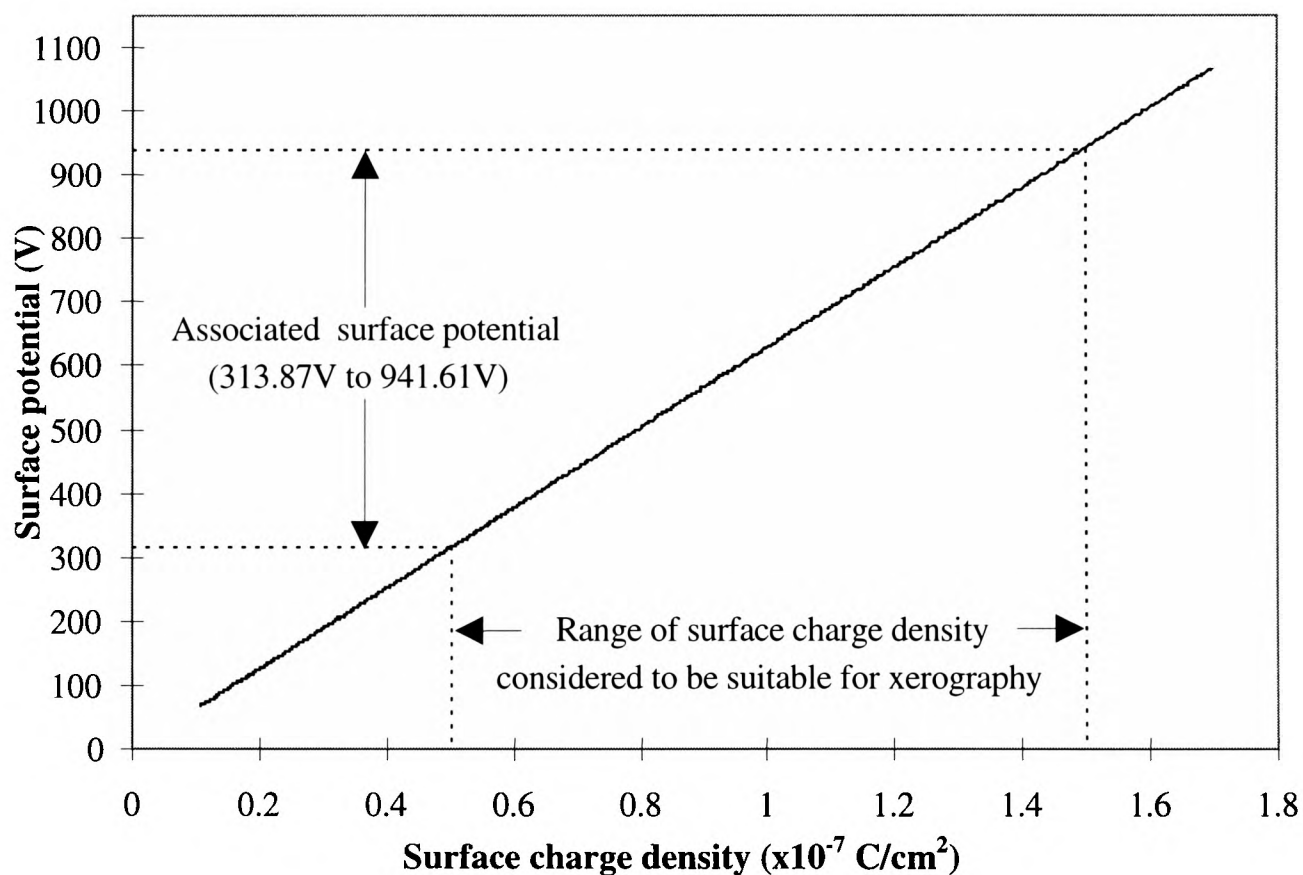


**Figure 5.2 Surface charge density vs. surface potential for a-As<sub>2</sub>Se<sub>3</sub>.**

The surface charge density ( $\delta$ ) could be calculated from the measured charge acceptance by the application of equations 3.1 and 3.2. Taking  $L$  as  $6 \times 10^{-3}$  cm,  $\epsilon_0$  as  $8.85 \times 10^{-14}$  F/cm,  $\epsilon_r$  as 10.8, and  $V_a$  as 1078.42V, equation 3.2 yielded a surface charge density of  $1.72 \times 10^{-7}$  C/cm<sup>2</sup> which was indicative of very good charge acceptance.

Figure 5.2 shows the magnitude of the surface charge density as the surface potential ( $V_s$ ) on the sample increases from the residual potential ( $V_{res}$ ) to  $V_a$  using data generated from the application of equation 5.2 upon the DDC data. Figure 5.2 shows that the surface charge density increases proportionally as  $V_s$  builds up upon the sample surface. Figure 5.2 also demonstrates the range of  $V_s$  required if  $\delta$  is to be kept within the recommended  $0.5 \times 10^{-7}$  to  $1.5 \times 10^{-7}$  C/cm<sup>2</sup> range. The initial electric field ( $E_0$ ) induced across the sample by the application of  $V_s$  could be calculated by the following (Vaezi-Nejad, 1984).

$$E_0 = \frac{V_s}{L} \text{ (V/cm)} \quad (5.1)$$

Thus the application of equation 5.1 to the required range of  $V_s$  yielded a range of electric field of  $0.52 \times 10^5$  V/cm to  $1.57 \times 10^5$  V/cm. All further experimentation in the xerographic mode was performed under three electric fields chosen from the lower, middle, and upper limits of the range of electric fields stated above. Table 5.1 shows the selected electric fields and the associated surface charge densities and surface potentials.

#### (ii) Dark decay

The next stage in the xerographic investigation was to record DDC data over the range of electric fields specified in table 5.1 and attempt to fit the experimental data to the xerographic depletion discharge (XDD) model proposed by Abkowitz *et al* (1985) described previously. Electric fields were induced in the samples under test by the application of surface potential that was limited to the desired magnitude by the control grid within the scorotron device. The resulting DDC's can be seen in figure 5.3. Analysis of the DDC's can give information as to the dark resistivity ( $\rho$ ) and the dark current density ( $j$ ) of the materials. Figure 5.4 shows the current density flowing through the a-As<sub>2</sub>Se<sub>3</sub> film at an electric field of  $0.66 \times 10^5$  V/cm. The current density was calculated by the application of equation 3.6. The current density could be seen to

diminish with time and surface potential. However, it could also be seen that the current density did not decay at a constant rate, but exhibited a clear change in the rate of decay which was indicative of a XDD mechanism.

According to XDD theory, the dark discharge mechanism in a-As<sub>2</sub>Se<sub>3</sub> follows a power law time dependence of the form

$$y = a b^x \quad (5.2)$$

Taking natural logarithms of both sides of equation 5.2 yields

$$\ln(y) = \ln(a) + x \ln(b) \quad (5.3)$$

By letting  $B = \ln(b)$ ,  $Y = \ln(y)$ , and  $A = \ln(a)$ , one obtains the linear regression formula

$$Y = A + xB \quad (5.4)$$

Thus a plot of  $\ln(|dV_s/dt|)$  vs  $\ln(t)$  should produce two linear time regions  $t < t_d$  and  $t > t_d$  (where  $t_d$  is the depletion time) if a power law dependence could be assumed. The experimental data were differentiated by the use of 3rd order polynomial curve fitting, linear interpolation, and the application of backwards difference equations using the MATLAB software package. Figure 5.5 shows a plot of  $\ln(|dV_s/dt|)$  vs  $\ln(t)$  for an electric field of  $0.66 \times 10^5$  V/cm. Figure 5.5 demonstrates that two linear regions were produced in the  $t < t_d$  and  $t > t_d$  time regimes. In order to establish  $t_d$ , first order polynomials were fitted to each of the two time regimes by the use of MATLAB. First order polynomials were fitted to the linear regions of the time regimes in order to establish the best mathematical 'fit' of a straight line to the linear regions of the experimental data. This process allowed the slopes of the linear regions and therefore the power regression coefficient (A) and the regression power (x) to be easily established.

Applied surface potential (V)	Surface charge density ( $C/cm^2$ )	Electric field (V/cm)
400	$0.64 \times 10^{-7}$	$0.66 \times 10^5$
600	$0.95 \times 10^{-7}$	$1 \times 10^5$
800	$1.27 \times 10^{-7}$	$1.33 \times 10^5$

**Table 5.1** Range of electric fields employed in the xerographic investigation.

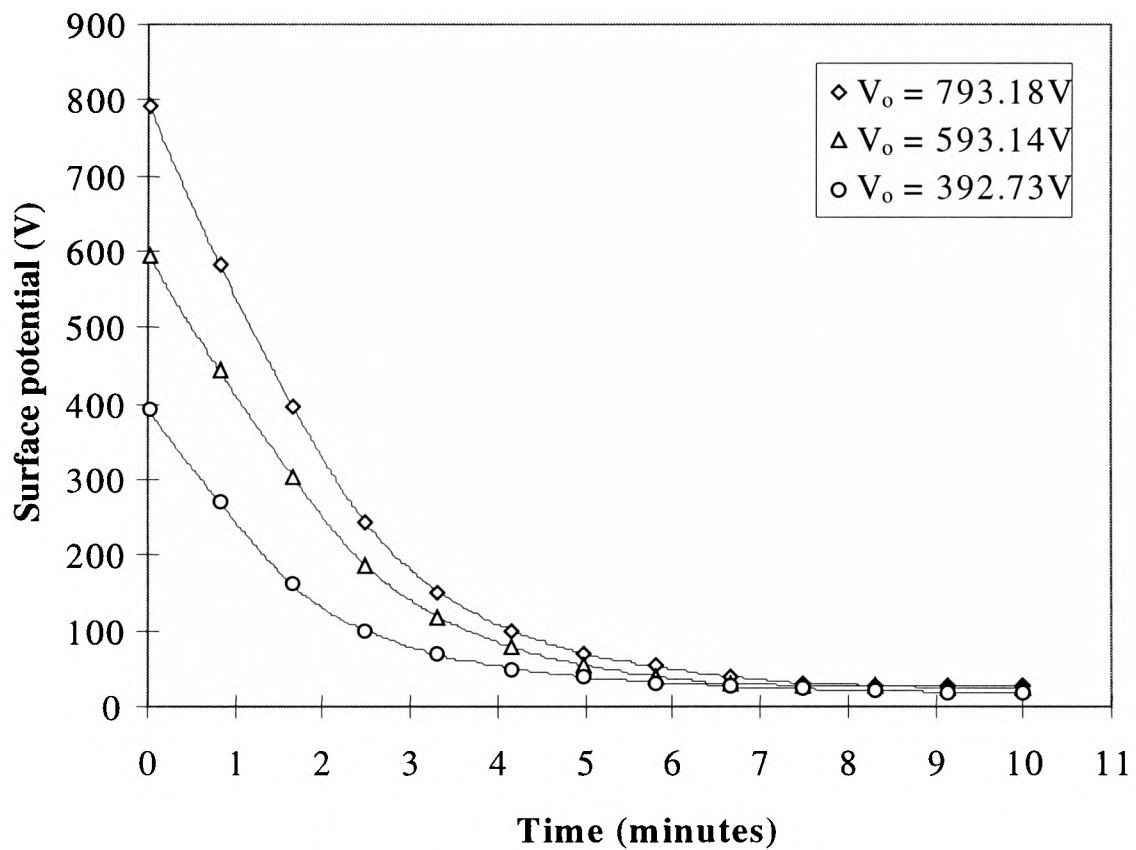


**Figure 5.3** DDC' for  $a-As_2Se_3$ .

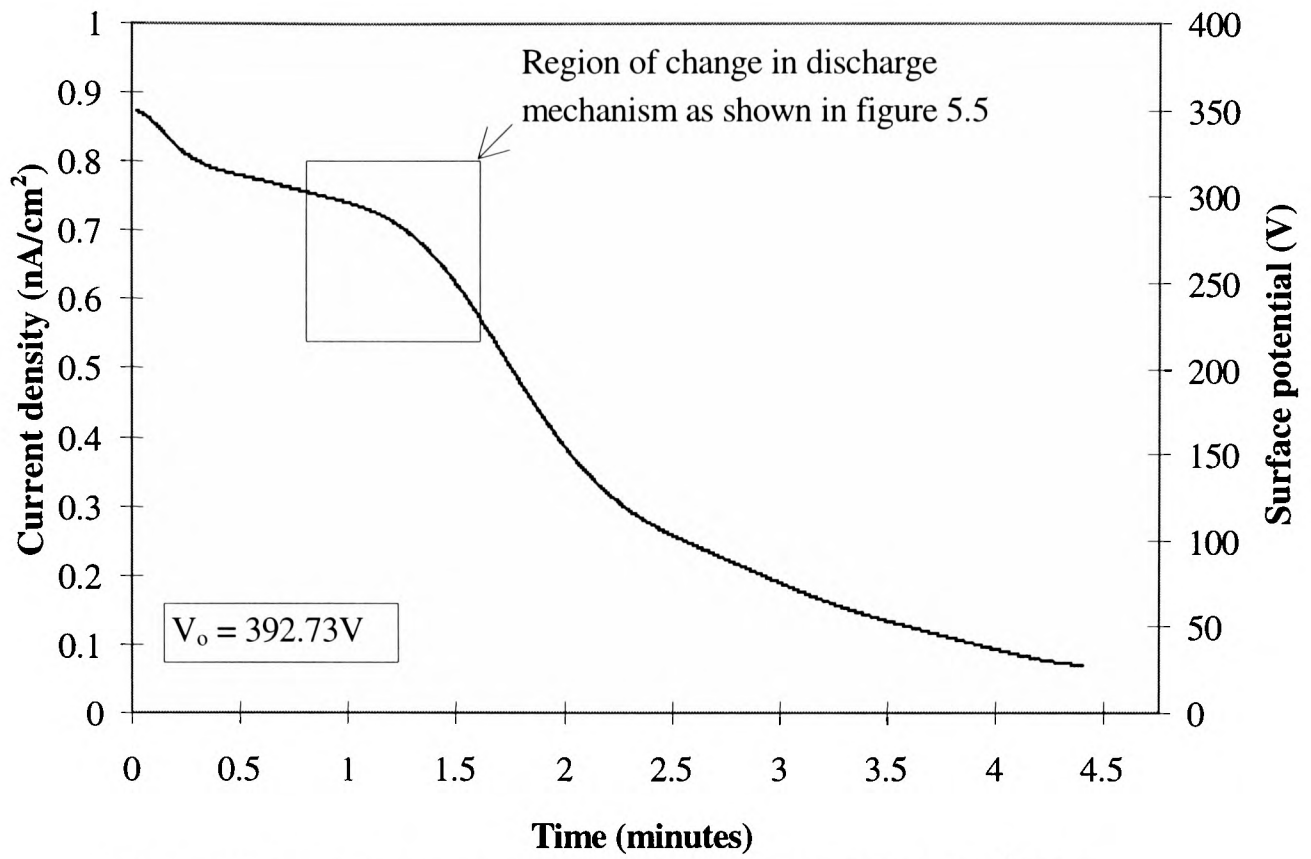


Figure 5.4 Dark current density Vs. time for  $E=0.66 \times 10^5$  V/cm.

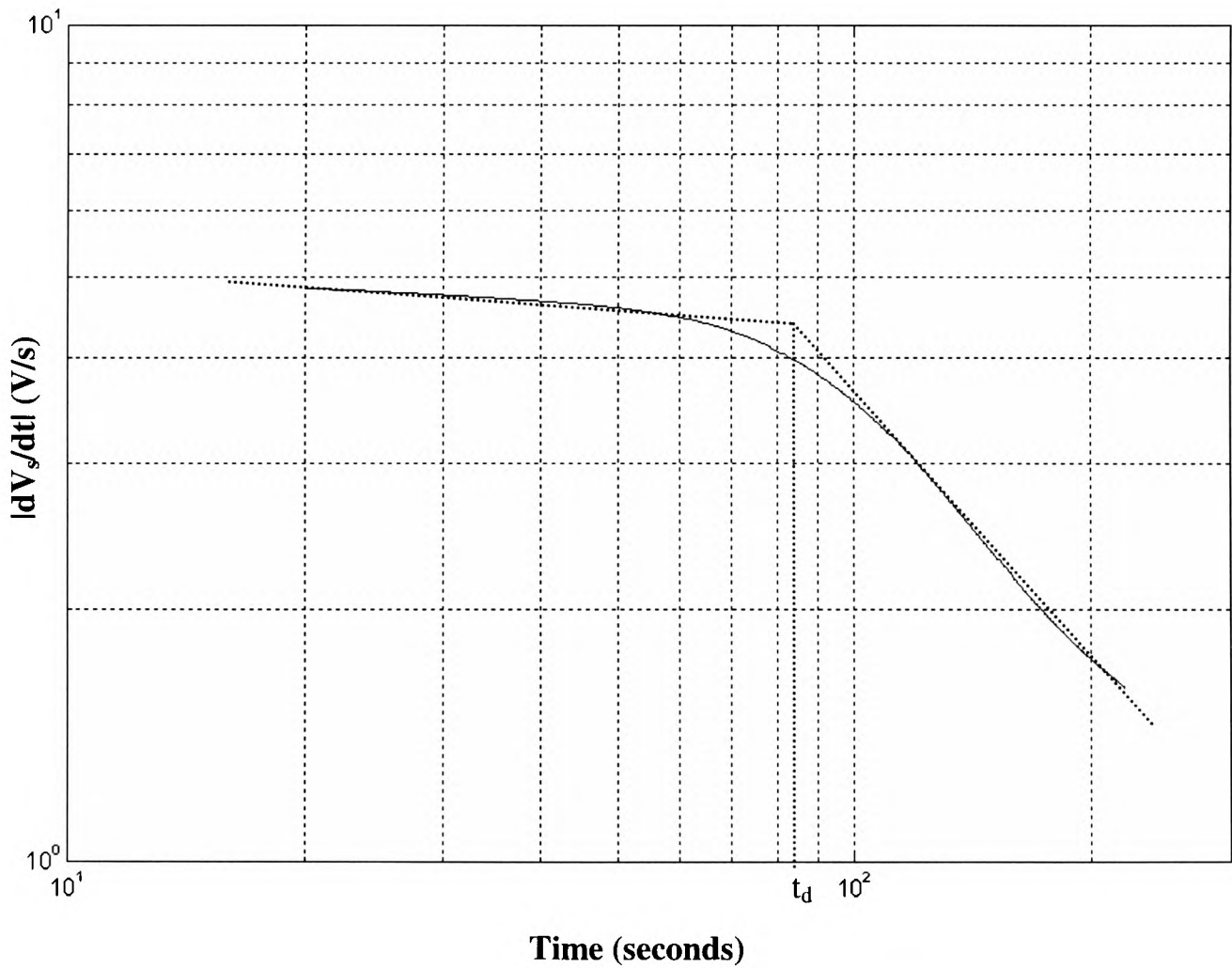


Figure 5.5 Loglog plot of establishment of depletion time,  $E=0.66 \times 10^5$  V/cm.

The depletion time assuming no contribution from surface injection according to the XDD theory presented in chapter 3, is located when the surface potential at  $t=0$  ( $V_o$ ) has decayed to 50% of its original value. For an electric field of  $0.66 \times 10^5$  V/cm as shown in figures 5.4 and 5.5,  $t_d$  would occur when  $V_o$  had decayed to 196.365V. The time required for  $V_s$  to reach  $V_o/2$  was determined from a lookup table containing the interpolated  $V_s$  vs  $t$  experimental data, and  $t_d(V_o/2)$  was found to occur at  $t=80.2s$ .

The Abkowitz model presented in section 3.5(i) states that if no contribution from the injection of current from the surface of the sample is present, then the depletion time would occur at  $V_o/2$ . Thus if the value of  $V_s(t_d)$  derived from the experimental data was lower in magnitude than the theoretical value of  $V_o/2$ , then the drop in surface potential must have been caused by the injection of current from the surface of the sample. In order to establish the contribution of surface charge injection to the DDC, the first order polynomials fitted to the two time regimes were extended to their intercept. The establishment of  $t_d$  was accomplished by the use of the graphical input command (ginput) available within MATLAB. Used in conjunction with a magnification function, the ginput command was used to accurately establish the time at which the first order polynomials intercepted. The point of interception ( $t_d$ ) was found to occur at  $t=89.26s$ . The surface potential at  $t=89.26s$  was 181.11V. Thus there was found to be a discrepancy of 4.53s between the theoretical and measured depletion times, and 15.5V between  $V_o/2$  and  $V_s(t_d)$ . Thus the surface potential in the  $t < t_d$  regime had decayed by 15.5V (approximately 4% of  $V_o$ ) due to the effects of current injected from the surface of the sample.

The next step in the dark decay analysis was to attempt to fit the Abkowitz model to the experimental data and calculate the time dependence of the current injected from the surface of the material. From Abkowitz, the rate of decay of the surface potential in the  $t < t_d$  time regime is given by.

$$\frac{dV}{dt} = - \left( \frac{L^2}{2\epsilon_r \epsilon_o} \right) a p t^{p-1} \quad (5.5)$$

Where  $a$  and  $p$  are constants with  $p \leq 1$ .

Equation 5.5 is of the form:

$$\frac{dV}{dt} = at^x \quad (5.6)$$

Thus letting  $\frac{dV}{dt} = Y$ ,  $-\left(\frac{L^2}{2\epsilon_r \epsilon_o}\right)ap = A$ , and  $p-1 = x$ , we obtain the linear regression formula  $Y = A + (xt)$ . The regression power ( $x$ ) is determined from the slope of the  $t < t_d$  time regime and was found to be  $-0.0725$  giving the constant ( $p$ ) as  $0.9275$ . MATLAB was used to return the power regression coefficient ( $A$ ) from the first order polynomial in the  $t < t_d$  regime and  $A$  was found to be equal to  $5.971$ . By transposing the term for the power regression coefficient in terms of the constant ( $a$ ) yielded.

$$a = \frac{A}{\left(\frac{-L^2}{2\epsilon_r \epsilon_o}\right)^p} \quad (5.7)$$

The constant ( $a$ ) was calculated to be  $-3.4186 \times 10^{-7}$ , and thus the Abkowitz model for the  $t < t_d$  regime was

$$\frac{dV}{dt} = 5.971 t^{-0.0725} \quad (5.8)$$

According to Abkowitz, the rate of change of the surface potential in the  $t > t_d$  time regime could be determined from

$$\frac{dV}{dt} = \frac{\epsilon_r \epsilon_o}{2a} \left(\frac{V_o}{L}\right)^2 p t^{-p-1} \quad (5.9)$$

Applying the same mathematical procedure for the determination of the Abkowitz model for the  $t < t_d$  time regime gave the constant ( $p$ ) as  $0.8166$ ,  $A$  as  $4.169 \times 10^3$ , and the constant ( $a$ ) as  $-4.4728 \times 10^{-7}$ . These parameters resulted in an Abkowitz model for the  $t > t_d$  time regime which was as follows

$$\frac{dV}{dt} = 4196.9 t^{-1.8166} \quad (5.10)$$

The two Abkowitz models were applied to the same interpolated timebase as the experimental data and a comparison of the Abkowitz models and the experimental data are shown in figure 5.6. Figure 5.6 demonstrates that a good fit of the

experimental data was obtained by the application of the Abkowitz model. Now that the validity of the Abkowitz model had been established, the thermally generated currents and current injected from the surface of the sample could be deconvoluted into their component parts in the  $t < t_d$  time regime.

From XDD theory it is known that  $V_o$  should decay to half its original value at  $t_d$  if no contribution from the injection of current from the surface of the sample is present. Given that  $V_o$ ,  $V_s(t_d)$ , and  $t_d$  had been established, and that it had been shown that  $\ln(|dV_s/dt|)$  vs.  $\ln(t)$  produces linear regions of the form  $Y = A + xB$ , by plotting the co-ordinates  $\ln V_o$ , and  $\ln V_s(t_d)$ , a straight line approximation representing  $\ln(|dV_s/dt|)$  vs.  $\ln(t)$  due to thermal generation within the bulk of the layer only could be produced. Figure 5.7 shows the results of fitting Abkowitz models to the theoretical and experimental data in the  $t < t_d$  time regime in order to deconvolute the thermally generated and surface injected currents.

Figure 5.7 demonstrates that the rate of dark discharge for the thermally generated current is approximately constant over the  $t < t_d$  regime. This was in agreement with XDD theory that states that no space charge region forms in the  $t < t_d$  regime, and that the dimension  $X(Z_o)$  extends from the surface of the sample to the substrate. Figure 5.7 also shows that the rate of change of the surface potential when surface injection is taken into account is greater over the  $t < t_d$  regime. This was also to be expected as the contribution from current injected from the surface of the sample would accelerate the dark discharge process. Table 5.2 shows the results of the dark decay analysis for varying levels of electric field.

### (iii) Photoinduced discharge (PID)

PID experimentation was performed in the xerographic mode of operation in order to provide an initial indication of the photoconductivity of the  $a\text{-As}_2\text{Se}_3$  material. PID experiments were performed over the same range of electric fields as shown in table 5.1. Figure 5.8 shows a comparison of the DDC to the PID for an electric field of  $1.33 \times 10^5$  V/cm. The L2441 xenon light source provides a maximum 65% relative light intensity at  $E_{in} = 0.1\text{J}$  which was termed  $I_{max}$ . All light intensities employed in the PID experiments were expressed as a percentage of  $I_{max}$ .

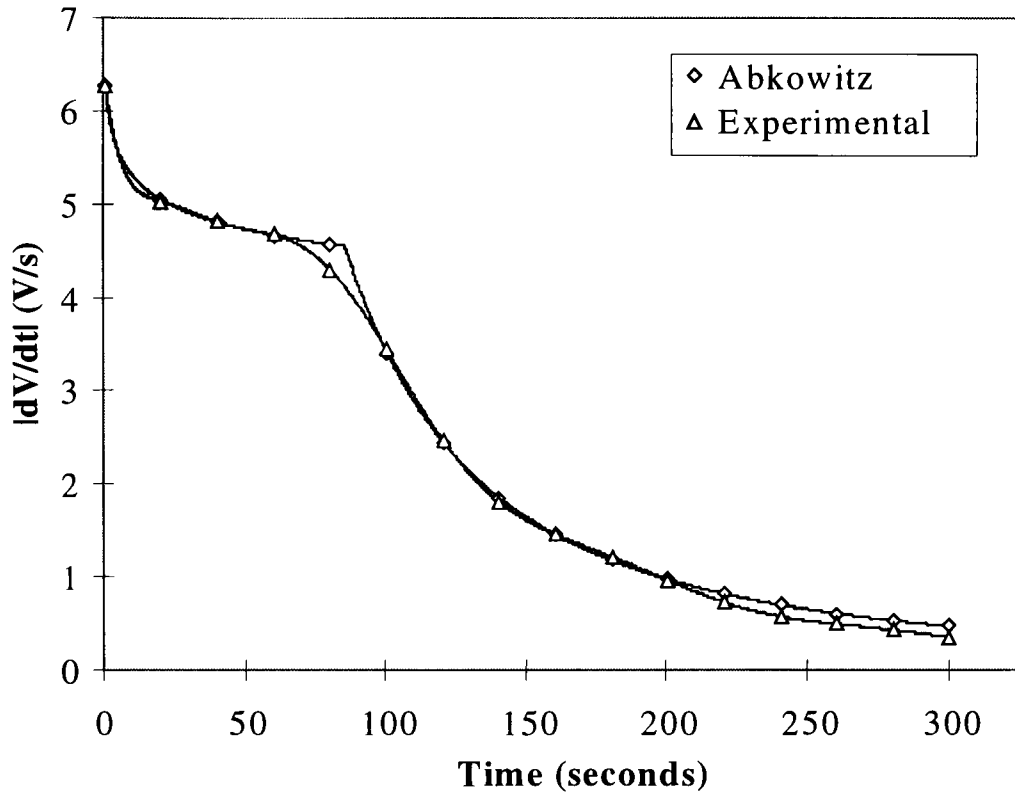


**Figure 5.6** Comparison of  $|dV/dt|$  according to the experimental data and the Abkowitz model,  $E=0.333 \times 10^5$  V/cm.

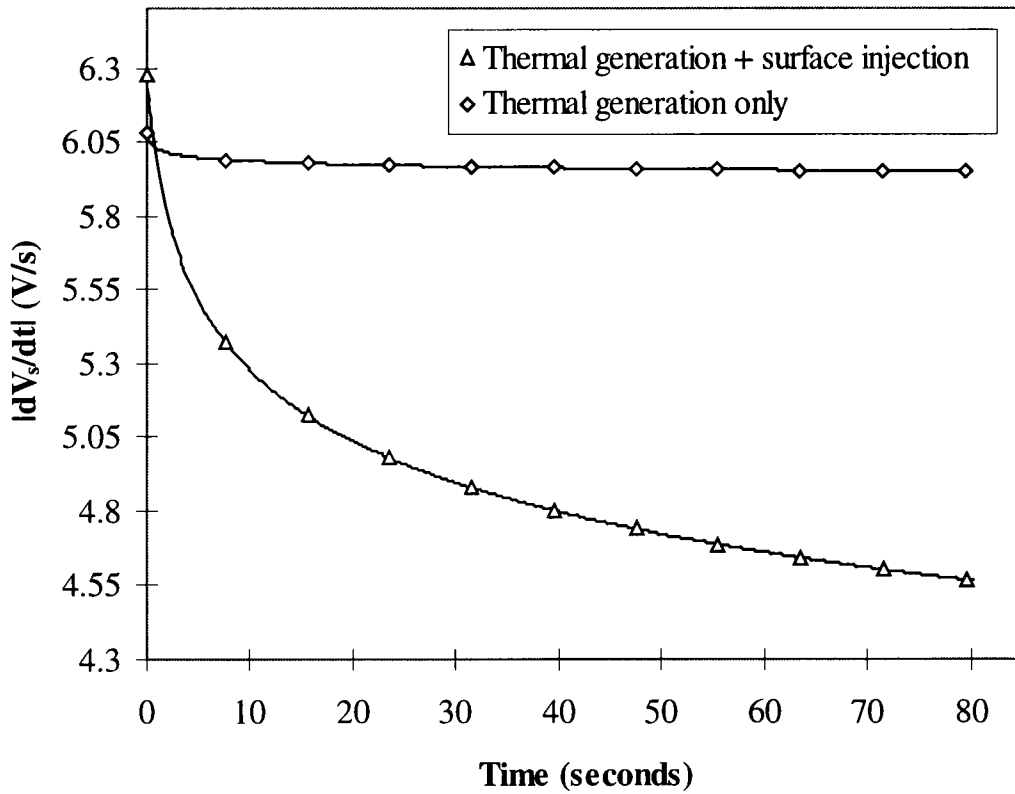


**Figure 5.7** Abkowitz models showing the rate of change of the surface potential due to thermal generation and surface injection, and thermal generation only,  $E=0.333 \times 10^5$  V/cm.

Electric field $E_o$	<b><math>0.66 \times 10^5</math></b> V/cm	<b><math>1 \times 10^5</math></b> V/cm	<b><math>1.33 \times 10^5</math></b> V/cm
Surface charge density $\delta_{(t=0)}$	$0.637 \times 10^{-7}$ C/cm <sup>2</sup>	$0.955 \times 10^{-7}$ C/cm <sup>2</sup>	$1.274 \times 10^{-7}$ C/cm <sup>2</sup>
Surface potential $V_{o(t=0)}$	392.73V	593.91V	793.18V
Surface potential $V_o/2$	196.36V	296.95V	396.59V
Surface potential $V_s(t_d)$	181.11V	234.97V	296.269
Residual potential $V_{res}$	19.12V	21.43V	20.13V
Half decay time $t(V_o/2)$	1.33min	1.65min	1.74min
Full decay time $t(V_{res})$	8.86min	11.32min	13.95min
Depletion time $t_d(V_o/2)$	80.2s	99.4s	104.9s
Measured depletion time ( $t_d$ )	89.26s	113.6s	129.6s
Power regression coefficient (A) ( $t < t_d$ )	5.97	8.92	13.14
Power regression coefficient (A) ( $t > t_d$ )	4196.9	36715	90456
Constant (a) ( $t < t_d$ )	$-3.41 \times 10^{-7}$	$-5.44 \times 10^{-7}$	$-8.253 \times 10^{-7}$
Constant (a) ( $t > t_d$ )	$-4.47 \times 10^{-7}$	$-1.52 \times 10^{-7}$	$-1.22 \times 10^{-7}$
Regression power (x) ( $t < t_d$ )	-0.072	-0.129	0.154
Regression power (x) ( $t > t_d$ )	-1.816	-1.98	-1.99
Constant (p) ( $t < t_d$ )	0.927	0.87	0.845
Constant (p) ( $t > t_d$ )	0.816	0.98	0.99
Sum of slopes	-1.88	-2.11	-2.14

**Table 5.2 Summary of dark decay analysis data**

Figure 5.8 shows that exposing the charged sample surface to a single light pulse of  $I_{\max}$  relative intensity, resulted in a large increase in the rate of change of the surface potential. The time required for the DDC to reach half its original value ( $V_0/2$ ) was 129.6s. For the PID, the time taken to reach  $V_0/2$  was 0.932s, thus the discharge under fast photo-excitation was approximately 130 times faster than for the DDC. Figure 5.9 shows the PID curves at electric fields of  $0.66 \times 10^5$  V/cm,  $1 \times 10^5$  V/cm, and  $1.33 \times 10^5$  V/cm.

The next PID experimentation was performed to determine if the a-As<sub>2</sub>Se<sub>3</sub> material was sensitive to changes in relative light intensity. The intensity of the light was reduced in increments of 15% and the tests were re-run. Figures 5.10 and 5.11 show the results of reducing the light intensity for an electric field of  $1.33 \times 10^5$  V/cm. Figures 5.10 and 5.11 show that the a-As<sub>2</sub>Se<sub>3</sub> material was sensitive to changes in light intensity and the rate at which the PID decayed was dependant upon the intensity of the light. Figures 5.10 and 5.11 also show that the rate at which the PID decayed, decreased with a decrease in relative light intensity. The findings of the xerographic investigation in the a-As<sub>2</sub>Se<sub>3</sub> material are discussed further in chapter 7.

### 5.1.2 Hydrogenated amorphous silicon

#### (i) Charge acceptance

The experimental procedure for the determination of the charge acceptance of the a-Si:H materials was the same as described in section 5.1.1(i). Figure 5.12 shows the charge acceptance for the a-Si:H material. The charge acceptance of the a-Si:H material was found to be in the order of 654V for the 27.1 $\mu$ m sample. The application of equation 5.2 taking L as  $2.71 \times 10^{-3}$  cm,  $\epsilon_r$  as 10.1, and  $V_a$  as 654.5V yielded a surface charge density of  $2.16 \times 10^{-7}$  C/cm<sup>2</sup> ( $E_0 = 2.41 \times 10^5$  V/cm) which again indicated very good charge acceptance. The thickness of the a-Si:H film was 27.1 $\mu$ m as opposed to 60 $\mu$ m for the a-As<sub>2</sub>Se<sub>3</sub> film which meant that less surface potential was required to produce comparable surface charge densities as can be seen in figure 5.13. In order to be able to compare the charge acceptance and DDC analysis in a-Si:H to a-As<sub>2</sub>Se<sub>3</sub> the samples had to be charged to the same electric fields as are shown in table 5.1. Table 5.3 shows the range of surface potentials that were required to produce the desired electric fields.

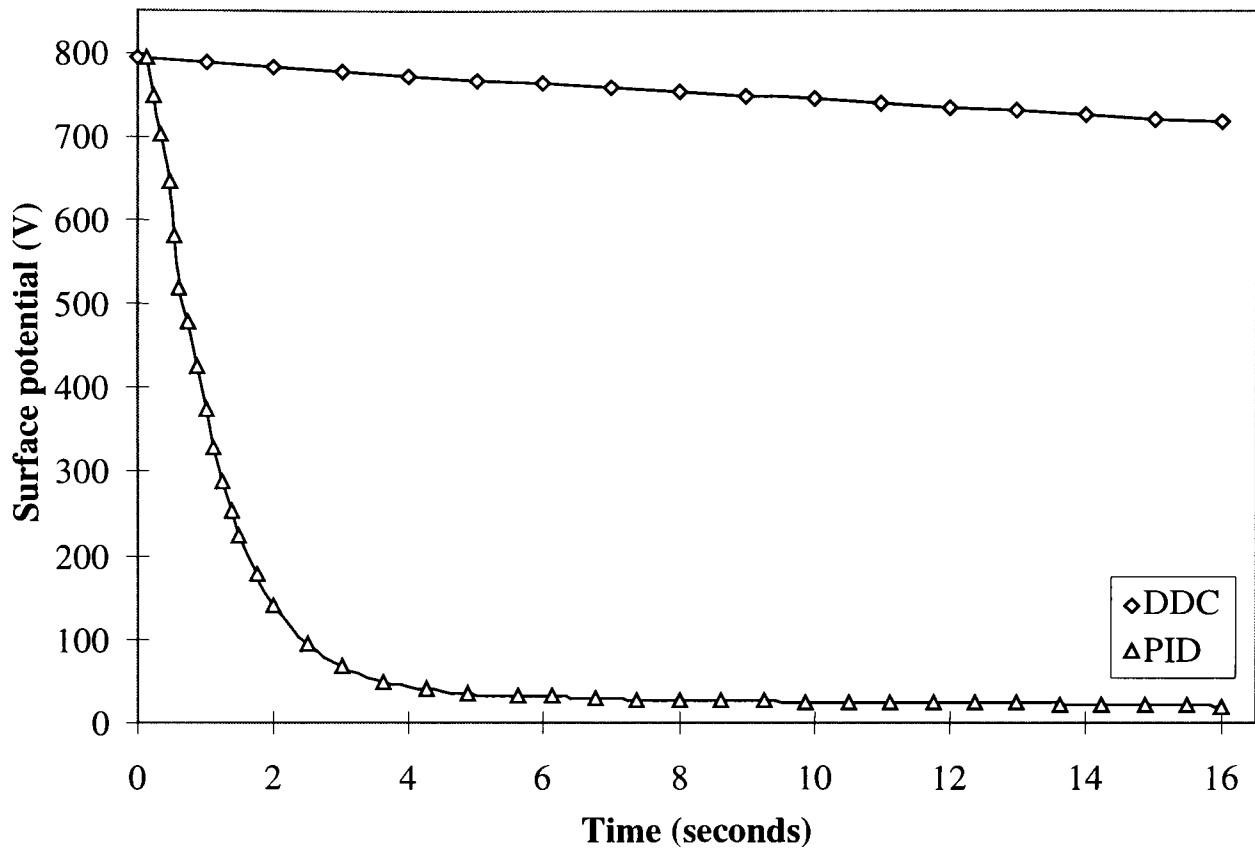


**Figure 5.8** Photoinduced and dark discharge curves for  $E=1.33 \times 10^5$  V/cm, relative light intensity =  $I_{max}$ .

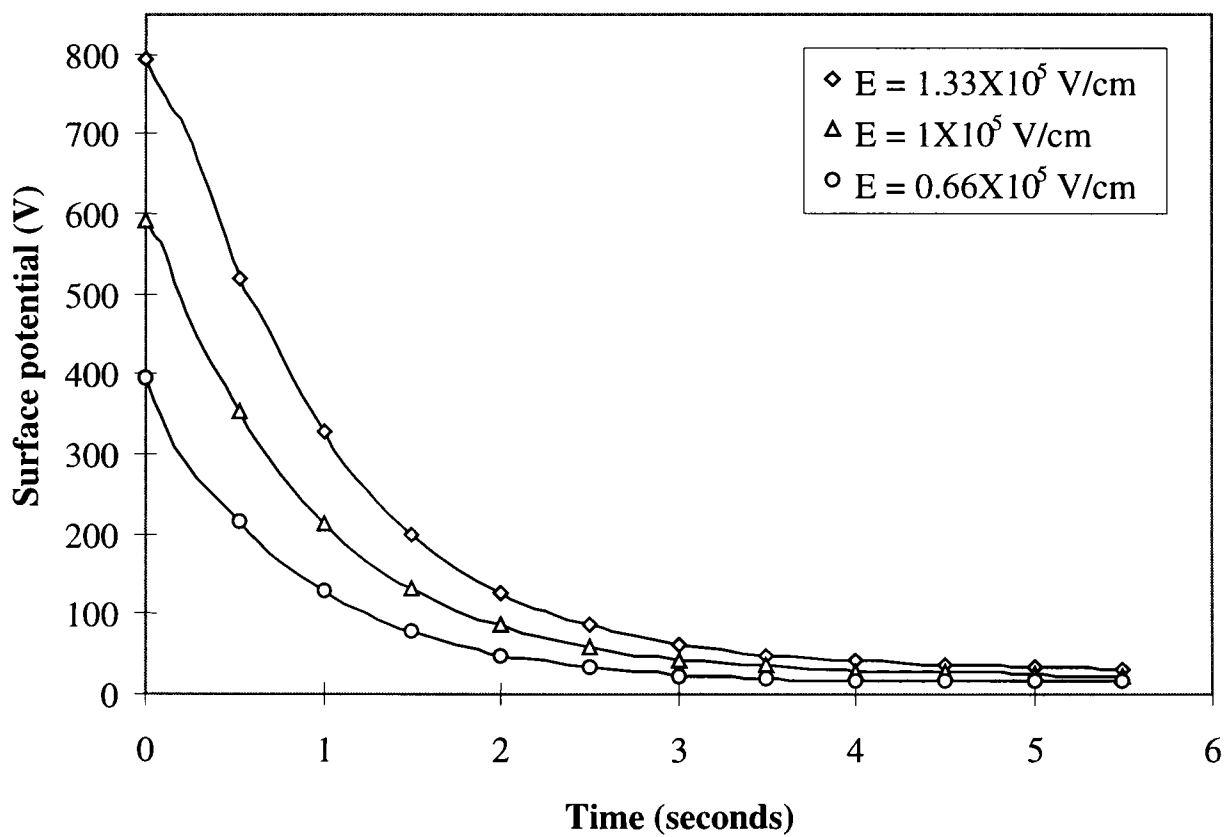


**Figure 5.9** Comparison of PID curves over varying electric fields, light intensity =  $I_{max}$ .

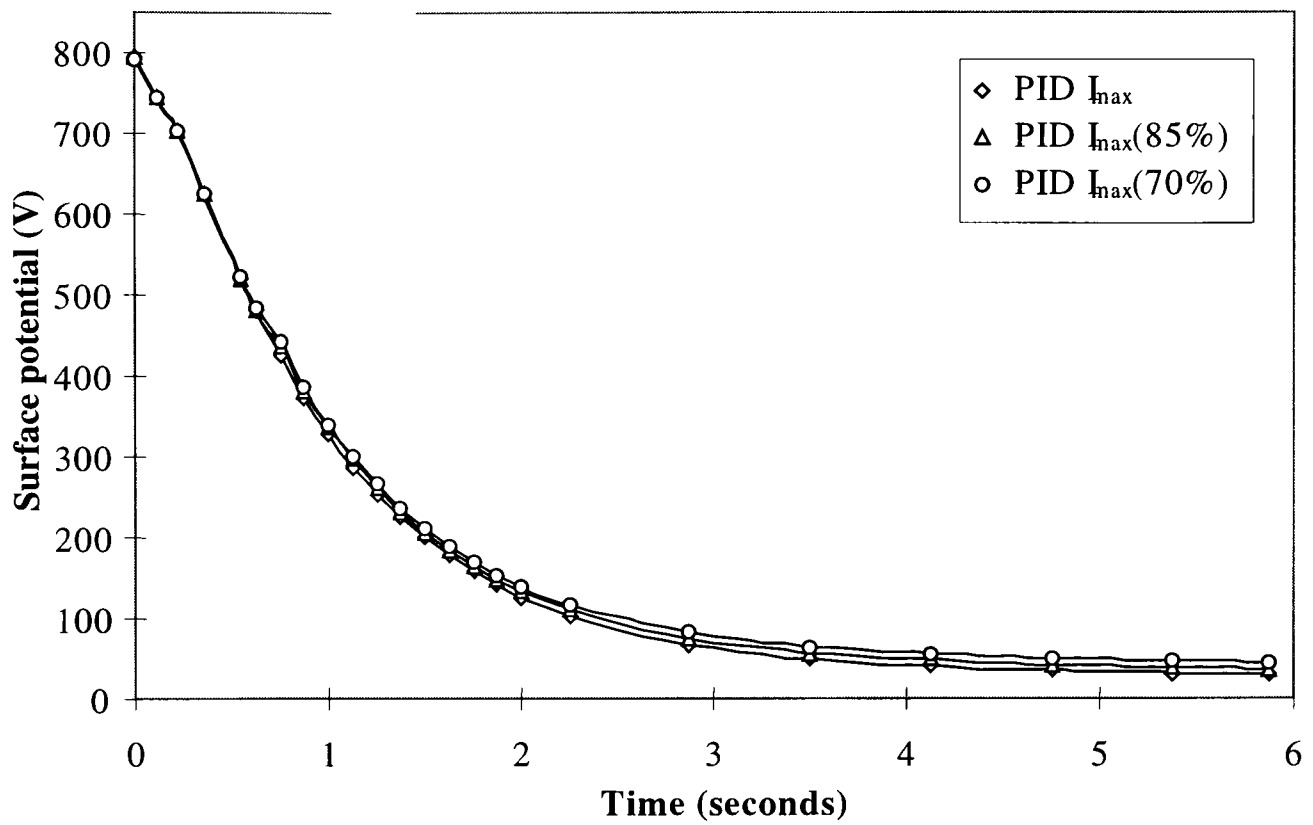


**Figure 5.10** PID curves due to varying levels of relative light intensity,  $E=1.33 \times 10^5$  V/cm.

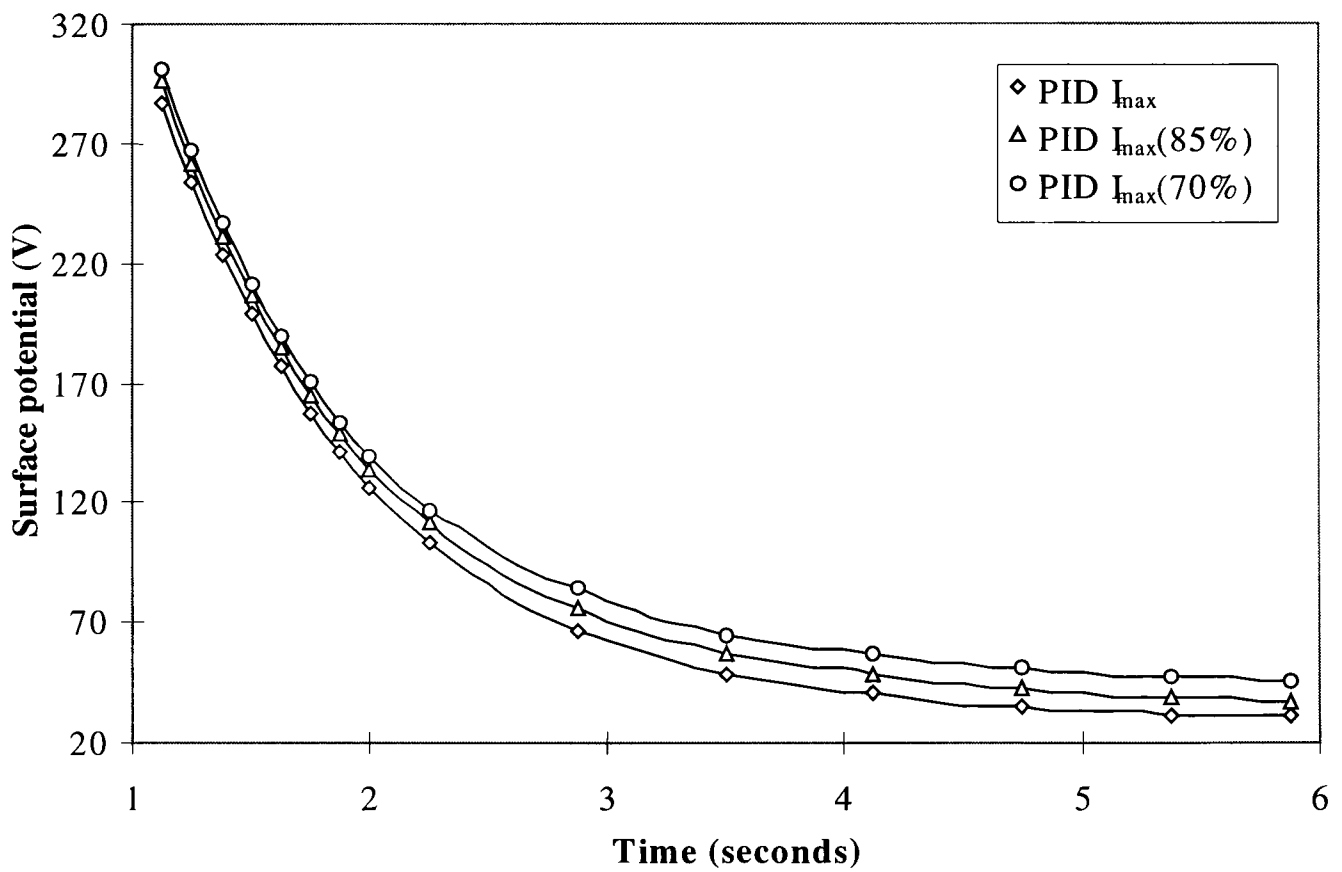


**Figure 5.11** Magnification of PID curves due to varying levels of relative light intensity,  $E=1.33 \times 10^5$  V/cm.

(ii) Dark decay

The exact nature of the dark decay mechanism in a-Si:H is still a matter of conjecture as is discussed in section 3.5(ii). As with the a-As<sub>2</sub>Se<sub>3</sub> materials, one of the aims of the current study of the dark decay process in a-Si:H was to attempt to examine the findings of past authors such as Nakayama *et al* (1987), Kakinuma and Wantanabe (1987), and Baxendale *et al* (1990) by applying existing theory to the experimental data. Nakayama *et al* sought to demonstrate that the dark discharge mechanism in a-Si:H materials was due to a XDD mechanism. The first step in the dark decay analysis was to see if phenomena indicative of a XDD mechanism could be observed in the a-Si:H material over the range electric fields previously described. The DDC's for the a-Si:H material are shown in figure 5.14. The DDC's were differentiated to determine if a change in the rate of dark discharge was observable. Figure 5.15 shows the results of this process. It was seen from figure 5.15 that there was no clear change in the rate of dark decay for the a-Si:H material as was evident in the dark discharge rate of the a-As<sub>2</sub>Se<sub>3</sub> material.

The differentiated DDC's were then plotted logarithmically in order to determine if linear regions were present in the responses. Figure 5.16 shows the logarithmic plot of the experimental data. It was seen from figure 5.16 that linear regions were not present at any of the electric fields investigated, and that the a-Si:H material gave a 'rounded' response. Nakayama *et al* also report a rounding of the response for the a-Si:H material on a simulated logarithmic plot of the dark discharge rate in which the rounded regions were treated as straight lines in order to establish a depletion time.

An attempt was made to fit first order polynomials to the experimental data, but the positioning of the polynomials was highly ambiguous due to the rounding of the responses. This ambiguity in positioning the polynomials meant that no apparent depletion time could be established. Thus the current investigation was in agreement with Kakinuma and Wantanabe (1987) and Baxendale *et al* (1990) who reported that no evidence of a XDD mechanism was observable in a-Si:H over the range of electric field employed in the current investigation.

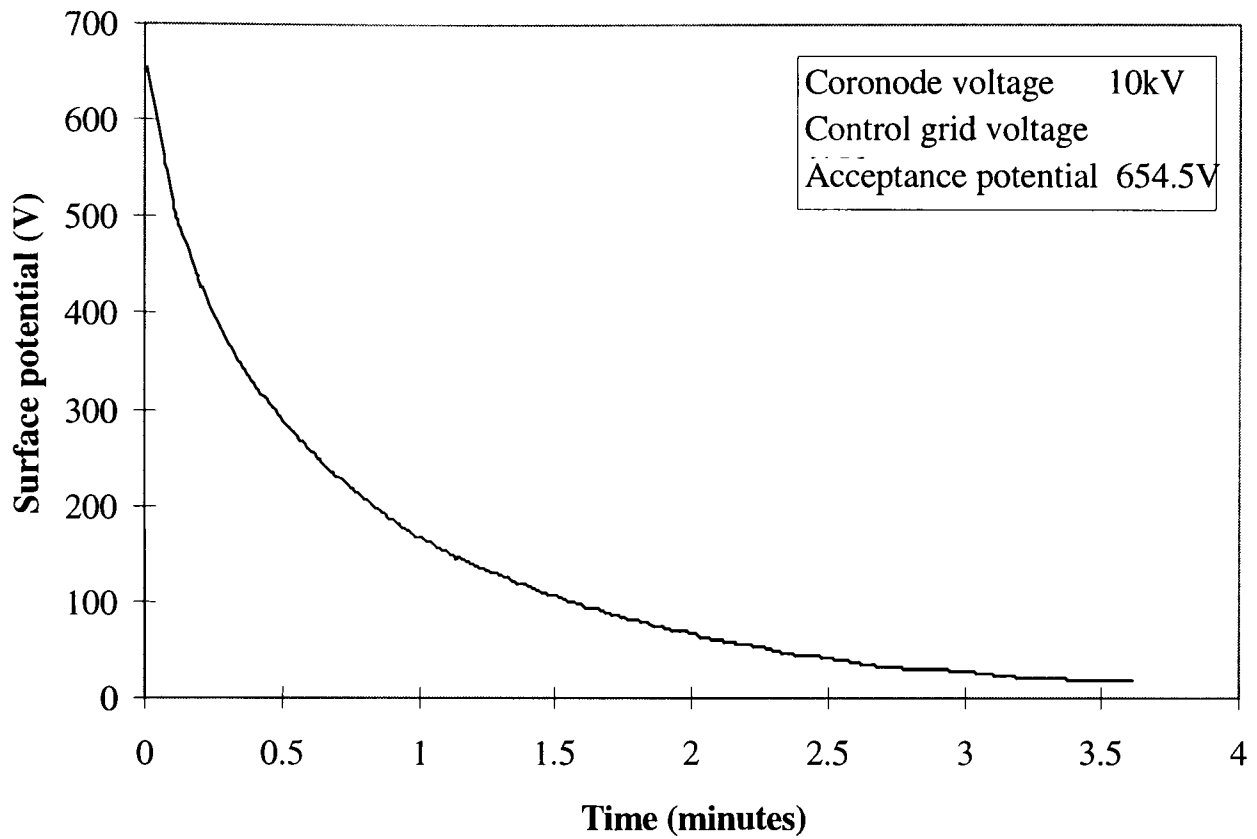


**Figure 5.12 DDC showing acceptance potential for a-Si:H sample.**

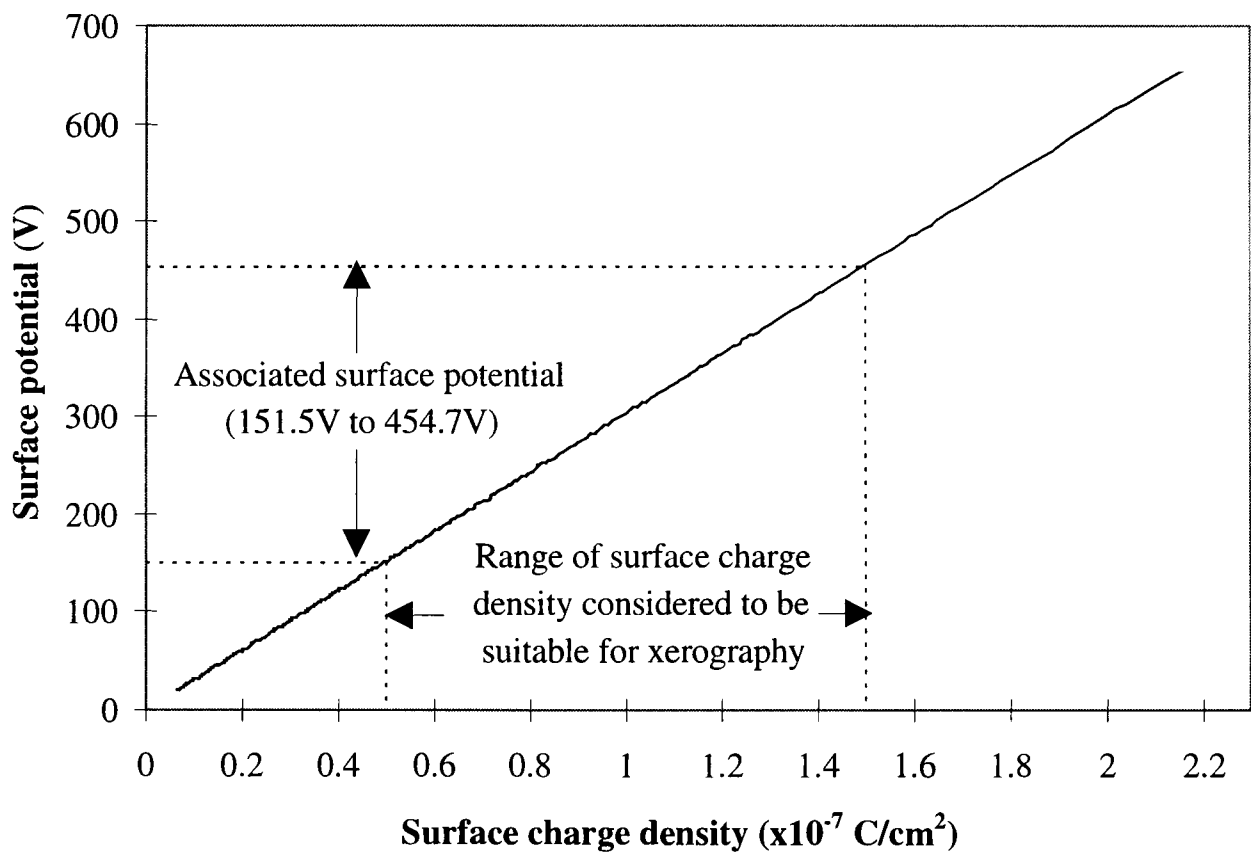


**Figure 5.13 Surface charge density vs. surface potential for 27.1µm a-Si:H sample.**

Applied surface potential (V)	Surface charge density (C/cm <sup>2</sup> )	Electric field (V/cm)
180.48	$0.59 \times 10^{-7}$	$0.66 \times 10^5$
271	$0.89 \times 10^{-7}$	$1 \times 10^5$
361.24	$1.19 \times 10^{-7}$	$1.33 \times 10^5$

**Table 5.3** Required surface potentials for maintenance of electric fields.

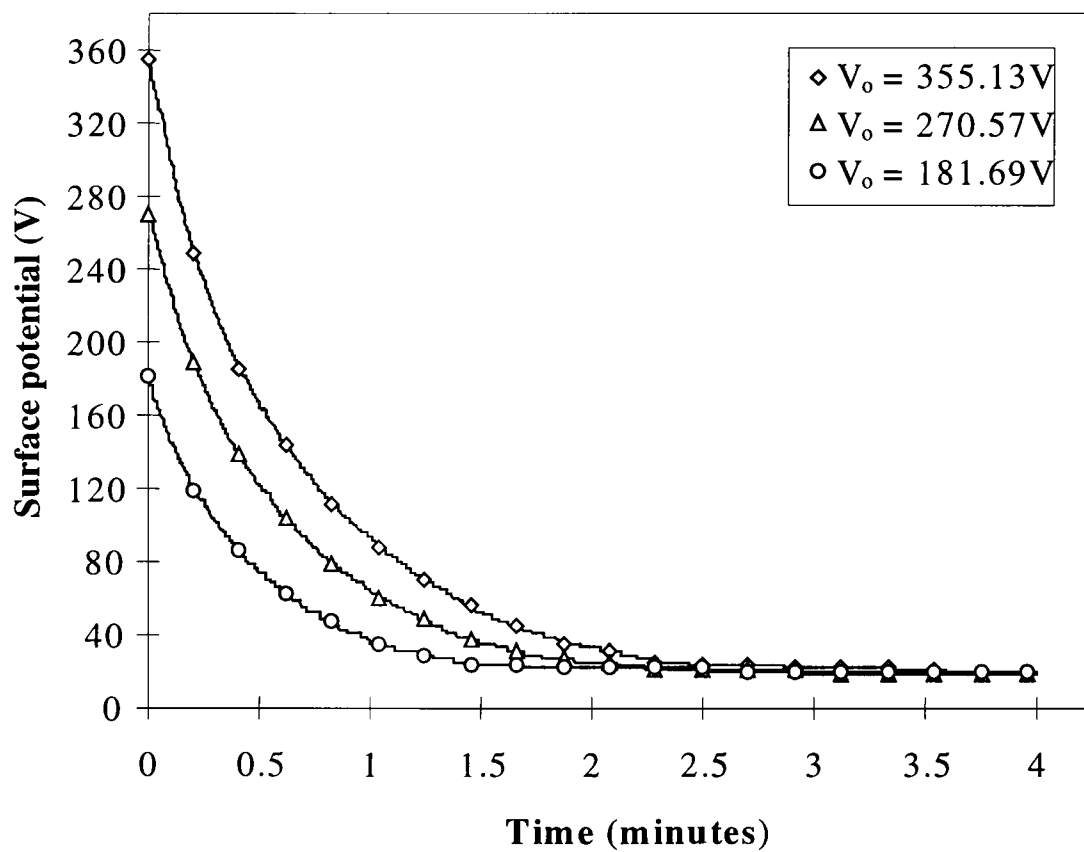


**Figure 5.14** DDC's for a-Si:H,  $E = 0.66 \times 10^5$ ,  $1 \times 10^5$ , and  $1.33 \times 10^5$  V/cm.

Both Baxendale *et al* and Kakinuma and Wantanabe concluded that the dark discharge mechanism in a-Si:H was due to a Poole-Frenkel type emission of mobile holes and electrons within the intrinsic region. Following the analysis of Kakinuma and Wantanabe, if  $\ln \frac{1}{L} \cdot \frac{dV_s}{dt}$  is plotted as a function of  $\sqrt{E}$  linear characteristics should be produced if the dark discharge is via a Poole-Frenkel mechanism. The gradient of this linear characteristic should be in agreement with the theoretical Poole-Frenkel coefficient for the intrinsic region namely,  $\beta_{PF} = 2.4 \times 10^{-4} (\text{V/cm})^{1/2} \text{ eV}$ . Figure 5.17 shows that plotting  $\ln \frac{1}{L} \cdot \frac{dV_s}{dt}$  as a function of  $\sqrt{E}$  did indeed produce approximately linear regions in the experimental data. In order to establish the gradient and therefore the experimental value of  $\beta$ , first order polynomials were fitted to the linear regions to obtain the best mathematical fit of the experimental data. The results of this process are shown in Table 5.4.

Table 5.4 shows that good comparison to the theoretical Poole-Frenkel coefficient was achieved over the range of electric fields specified. Kakinuma and Wantanabe went on to deconvolute the dark currents flowing within the a-Si:H film by plotting the surface current density as a function of a-Si:H film thickness. However, a-Si:H films of various thickness were not available to the research project and the dark currents could not be deconvoluted for this material.

### (iii) Photoinduced discharge

The first PID experimentation to be performed on the a-Si:H materials was to establish the PID due to light of  $I_{\max}$  relative intensity at an electric field of  $1.33 \times 10^5 \text{ V/cm}$ . Figure 5.18 shows the results of this process. As with the a-As<sub>2</sub>Se<sub>3</sub> material, the surface charge discharge was found to greatly increase under illumination. The time taken for the DDC to reach  $V_0/2$  was 26.9s, and 1.375s for the PID curve, thus the discharge under illumination was approximately 20 times faster than for the DDC. Figure 5.19 shows the PID curves at varying levels of electric field.

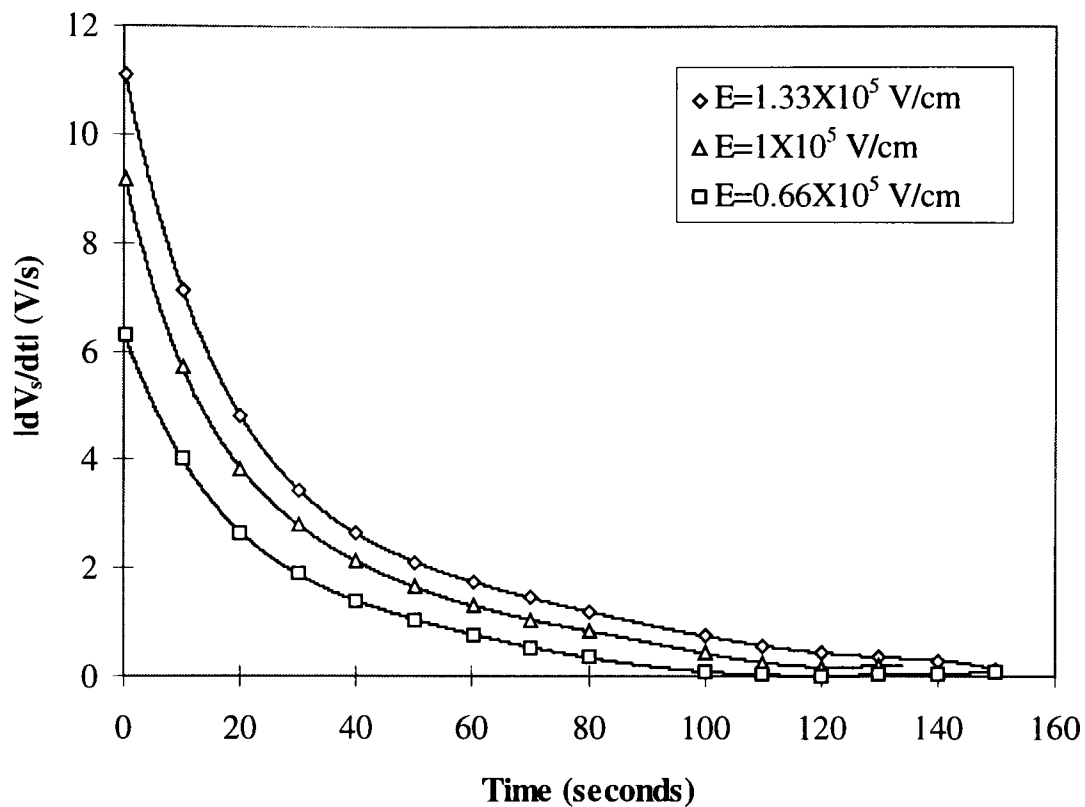


Figure 5.15 Dark discharge rate vs. time for a-Si:H.

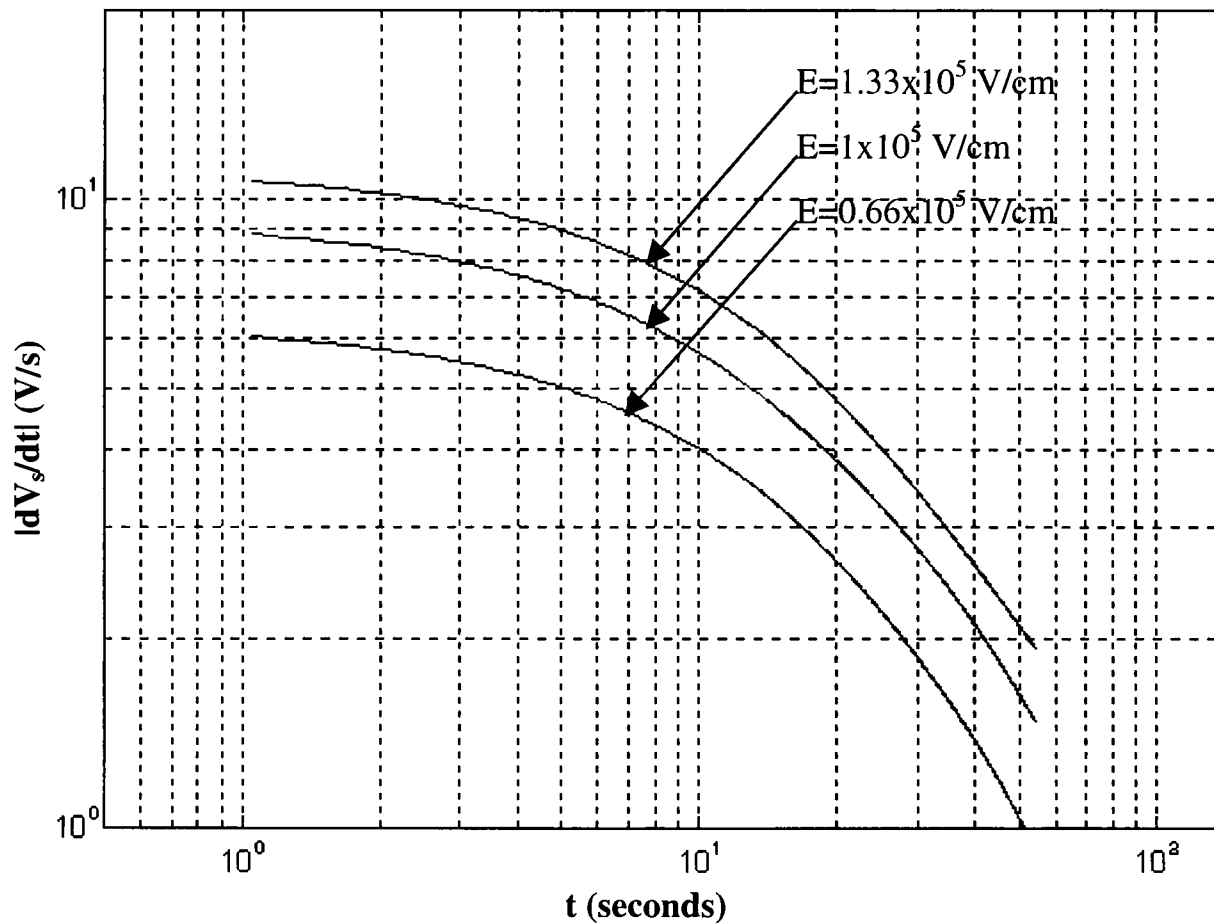


Figure 5.16 Loglog plot of the dark discharge rate vs. time for a-Si:H.

The next PID experimentation to be performed was to see if the a-Si:H material was sensitive to 15% changes in  $I_{\max}$ . The results of this process for an electric field of  $1.33 \times 10^5$  V/cm are shown in figure 5.20. Figure 5.20 shows that the rate of change of the surface potential under illumination is approximately constant up until  $V_0/2$ . The results of the xerographic investigation upon the a-Si:H material are discussed further in chapter 7.

## 5.2 Chapter summary

In this chapter I sought to establish the xerographic properties of the a-As<sub>2</sub>Se<sub>3</sub> and a-Si:H samples in the possession of the research project thereby confirming the integrity of the samples.

It has been shown that both a-As<sub>2</sub>Se<sub>3</sub> and a-Si:H have high charge acceptance and can be charged to surface charge densities in excess of what is considered to be suitable for xerographic application. Both materials have been shown to exhibit slow dark discharge rates with the decay half times that are also as stated as being suitable for xerographic application. Both materials have been shown to exhibit low residual potentials in the order of less than a few tens of volts typically less than 20V. Both materials exhibit enhanced conductivity when exposed to illumination and also exhibit sensitivity to changes in illumination intensity.

The dark discharge curves for both materials have been analysed using established mathematical models to establish their discharge mechanisms. The aim of this exercise was to replicate the findings of past authors and thus confirm the integrity of the a-As<sub>2</sub>Se<sub>3</sub> and a-Si:H samples. It has been shown in the case of a-As<sub>2</sub>Se<sub>3</sub>, that the application of the XDD model proposed by Abkowitz *et al* (1985) to the current experimental data yielded very good comparison of the characteristics of the discharge mechanism in this material. In the case of a-Si:H, application of the models proposed by Kakinuma and Wantanabe (1987) and Baxendale *et al* (1990) to the current experimental data also yielded very good comparison of the characteristics of the discharge mechanism in this material.

It has therefore been shown that both the a-As<sub>2</sub>Se<sub>3</sub> and a-Si:H materials employed in the current research possess all of the characteristics required for use in xerographic

application. The efficiency and accuracy of the experimental apparatus developed to perform the xerographic investigation has been confirmed by the results of the study into the discharge mechanism in the materials. Thus the results of the xerographic investigation have been shown to be reliable and the integrity of the samples has been confirmed.

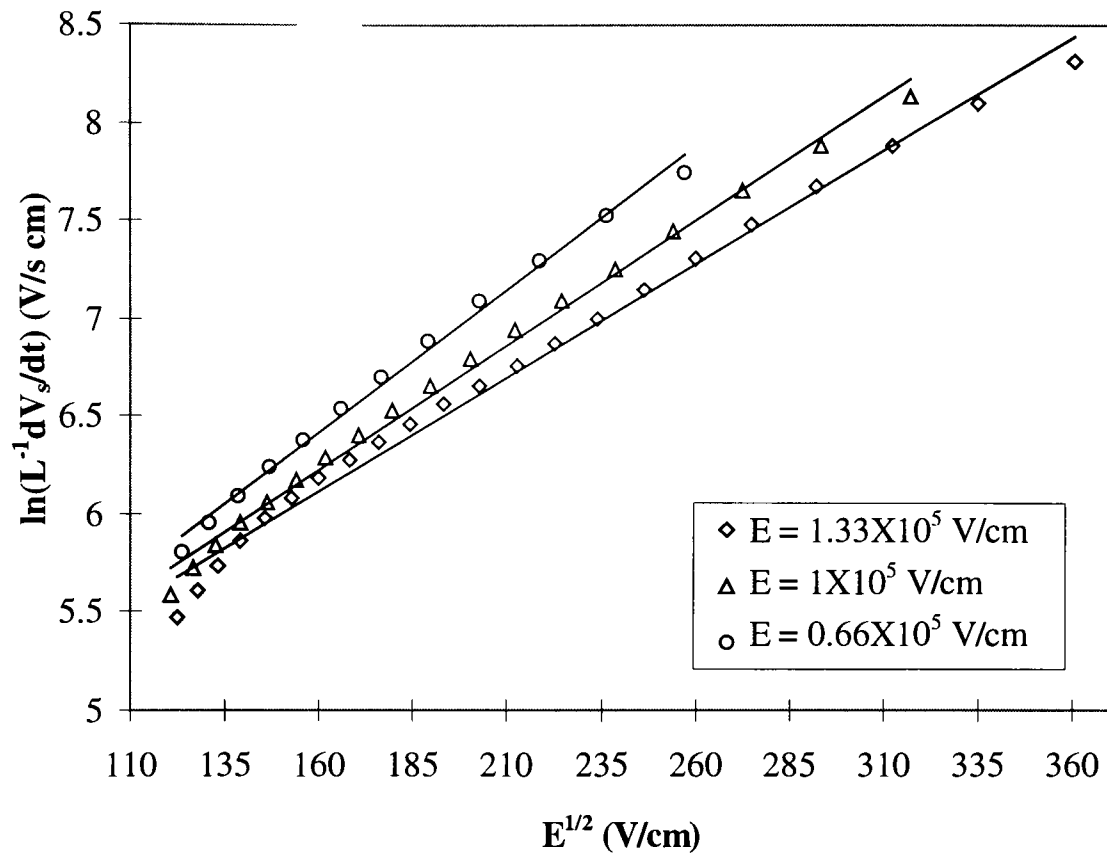


**Figure 5.17** Determination of experimental Poole-Frenkel coefficient.

Electric field (E) ( $\times 10^5$ V/cm)	0.66	1	1.33
Surface potential $V_o$ (V)	181.69	270.57	355.13
Surface charge density $\delta_{(t=0)}$ ( $\times 10^{-7}$ C/cm <sup>2</sup> )	0.59	0.88	1.16
Residual potential ( $V_{res}$ ) (V)	19.58	19.13	21.14
Half decay time $t(V_o/2)$ (s)	22.32	25.44	26.76
Decay time to residual potential $t(V_{res})$ (mins)	2.71	2.93	3.63
Experimental Poole-Frenkel coefficient ( $\beta_{PF}$ ) ( $\times 10^{-4}$ (V/cm) <sup>1/2</sup> eV)	2.39	2.36	2.38
Calculated dielectric constant ( $\epsilon_r$ ) <sup>†</sup>	10.04	10.33	10.12

**Table 5.4** Results of dark decay analysis on a-Si:H.

<sup>†</sup> The dielectric constant  $\epsilon_r$ , should remain at the same level regardless of the value of applied electric field. The small variation in the experimentally determined value of  $\epsilon_r$  is due to the process of fitting first order polynomials to the experimental data in order to establish  $\beta_{PF}$ .

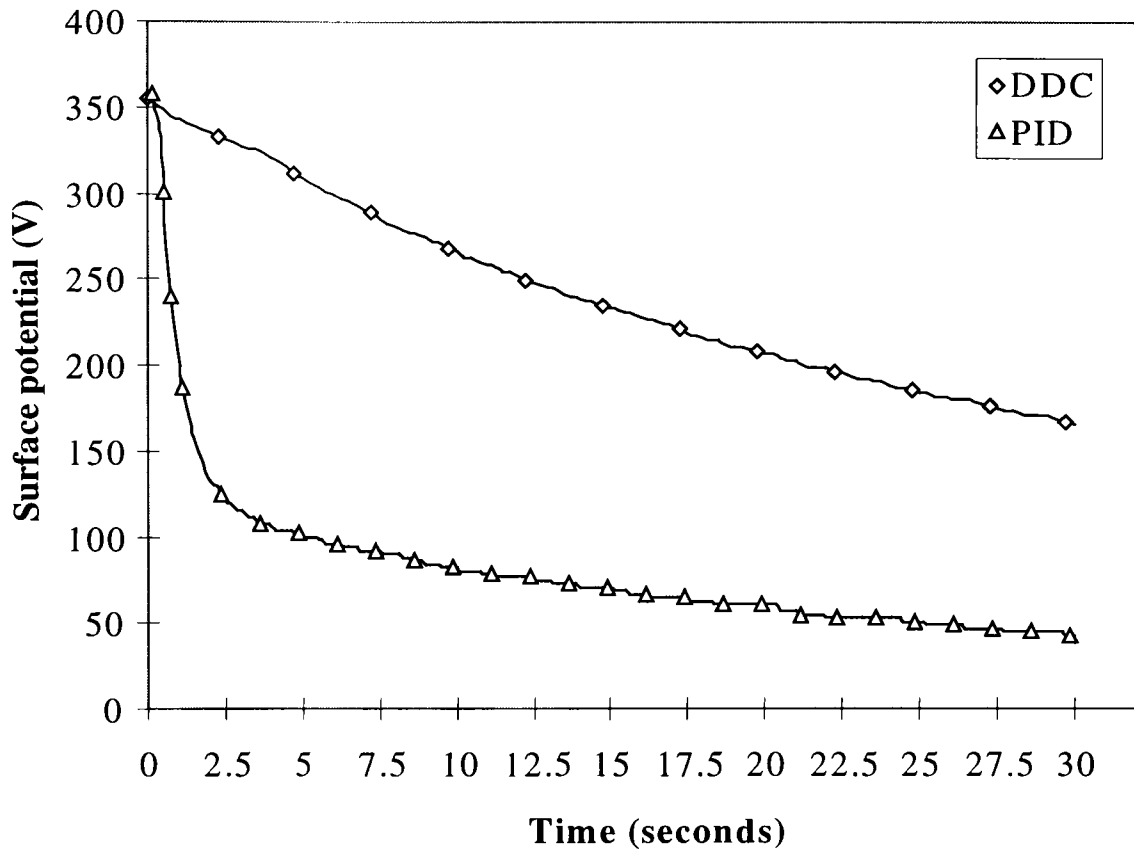


**Figure 5.18** Comparison of DDC and PID curves for  $E = 1.33 \times 10^5$  V/cm, Relative light intensity =  $I_{max}$ .

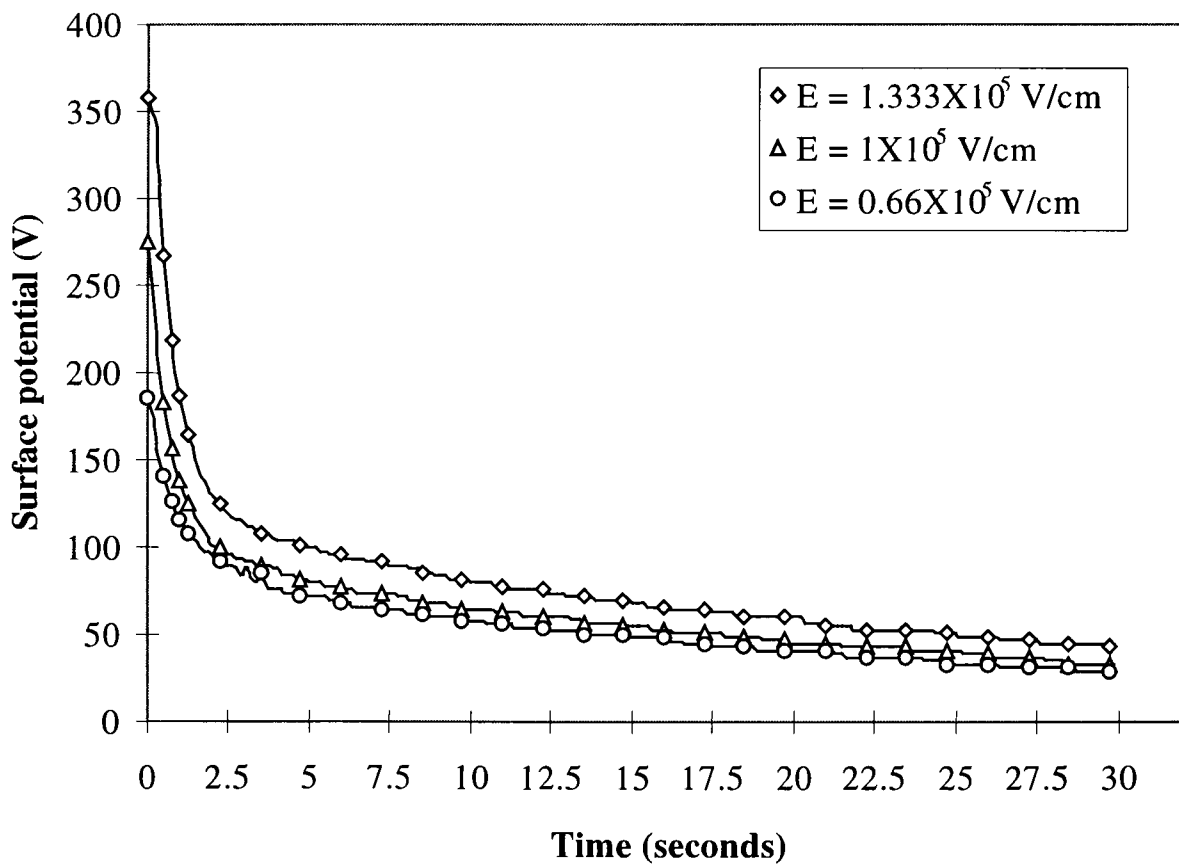


**Figure 5.19** PID curves at various electric field, relative light intensity =  $I_{max}$ .

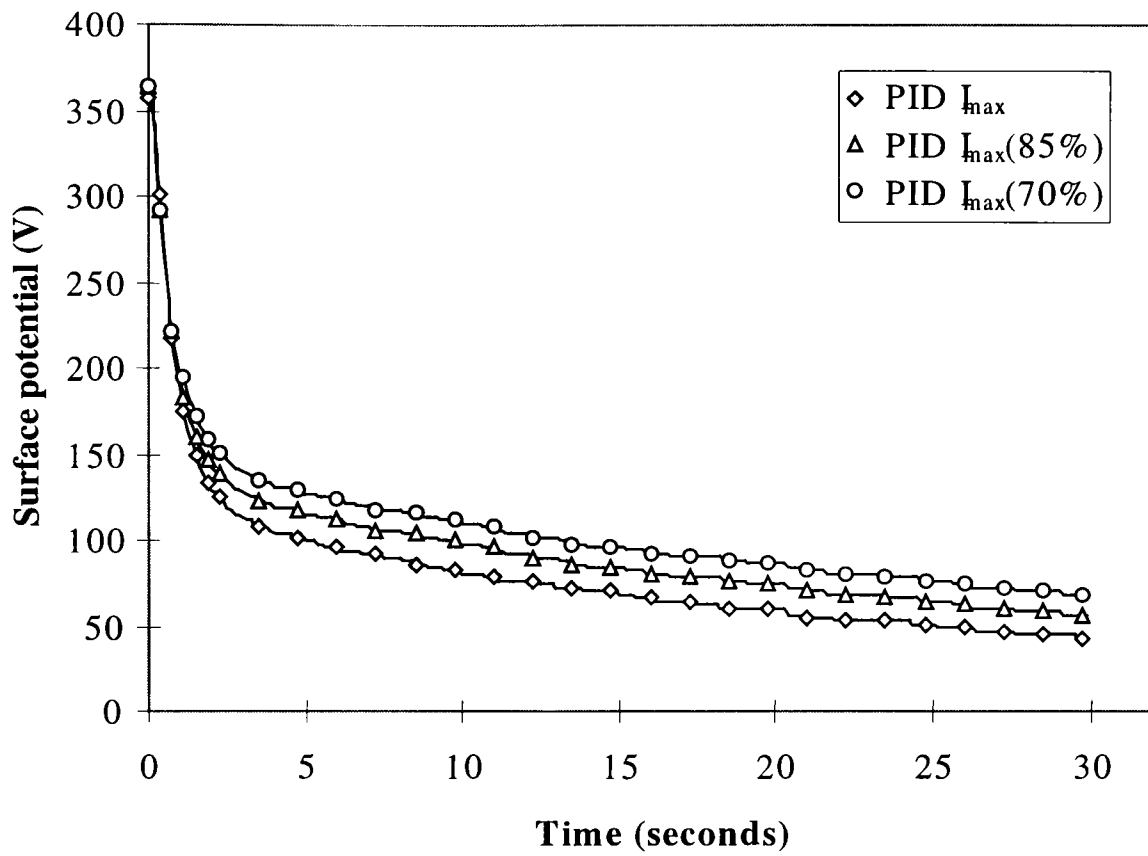


Figure 5.20 PID curves due to 15% to 30% changes in  $I_{\max}$ ,  $E=1.33 \times 10^5$  V/cm.

## CHAPTER 6

### RESULTS OF TOMOGRAPHIC INVESTIGATION

The aim of the tomographic investigation performed in the electroded mode, was to study the electrical properties of a-As<sub>2</sub>Se<sub>3</sub> and a-Si:H under tomographic conditions and establish their suitability as hard field sensors for OPT applications. The investigation involved the study of the detectivity, steady state photocurrent, photoinduced fatigue, responsivity, dark current, production of quantitative and qualitative data, and the formation of basic images. The chapter has been divided into two sections which deal with the a-As<sub>2</sub>Se<sub>3</sub> and a-Si:H materials separately.

#### 6.1 Amorphous arsenic triselenide

##### 6.1.1 Detectivity

The detectivity of a material is traditionally defined as the lowest radiation limit to which the photodetector can respond. However, this signal is not necessarily suitable for tomographic measurements as the resulting peak signal current ( $I_s$ ) may be difficult to accurately determine or repeat due to the effects of noise. In the current investigation, the detectivity is referred to as the minimum level of irradiance ( $H_{min}$ ) required to produce a stable and repeatable  $I_s$ .  $H_{min}$  was established by applying single light pulses of varying radiant intensity ( $I_e$ ) (power emitted by the light source) and duration ( $t_{ph}$ ) to the sample surface and monitoring the resulting  $I_s$  over a range of electric fields. Each experiment was performed four times in order that comparison of the recorded  $I_s$  could be accomplished. The stated values for  $I_s$ , the dark current ( $I_d$ ), the signal response ( $R$ ), and the responsivity ( $\gamma$ ) refer to the mean values averaged over the four test runs.

The incident light power detected by the photodiode ( $\phi_{ei}$ ) was determined by the use of the light detection mechanism detailed in section 4.2.4. The radiant intensity and the irradiance incident upon the sample surface ( $H_e$ ) could be determined from the following. Mooney (1991) states that for a point source (a source that radiates power equally in all directions) the irradiance incident upon the detector can be estimated from:

$$H_e = \frac{\phi_{ei}}{A} (\text{W/cm}^2) \quad (6.1)$$

Where  $A$  is the area of the detector ( $\text{cm}^2$ ).  
 $\phi_{ei}$  is the power intercepted by the detector in Watts (W).

The radiant intensity ( $I_e$ ) from the source can be determined from

$$I_e = \frac{\phi_{ei}}{w} (\text{W/sr}) \quad (6.2)$$

Where  $w$  is the solid angle (in steradians) and can be determined from

$$w = \frac{A}{d^2} (\text{sr}) \quad (6.3)$$

Where  $d$  is the distance from the source to the detector surface (cm).

Figures 6.1, 6.2, and 6.3 show  $I_s$  generated by single light pulses over the range of electric fields previously stated under varying levels of irradiance. It could be seen that the magnitude of irradiance required to produce a repeatable peak  $I_s$  ( $H_{\min}$ ) over a range of electric fields varied in accordance with the applied electric field, and that lower levels of irradiance were required for higher electric fields in order that a repeatable signal be produced. This was to be expected as it was found that  $I_s$  and  $R$  were dependant upon the electric field and the intensity and duration of the issued light pulse. Table 6.1 details the results of the detectivity experiments and shows the levels of  $H_{\min}$  and  $t_{ph}$  required to produce repeatable  $I_s$  over the range of electric fields stated. The values of  $H_{\min}$  stated form the minimum irradiance levels for the current system. The measure of the peak responsivity ( $\gamma$ ) (the ratio of the peak output current to the incident input power) of the  $a\text{-As}_2\text{Se}_3$  material under varying levels of electric field and irradiance, can also give information as to whether the Au contacts are ohmic. Joshi (1990) states that if the responsivity is plotted against applied electric field, a linear response should be obtained if the contacts follow ohms law. Figure 6.4 shows the responsivity vs electric field data for irradiance of  $0.61\text{mW/cm}^2$  to  $9.573\text{mW/cm}^2$ .

The responsivity stated in this thesis was transient in nature being related to the peak signal response, and was determined by the use of a photodiode with a wavelength of 320nm to 1100nm.

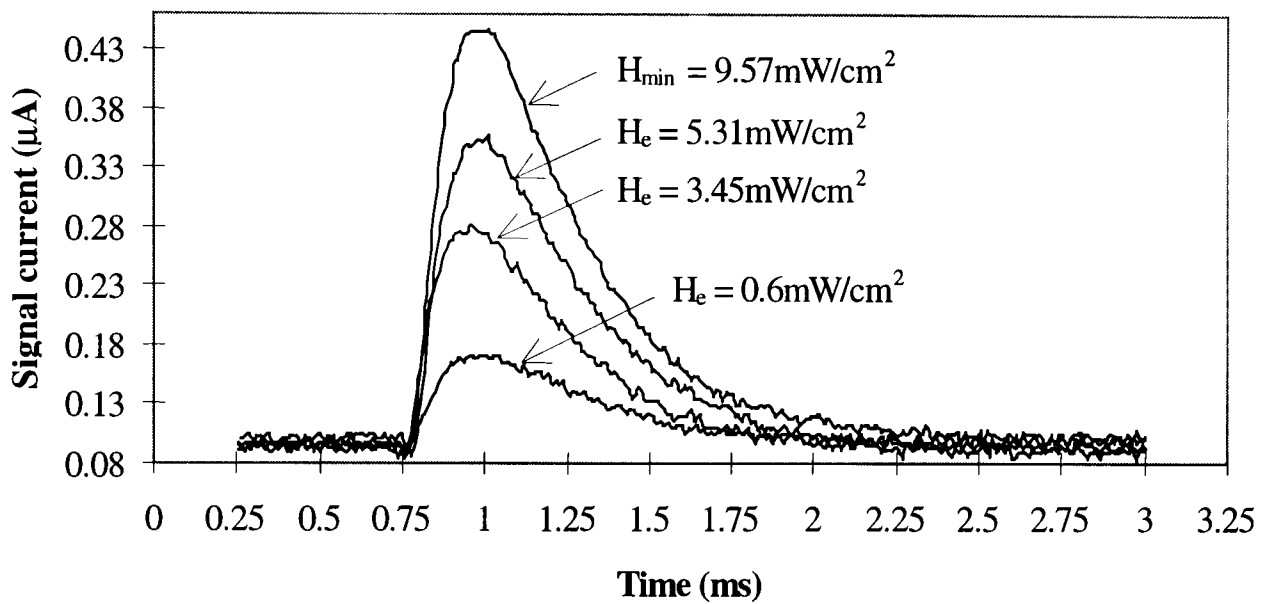


**Figure 6.1** Typical photogenerated current pulses due to varying levels of irradiance,  $E=0.66 \times 10^5$  V/cm,  $t_{ph}=360$ ns.

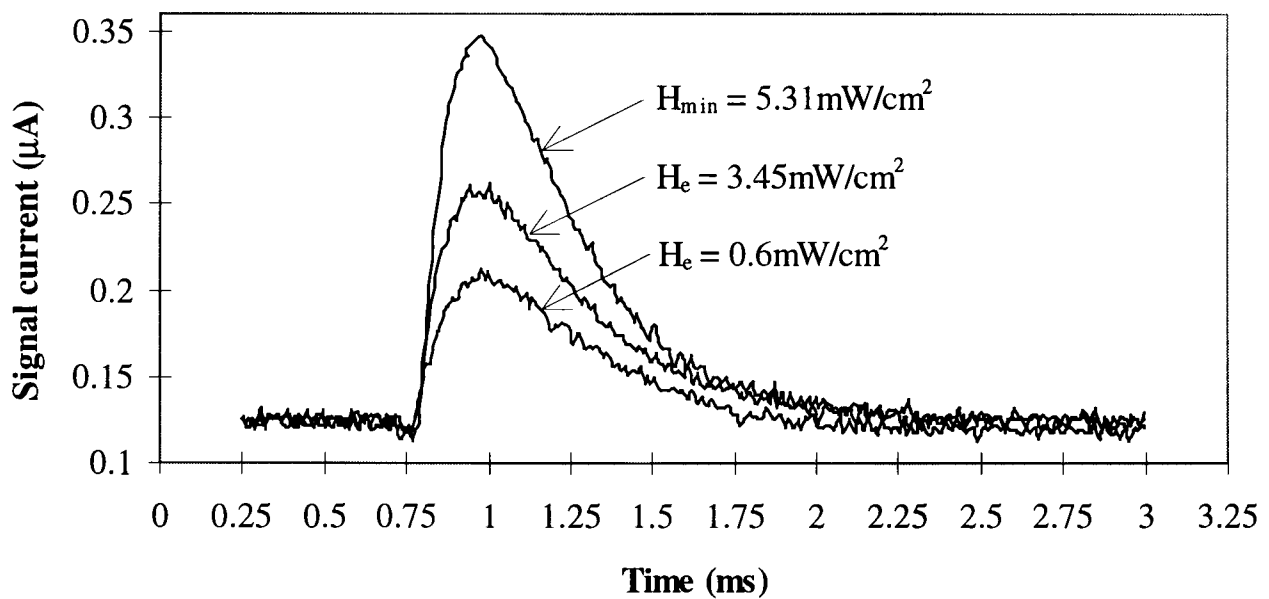


**Figure 6.2** Typical photogenerated current pulses due to varying levels of irradiance,  $E=1 \times 10^5$  V/cm,  $t_{ph}=360$ ns.

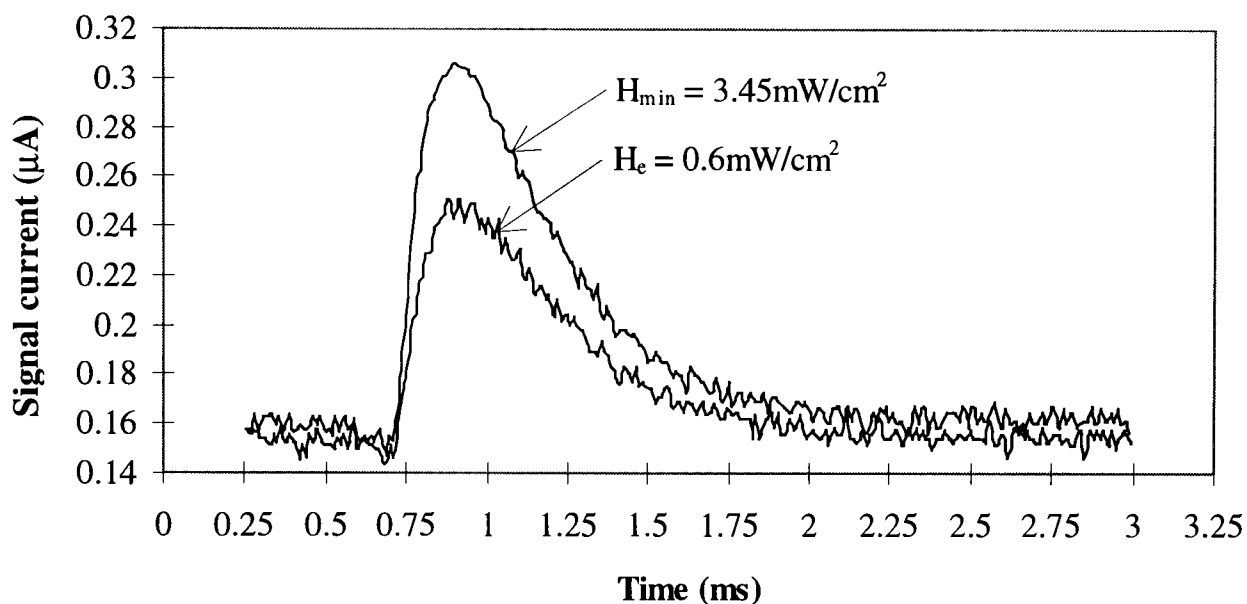


**Figure 6.3** Typical photogenerated current pulses due to varying levels of irradiance,  $E=1.33 \times 10^5$  V/cm,  $t_{ph}=360$ ns.

	Electric field $\times 10^5$ V/cm		
	0.66	1	1.33
Input energy to source $E_{in}$ (mJ)	1.25	1.01	0.8
Radiant intensity $I_e$ (mW/sr)	404.4	224.4	145.8
Incident power $\phi_{ei}$ (mW)	3.93	2.17	1.02
Irradiance $H_{min}$ (mW/cm <sup>2</sup> )	9.57	5.31	3.45
Light pulse half time $t_{ph}$ (ns)	360	360	360
Peak signal current $I_s$ (nA)	446	347	305.9
Average dark current $I_d$ (nA)	101.13	125.25	157.8
Signal response R (nA)	344.86	221.75	148.1
Responsivity $\gamma$ ( $\mu$ A/W)	87.86	102.18	145.19

**Table 6.1** Summary of detectivity experimentation showing minimum light conditions for the current system.

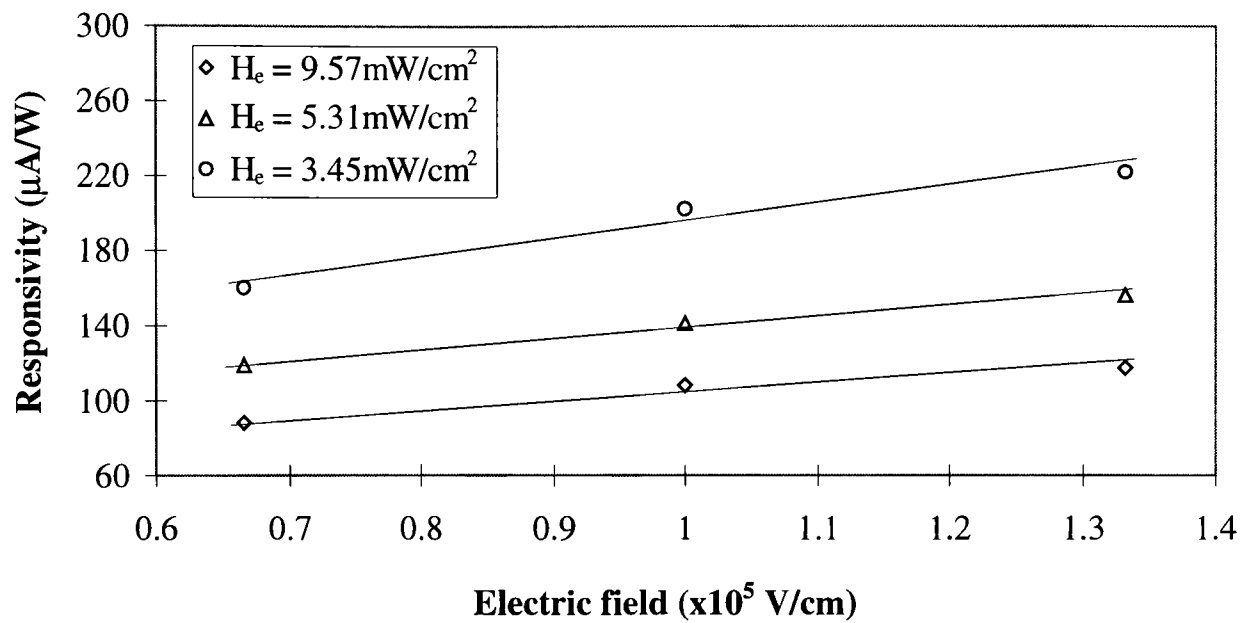


**Figure 6.4** Graph showing linear relationship between responsivity and electric field over a range of irradiance.

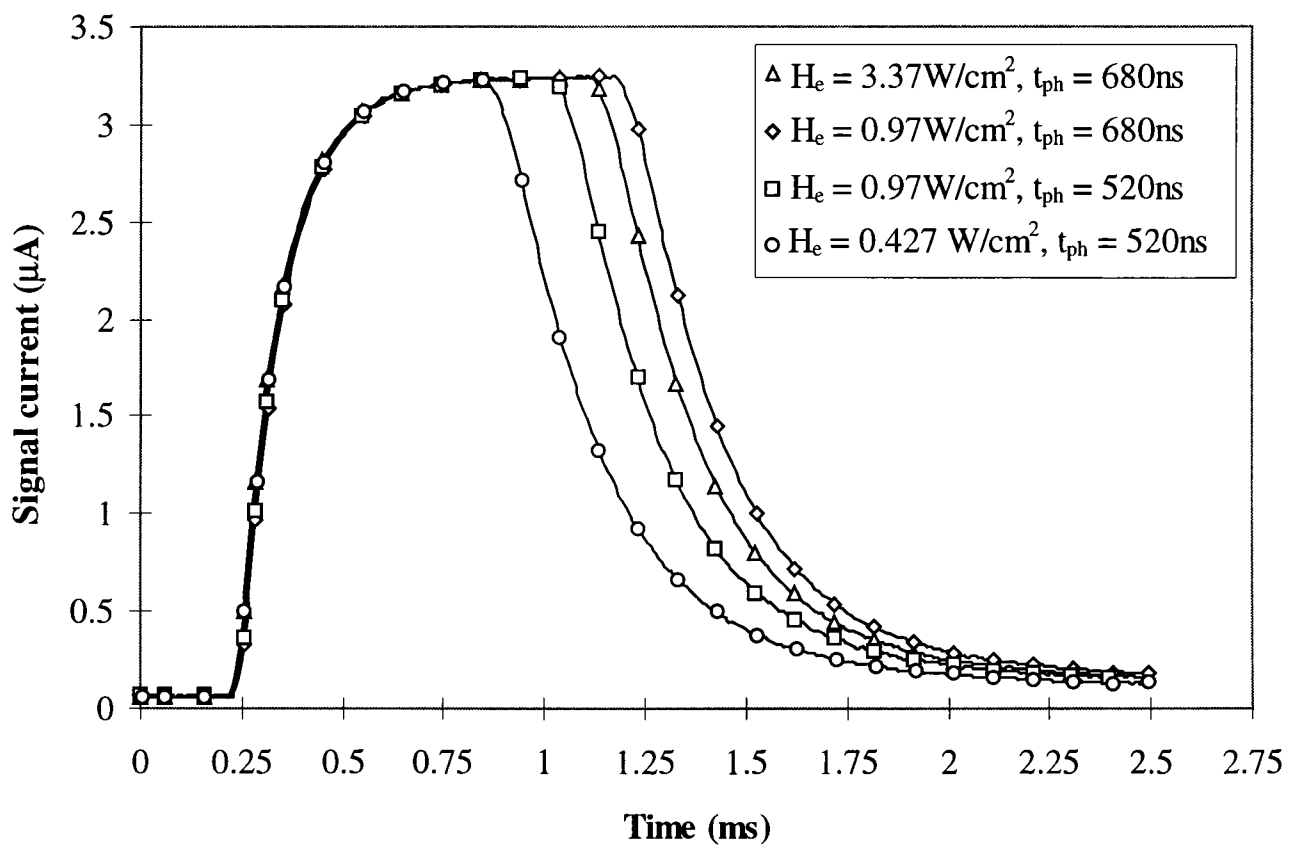


**Figure 6.5** Typical steady state conditions for a-As<sub>2</sub>Se<sub>3</sub>,  $E=0.66 \times 10^5 \text{ V/cm}$ .

From the graph it could be seen that a linear relationship between the electric field and responsivity was observed thus indicating that the Au contacts were ohmic over the range of electric field and irradiance stated.

### 6.1.2 Production of steady state current

The aim of the steady state experimentation was to establish the values of  $I_e$ ,  $t_{ph}$ , and maximum irradiance ( $H_{max}$ ) that produced steady state  $I_s$  over the range of electric field previously described. The steady state  $I_s$  was the maximum photogenerated current that could be produced by the sample. The production of steady state  $I_s$  was found to be dependant upon the area of the Au contact, the magnitude of the applied electric field, and the duration, intensity, and irradiance of the applied light pulse. Once the required light limits had been established, the maximum light conditions could be used in conjunction with the results from the detectivity experiments, to establish the maximum and minimum light limits for the current system.

The light conditions required to achieve steady state  $I_s$  were determined by recording the photocurrent due to single light pulses of varying duration and intensity over a range of electric fields. Figure 6.5 shows the light conditions required to drive  $I_s$  into the steady state for an electric field of  $0.66 \times 10^5$  V/cm. Figure 6.5 demonstrates that steady state  $I_s$  could be achieved by the application of a light pulse of  $t_{ph}=680$ ns and  $H_e=3.37$ W/cm<sup>2</sup> which resulted in a steady state  $I_s$  of approximately 3.25 $\mu$ A. Figure 6.5 also demonstrates that a reduction in irradiance of approximately 70% for the same pulse width of 680ns resulted in a reduction in peak  $I_s$  of just a few nA. Thus the a-As<sub>2</sub>Se<sub>3</sub> material was essentially insensitive to large changes in  $H_e$  if the duration of the light pulse and the applied electric field were sufficient to allow the production of steady state  $I_s$ . However, it can be seen from figure 6.5 that maintaining  $H_e$  at 0.97W/cm<sup>2</sup> but reducing  $t_{ph}$  to 520ns resulted in a further reduction in  $I_s$ . The irradiance was then reduced by approximately 50%. This time the change in  $H_e$  produced a much larger change in peak  $I_s$ , thus the sensitivity to changes in  $H_e$  could be increased by moving the peak response away from the steady state by the reduction of  $t_{ph}$ . This topic is discussed further in chapter 7.

Although the maximum signal response ( $R_{\max}$ ) occurred at the steady state condition, the steady state condition was not suitable for the collection of quantitative/qualitative data, or for the production of images due to the insensitivity to changes in  $H_e$  in this region. Maximum sensitivity to changes in  $H_e$  was determined by positioning the peak  $I_s$  just under the steady state condition by the adjustment of  $t_{ph}$  and  $H_e$ .

Figure 6.6 shows the responses for a 44mm (internal diameter) pipeline full of water and an empty pipeline under two conditions. In the first condition, the level of  $H_e$  and  $I_e$  were set to allow  $I_s$  to reach approximately steady state conditions ( $H_e=573\text{mW/cm}^2$ ,  $t_{ph}=440\text{ns}$ ) with the full pipeline in-situ above the sample. The resulting peak  $I_s$  was then recorded. An empty section of pipeline was then inserted in-situ above the sample and the tests were re-run. For the same radiant intensity ( $I_e$ ) and  $t_{ph}$ , the insertion of the empty pipeline caused a 67% reduction in  $H_e$ . The reduction in  $H_e$  led to a difference of approximately 42nA between  $I_s$  for the full and empty pipelines. In the second condition, the peak  $I_s$  was positioned just below the steady state for the full pipeline by reducing  $t_{ph}$  to 340ns.  $H_e$  and peak  $I_s$  for the full and empty pipelines were then recorded. The 100ns reduction in  $t_{ph}$  led to a difference of 911nA in the responses for the full and empty pipelines. Thus for the same 67% reduction in  $H_e$  caused by the insertion of the empty pipeline, the positioning of the peak  $I_s$  to just under the steady state condition led to a 22 fold increase in the separation between the full and empty pipelines.

In terms of the collection of quantitative/qualitative data and the production of images, it was important to establish the maximum separation between the pipeline limits thus producing maximum resolution for the system. The procedure of positioning the peak  $I_s$  to just under the steady state in order to obtain maximum sensitivity to changes in  $H_e$  has been used throughout the experimental work. Thus the establishment of the light conditions required to produce steady state  $I_s$  was important in that  $R_{\max}$  could be established. Additionally, the establishment of the steady state  $I_s$  provided a 'template' to which the peak  $I_s$  could be positioned. Table 6.2 summarises the light conditions required to produce steady state  $I_s$  over the range of electric field previously described. The term  $H_{\max}$  refers to the level of irradiance required to drive the signal current just into what is considered to be the steady state for a given value of  $t_{ph}$ . The procedure

for the positioning of the peak photocurrent in order to maximise sensitivity and therefore resolution of the system is discussed further in the appropriate sections.

### 6.1.3 Establishment of maximum operating speed by the determination of the effects of photoinduced fatigue.

An important aspect in the determination of the suitability of a-As<sub>2</sub>Se<sub>3</sub> as a sensor for OPT applications, was the materials ability to produce repeatable levels of  $I_s$  at speeds required for OPT over extended periods of time. The flash repetition rate (FRR) at which no deterioration of the signal response was observable over an extended time period, determined the maximum operating speed of the a-As<sub>2</sub>Se<sub>3</sub> material.

The maximum FRR was established by initially setting  $H_e$  and  $t_{ph}$  in order that the peak  $I_s$  be positioned just under the steady as previously described. Each experiment was performed over a half hour period with a photogenerated current pulse being recorded every 30s. The peak  $I_s$  was calculated for each of the recorded current pulses and the signal response (R) was calculated by subtraction of  $I_d$  from  $I_s$ . The autostore function within the Ono Sokki CF-4220 FFT analyser used to record  $I_s$  over the 30 minute test period could not record data at  $t=0$  and then at 30s intervals thereafter. This meant that the value of  $I_s$  at the start of the test runs could not be recorded. In order to remedy this problem, when a test run was to be performed a single light pulses was issued and the resulting  $I_s$  was recorded manually. This manually recorded  $I_s$  represented  $I_s$  at  $t=0$ . Light pulses at the desired FRR were then applied to the sample surface and the FFT analyser was put into the autostore mode to sample the data at the desired 30s sampling rate.

The dark current was found not to be constant but exhibited fluctuations as can be seen in figure 6.7. This meant that the average DC value of  $I_d$  had to be calculated in order to establish R. The signal response for each sampled current pulse was recorded using the FFT analyser with a 10ms timebase. The trigger position of the FFT analyser was set so that 1ms of dark current data was recorded as the issued light pulse triggered the FFT. The FFT analyser sampled the output from the picoammeter 1000 times over the 10ms period, thus the average dark current was determined from 100 samples over the 1ms calculation period.

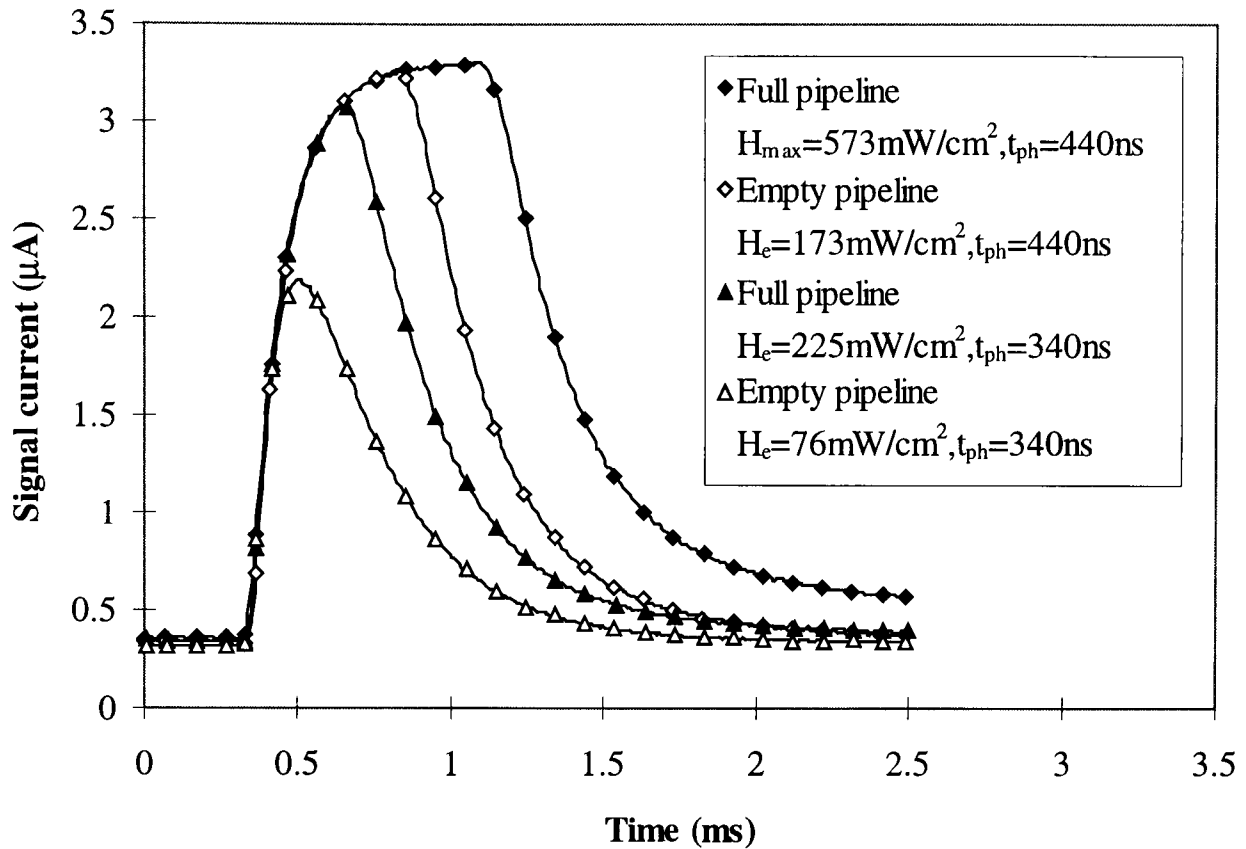


**Figure 6.6** Graph showing how increased sensitivity to changes in irradiance can be achieved by the positioning of the peak photocurrent under steady state conditions by reducing  $t_{ph}$ ,  $E=1.33 \times 10^5 \text{ V/cm}$ .

	Electric field $\times 10^5 \text{ V/cm}$		
	0.66	1	1.33
Input energy to source $E_{in}$ (mJ)	27	17.28	11.4
Radiant intensity $I_e$ (W/sr)	61.91	29.3	13.51
Incident power $\phi_{ei}$ (mW)	600	284	131
Irradiance $H_{max}$ ( $\text{W/cm}^2$ )	1.46	0.69	0.32
Light pulse half time $t_{ph}$ (ns)	520	520	520
Peak signal current $I_s$ ( $\mu\text{A}$ )	3.24	3.24	3.24
Average dark current $I_d$ (nA)	59.07	68.5	76.2
Signal response $R$ ( $\mu\text{A}$ )	3.18	3.17	3.16
Responsivity $\gamma$ ( $\mu\text{A/W}$ )	5.3	11.16	24.83

**Table 6.2** Summary of steady state experimentation showing maximum light conditions for the current system.

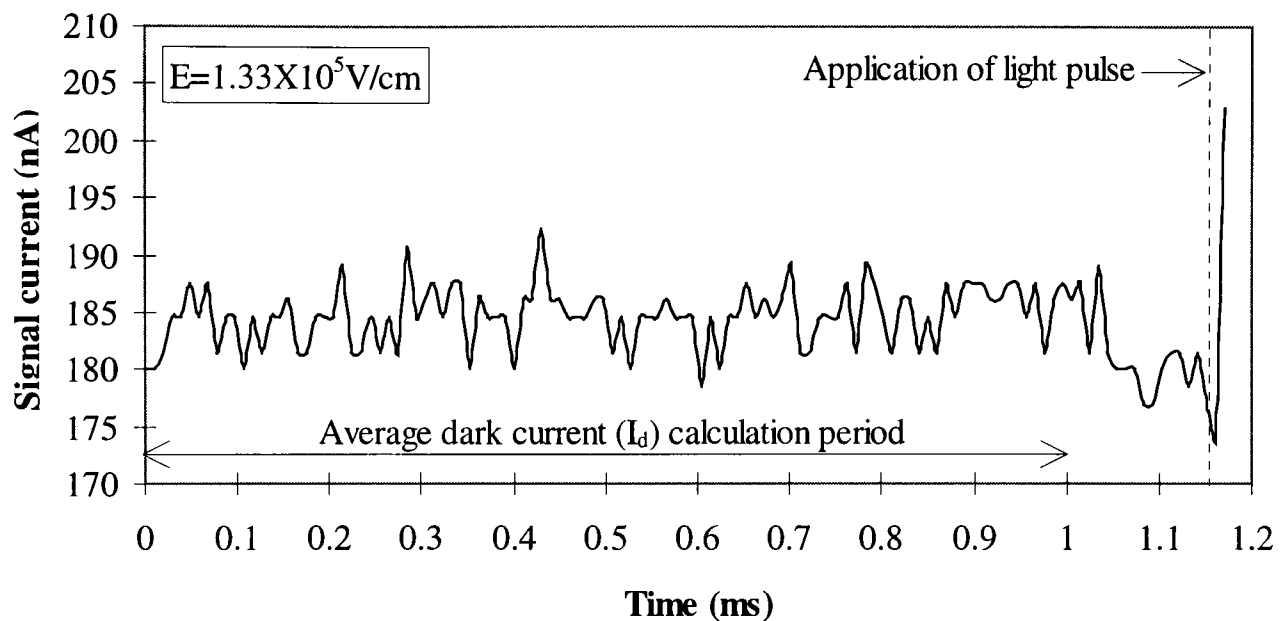


Figure 6.7 Graph showing the calculation period of the average dark current.

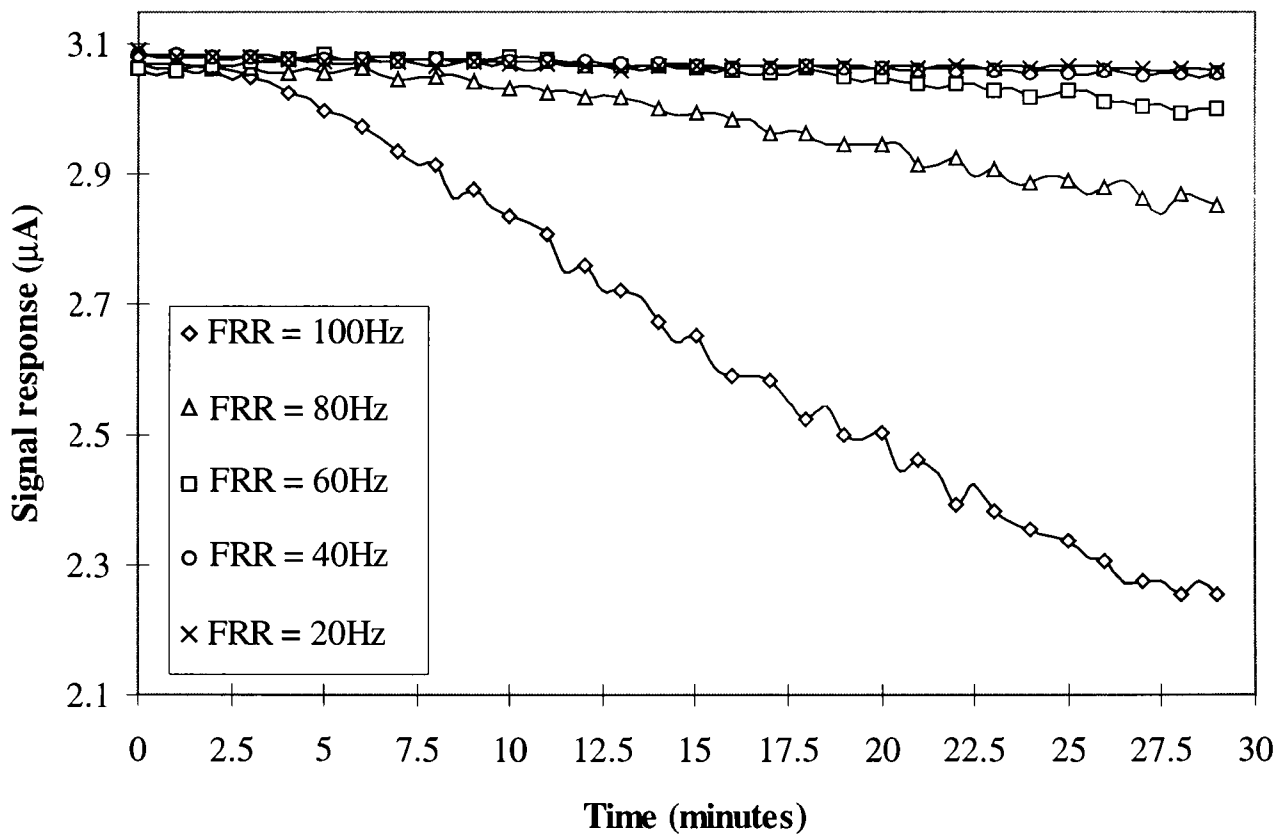


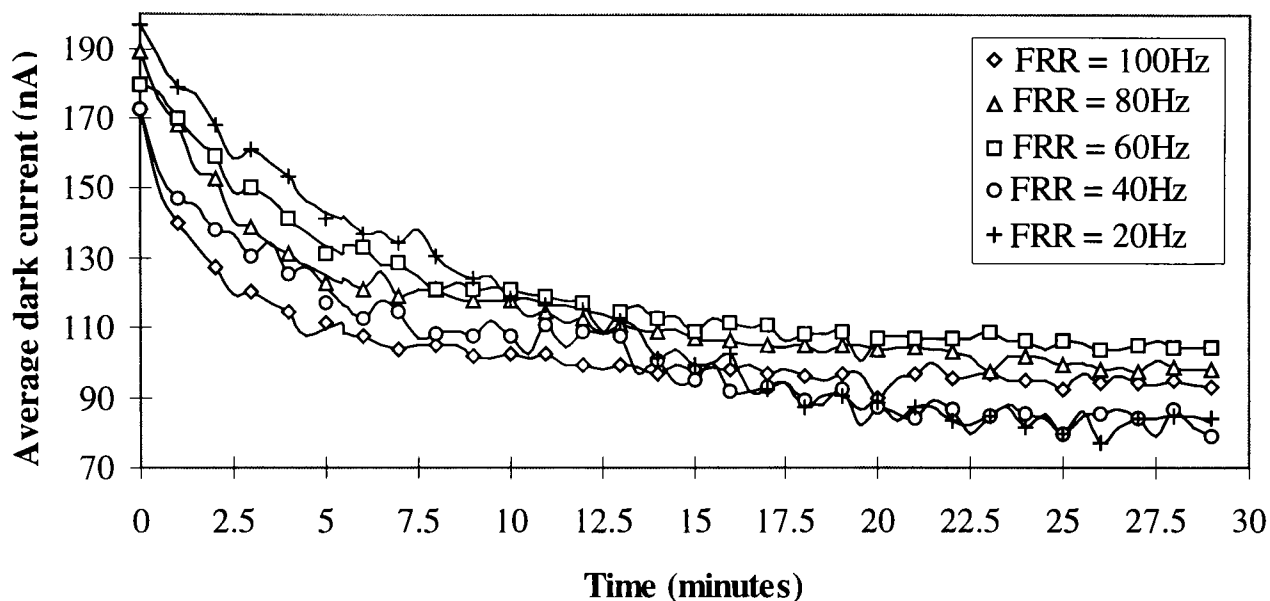
Figure 6.8 Graph showing the effect of increasing the FRR from 20Hz to 100Hz for  $E = 1.33 \times 10^5 \text{ V/cm}$ ,  $H_e = 319 \text{ mW/cm}^2$ ,  $t_{ph} = 520 \text{ ns}$ .

The average dark current was calculated for each of the 60 current pulse samples and R was determined for the 30 minute test period.

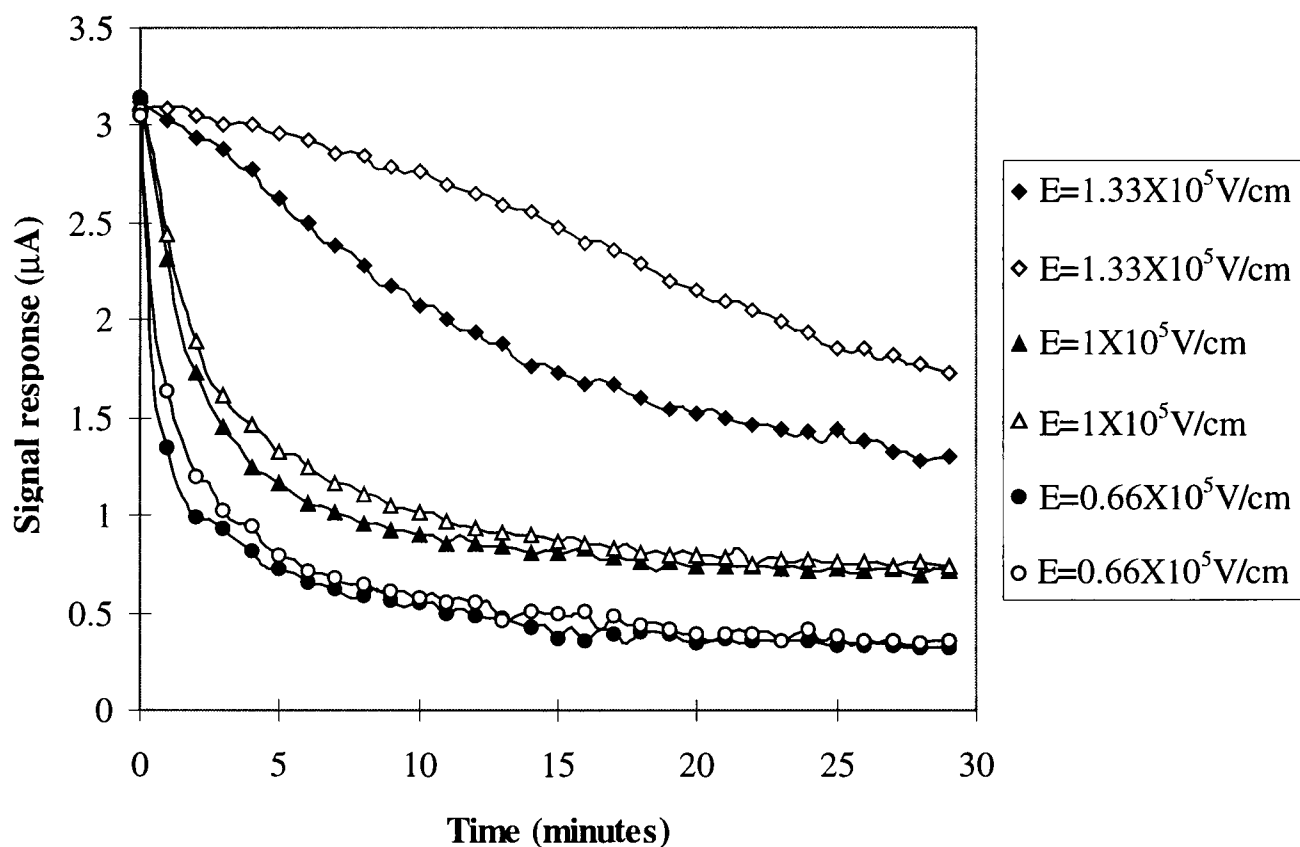
The first tests to be performed were to observe the effect of varying the FRR from 20Hz to 100Hz in 20Hz increments for constant values of electric field and irradiance. Figure 6.8 shows the result of this process. Figure 6.8 demonstrates that the mean signal response deteriorated over the 30 minute test period at high FRR's, and that the higher the FRR the greater the rate of deterioration observed in the signal response. The signal response was seen to deteriorate significantly for FRR's of 100, 80, and 60Hz and the rate of deterioration increased with an increase in FRR. The signal response was not seen to stabilise over time.

Figure 6.9 shows the associated values of  $I_d$  over the 30 minute test period. The ambient temperature (T) during experimentation was within a few °C for all test runs. It could be seen that  $I_d(t=0)$  was in the order of approximately 170nA to 200nA for all FRR's and that  $I_d$  also decayed with time. However, the rate of decay observed in  $I_d$  did not account for the large deterioration observed in the signal responses for FRR's of greater than 40Hz. For example, the average dark current for the test run at an FRR=100Hz decayed by approximately 80nA over the 30 minute test period. However, the associated signal response decayed by 815nA over the test period. Thus the observed deterioration was attributed to photoinduced fatigue and is discussed further in chapter 7.

The next series of experiments to be performed were to establish if the rate of fatigue was effected by a change in electric field and  $H_e$ . In keeping within the framework of tomographic experiments,  $H_e$  was reduced by the insertion of full and empty pipelines of 44mm internal diameter in-situ above the sample surface. Figure 6.10 shows the effect of changing the electric field and irradiance for the maximum FRR of 100Hz over the range of electric field previously described. It could be seen that the deterioration of the signal response was related to the applied electric field and the level of  $H_e$ .



**Figure 6.9** Graph showing average dark currents over a 30 minute test period for a range of FRR,  $E=1.33 \times 10^5$  V/cm,  $H_e=319$  mW/cm<sup>2</sup>,  $t_{ph}=520$  ns.



**Figure 6.10** Graph showing the effect of altering the electric field and irradiance on the rate of photoinduced fatigue. Solid data markers refer to a pipeline full of water with  $H_e=240$  mW/cm<sup>2</sup>, the empty data markers refer to an empty pipeline with  $H_e=159.8$  mW/cm<sup>2</sup>. FRR=100Hz, and  $t_{ph} = 520$  ns in both cases.

Lowering the electric field had an adverse effect upon the rate of fatigue, with the rate of deterioration of the signal response increasing with each successive decrease in applied electric field. Lowering the level of  $H_e$  had a positive effect upon the rate of fatigue over the electric fields investigated indicating that the rate of fatigue was dependant upon the radiant power issued from the light source. Figure 6.11 shows the associated  $I_d$  for the preceding experiment. It was noted that  $I_d$  again reduced with time for all electric fields and that  $I_d(t=0)$  was seen to increase with applied electric field. Again the magnitude of  $I_d$  did not account for the deterioration observed in the signal responses. This issue is discussed further in chapter 7.

The next experiment to be performed was to repeat the previous experiment but with a FRR of 20Hz to see the effect of reducing the FRR on the rate of fatigue. Figure 6.12 shows the result of this process. The reduction in FRR from 100Hz to 20Hz produced a significant reduction in the deterioration of the signal response over the 30 minute test period. The lower levels of  $H_e$  produced less fatigue of the signal response. As before, the lowering of the electric field increased the amount of fatigue observed. The dark current for this experiment is shown in figure 6.13. As with previous experiments,  $I_d$  seemed to deteriorate over time and an increase in  $I_d(t=0)$  was observed with an increase in applied electric field.

Figure 6.14 shows the normalised signal responses for FRR's of 100Hz and 20Hz. The data summarised in figure 6.14 indicates that for the a- $As_2Se_3$  material, the electric field needs to be kept as high as possible in order to minimise the effects of photoinduced fatigue. Figures 6.8 and 6.14 also demonstrate that the FRR needs to be kept at a maximum 20Hz or lower if a stable signal response is to be obtained over a reasonable operational period. Figure 6.15 shows the mean signal responses for the full and empty pipelines over the 30 minute test period at an electric field of  $1.33 \times 10^5$  V/cm and the maximum FRR of 20Hz. Both signal responses exhibited a standard deviation of approximately 8nA for the whole population of the sampled data which was approximately equal to 0.24% of the mean signal response.

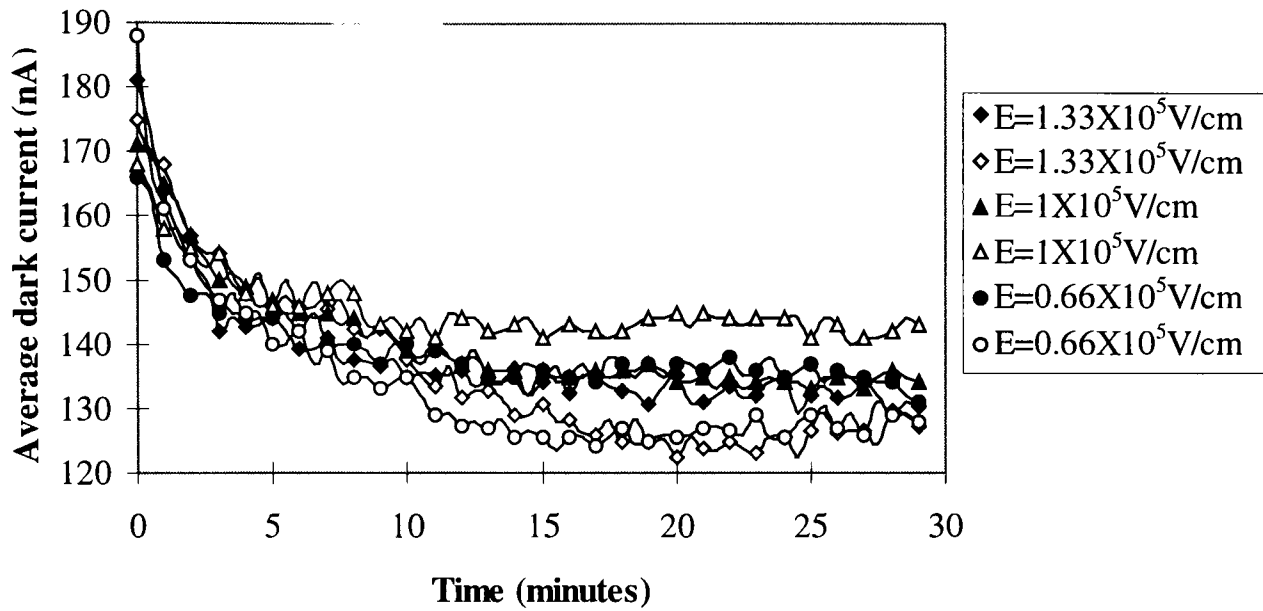


**Figure 6.11** Average dark current over a range of electric field. Solid data markers refer to a pipeline full of water with  $H_e=240\text{mW/cm}^2$ , the empty data markers refer to an empty pipeline with  $H_e=159.8\text{mW/cm}^2$ ,  $t_{ph}=520\text{ns}$ ,  $\text{FRR}=100\text{Hz}$  in both cases.

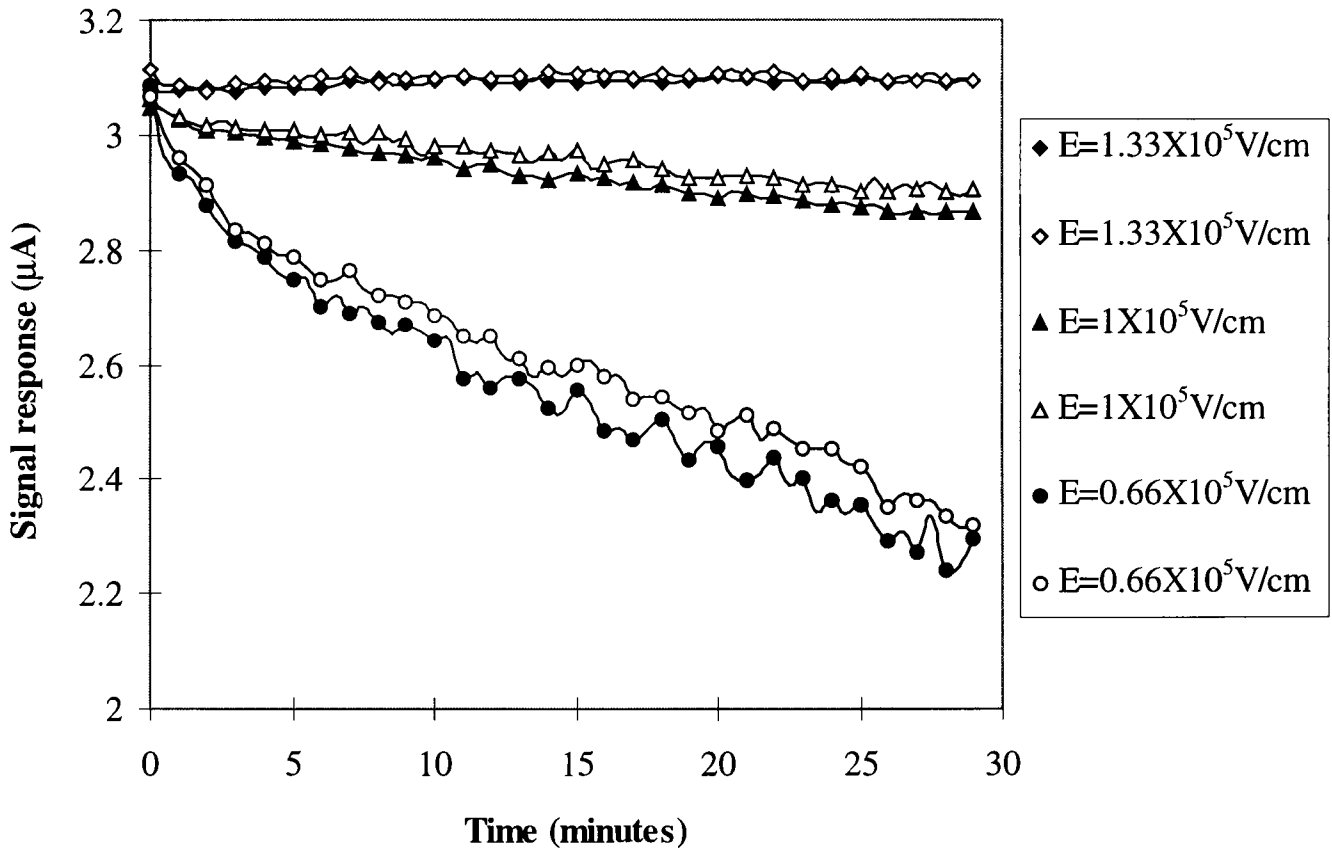


**Figure 6.12** Effect of altering the electric field and irradiance on the rate of photoinduced fatigue. Solid data markers refer to a pipeline full of water with  $H_e=240\text{mW/cm}^2$ , the empty data markers refer to an empty pipeline with  $H_e=159.8\text{mW/cm}^2$ .  $\text{FRR}=20\text{Hz}$ , and  $t_{ph}=520\text{ns}$  in both cases.

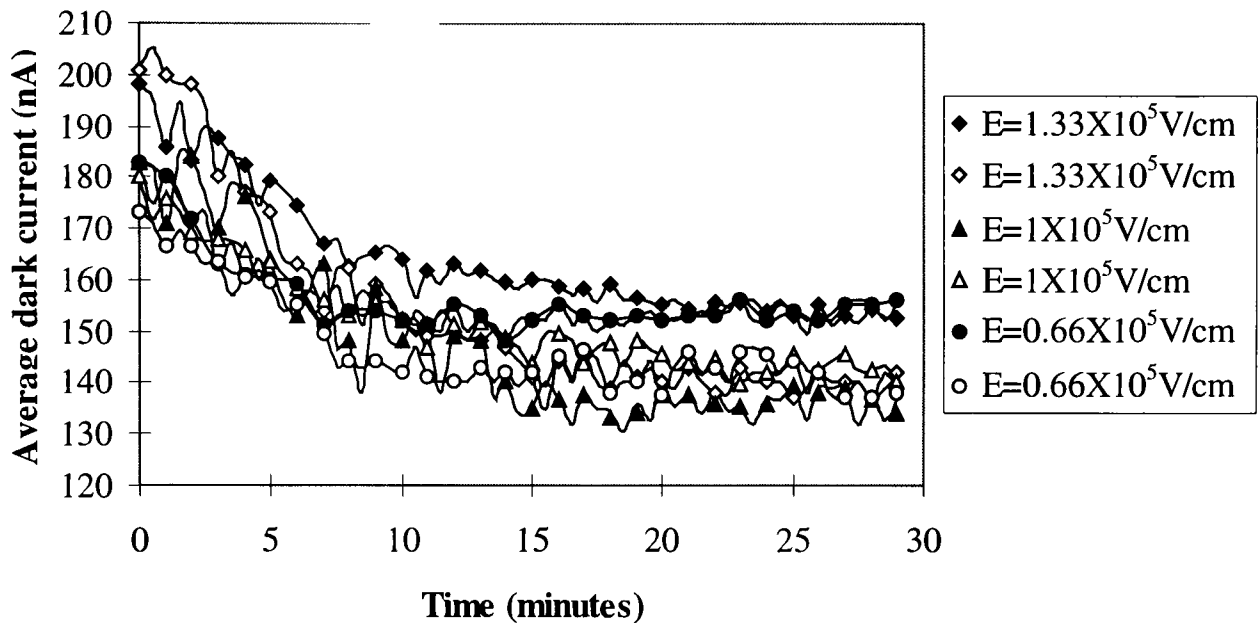


**Figure 6.13** Average dark current over a range of electric field. Solid data markers refer to a pipeline full of water with  $H_e=240\text{mW/cm}^2$ , the empty data markers refer to an empty pipeline with  $H_e=159.8\text{mW/cm}^2$ ,  $t_{ph}=520\text{ns}$ ,  $\text{FRR}=20\text{Hz}$  in both cases.

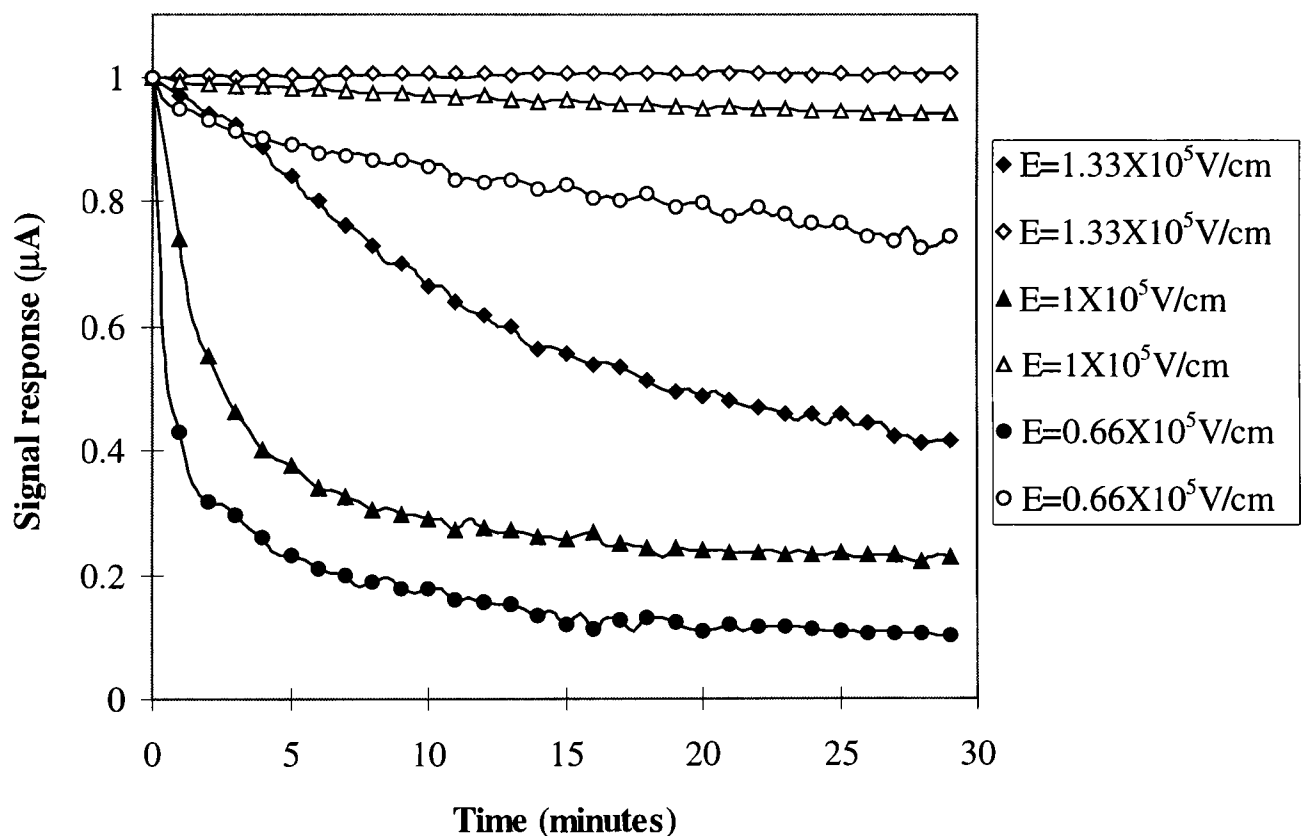


**Figure 6.14** Normalised signal responses over a range of electric field. Solid data markers relate to a FRR of 100Hz, empty data markers relate to a FRR of 20Hz.  $H_e=240\text{mW/cm}^2$ ,  $t_{ph}=520\text{ns}$ .

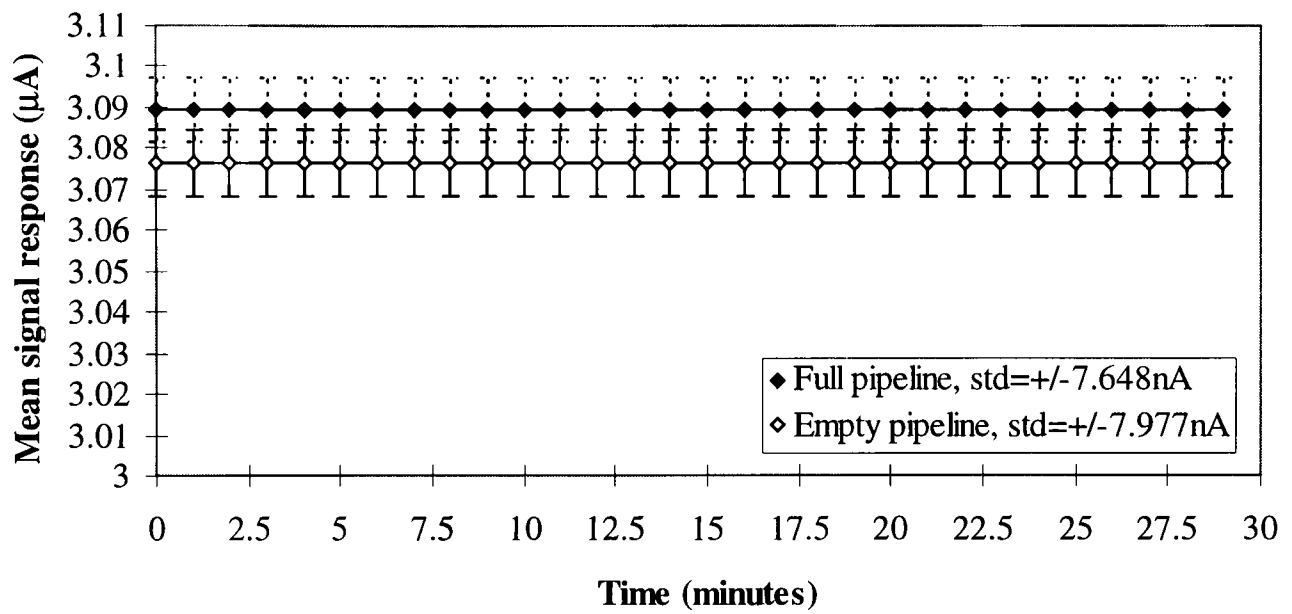


**Figure 6.15** Mean signal response for full and empty pipes,  $E=1.33 \times 10^5$  V/cm  
FRR=20Hz.

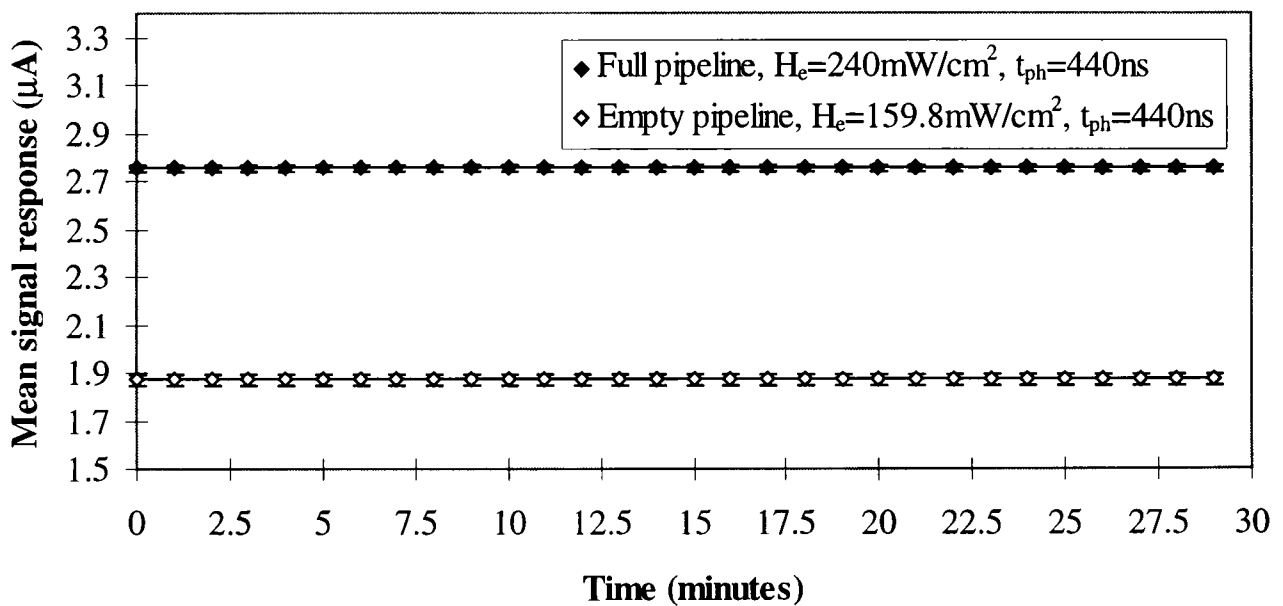


**Figure 6.16** Maximum separation between full and empty pipelines.  
 $E=1.33 \times 10^5$  V/cm, Error bars show standard deviation  
(12.5nA for the full pipeline, 18.5nA for the empty pipeline).

$I_d$  has been shown to decay with time over all electric fields and FRR's. As  $I_d$  had to be subtracted from  $I_s$  in order to establish R, the decaying  $I_d$  had a detrimental effect upon the standard deviation of the signal response. The decaying  $I_d$  means that the signal response will increase over the same time period as the dark current decay. This had the effect of increasing the standard deviation over the whole time scale of the experiment. However, figures 6.9, 6.11, and 6.13 show that  $I_d$  is at its most stable during the last 15 minutes of the test period. Recalculating the standard deviation over the last 15 minutes of the test run gives a standard deviation of approximately 5nA for both the full and empty pipelines which relates to approximately 0.17% of the mean signal response. Thus by calculating the standard deviation from the last 15 minutes of the test run, the standard deviation was reduced by approximately 30%.

Figure 6.15 shows that negligible separation existed between the signal responses for the full and empty pipelines. This was due to the fact that the peak  $I_s$  was too close to the steady state for both the full and empty pipelines. By positioning the peak  $I_s$  further under the steady state using the technique previously described, a maximum separation of 0.885 $\mu$ A was achieved between the signal responses for the full and empty pipelines as can be seen in figure 3.16.

The established maximum FRR of 20Hz and apparent instability of the signal response over the first 15 minutes of operation had serious implications as to the a-As<sub>2</sub>Se<sub>3</sub> materials suitability for application in OPT systems which are discussed in chapter 7.

## 6.2 Hydrogenated amorphous silicon

### 6.2.1 Detectivity

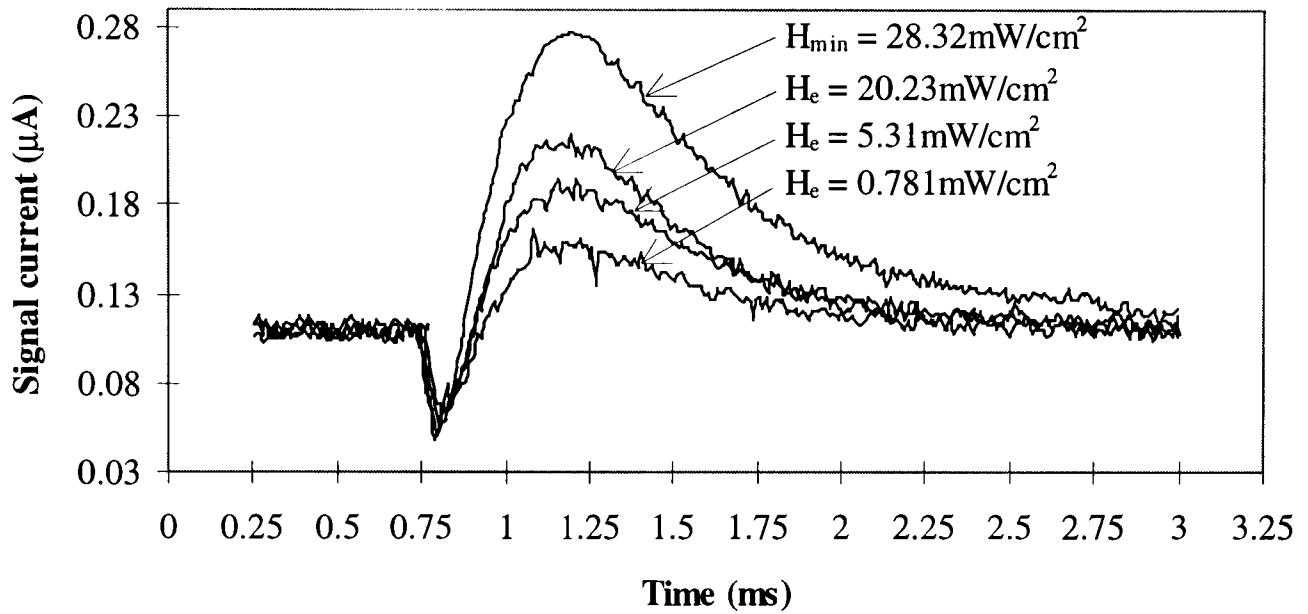
Detectivity experiments in a-Si:H were performed in the same manner as described in section 6.1(i) over the same range of electric fields. Figures 6.17 to 6.19 show the signal currents under varying levels of irradiance. It was noted that as in a-As<sub>2</sub>Se<sub>3</sub>, the level of irradiance required to produce a clean and repeatable signal ( $H_{min}$ ) decreased for an increase in applied electric field material. However, it could also be seen that  $H_{min}$  was of higher magnitude over all electric fields than for a-As<sub>2</sub>Se<sub>3</sub> indicating that the a-Si:H material was less responsive to illumination.

Figure 6.20 shows the relationship between responsivity and the applied electric field. It could be seen that an approximately linear relationship was observed for all levels of irradiance and electric field stated. However, it could be seen that under identical levels of irradiance and electric field as employed in the detectivity study of a-As<sub>2</sub>Se<sub>3</sub>, the responsivity of the a-Si:H was of smaller magnitude in all cases. The inferior responsivity meant that higher levels of irradiance were required to produce a clean and repeatable signal in this material. The fact that higher levels of irradiance and therefore incident power were required to produce a clean and repeatable signal, could possibly lead to a detrimental effect upon any photoelectric fatigue observed in the a-Si:H material. Table 6.3 summarises the results of the detectivity experimentation in a-Si:H and states the minimum light conditions required for the current system.

### 6.2.2 Production of steady state current

The investigation into the production of steady state current in a-Si:H was performed in the same manner as detailed in section 6.1(ii). Figure 6.21 shows the light conditions required to drive  $I_s$  into the steady state for an electric field of  $0.66 \times 10^5$  V/cm. According to this figure, steady state conditions could be achieved by the application of a light pulse of 880ns duration and an irradiance of  $2.62 \text{ W/cm}^2$ . The application of the light pulse resulted in a steady state  $I_s$  of approximately  $3.25 \mu\text{A}$  which was of the same magnitude as the steady state  $I_s$  obtained with the a-As<sub>2</sub>Se<sub>3</sub> material employing the same electric field and Au contact geometry but with a shorter light pulse duration's and lower levels of irradiance.

Table 6.4 summarises the steady state experimentation data. As in the case of detectivity, the responsivity ( $\gamma$ ) of the a-Si:H material was seen to be of a lower magnitude when compared with a-As<sub>2</sub>Se<sub>3</sub>. The lower value of  $\gamma$  of the a-Si:H material again led to the necessity of increasing the level of  $H_e$  and  $t_{ph}$  in order to achieve steady state  $I_s$  conditions over the range of electric fields specified. As stated previously, increased  $H_e$  and  $t_{ph}$  could have a detrimental effect upon possible photoinduced fatigue in the a-Si:H material. The study of photoinduced fatigue in a-Si:H formed the next series of experimentation to be performed.



**Figure 6.17** Typical photogenerated current pulses due to varying levels of irradiance,  $E=0.66 \times 10^5$  V/cm,  $t_{ph}=360$ ns.

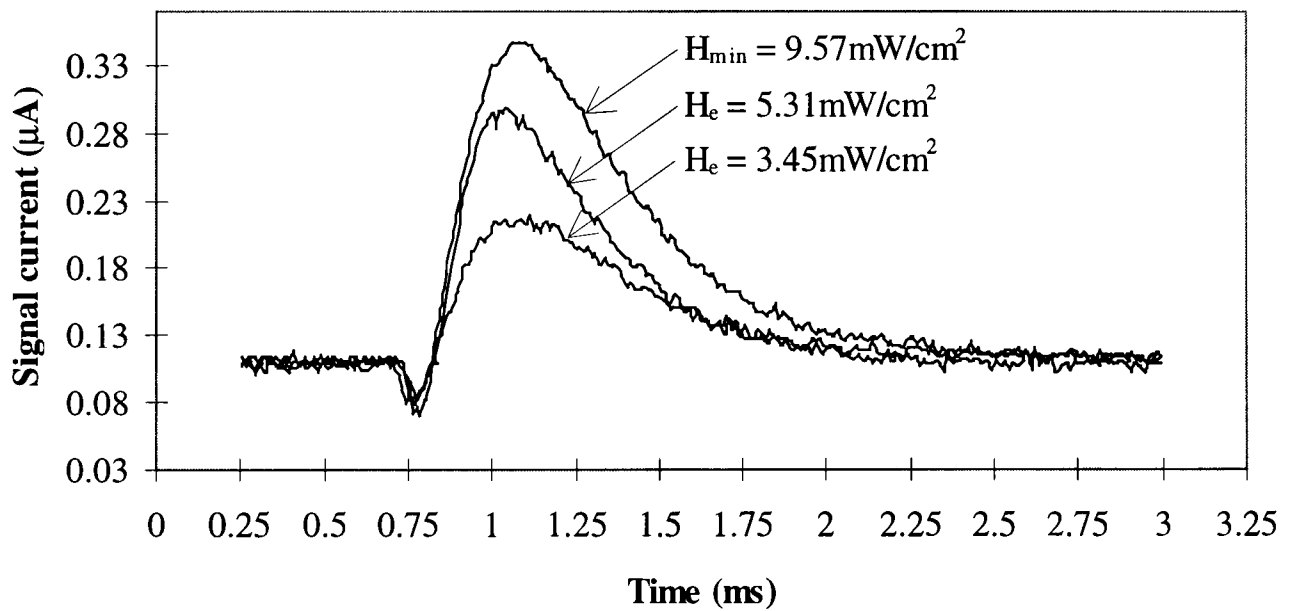


**Figure 6.18** Typical photogenerated current pulses due to varying levels of irradiance,  $E=1 \times 10^5$  V/cm,  $t_{ph}=360$ ns.

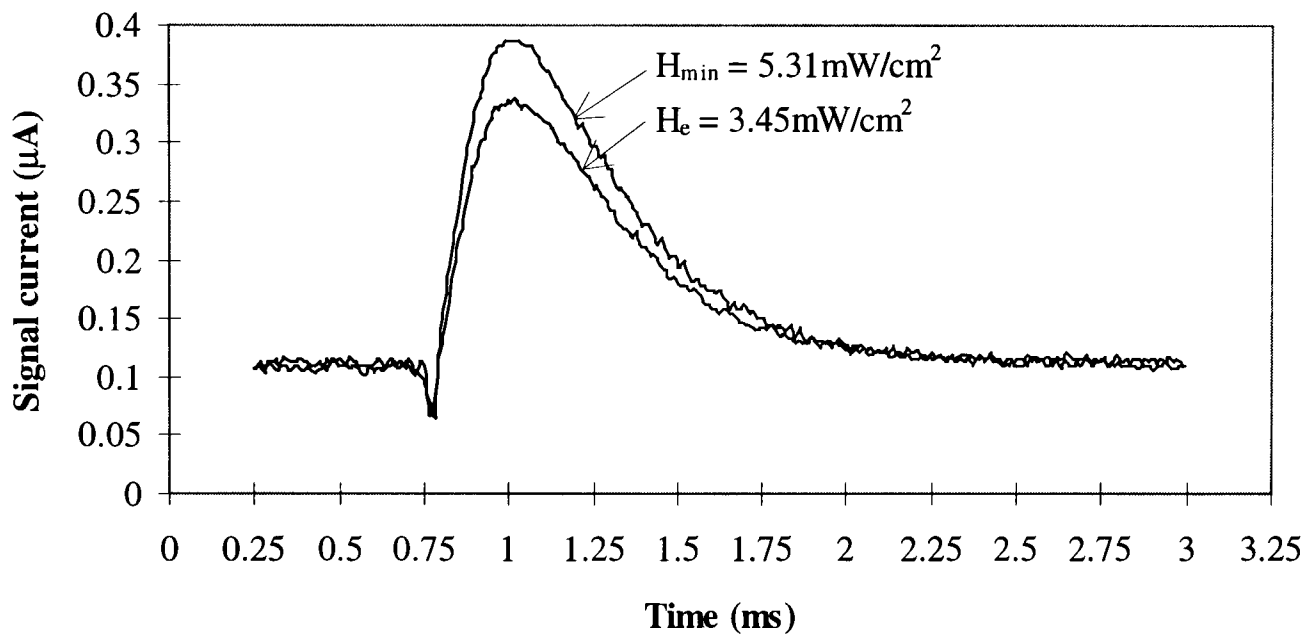


**Figure 6.19** Typical photogenerated current pulses due to varying levels of irradiance,  $E=1.33 \times 10^5$  V/cm,  $t_{ph}=360$ ns.

	Electric field $\times 10^5$ V/cm		
	0.66	1	1.33
Input energy to source $E_{in}$ (mJ)	2.11	1.25	1.012
Radiant intensity $I_e$ (W/sr)	1.19	0.4	0.23
Incident power $\phi_{ei}$ (mW)	11.61	3.93	2.17
Irradiance $H_{min}$ (mW/cm <sup>2</sup> )	28.32	9.57	5.31
Light pulse half time $t_{ph}$ (ns)	360	360	360
Peak signal current $I_s$ (nA)	277.5	346.8	337.23
Average dark current $I_d$ (nA)	112.69	107.27	111.95
Signal response $R$ (nA)	164.8	239.53	225.28
Responsivity $\gamma$ ( $\mu$ A/W)	14.19	60.94	103.81

**Table 6.3** Summary of detectivity experimentation showing minimum light conditions for the current system.

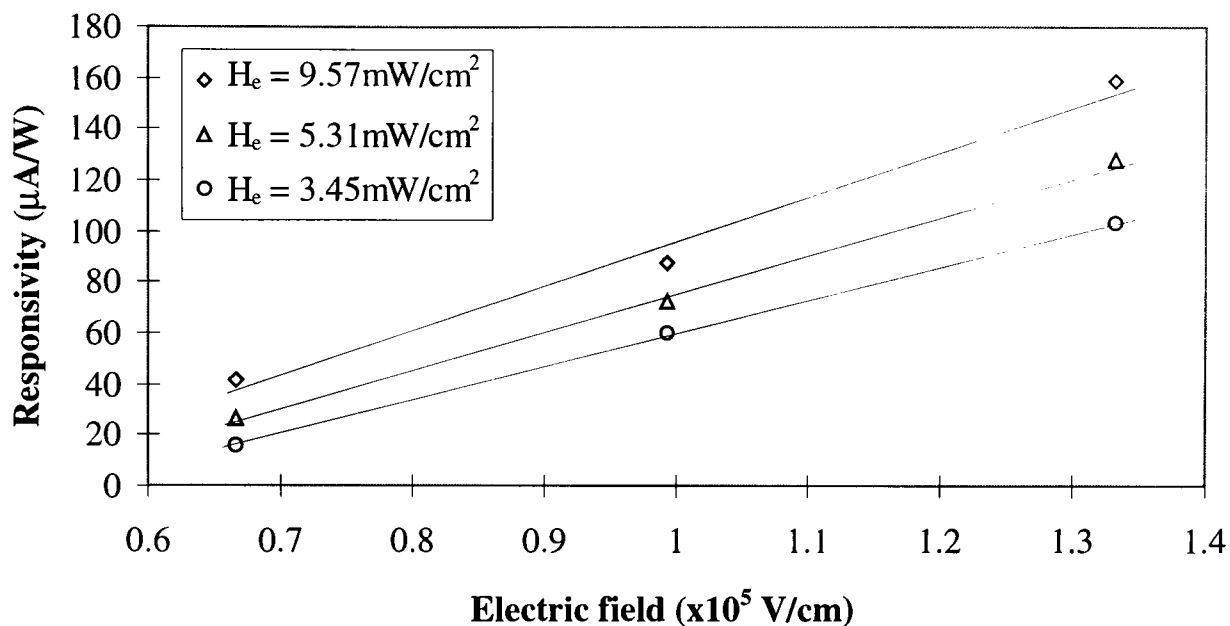


**Figure 6.20** Graph showing linear relationship between responsivity and electric field over a range of irradiance.

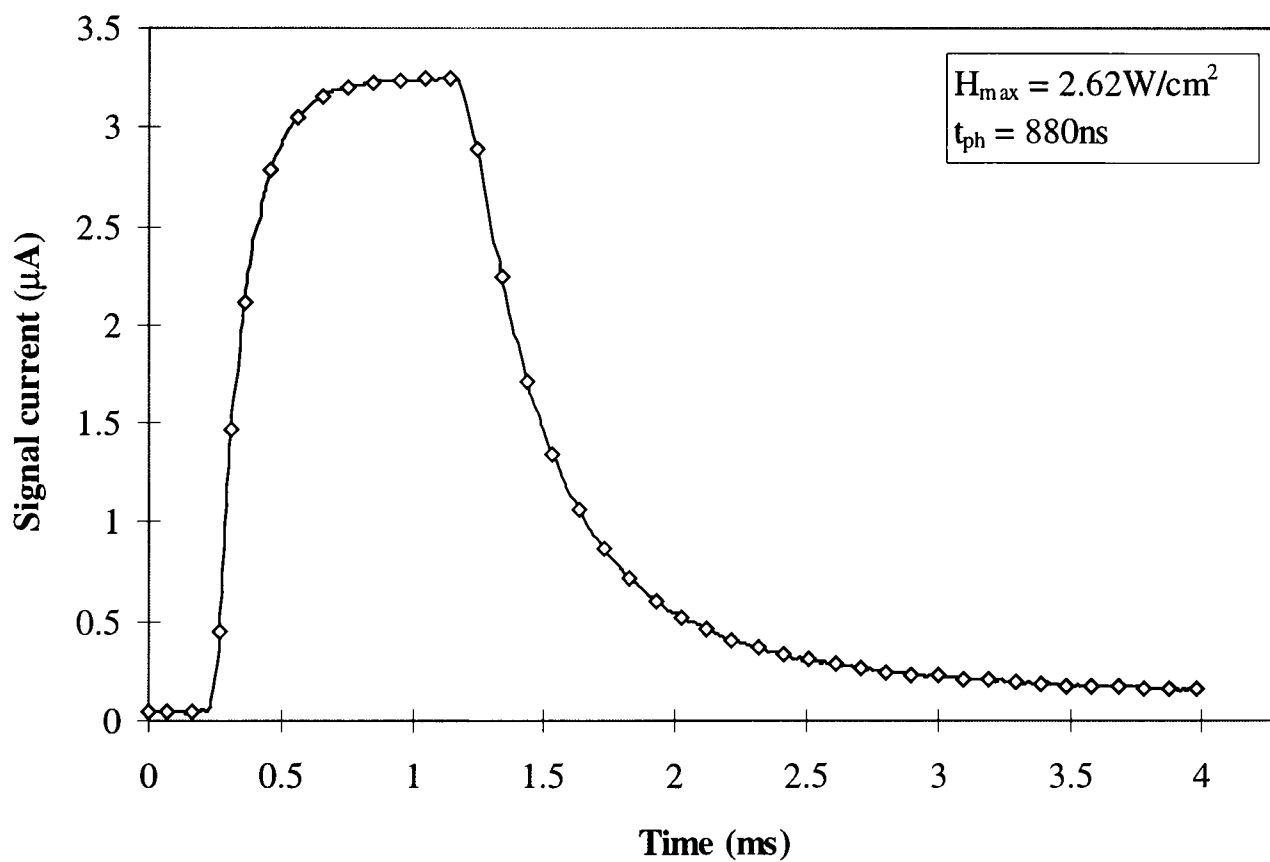


**Figure 6.21** Typical steady state photocurrent for a-Si:H,  $E = 0.66 \times 10^5$  V/cm.

### 6.2.3 Establishment of maximum operating speed by the determination of the effects of photoinduced fatigue.

As with the a-As<sub>2</sub>Se<sub>3</sub> material, the first tests to be performed in establishing the maximum operating speed of the a-Si:H material was to observe the signal response at FRR's from 20Hz to 100Hz in 20Hz increments. Figure 6.22 shows the results of this process for an electric field of  $1.33 \times 10^5$  V/cm. It was noted that the mean signal response over the 30 minute test period was far more stable at all FRR's than the a-As<sub>2</sub>Se<sub>3</sub> material. A large initial decay was observed in the first minute of the experiment, but after this initial decay, the mean signal response for all FRR's stabilised and no further deterioration of the signal response was observed.

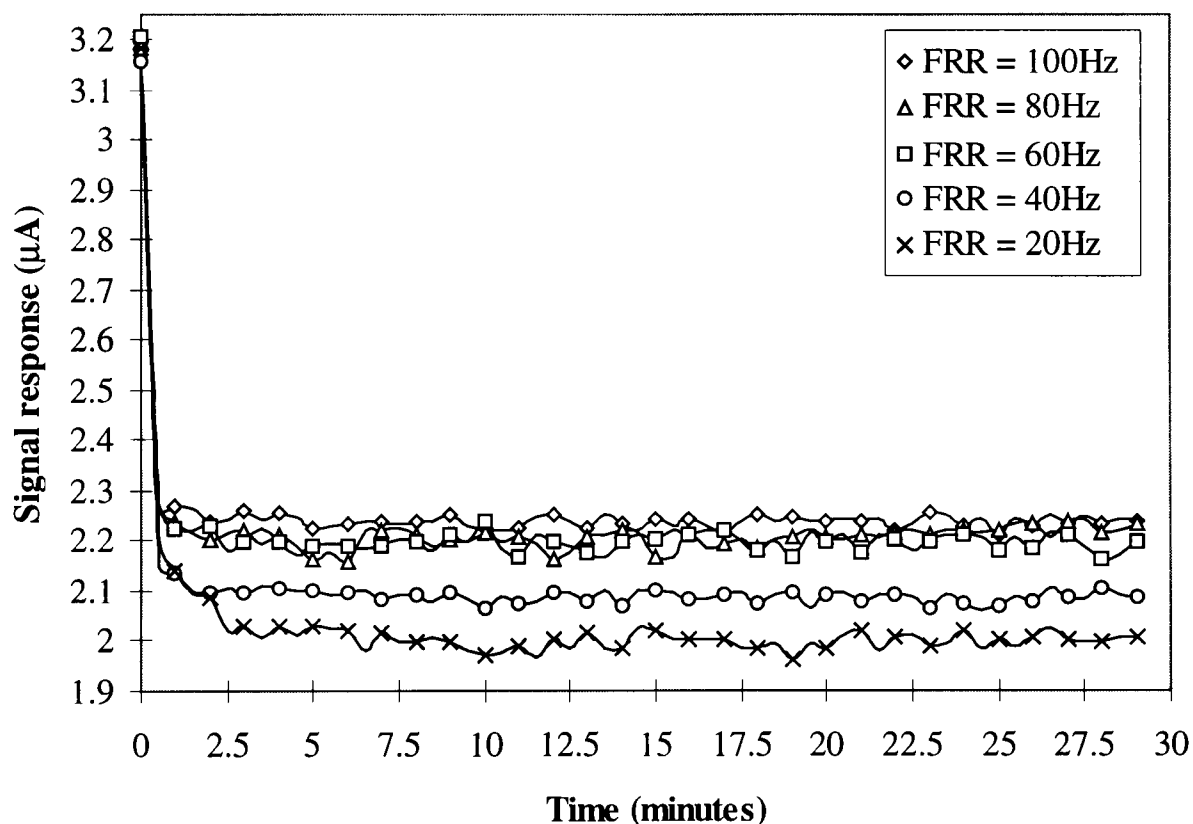
A feature of the mean signal responses not seen in the a-As<sub>2</sub>Se<sub>3</sub> material was an apparent increase in the magnitude of the mean signal response with an associated increase in FRR. In order to ascertain if the apparent increase in mean signal response was repeatable, the experiment was performed a further two times. The results of this process can be seen in figure 6.23. It could be seen that although there was some variation in the mean signal response for identical flash repetition rates (typically <60nA), the apparent increase in mean signal response was repeated.

Figure 6.24 shows  $I_d$  associated with figure 6.22. The ambient temperature was within a few °C for all test runs. It could be seen that  $I_d$  increased with time over all FRR's which was the opposite effect observed in a-As<sub>2</sub>Se<sub>3</sub>. The magnitude of  $I_d$  also appeared to increase with an increase in FRR. In order to see if the apparent increase in  $I_d$  was repeatable, the mean value of  $I_d$  was calculated for all FRR's over each of the three test runs previously described. The results of this process can be seen in figure 6.25. From figure 6.25 it could be seen that the increase in  $I_d$  was repeatable over all FRR's.

Figures 6.26 and 6.27 show the normalised relaxation curves for the varying FRR's. The relaxation curves were taken from the photogenerated current pulses sampled at  $t=29$ mins for all FRR's. Figure 6.26 demonstrated that the relaxation curves decayed at a constant rate up until approximately  $t=0.75$ ms after which point the relaxation curves decayed at differing rates. The time at which the rate of change of the relaxation curves started to decay at differing rates was determined by the use of a

	Electric field $\times 10^5$ V/cm		
	0.66	1	1.33
Input energy to source $E_{in}$ (mJ)	54.08	35.7	25.56
Radiant intensity $I_e$ (W/sr)	110.7	56.61	29.3
Incident power $\phi_{ei}$ (W)	1.07	0.54	0.28
Irradiance $H_{max}$ (W/cm <sup>2</sup> )	2.62	1.33	0.69
Light pulse half time $t_{ph}$ (ns)	880	880	880
Peak signal current $I_s$ ( $\mu$ A)	3.24	3.24	3.24
Average dark current $I_d$ (nA)	44.78	39.53	35.7
Signal response $R$ ( $\mu$ A)	3.2	3.2	3.21
Responsivity $\gamma$ ( $\mu$ A/W)	2.98	5.84	11.3

**Table 6.4** Summary of steady state experimentation showing maximum light conditions for the current system.

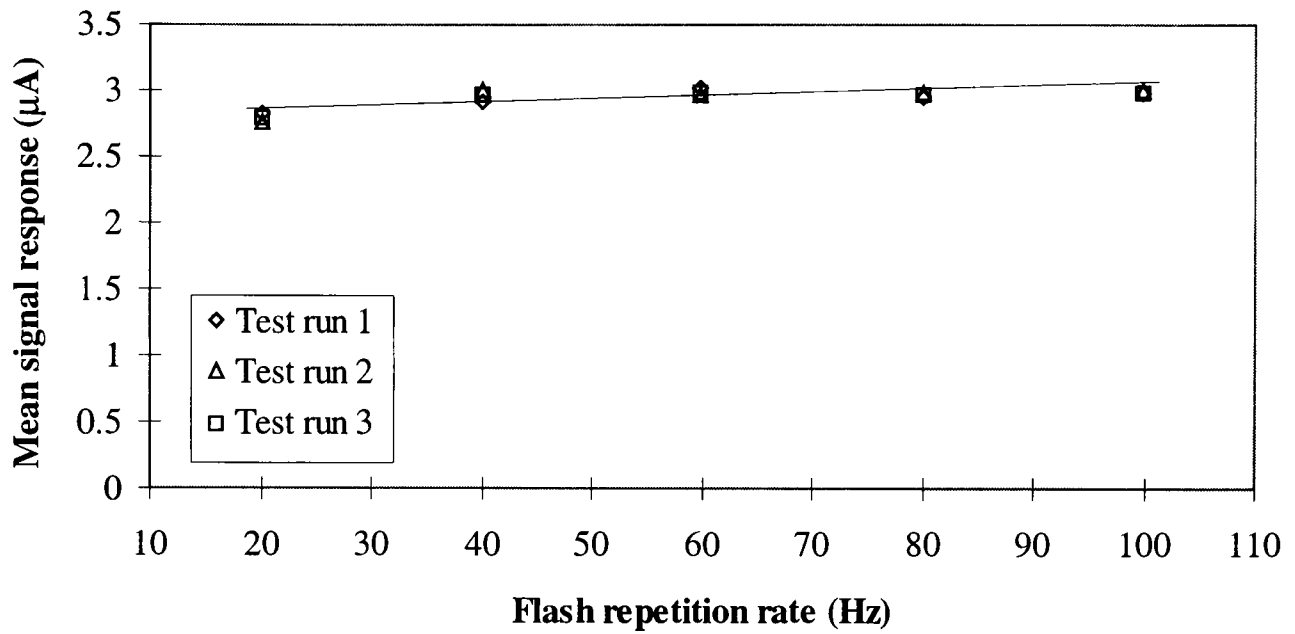


**Figure 6.22** Effect of increasing the FRR from 20 Hz to 100Hz in increments of 20Hz for  $E=1.33 \times 10^5$  V/cm,  $H_e=693 \text{mW/cm}^2$ ,  $t_{ph}=880 \text{ns}$ .

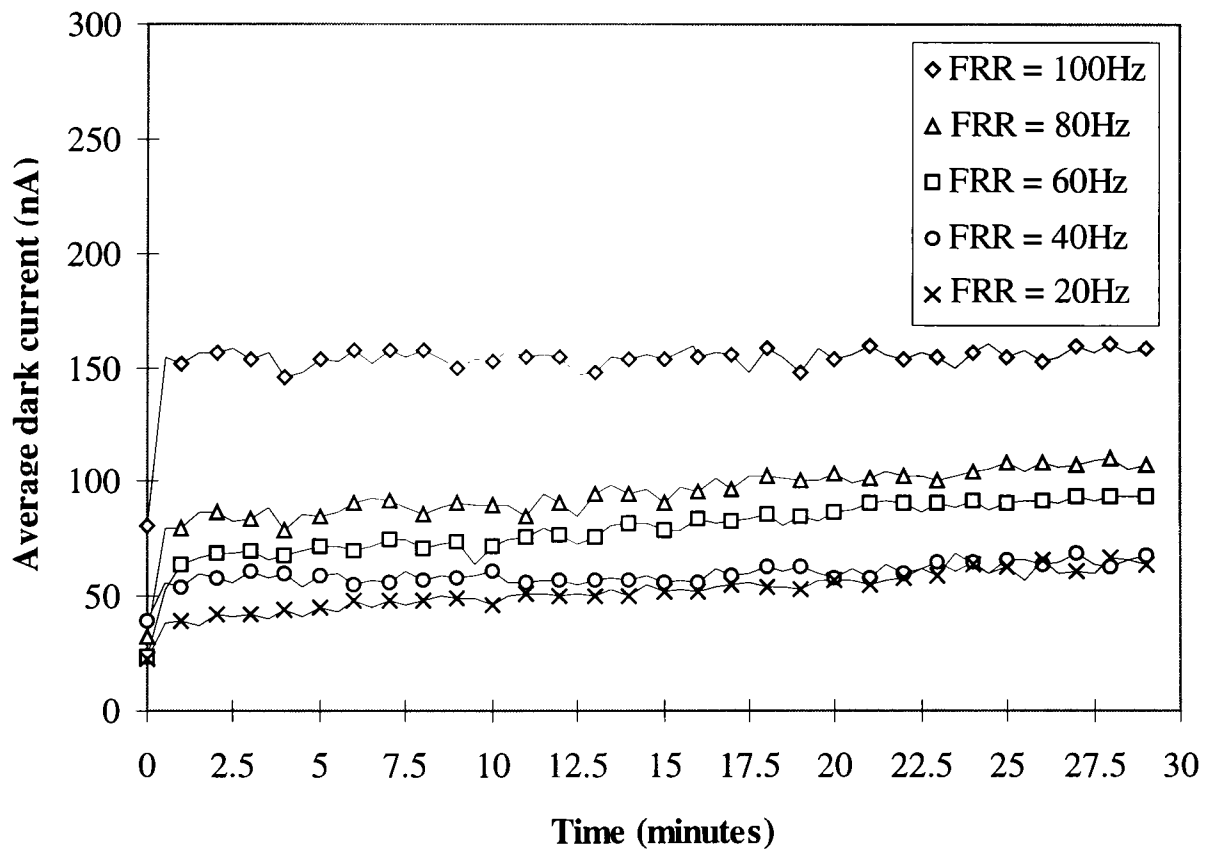
lookup table containing the interpolated differentiated data set. It could be seen that the higher the FRR, the slower the relaxation curve decayed in the  $t > 0.75\text{ms}$  time regime. Figure 6.27 shows a 'magnification' of the relaxation curves in the last 1ms of the experiment. It could be seen that the rate of decay of the relaxation curves was dependant upon the FRR, the differences in magnitude between the relaxation curves being very similar to the values of  $I_d$  shown in figure 6.24.

Figure 6.27 demonstrated that at times greater than 0.75ms  $I_s$  was of a higher magnitude for faster FRR's. This had the effect that on each successive light pulse issued, the signal response was seen to increase due to the effective increase in  $I_d$ . The difference in magnitude between  $I_d$  at the various rates of FRR were found to be in reasonable agreement with the differences in signal response observed over the range of FRR. Thus the increase in signal response observed over the 30 minute test period was attributed to the increase in  $I_s$  observed over the same period. The increase in magnitude of  $I_d$  was in turn attributed to the fact that  $I_s$  was unable to return to its original value prior to a light pulse being issued due to the FRR being greater than the relaxation time of the a-Si:H material. This issue is discussed further in chapter 7.

From the steady state experimentation previously undertaken, it had been found that for  $H_{\text{max}}=693\text{mW/cm}^2$  and  $t_{\text{ph}}=880\text{ns}$ , a steady state  $I_s$  of approximately  $3.25\mu\text{A}$  could be produce for an electric field of  $1.33 \times 10^5 \text{ V/cm}$ . It could be seen from figure 6.22 that at  $t=0$  the magnitude of the signal response was at approximately steady state conditions. The data point at  $t=0$  relates to the first light pulse to be issued in the test run which was a single light pulse recorded manually as previously described. As the light pulse associated with  $t=0$  was a single light pulse, no fatigue was observed and the magnitude of the signal response was approximately at steady state conditions. Once the data at  $t=0$  had been recorded, the 100Hz pulse train was applied to the sample and a current pulse was recorded every 30s, thus 3000 light pulses were issued in the interval between the reading at  $t=0$  and the reading taken at  $t=30\text{s}$ . Figure 6.22 demonstrated that the magnitude of the signal responses at  $t=30\text{s}$  was approximately 900nA less that at  $t=0$ . The increase in  $I_d$  as shown in figure 6.24 did not account for the large decrease in the signal response at times greater than  $t=0$ , so the deterioration of the signal response was attributed to the effects of photoinduced fatigue which are discussed further in chapter 7.



**Figure 6.23** Effect of varying flash repetition rate on mean signal response.  
 $E=1.33 \times 10^5$  V/cm,  $H_e=693$  mW/cm<sup>2</sup>,  $t_{ph}=880$  ns.



**Figure 6.24** Average dark currents for a range of FRR,  $E=1.33 \times 10^5$  V/cm,  
 $H_e=693$  mW/cm<sup>2</sup>,  $t_{ph}=880$  ns.

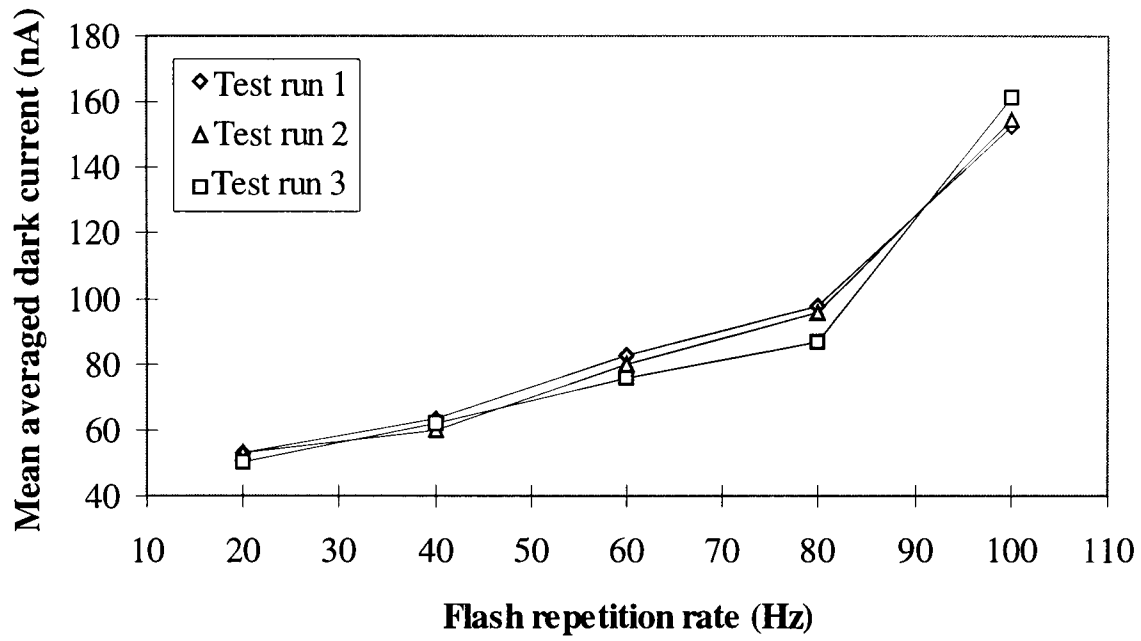


**Figure 6.25** Graph showing increase in mean average dark current due to an increase in FRR.  $E=1.33 \times 10^5$  V/cm,  $H_e=693$  mW/cm<sup>2</sup>,  $t_{ph}=880$  ns.

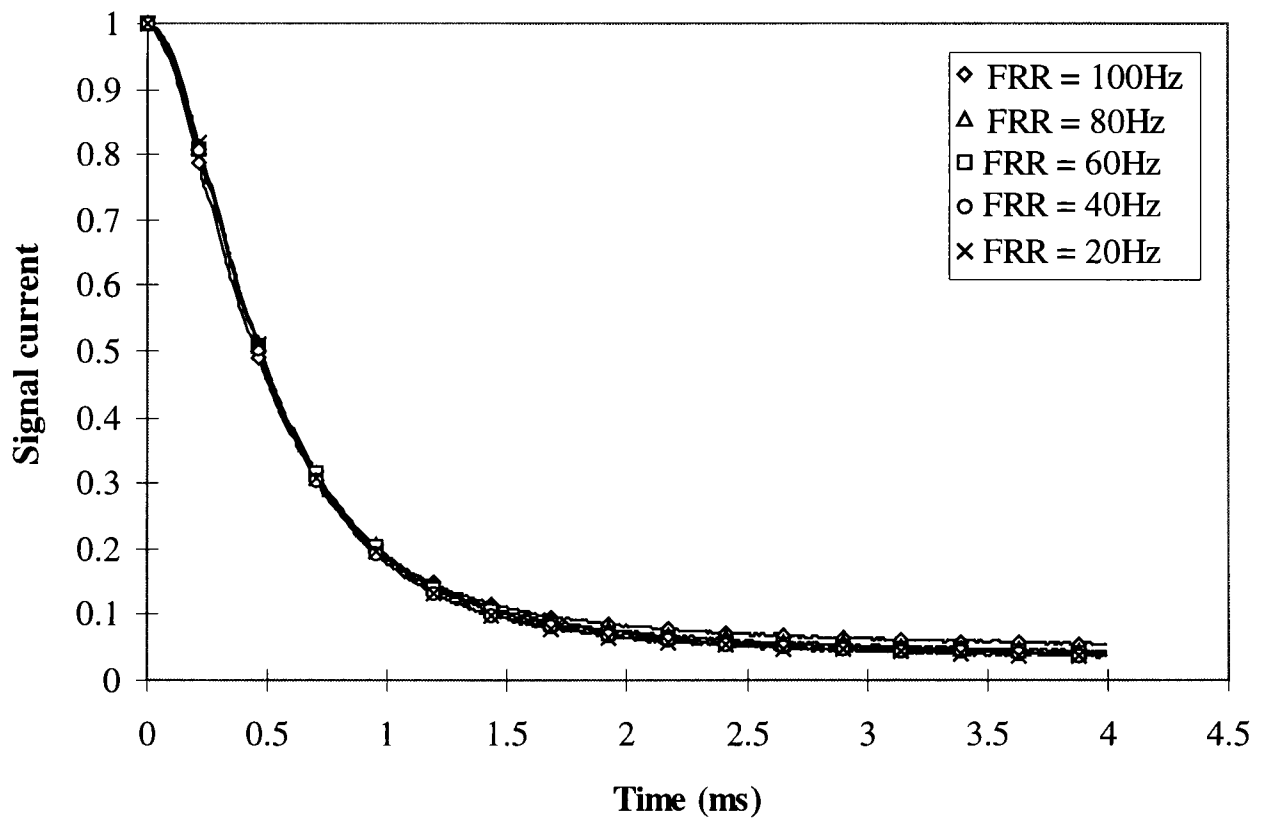


**Figure 6.26** Normalised relaxation curves due to varying rates of FRR.  $E=1.33 \times 10^5$  V/cm,  $H_e=693$  mW/cm<sup>2</sup>,  $t_{ph}=880$  ns.

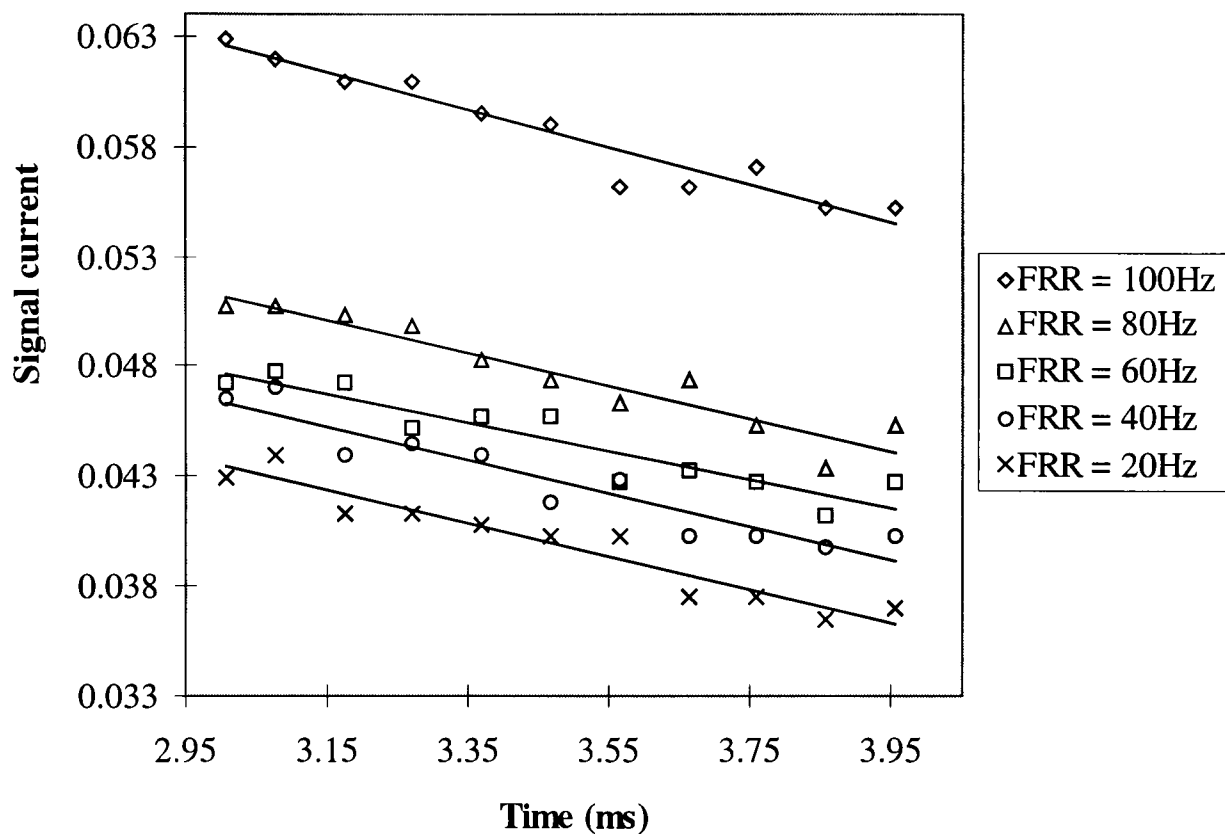


Figure 6.27 Normalised relaxation curves due to varying rates of FRR over last 1ms of experiment.  $E=1.33 \times 10^5$  V/cm,  $H_e=693$  mW/cm<sup>2</sup>,  $t_{ph}=880$  ns.

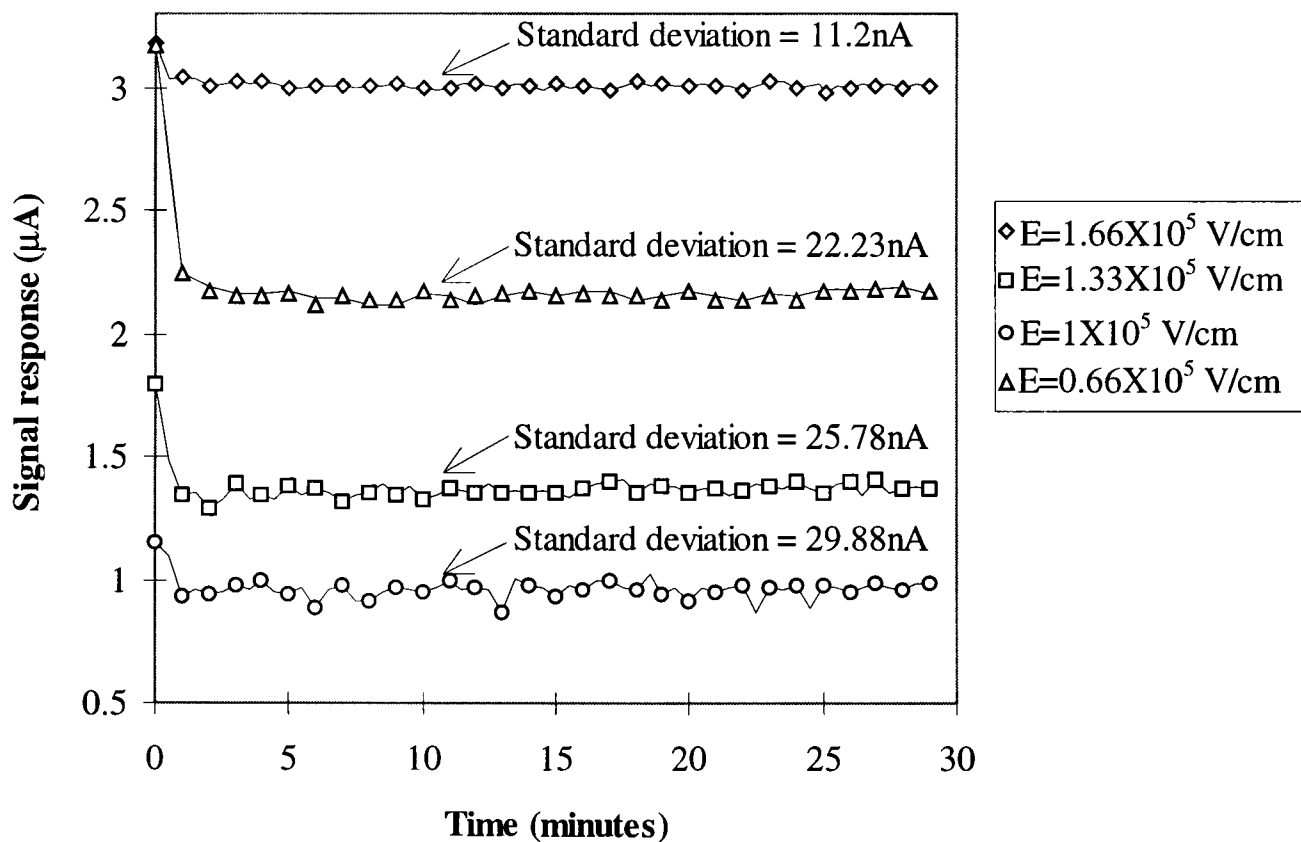


Figure 6.28 Signal response due to varying levels of electric field, FRR=100Hz,  $H_e=693$  mW/cm<sup>2</sup>,  $t_{ph}=880$  ns.

The next experiments to be performed were to establish the effect of changing the electric field on the signal response. Figure 6.28 shows the result of this process. It should be noted that again a large decay of the signal response in the first 30s of the test period for all electric fields was observable. It could also be seen that the lower electric fields produced less photocurrent which was as would be expected. However, an increase in standard deviation was also observed at lower levels of electric field. This was attributed to the fact that the peak signal response had moved significantly away from the steady state due to the decreased production of photocurrent caused by the lower levels of electric field. It was shown previously that the signal response became more sensitive to changes in  $H_e$  as the signal response was moved away from the steady state. This would have the effect that any small fluctuations in  $H_e$  caused by instability in the light source would lead to a higher standard deviation at lower electric fields.

As OPT measurements rely upon variation in  $H_e$  and therefore signal response in order to establish quantitative and qualitative data, it was essential to have as small as possible standard deviation in the signal response. In order to see if an improvement in standard deviation could be achieved, further test runs were performed at an electric field of  $1.66 \times 10^5$  V/cm, a typical signal response of which can be seen in figure 6.28. The magnitude of the signal response was seen to increase with the increase in electric field. The increased production of photocurrent had two positive effects upon the signal response. Firstly, as also seen in a- $As_2Se_3$ , the higher electric fields seem to decrease the amount of photoelectric fatigue observed in the signal response. Secondly, the increase in signal response moved the peak signal response closer to the steady state which had the effect of reducing the standard deviation by approximately 50% over the 30 minute test period when compared to an electric field of  $1.33 \times 10^5$  V/cm. Both of these observations suggested that the a-Si:H sample should be operated at the higher value of electric field.

The associated values of  $I_d$  for the signal responses shown in figure 6.28 are shown in figure 6.29. As with the values of  $I_d$  shown in figure 6.24, a sharp increase in  $I_d$  was observed in the interval  $t=0$  to  $t=30s$  as previously described. The average dark currents were seen to increase with time also as previously described. As also

observed in a-As<sub>2</sub>Se<sub>3</sub>, the magnitude of  $I_d$  was seen to increase with an increase in applied electric field.

The results of the experimentation into the effects of photoinduced fatigue in a-Si:H have shown that the material can be operated at speeds required for OPT applications (100Hz), and that a repeatable and stable signal response was achievable. The effects of photoinduced fatigue upon the suitability of the a-Si:H material for application in OPT are discussed in chapter 7.

#### 6.2.4 Establishment of pipeline limits.

Now that the a-Si:H material had been shown to exhibit a stable and repeatable signal response at FRR's up to 100Hz, experimentation focused on establishing the maximum separation that could be achieved between a pipeline full of water and an empty pipeline for an electric field of  $1.66 \times 10^5$  V/cm and the maximum FRR of 100Hz. The aim of the experimentation was to determine if the a-Si:H material was sensitive enough to distinguish between a pipeline full of water and an empty pipeline, and give sufficient resolution for possible application in the measurement of air bubble/plug flow. Figure 6.30 shows the maximum separation between the full and empty pipelines achievable with the a-Si:H material. The maximum separation in signal response ( $R_{max}$ ) was achieved by positioning the peak  $I_s$  just under the steady state by reducing  $H_e$  to  $278.6 \text{ mW/cm}^2$  and  $t_{ph}$  to 340ns. This procedure resulted in  $R_{max}$  being equal to  $1.34 \mu\text{A}$  in magnitude which resulted in an increase in  $R_{max}$  of 34% over the a-As<sub>2</sub>Se<sub>3</sub> material.

Now that  $R_{max}$  had been established the limits of the full and empty pipelines had to be established. All tomographic experimentation would then relate to the established pipeline limits. The pipeline limits were established by performing the test runs for the full and empty pipelines four times in order to establish an accurate mean value for the pipeline limits. The standard deviation for the four test runs could then be averaged to determine a mean standard deviation. Figure 6.31 shows the results of the four test runs for the full and empty pipelines. From the results it could be seen that good reproducibility of the signal response was achieved over the four test runs for both the full and empty pipelines. Table 6.5 summarises the test run data.

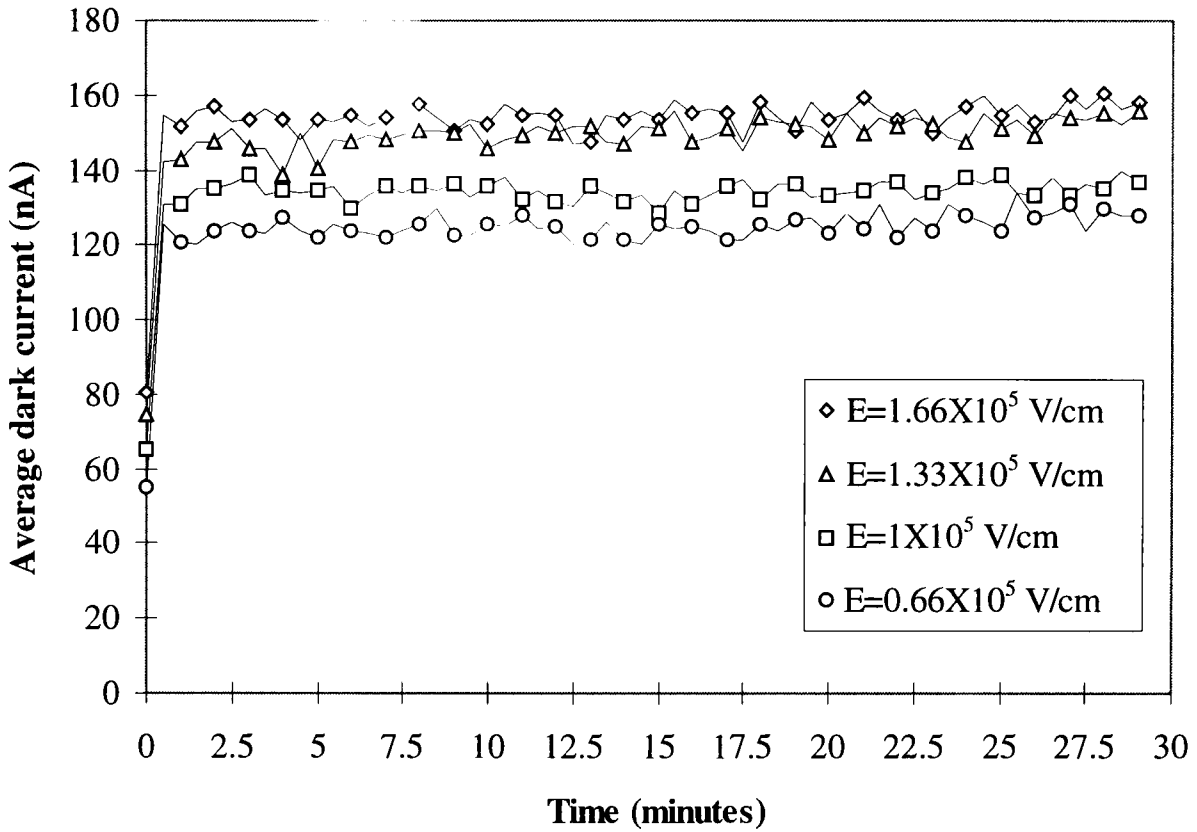


**Figure 6.29** Average dark currents over a range of electric field, FRR=100Hz,  $H_e=693\text{mW/cm}^2$ ,  $t_{ph}=880\text{ns}$ .

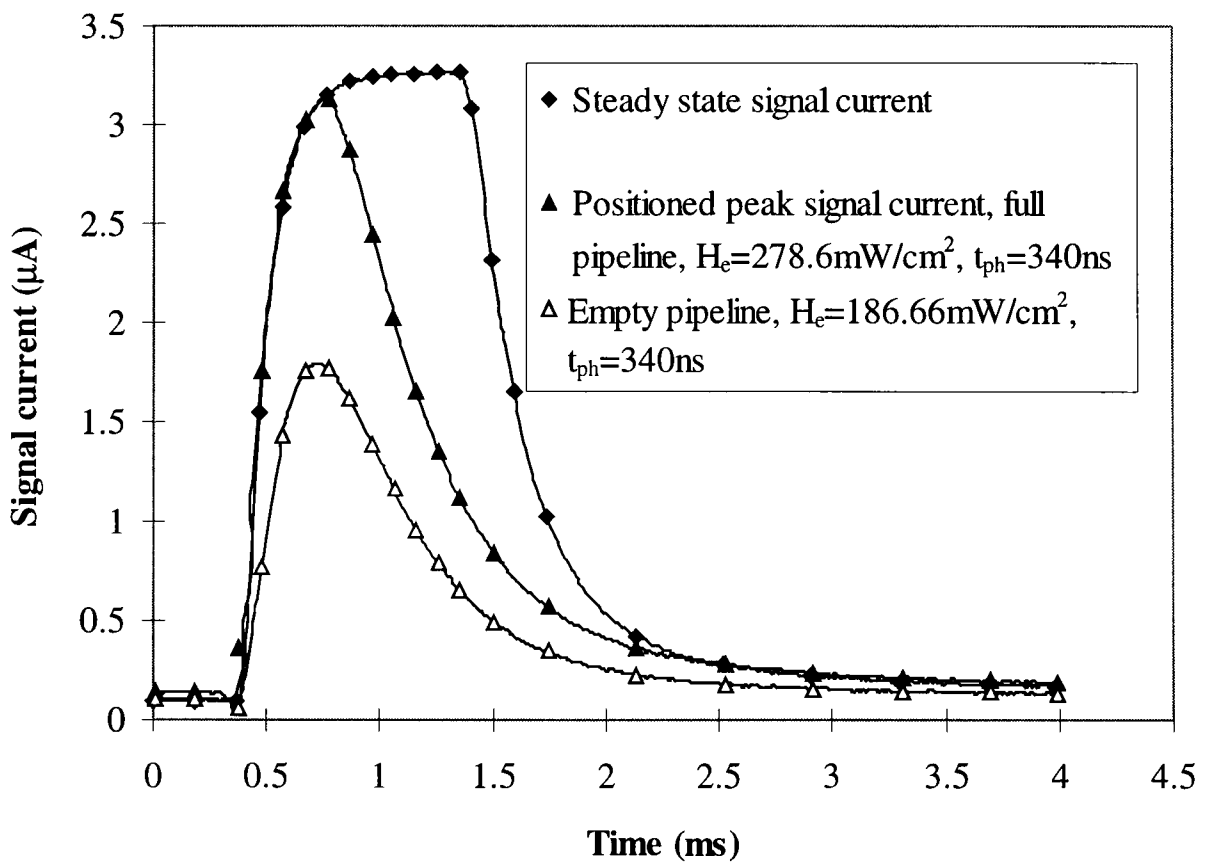


**Figure 6.30** Maximum separation between full and empty pipelines,  $E=1.66 \times 10^5$  V/cm, FRR=100Hz.

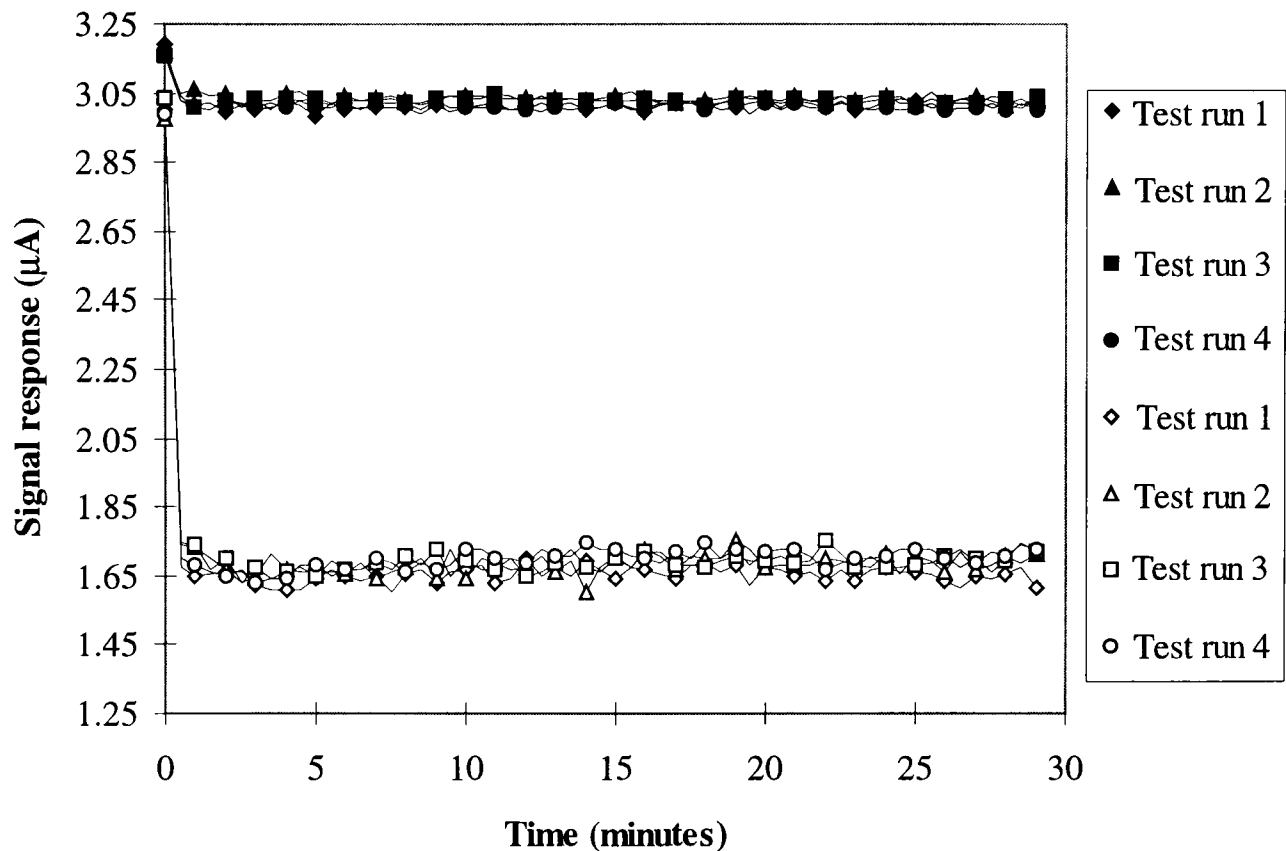


**Figure 6.31** Maximum separation between full and empty pipelines. Solid data markers refer to the full pipeline, empty data markers refer to the empty pipeline.  $E=1.66 \times 10^5$  V/cm, FRR=100Hz,  $H_e=278.6 \text{ mW/cm}^2$  (full pipeline),  $H_e=186.66 \text{ mW/cm}^2$  (empty pipeline),  $t_{ph}=340 \text{ ns}$  in both cases .

Pipeline	Full				Empty			
	1	2	3	4	1	2	3	4
Peak signal current ( $\mu\text{A}$ )	3.13	3.18	3.18	3.16	1.76	1.79	1.8	1.81
Mean dark current (nA)	122.1	149.9	151.6	151.4	107.5	110.4	110.9	112.8
Mean signal response ( $\mu\text{A}$ )	3.01	3.03	3.03	3.01	1.65	1.68	1.69	1.71
Standard deviation (R) (nA)	12.39	9.04	8.09	8.89	21.81	27.72	24.09	23.84
Standard deviation ( $I_d$ ) (nA)	6.56	4.94	6.22	3.46	4.06	5.31	4.78	2.72

**Table 6.5** Test data for the establishment of pipeline limits

Pipeline limits	Full	Empty
Signal response ( $\mu\text{A}$ )	3.02	1.68
Standard deviation (nA)	9.61	24.36

**Table 6.6** Definitive limits for the full and empty pipelines.

From table 6.5 it was seen that the magnitude of the signal response was within 0.6% of the mean value of signal response averaged over the four test runs for the full pipeline and within 3% of the mean signal response for the empty pipeline. Table 6.5 also demonstrates that the standard deviation of the signal response for the full pipeline was typically less than 50% of the magnitude of standard deviation for the empty pipeline. The increase in standard deviation and variation in the mean signal response increases for the empty pipeline is due to the fact that the peak signal response was at a considerable distance from the steady state condition as can be seen in figure 6.30. This fact implied that the resolution of the measuring system would deteriorate at lower levels of irradiance.

Figure 6.33 shows the average dark currents for the four test runs previously described. The ambient temperature ( $T$ ) was  $22^{\circ}\text{C} \pm 0.5^{\circ}\text{C}$  for all test runs for both the full and empty pipelines. Although the dark current could be thought of as noise, the previous experiments showed that the mean value of  $I_d$  was typically within a few nA for all of the test runs performed, and that the standard deviation of  $I_d$  was also fairly stable over all of the test runs being in the order of approximately 4nA to 6nA in magnitude. The exception to this observation was test run 1 for the full pipeline in which the magnitude of  $I_d$  was approximately 20nA less in magnitude than the other three runs for the full pipeline. All test runs in the establishment of the pipeline limits were performed on the same day with the sample being allowed to rest in the dark for an hour between each test run. The only exception to this procedure was test run 1 for the full pipeline which was the first test run to be performed and the sample had not been used for a 48 hour period prior to the start of experimentation. The test results suggested that the longer period of dark rest resulted a smaller magnitude of  $I_d$  upon the commencement of experimentation due to the extended rest period allowing a greater number of charge carriers to be released from deep traps within the a-Si:H layer. All of the  $I_d$  responses shown in figure 6.33 were seen to increase slightly with time as previously described and at a constant rate for all test runs. Test run 1 for the full pipeline again was the exception to this observation. The  $I_d$  response for test run 1 was seen to increase in magnitude at a much faster rate than all other test runs and was seen to approach the magnitude of the other test runs for the full pipeline by the end of the experiment. In order to see if the reduction in  $I_d$  was repeatable, the sample was dark rested for 48 hours and the test for the full pipeline was re-run. Good comparison

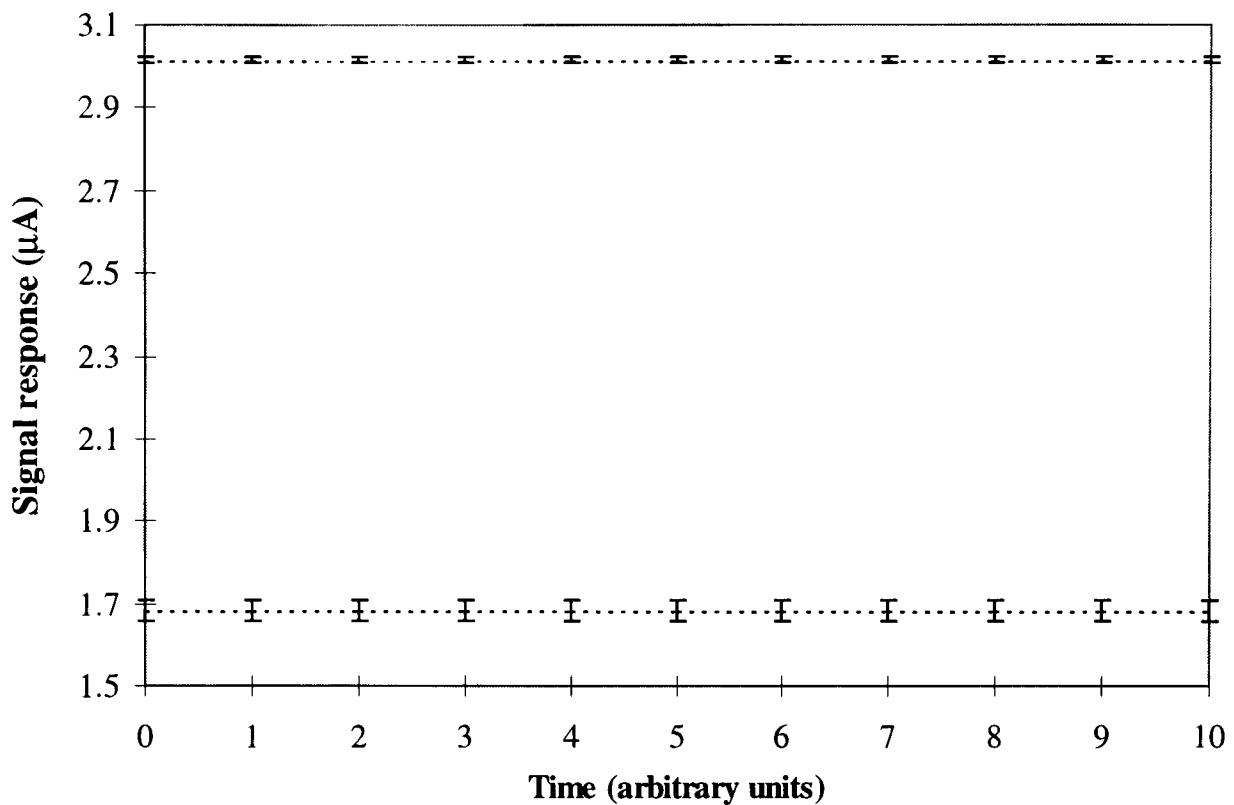
of the two test runs was achieved and  $I_d$  was shown to be of a lower magnitude after the extended rest period. The fact that  $I_d$  was of a lower magnitude after a longer rest period did not have a significant effect upon the signal response as the difference in dark current was in the order of 20nA. Thus the lower  $I_d$  encountered after an extended rest period was not considered to be significant in the operation of any potential tomographic device.

Table 6.5 shows that the magnitude of dark current encountered for the test runs upon the empty pipeline were approximately 40nA lower in magnitude over all test runs than for the full pipeline. This was attributed to the fact that the relaxation curves of the  $I_s$  pulses decayed at a faster rate than for the full pipeline due to the smaller magnitude of peak  $I_s$  as demonstrated in figure 6.30. This meant that  $I_d$  decayed to a lower magnitude over the same time period as the dark current for the full pipeline before the next light pulses was issued. This issue is discussed further in chapter 7.

Table 6.6 shows the definitive pipeline limits for the a-Si:H material. All future tomographic experimentation relate to these limits. The next experiments to be performed were to establish the signal response due to varying levels of water contained within the pipeline to determine the resolution of the system.

#### 6.2.5 Establishment of quantitative data

Now that the pipeline limits had been determined, experimentation focused on determining if the a-Si:H material was sensitive enough to distinguish between predetermined levels of water inserted into the tomographic prototypes, thereby obtaining quantitative data. Water was measured by height from the bottom internal surface of the pipeline. As good reproducibility of results had been previously determined over the 30 minute test period, the test period was reduced to 15 minutes with  $I_s$  being sampled every 15s. Water was initially added to the prototype at increments of 5mm with exception of the last reading to be taken at which point 4mm of water was added to completely fill the pipeline (internal pipeline diameter = 44mm).



**Figure 6.32** Pipeline limits for full and empty pipelines. Dashed lines refer to the mean signal response averaged over four test runs, error bars refer to the +/- standard deviation averaged over four test runs.

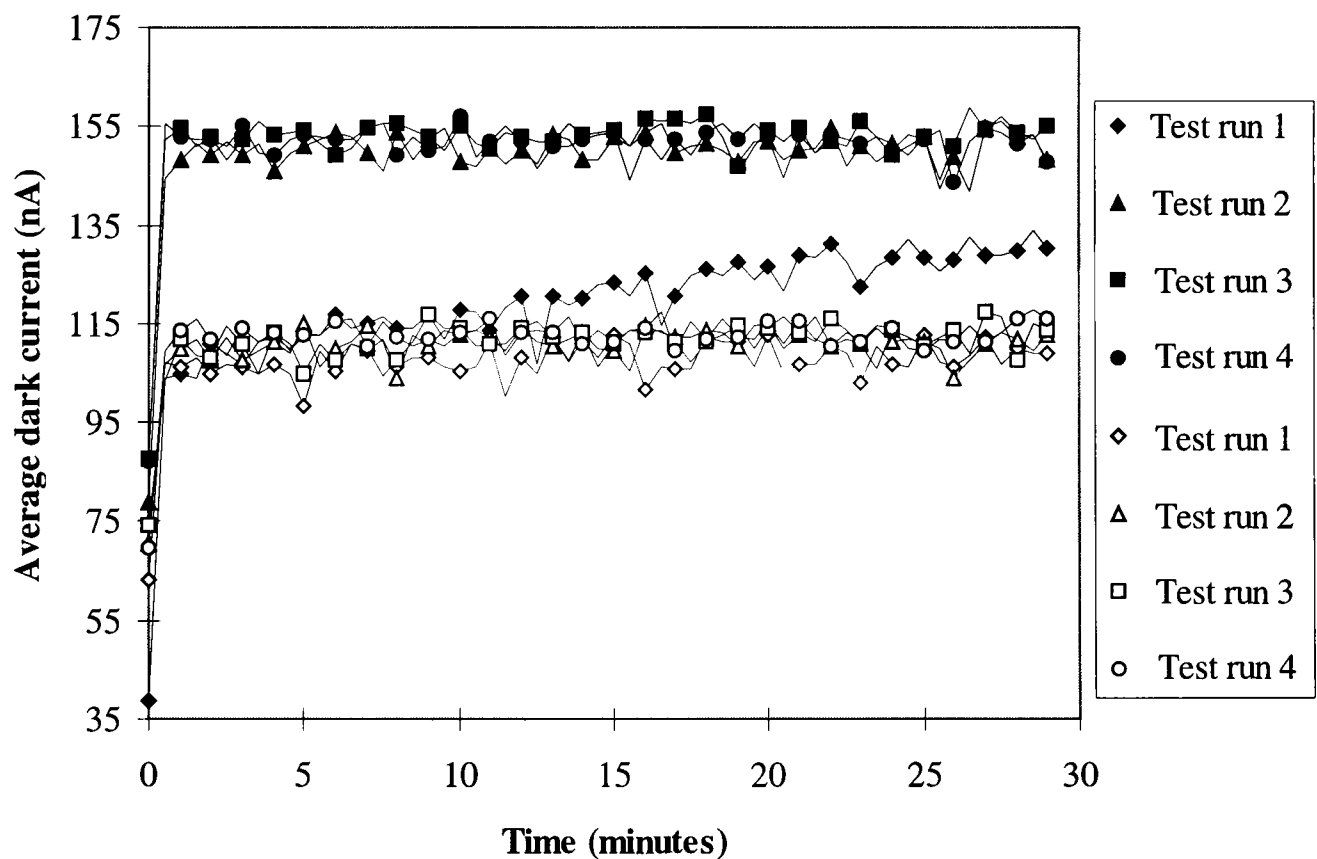


**Figure 6.33** Average  $I_d$  for full and empty pipelines. Solid data markers refer to the full pipeline, empty data markers refer to the empty pipeline,  $E=1.66 \times 10^5 \text{ V/cm}$ ,  $FRR=100\text{Hz}$ ,  $T=22^\circ\text{C} \pm 0.5^\circ\text{C}$ .

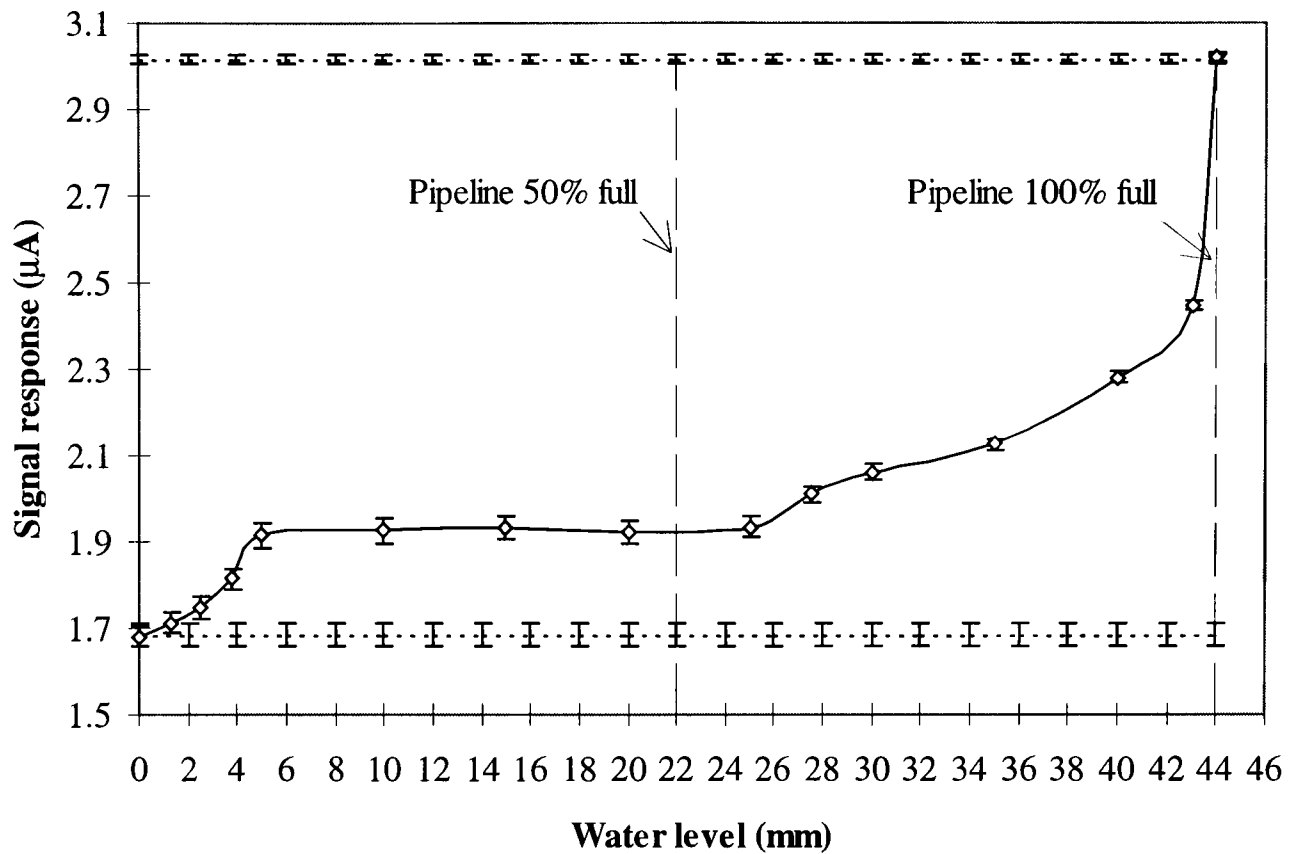


**Figure 6.34** Signal response due to varying levels of water. Each data point relates to the mean signal response averaged over three test runs for the specified water level. Error bars relate to the standard deviation averaged over the three test runs.  $E=1.66 \times 10^5$  V/cm, FRR=100Hz.

Water level (mm)	Mean signal response (µA)	Mean standard deviation (nA)
0	1.68	24.30
1.25	1.72	23.65
2.5	1.74	25.35
3.75	1.81	23.54
5	1.91	28.74
10	1.92	28.64
15	1.93	28.76
20	1.92	26.42
25	1.93	24.22
27.5	2.01	19.53
30	2.06	16.45
35	2.12	14.23
40	2.28	12.21
43	2.45	10.11
44	3.02	8.89

**Table 6.7** Summary of quantitative data

In order to obtain accuracy of results, three test runs were performed at each level of water. The signal response and standard deviation were then averaged over the three test runs. Water was then added in smaller increments until the smallest detectable and repeatable change in water level had been established. The results of this process can be seen in figure 6.34.

Figure 6.34 demonstrated that the sensitivity to changes in water level was not constant across the diameter of the pipeline, but exhibited large variation depending on the location of the water level within the pipeline. It could be seen that the areas of greatest sensitivity were located in the first 5mm and last 25mm of the pipeline where changes in water level of 1mm were accurately distinguishable. However, a 'flat' response was observable between the two regions of greatest sensitivity where 5mm changes in water level were not distinguishable. Further reduction in water level was not undertaken due to experimental difficulty in accurately measuring the water level height at increments of less than 1mm.

The variation in sensitivity was attributed to the curvature of the pipeline wall. The light passed through tomographic prototype did not undergo attenuation but was magnified by the effects of reflection/refraction due to the pipeline wall, thus the irradiance incident upon the sample surface increased for an increase in water level in the 0 to 5mm, and 25 to 44mm regions. In order to estimate the contribution of reflection/refraction upon the magnitude of signal response, a further test run was performed using a new prototype. The prototype was comprised of the same pipeline as previously employed, but the inside of the pipeline was painted matt black to minimise the effects of reflection/refraction as the light passed through the prototype. A 3mm diameter transparent window was left at the top and bottom of the pipeline to columnise the light as it passed through the prototype to the sample surface. The test runs for the full and empty pipeline were then repeated. The results of this process can be seen in figure 6.35.

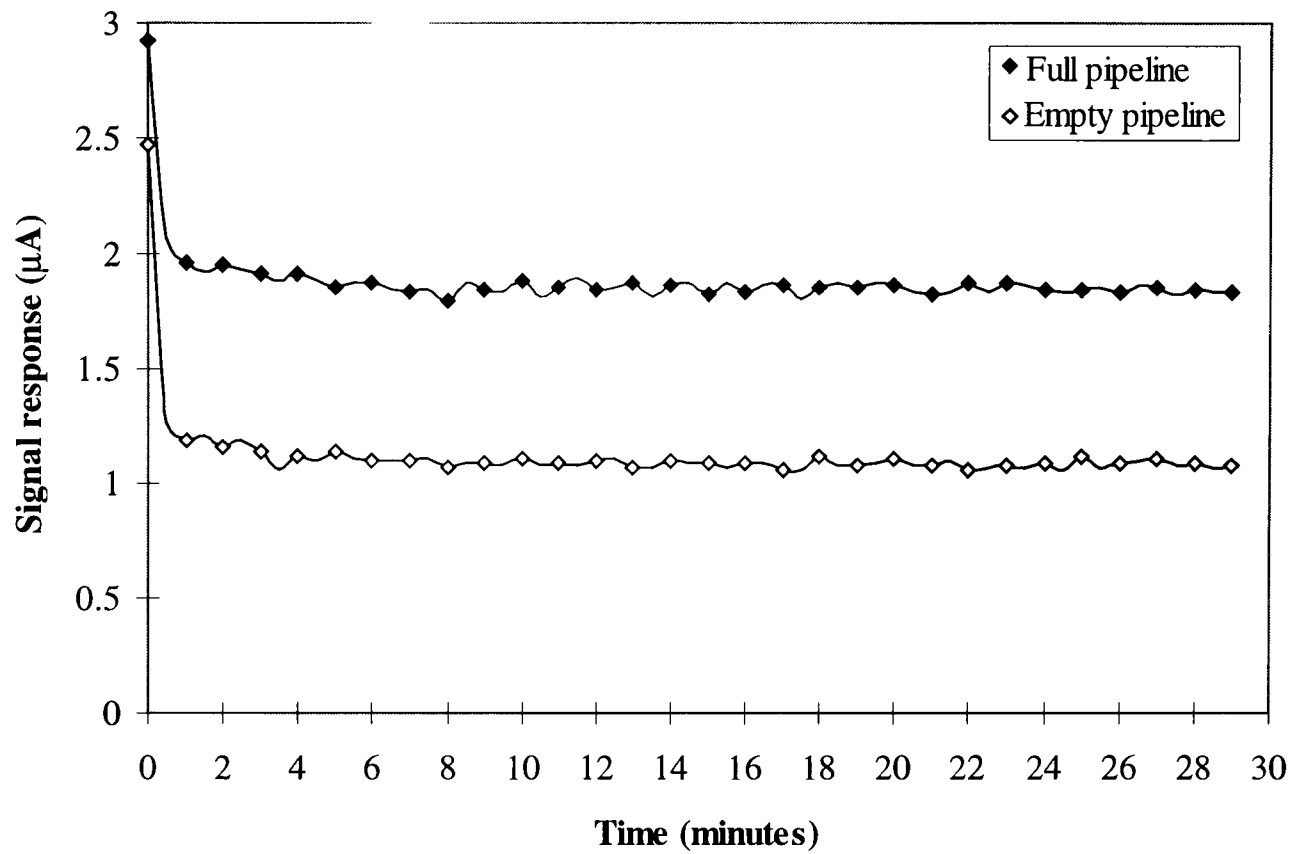


**Figure 6.35** Signal response due to columnised light beam.  $E=1.66 \times 10^5$  V/cm, FRR=100Hz.

It could be seen that the mean signal response for the columnised light beam was  $1.848\mu\text{A}$  which was approximately  $1.2\mu\text{A}$  less than for the clear pipeline. The signal response for the empty pipeline due to the columnised light beam was  $1.0844\mu\text{A}$  which was approximately  $600\text{nA}$  less than for the clear pipeline. Thus the separation between the full and empty pipelines was  $763\text{nA}$ . The results showed that although the magnitude of the signal response had been reduced due to less irradiance falling upon the surface of the sample as a result of columnising the light beam, the signal response for the full pipeline was still considerably higher in magnitude than the empty pipeline. Thus the irradiance incident on the sample surface was still being increased in magnitude by the action of reflection/refraction as the light passed through the prototype. The fact that the profile of the signal response through the pipeline as shown in figure 6.34 was due to reflection/refraction and not attenuation was deemed not to be problematic. Good repeatability of results was achieved over all water levels contained within the pipeline and changes in water level of  $1\text{mm}$  were detectable and repeatable in water levels of  $0\text{mm}$  to  $5\text{mm}$ , and  $25\text{mm}$  to  $44\text{mm}$ . The significance of the 'flat' response observed in water levels of between  $5\text{mm}$  and  $25\text{mm}$  on the a-Si:H materials suitability for application in air bubble or plug flow monitoring is discussed further in chapter 7.

#### 6.2.6 Establishment of qualitative data

The aim of the experimentation into the collection of qualitative data was to see if the a-Si:H material could distinguish between changes in fluid colour contained within the tomographic prototype. In this way, the a-Si:H materials suitability for possible application in batch monitoring of fluids could be established. The term 'fluid mix' refers to a mixture of water and a water based coloured concentrate added to the water in percentage increments measured by volume. Experimentation proceeded by setting the peak  $I_s$  to just under the steady state condition by the technique previously described for a pipeline full of water, i.e.  $0\%$  fluid mix. Coloured concentrate was added to the fluid mix initially in increments of  $10\%$  until the changes in fluid mix became indistinguishable, i.e. until the maximum fluid mix had been established. Coloured concentrate was then added in smaller percentage increments depending on the sensitivity of the signal response.

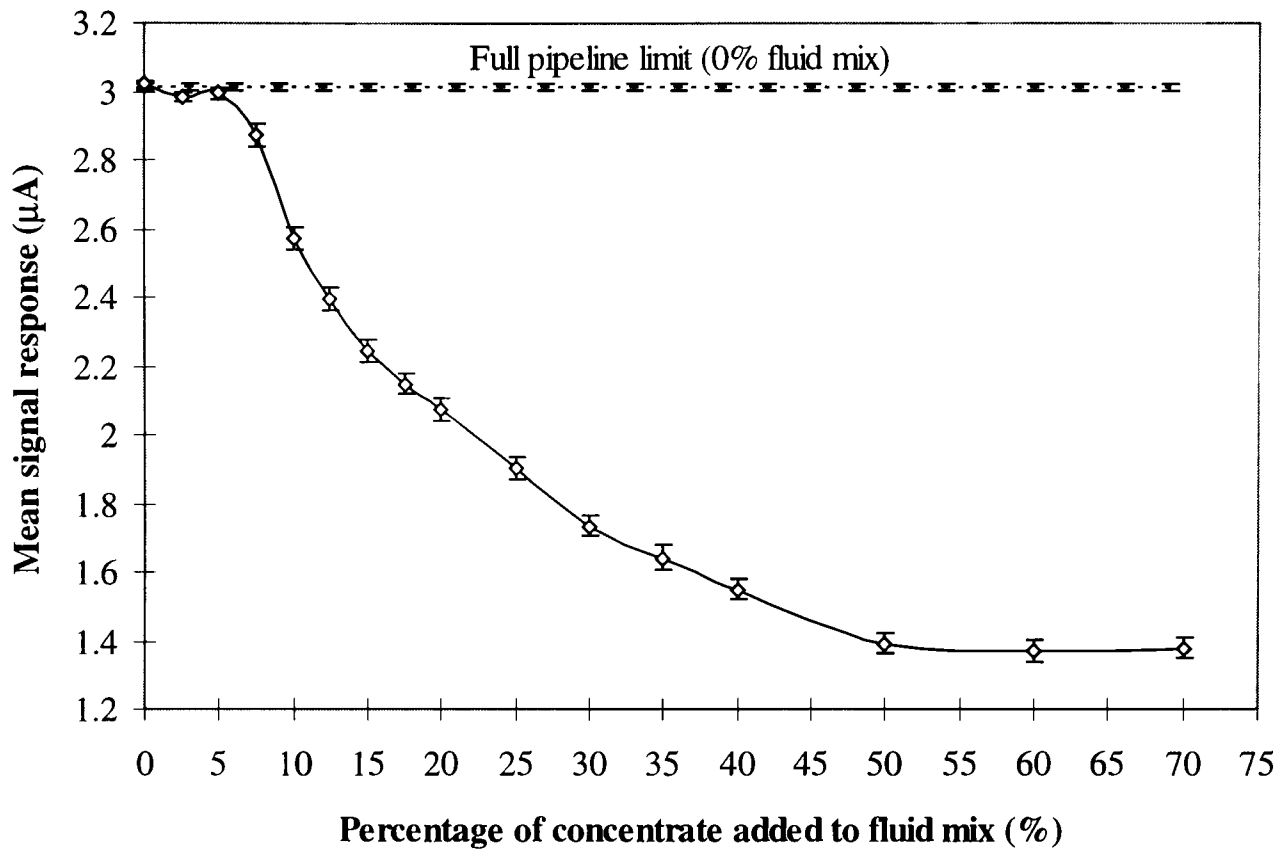


**Figure 6.36** Mean signal response due to varying levels of additive concentration.  $E=1.66 \times 10^5$  V/cm, FRR=100Hz. Error bars relate to the mean standard deviation averaged over three test runs.

Percentage of concentrate added to fluid mix (%)	Mean signal response (µA)	Mean standard deviation (nA)
0	3.02	9.600
2.5	2.98	15.10
5	2.99	14.70
7.5	2.87	32.10
10	2.57	34.23
12.5	2.39	33.94
15	2.24	33.84
17.5	2.15	31.72
20	2.07	33.57
25	1.9	31.86
30	1.73	31.82
35	1.64	34.12
40	1.55	32.45
50	1.39	32.11
60	1.37	31.46
70	1.38	31.57

**Table 6.8** Summary of results for the collection of qualitative data.

The results of this process are shown in figure 6.36. For accuracy, three test runs were performed for each batch of fluid mix. Data points shown in figure 6.36 and values of signal response stated in table 6.8 relate to the mean value of signal response averaged over the three test runs. Error bars shown in figure 6.36 and values of standard deviation stated in table 6.8 relate to the mean value of standard deviation averaged over the three test runs.

It could be seen that as with in the collection of quantitative data, the profile of signal response shown in figure 6.36 showed various levels of sensitivity. Increments of 10% fluid mix could be distinguished up until 50% fluid mix. At fluid mixes of greater than 50% however, 10% changes in fluid mix could not be distinguished due to a significant decrease in sensitivity. The fluid mix was then altered in increments of 5% and it was found that the 5% changes of fluid mix were distinguishable from fluid mixes of 5% to 30%. Above or below these values the 5% changes in fluid mix were indistinguishable. The fluid mix was then altered in increments of 2.5%. It was seen that the 2.5% changes in fluid mix could be distinguished in fluid mixes of 5% to 15% at which point difficulty was experienced in distinguishing between the changes in fluid mix due to the 'overlap' of the standard deviation.

The results showed that the sensitivity of the a-Si:H materials ability to detect changes in fluid mix was decreasing with an increase in fluid mix. The decrease in sensitivity was attributed to the fact that the attenuation of the light as it passed through the higher levels of fluid mix moved the peak  $I_s$  further away from the steady state and thus further away from the region of signal response which is most sensitive to changes in irradiance. Table 6.8 also shows that the standard deviation in the signal response increased as the peak  $I_s$  moved away from the near steady state condition due to the attenuation of the light as it passed through the prototype at higher levels of fluid mix. The experimental results suggest that if maximum sensitivity to changes in irradiance were to be achieved for any fluid mix, the peak  $I_s$  would have to be positioned just under the steady state for the required fluid mix. By applying this technique, it was envisaged that increased sensitivity to changes in irradiance would be achieved and also that the standard deviation would be reduced thus increasing the resolution of the system.

In order to test this theory, the peak  $I_s$  was positioned just under the steady state for a 7.5% fluid mix by increasing  $H_e$  from  $278.6\text{mW/cm}^2$  to  $696.9\text{mW/cm}^2$  and  $t_{ph}$  from 340ns to 380ns. The fluid mix was increased from 7.5% in 0.5% increments and the results of this investigation show that the mean signal responses for the 0.5% changes in fluid mix were distinguishable as can be seen in figure 6.37. It was found in all cases that the minimum value of signal response for each of the test runs was higher in magnitude than the maximum signal response of the following 0.5% increment in fluid mix. Thus the mean, maximum, and minimum signal responses over all increments of fluid mix were completely distinguishable from each other.

As expected, the repositioning of  $I_s$  to just below the steady state for the 7.5% fluid mix, had the effect of reducing the mean standard deviation. In the previous experiment, the peak  $I_s$  was positioned under the steady state condition for 0% fluid mix (i.e. clear water) which resulted in a standard deviation of 32.1nA at a 7.5% fluid mix. By repositioning the peak  $I_s$  to just under the steady state, the standard deviation for the 7.5% fluid mix was reduced to approximately 8nA, thus the repositioning of the peak  $I_s$  reduced the standard deviation by approximately 75% which resulted in increased resolution for the system.

The suitability of the a-Si:H materials application for batch monitoring and control of fluids is discussed further in chapter 7.

### 6.2.7 Production of basic images using a contact array

#### (i) Curvature of the pipeline

The aim of this experimentation was initially to see if the bottom curvature of the pipeline could be determined by the use of a contact array positioned underneath the pipeline. The contact array comprised of a single a-Si:H sample containing sixteen  $2.5\text{mm}^2$  Au contacts as previously described in section 4.2.(vi). Figure 6.38 shows the Au contact positioning arrangement for the a-Si:H sample. Figure 6.39 shows the mean signal responses for the contact array.

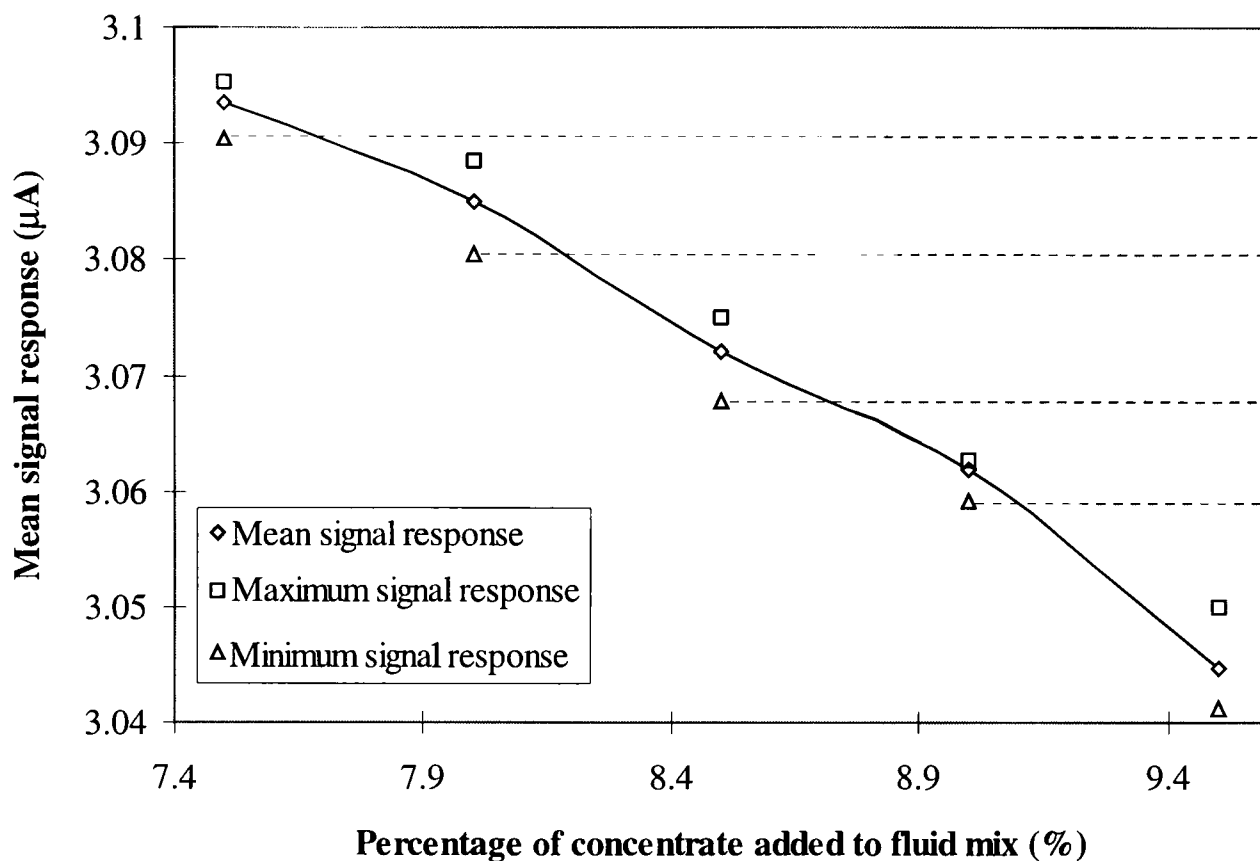


**Figure 6.37** Mean signal response due to varying levels of additive concentration.  $E=1.66 \times 10^5$  V/cm, FRR=100Hz,  $H_e=696.9$  mW/cm<sup>2</sup>,  $t_{ph}=380$  ns.

Concentration of additive to fluid mix (%)	Mean signal response (µA)	Maximum signal response (µA)	Minimum signal response (µA)	Mean standard deviation (nA)
7.5	3.093	3.095	3.090	7.845
8	3.085	3.088	3.080	6.965
8.5	3.072	3.075	3.067	7.230
9	3.061	3.062	3.059	6.880
9.5	3.044	3.049	3.041	5.850

**Table 6.9** Summary of results for the collection of qualitative data

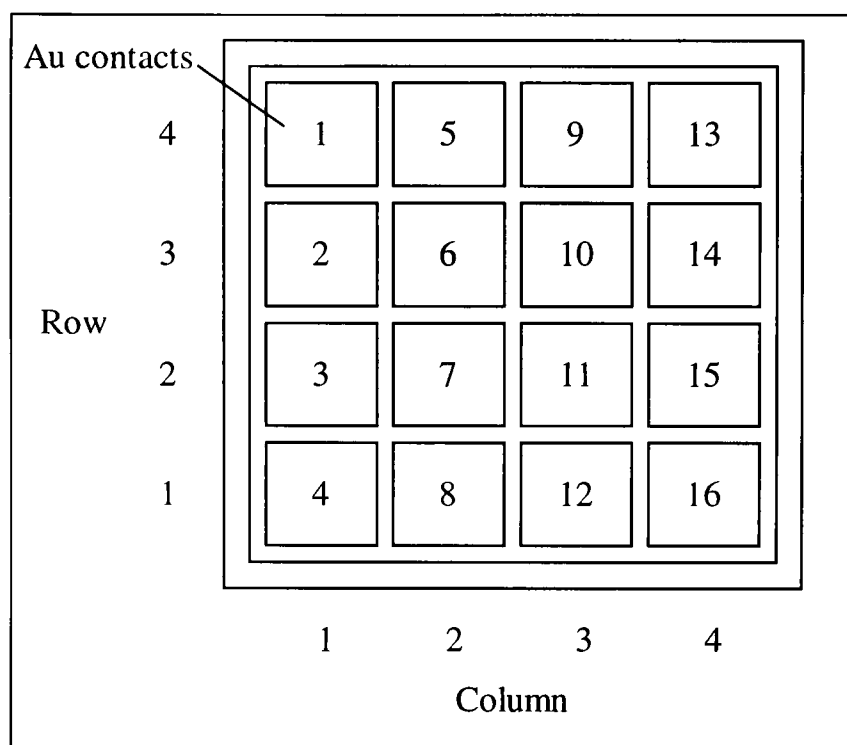


Figure 6.38 Au contact positioning for contact array.

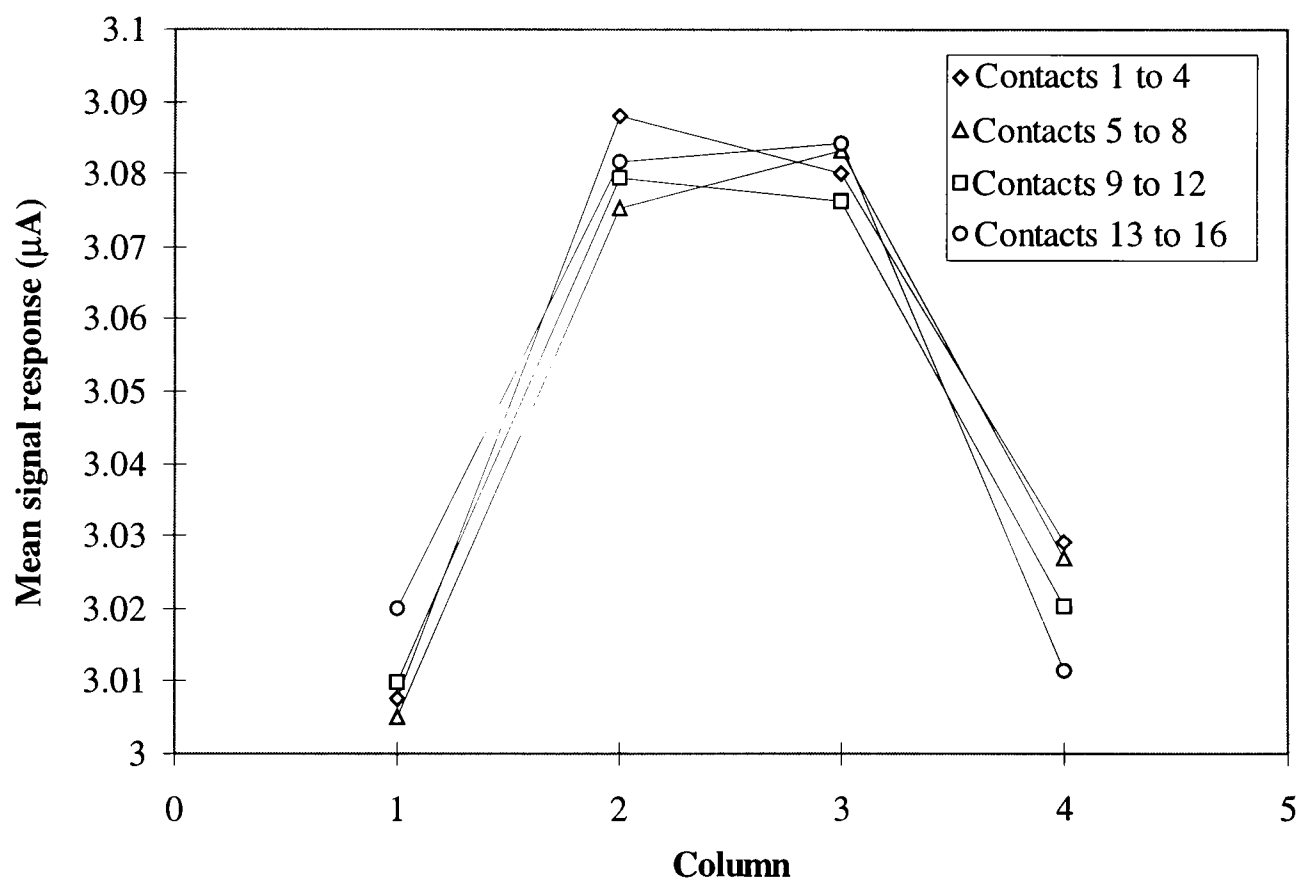


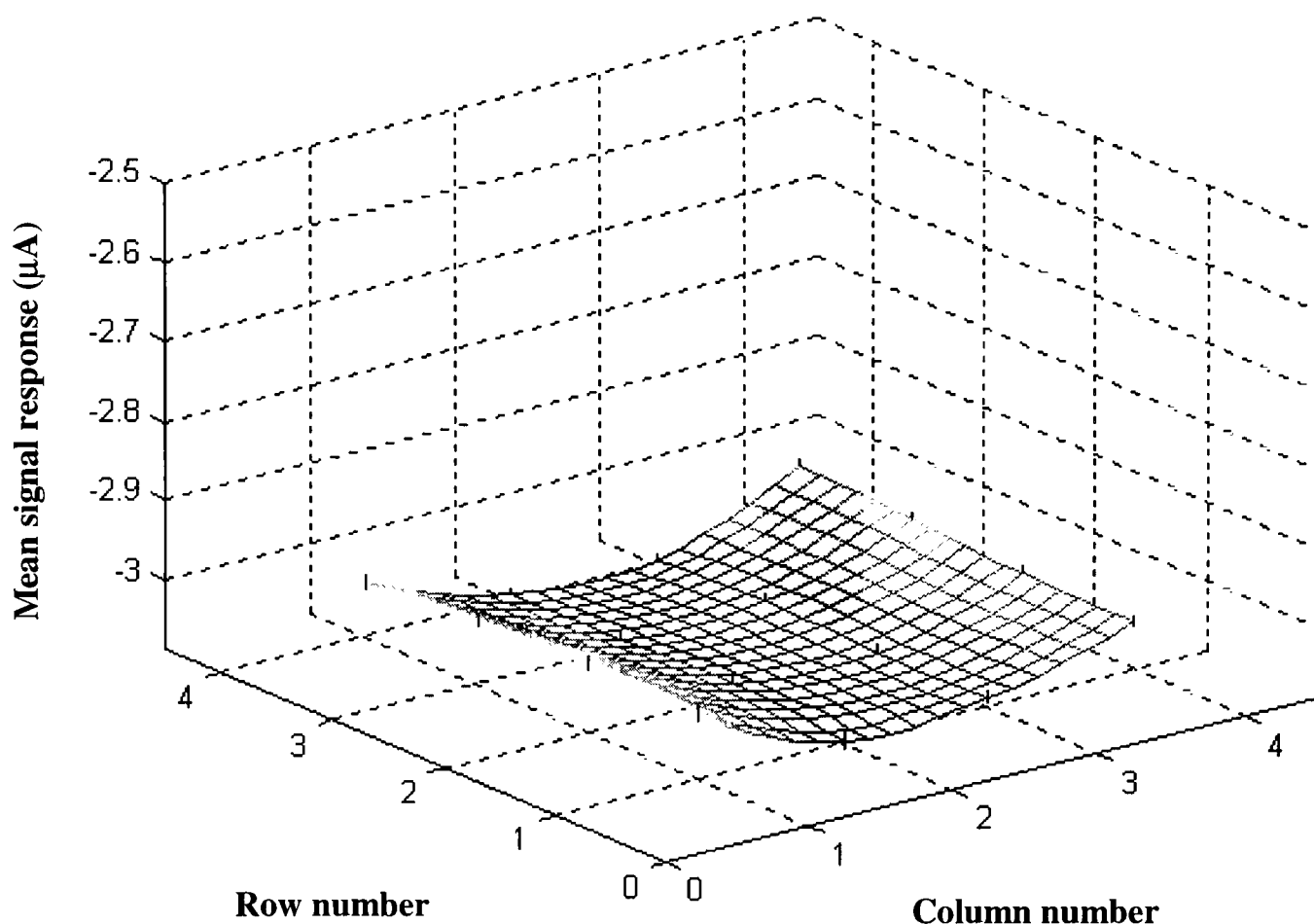
Figure 6.39 Mean signal response for contact array.  $E=1.66 \times 10^5$  V/cm, FRR=100Hz.

Figure 6.39 showed that the Au contacts in columns 2 and 3 exhibited a higher magnitude of signal response than observed for columns 1 and 4. This was to be expected as columns 2 and 3 were located towards the centre of the a-Si:H sample. As the surface of the a-Si:H sample was curved as the samples are cut from drums, columns 2 and 3 were located at a closer distance to the bottom of the pipeline than columns 1 and 4. Additionally, the curvature of the pipeline wall meant that the distance from the bottom of the pipeline to columns 1 and 4 was increased. This had the result that the irradiance incident on columns 1 and 4 was of a smaller magnitude than columns 2 and 3 and as such the signal response decreased accordingly. The irradiance incident on each contact within the contact array was not determined due to experimental difficulty in manufacturing a light detection mechanism that could accurately determine the irradiance falling on each of the  $2.5\text{mm}^2$  contacts in the array.

The fact that the two central columns (2 and 3) were located closer to the bottom curvature of the pipeline, meant that a higher order of magnitude in signal response was encountered for the contacts within these columns as previously described. This had the effect of presenting a positive going curvature as can be seen in figure 6.39. The experimental data were imported into MATLAB and interpolated using bi-cubic interpolation in which a 3rd order polynomial is fitted between each data point in the data set in order to provide a smooth transition between said data points. Figure 6.40 shows a three dimensional plot of the interpolated data. Error bars represent the +/- standard deviation averaged over the three test runs and also distinguish between the experimental data points and the interpolated data. The data in the z plane has been inverted to produce a negative going curvature to represent the correct orientation of the pipeline.

#### (ii) Phantom object

Now that the bottom curvature of the pipeline had been established, experimentation went on to determine if a phantom object located in the bottom of the pipeline as previously described, could be distinguished using the contact array. Figure 6.41 shows the mean signal response for this process.



**Figure 6.40** 3D representation of the bottom curvature of the pipeline using the 16 contact array.  $E=1.66 \times 10^5$  V/cm, FRR=100Hz.

	1	5	9	13
4	3.007µA Std +/-11.53nA	3.088µA Std +/-11.10nA	3.081µA Std +/-10.21nA	3.019µA Std +/-7.340nA
3	2	6	10	14
3	3.005µA Std +/-12.30nA	3.075µA Std +/-12.70nA	3.079µA Std +/-11.80nA	3.009µA Std +/-9.770nA
2	3	7	11	15
2	3.027µA Std +/-8.33nA	3.083µA Std +/-8.560nA	3.076µA Std +/-10.35nA	3.020µA Std +/-8.970nA
1	4	8	12	16
1	3.029µA Std +/-10.62nA	3.080µA Std +/-9.24nA	3.084µA Std +/-8.690nA	3.011µA Std +/-9.820nA
	1	2	3	4
	Column			

**Table 6.10** Mean signal response for the contact array. Std denotes the mean standard deviation.

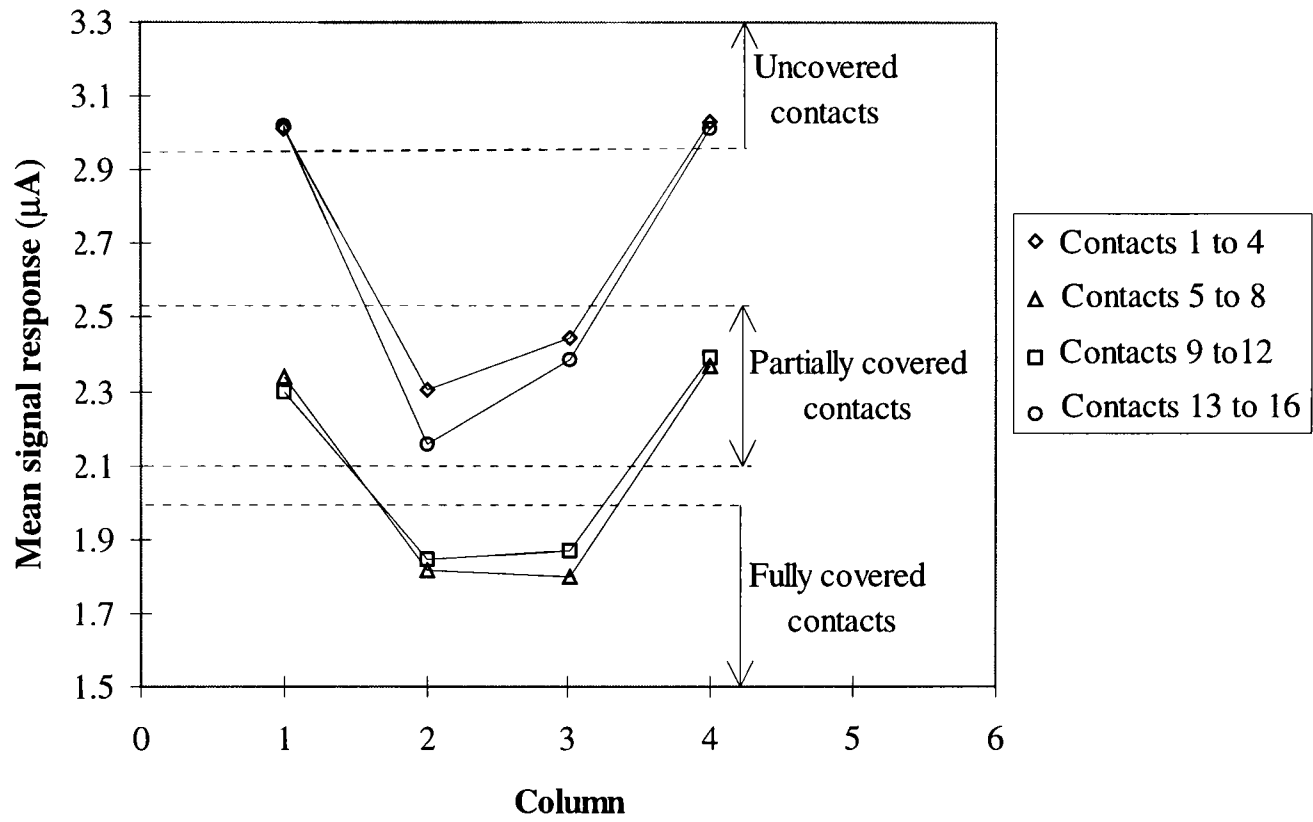


**Figure 6.41 Mean signal response due to insertion of phantom object.**  
 **$E=1.66 \times 10^5$  V/cm, FRR=100Hz.**

Figure 6.41 demonstrated that very good reproducibility from the uncovered contacts (contacts 1, 4, 13, and 16) was achievable with approximately 18nA separating the maximum and minimum values of mean signal response. The four corner contacts in the array were left uncovered in order that, (i) good contrast in magnitude in the signal response be achieved. (ii) The signal responses could be aligned with the signal responses obtained for the four corner contacts in the establishment of the bottom curvature of the pipeline. In this manner the signal responses obtained for the phantom object could be correctly orientated in relation to the bottom curvature of the pipeline, i.e. the four uncovered corner contacts were used as datum points.

It could also be seen from figure 6.41 that the signal responses for the fully covered contacts (contacts 6, 7, 10, and 11) exhibited a greater separation in the maximum and minimum mean signal responses (approximately 70nA) than for the uncovered contacts. This was attributed to two factors. Firstly as it has been previously described, the reduction in signal response due to attenuation of the issued light pulses as it passes through the tomographic prototype causes the peak  $I_s$  to move further away from the steady state condition. This has the effect of increasing the standard deviation observed in the signal response. Secondly, the top and bottom surfaces of the phantom object were shaped by hand thus inconsistencies existed in the surfaces of the phantom object which may also have led to discrepancies in the magnitude of the mean signal response for the fully covered contacts.

The greatest variation in mean signal response was exhibited by the partially covered contacts (contacts 2, 3, 5, 8, 9, 12, 14, and 15) where a difference in magnitude of approximately 290nA existed between the maximum and minimum mean signal responses. The variance in magnitude in the mean signal responses was attributed to the reasons stated above and also to the fact that the contacts were partially covered by the phantom object. It was experimentally very difficult to position the phantom object above the contact array in such a manner that each of the partially covered contacts was covered by exactly the same amount. Incorrect positioning of the phantom object would lead to variation in the exposed area of the contacts which would in turn lead to variation in mean signal response. As previously described, a mechanical device was used in conjunction with datum marks located upon the sample support structure to position the phantom object as accurately as possible.

As with the mean signal response data for the bottom curvature of the pipeline, the collected data for the phantom object was imported into MATLAB and interpolated by the use of bi-cubic interpolation. Figure 6.42 shows the results of this process. Error bars represent the +/- mean standard deviation averaged over the three test runs and also mark the location of the experimental data points. As with the bottom curvature of the pipeline, the mean signal response has been inverted to represent the phantom objects position in relation to the bottom of the pipeline which is also shown in figure 6.42 for reference purposes. It should be noted that the data portrayed in figure 6.42 represents the variation in the signal response due to the insertion of the phantom object and is not an image of the phantom object. Figure 6.42 represents the data collected for one view through the pipeline only. In order to be able to accurately image the phantom object, multiple views would be required which is discussed further in chapter 7. The MATLAB program which relates to figure 6.42 can be seen in appendix 6A.

### 6.3 Chapter summary

In this chapter I sought to demonstrate the suitability of the a-As<sub>2</sub>Se<sub>3</sub> and a-Si:H materials for application in OPT. I have reported the results of a tomographic investigation in which I recorded such qualities as detectivity, production of steady state photocurrent, effects of photoinduced fatigue, and responsivity to illumination over a range of electric fields and made the following observations.

I have shown that the a-As<sub>2</sub>Se<sub>3</sub> material exhibits greater sensitivity to visible light than a-Si:H. Detectivity experiments have shown that for identical levels of electric field and light duration, a smaller level of irradiance is required to produce the smallest clean and repeatable current signal obtainable in a-As<sub>2</sub>Se<sub>3</sub> than is required in a-Si:H. I have also demonstrated that a-As<sub>2</sub>Se<sub>3</sub> is more responsive to incident visible light, i.e. a-As<sub>2</sub>Se<sub>3</sub> produces a greater magnitude of photocurrent than a-Si:H for the same light conditions and electric field.

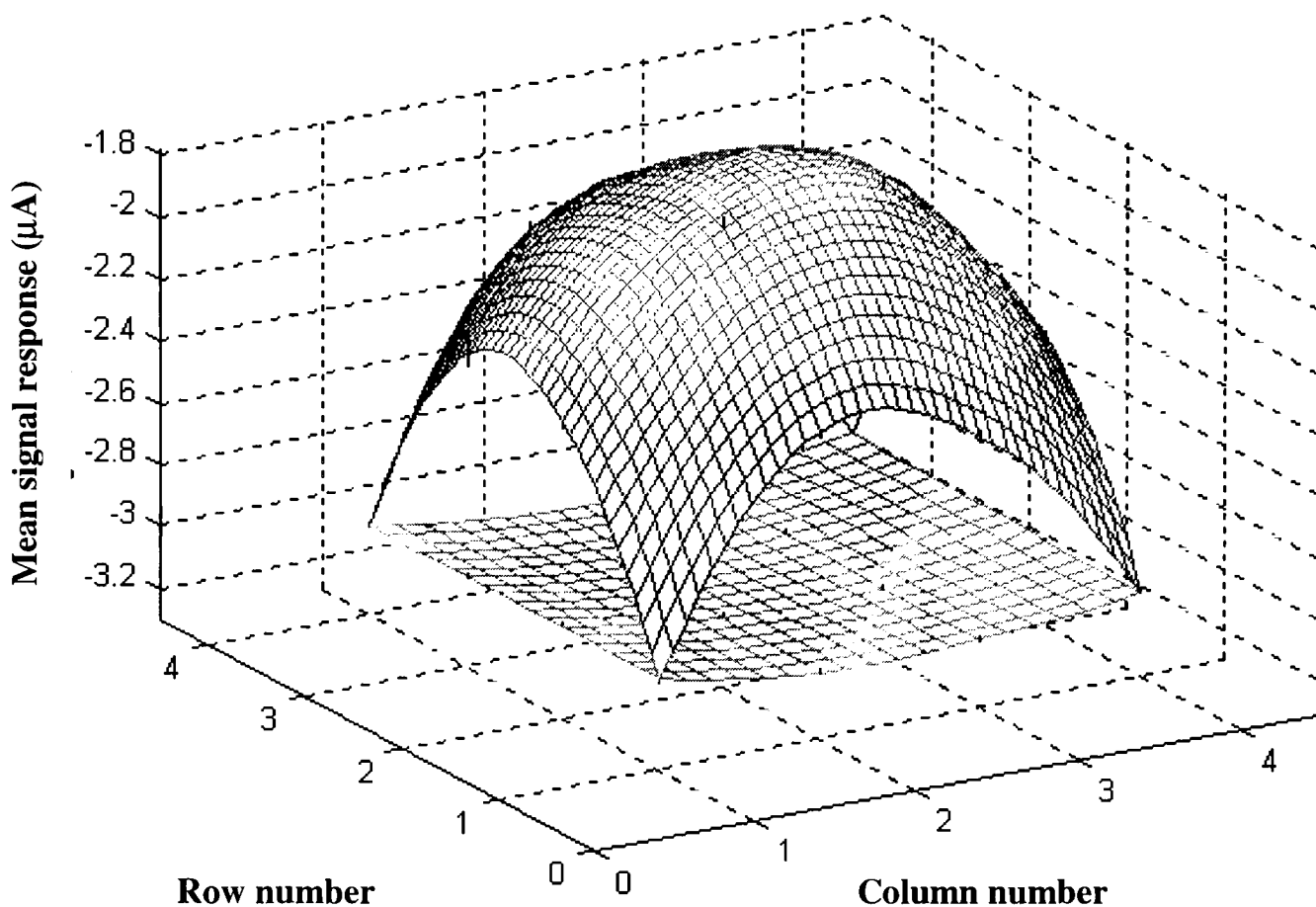


**Figure 6.42** 3D representation of the mean signal response due to the phantom object.  $E=1.66 \times 10^5$  V/cm, FRR=100Hz.

	1	5	9	13
4	3.014µA Std +/-11.53nA	2.336µA Std +/-24.23nA	2.295µA Std +/-23.17nA	3.020µA Std +/-9.340nA
3	2.306µA Std +/-35.14nA	1.817µA Std +/-36.17nA	1.843µA Std +/-37.23nA	2.155µA Std +/-23.46nA
2	2.442µA Std +/-33.92nA	1.797µA Std +/-34.14nA	1.867µA Std +/-35.05nA	2.383µA Std +/-21.96nA
1	3.027µA Std +/-11.21nA	2.366µA Std +/-24.41nA	2.393µA Std +/-26.48nA	3.012µA Std +/-10.88nA
	1	2	3	4

Column number

**Table 6.11** Mean signal response for the contact array, Std denotes mean standard deviation.

Our steady state experiments have shown that the two materials produce approximately the same magnitude of steady state photocurrent. However I have also demonstrated that the a-As<sub>2</sub>Se<sub>3</sub> has a faster response time and reaches steady state conditions faster than the a-Si:H material. Although I have demonstrated that the a-As<sub>2</sub>Se<sub>3</sub> material exhibits superiority over a-Si:H in many of the experimental parameters I have reported, our investigation as to the effects of photoinduced fatigue in this material have determined that the a-As<sub>2</sub>Se<sub>3</sub> material can only be operated at a FRR of 20Hz if degradation of the signal response is to be avoided. The maximum FRR of 20Hz was insufficient for OPT applications and so a-As<sub>2</sub>Se<sub>3</sub> was eliminated from further tomographic enquiry.

I have shown that although photoinduced fatigue was observed in a-Si:H, the deterioration of the signal response due to pulse light was very rapid and the signal response was seen to settle to a constant level. I have demonstrated that a-Si:H is sensitive to changes in irradiance at speeds required for OPT applications. A experimental technique that maximises sensitivity to changes in irradiance due to the positioning of the peak signal current to under the steady state condition has been described. I have shown that application of this experimental technique resulted in the signal responses for a pipeline full of water and an empty pipeline to be clearly distinguished and that the separation between the two responses was sufficient for tomographic applications.

An investigation to determine if quantitative data could be obtained from the a-Si:H device at speeds required for OPT has been described. Our results showed that changes of 1mm in water level could be accurately detected by the a-Si:H device. Further investigation to establish if qualitative data could be obtained by the use of the a-Si:H device revealed that 0.5% changes in fluid colour could be accurately distinguished.

I have also shown that by using a sensor array, the variance in signal response produced by the a-Si:H device due to the insertion of an empty pipeline can be used to produce a 3D representation of the bottom curvature of the pipeline. I have also demonstrated that the sensor array can be used to give information as to the position and geometry of a phantom object located within the pipeline.

## CHAPTER SEVEN

### DISCUSSION OF EXPERIMENTAL RESULTS

This chapter is concerned with discussing the observations of the xerographic and tomographic investigations presented in chapters 5 and 6 and their relevance as to the a-As<sub>2</sub>Se<sub>3</sub> and a-Si:H materials suitability for application in OPT.

#### 7.1 Xerographic investigation

##### 7.1.1 Charge acceptance

###### (i) Amorphous arsenic triselenide

The charge acceptance of the 60 $\mu$ m a-As<sub>2</sub>Se<sub>3</sub> material employed in the current research was in the order of approximately 1080V. This related to a surface charge density of approximately  $1.7 \times 10^{-7}$  C/cm<sup>2</sup> which was well in excess of the  $0.5 \times 10^{-7}$  C/cm<sup>2</sup> to  $1.5 \times 10^{-7}$  C/cm<sup>2</sup> range of surface charge density generally considered to be suitable for xerographic applications. The high charge acceptance indicated very high dark resistivity which is a requirement of a good photoreceptor. Kasap (1991) states that a-As<sub>2</sub>Se<sub>3</sub> has a dark resistivity in the order of approximately  $1 \times 10^{12}$   $\Omega$ /cm. The dark resistivity of the a-As<sub>2</sub>Se<sub>3</sub> material employed in the current research could be estimated by the application of equation 3.5 to the experimental charge acceptance data. This process yielded an estimated dark resistivity of approximately  $0.76 \times 10^{12}$   $\Omega$ /cm.

###### (ii) Hydrogenated amorphous silicon

The charge acceptance of the 27.1 $\mu$ m a-Si:H material was found to be in the order of approximately 650V which related to a surface charge density of approximately  $2 \times 10^{-7}$  C/cm<sup>2</sup> which again was well in excess of what is considered to be suitable for xerographic applications. The high charge acceptance of the a-Si:H material was again indicative of high dark resistivity. Mort (1991) states that a-Si:H has a dark resistivity in the order of approximately  $1 \times 10^{13}$   $\Omega$ /cm.

### 7.1.2 Dark decay

#### (i) Amorphous arsenic triselenide

It has been demonstrated in chapter 4 that surface potentials of a predetermined magnitude can be accurately applied to the surface of the sample under test by the use of the developed scorotron charger. Surface potentials of 400V, 600V, and 800V were chosen to give the lower, middle, and upper range of surface charge density considered to be suitable for xerographic purposes. A requirement of a good photoreceptor is that the applied surface has a sufficient life span for the xerographic process to take place, i.e. for exposure and development of a latent image to be performed. The length of time required for this process is highly application specific, but in general a photoreceptor is required to have a half time  $t(V_0/2)$  of greater than 1 minute (Schaffert 1975). However, in automated xerographic imaging systems where rapid exposure and development are commonplace much shorter half times can be tolerated (Mort, 1991). Table 5.2 shows that the half decay times for the electric fields investigated ranged from 1.34 minutes to 1.75 minutes, thus indicating that the charge retention of the a-As<sub>2</sub>Se<sub>3</sub> material was sufficient for xerographic applications. A further requirement of a good photoreceptor is that it has low residual potential. The residual potential for the a-As<sub>2</sub>Se<sub>3</sub> material was found to be approximately 20V in magnitude for all electric fields investigated which was between 2.5% to 5% of  $V_0$ .

The investigation as to the dark discharge mechanism in a-As<sub>2</sub>Se<sub>3</sub> confirmed previous published works indicating that the dark discharge mechanism proceeded via a xerographic depletion discharge mechanism. In agreement with Abkowitz *et al* (1985), and Kasap 1991, a clear change in the rate of dark discharge was observed. Following the analysis of Abkowitz *et al*, two linear regions in the rate dark discharge were observed with the point of intersection denoting a depletion time. In agreement with both Abkowitz *et al* and Kasap the surface potential determined at the depletion time was lower in magnitude and longer in duration when compared to the theoretical depletion time of  $V_0/2$ . Also in accordance with XDD theory the sum of the slopes of the two linear regions was found to be in the order of approximately -2.

### (ii) Hydrogenated amorphous silicon

The dark decay experiments conducted upon the a-Si:H material under the same electric fields previously described, yielded dark decay half times of approximately 22 seconds to 27 seconds. This figure is in reasonable agreement with Baxendale *et al* (1990) who state a half time of approximately 23seconds for an electric field of  $2.7 \times 10^5$  V/cm. The residual potential observed in the a-Si:H material was again found to be of the order of approximately 20V corresponding to 5.6% to 11% of  $V_o$ .

The investigation into the dark discharge mechanism concurred with past published works that concluded that the mechanism proceeded via a Poole-Frenkel lowering of a coulombic barrier. Attempts to observe a XDD process in the a-Si:H material concluded that no phenomena indicative of a XDD mechanism could be observed over the range of electric fields investigated in agreement with both Kakinuma and Wantanabe (1987) and Baxendale *et al* (1990). However, good agreement was obtained by following the analysis of these investigators.

Both Baxendale *et al* and Kakinuma and Wantanabe (KW) concluded that the dark discharge in a-Si:H was due to a Poole-Frenkel emission of mobile holes and electrons within the intrinsic region. Following the analysis of KW, a linear characteristic should be produced if the dark discharge follows a Poole-Frenkel mechanism, and that the slope of the characteristic should yield a  $\beta_{PF}$  which is similar to its theoretical value. The results of this analysis produced a linear characteristic under all electric fields investigated, with the slopes of the characteristic ranging from  $2.36 \times 10^{-4}$  (V/cm)<sup>1/2</sup> eV to  $2.39 \times 10^{-4}$  (V/cm)<sup>1/2</sup> eV which were in very good agreement with the one dimensional theoretical Poole-Frenkel coefficient of  $2.4 \times 10^{-4}$  (V/cm)<sup>1/2</sup> eV.

## 7.2 Tomographic investigation

### 7.2.1 Detectivity

#### (i) Amorphous arsenic triselenide

The investigation into the detectivity of the a-As<sub>2</sub>Se<sub>3</sub> material under varying levels of electric field established the minimum light levels ( $H_{min}$ ) that could be employed in the current system if a clean and repeatable photogenerated current signal was to be produced. For the a-As<sub>2</sub>Se<sub>3</sub> material, the value of  $H_{min}$  seemed to decrease for an

increase in electric field as shown in figure 7.1. This was to be expected as charge carriers are drawn into the bulk of the material at a higher rate and therefore density with an increase in electric field (Mort and Pai 1975). Figure 6.4 shows that the responsivity (the ratio of the peak output current to the incident light input power) of the a-As<sub>2</sub>Se<sub>3</sub> material also increases with an increase in electric field. This was attributed to the fact that for an identical level of irradiance, a greater current density was produced by the higher electric field for the reason previously explained.

For the a-As<sub>2</sub>Se<sub>3</sub> material, the optimum value of  $H_{\min}$  was found to be 3.45mW/cm<sup>2</sup> with  $t_{\text{ph}}=360\text{ns}$  at  $E=1.33 \times 10^5$  V/cm<sup>2</sup>. These experimental parameters resulted in a peak  $I_s$  of approximately 300nA. The time required for the a-As<sub>2</sub>Se<sub>3</sub> material to reach the peak  $I_s$  after the application of the light pulse was found to be approximately 200 $\mu\text{s}$ . This value was determined by fitting a 3rd order polynomial to the experimental data and performing cubic interpolation to establish a current verses time data set using the MATLAB software package. The time difference between the application of the light pulse and the resulting peak  $I_s$  could then be determined.

#### (ii) Hydrogenated amorphous silicon

Figure 7.1 also demonstrates that as in a-As<sub>2</sub>Se<sub>3</sub>, the value of  $H_{\min}$  seemed to decrease for an increase in applied electric field. However, figure 7.1 also demonstrates that higher levels of irradiance are required in the a-Si:H material to reach  $H_{\min}$  under identical electric fields, light pulse duration's ( $t_{\text{ph}}=360\text{ns}$ ), and Au contact geometry (3mm dia). This indicated that the a-Si:H material was less photoconductive than the a-As<sub>2</sub>Se<sub>3</sub> material as was previously established by the PID experiments detailed in chapter 5. As in a-As<sub>2</sub>Se<sub>3</sub>, the responsivity of the a-Si:H material was seen to increase with applied electric field.

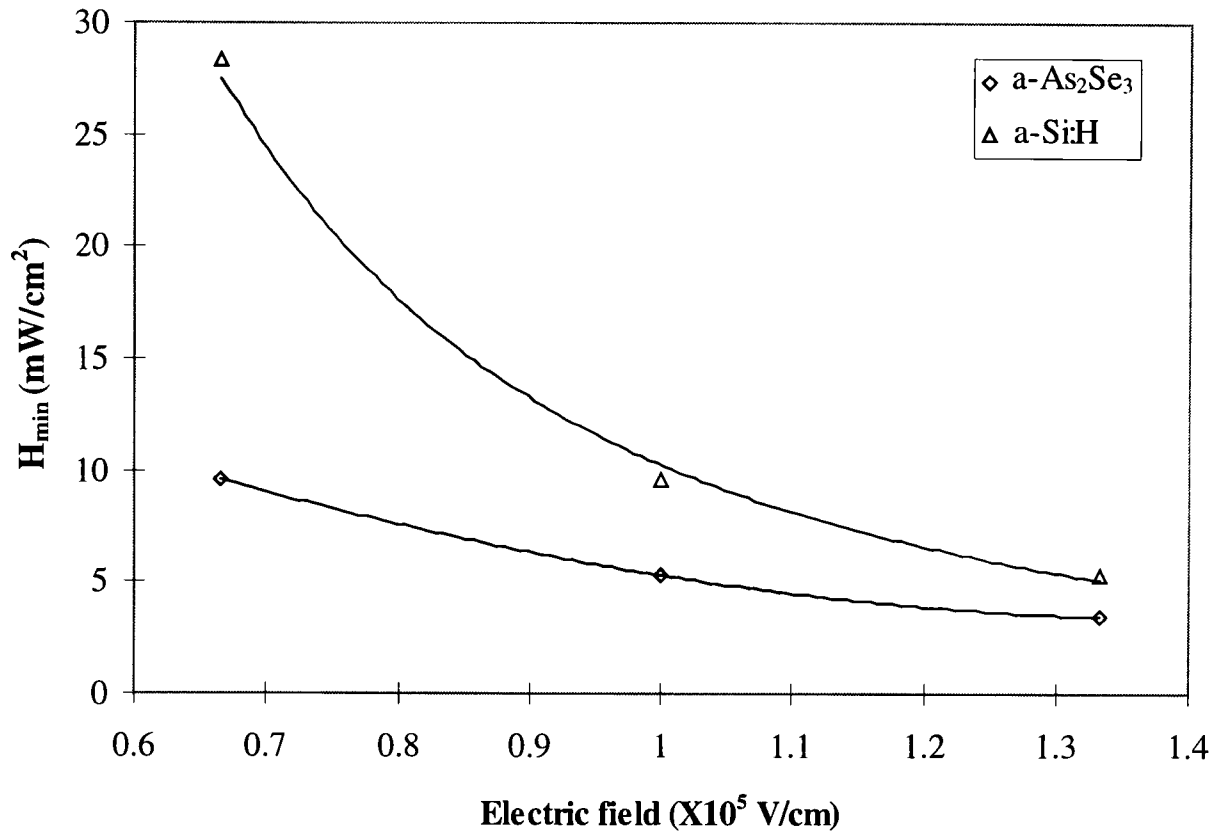


**Figure 7.1** Dependence of minimum irradiance ( $H_{\min}$ ) upon applied electric field.

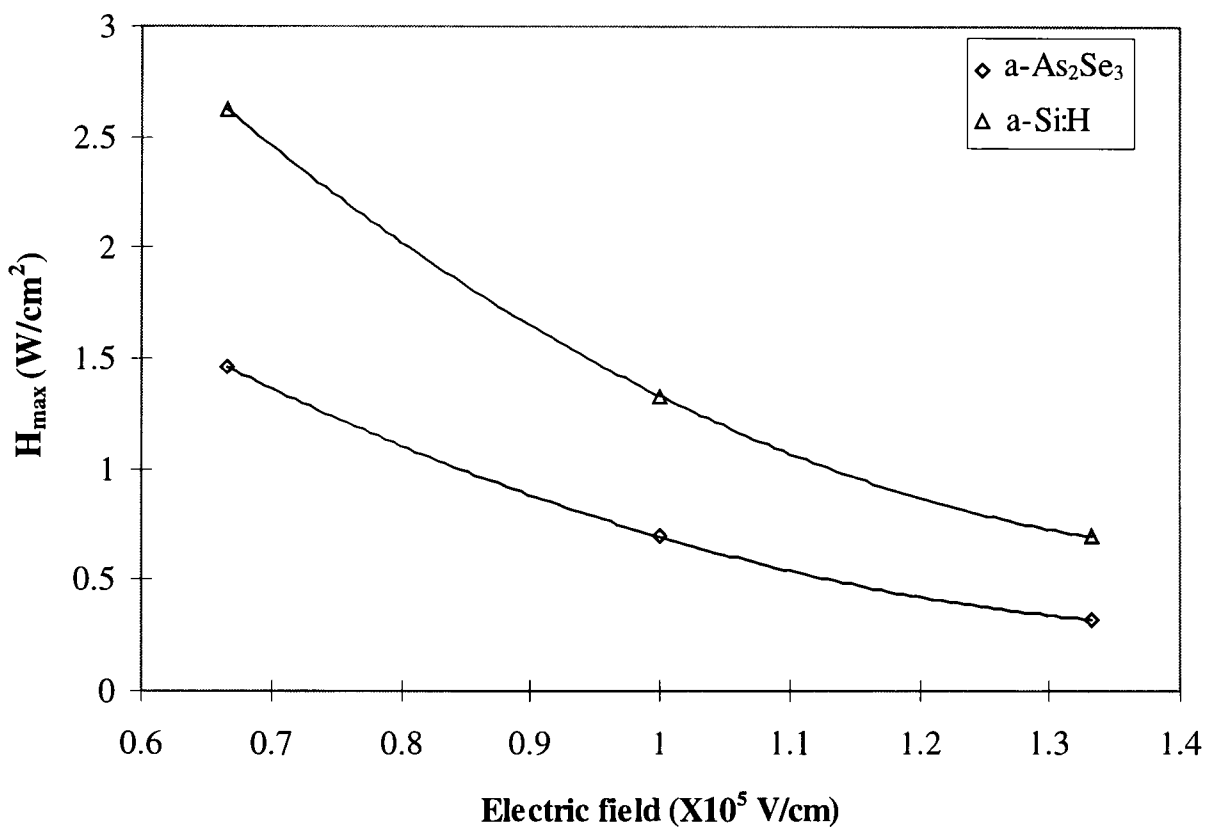


**Figure 7.2** Dependence of maximum irradiance ( $H_{\max}$ ) upon applied electric field.

The optimum value of irradiance for the a-Si:H material was found to be approximately  $5.31\text{mW/cm}^2$  with  $t_{\text{ph}}=360\text{ns}$  and  $E=1.33\times 10^5\text{ V/cm}$ . These experimental parameters resulted in a peak  $I_s$  of approximately  $340\text{nA}$ . This resulted in an approximate increase of 53% in irradiance when compared to the a-As<sub>2</sub>Se<sub>3</sub> material, if a clean and repeatable signal was to be achieved in the a-Si:H material. The time required for the a-Si:H material to reach the peak  $I_s$  after application of a light pulse, was typically in the order of  $280\mu\text{s}$ . This related to an increase of approximately 40% when compared to the a-As<sub>2</sub>Se<sub>3</sub> material.

The detectivity of a material is an important parameter in a potential OPT system as  $H_{\text{min}}$  dictates the minimum light levels for the system. In order that a clean and repeatable signal be produced, irradiance of  $H_{\text{min}}$  must fall upon the surface of the sensor after attenuation (or magnification) of the applied light pulse after being passed through the pipeline and medium under test. The magnitude of  $H_{\text{min}}$  has implications as to the intensity and type of the light source, diameter of pipeline, and density of medium that can be employed in a OPT system. Ideally  $H_{\text{min}}$  needs to be as small in magnitude as possible to allow the intensity of issued light to be kept to the minimum. This would allow a greater range of light intensities available from the light source to be employed in the OPT system. For example, for any given light source, a maximum available light intensity will exist. The value of  $H_{\text{min}}$  will dictate the minimum value of light intensity from the source for a given application. The higher in magnitude  $H_{\text{min}}$  is, the smaller the range of light intensity available for tomographic purposes. The range of available light intensity could limit the diameter of pipeline and the type of medium that could be employed in a potential imaging system.

The experimental results have shown that in order to keep  $H_{\text{min}}$  to a minimum, the electric field should be kept as high as possible. Maintaining a high electric field in the sample also has the effect of increasing the responsivity of the sensor which is a highly desirable feature as this will again lead to greater flexibility in the choice of light source, diameter of pipeline, and type of medium that can be monitored. The results of the investigation detailed in chapter 6, have shown that in terms of detectivity, the a-As<sub>2</sub>Se<sub>3</sub> material has exhibited greater photoconductivity, responsivity, and speed of response when compared to the a-Si:H material.

### 7.2.2 Production of steady state photocurrent.

#### (i) Amorphous arsenic triselenide

The determination of the light conditions required to drive the signal current into the steady state ( $H_{\max}$ ) identified the maximum available signal current for the a-As<sub>2</sub>Se<sub>3</sub> material for a range of electric fields. The production of photocurrent was found to be dependant upon the size of the Au contact, the applied electric field, the irradiance incident upon the sample surface, and the duration of the light pulse. Figure 7.2 shows the dependence of  $H_{\max}$  upon the applied electric field. As seen with  $H_{\min}$ , the level of irradiance required to produce  $H_{\max}$  decreased with an increase in applied electric field. This was again attributed to the increased density of current due to the higher electric fields as stated previously. As expected much higher levels of irradiance were required to drive the photocurrent into the steady state (319mW/cm<sup>2</sup> for  $H_{\max}$  as opposed to 3.45mW/cm<sup>2</sup> for  $H_{\min}$  at  $E=1.33 \times 10^5$  V/cm). The duration of the applied light pulse was found to be an important factor in the production of photocurrent.

For a light pulse half time of 360ns as employed in the detectivity experiments, the intensity of the issued light had to be greatly increased to give an irradiance incident upon the sample surface of approximately 1.17W/cm<sup>2</sup> to 4.28W/cm<sup>2</sup> for the range of electric field stated in order to drive the photocurrent into the steady state. This had the detrimental effect of reducing the range of available light intensity from the source for tomographic purposes. The L2441 xenon source has a maximum input energy ( $E_{\text{in}}$ ) of 0.1J. In order to produce the maximum irradiance of 4.28W/cm<sup>2</sup> upon the surface of the sample,  $E_{\text{in}}$  needed to be in the order of approximately 88mJ for the electric field of  $0.66 \times 10^5$  V/cm, thus leaving only 12mJ of adjustment in the intensity of the applied light pulse. In order to obtain maximum available range in light intensity, the duration of the light pulse was increased from 360ns to 520ns. The extension of the illumination period allowed the production of more photocurrent and allowed the intensity of the issued light pulse to be reduced. The longer illumination period meant that irradiance from 319mW/cm<sup>2</sup> to 1.46W/cm<sup>2</sup> could be employed to drive the photocurrent into the steady state, thus the irradiance required to drive the photocurrent into the steady state was reduced by approximately 27% to 34% for the range of electric fields specified. This reduction in required irradiance allowed  $E_{\text{in}}$  to be reduced to 27mJ for an electric field of  $0.66 \times 10^5$  V/cm, thus now leaving 73mJ for adjustment of the intensity of the issued light pulse.

The maximum available photocurrent from the 3mm dia Au contact on the a-As<sub>2</sub>Se<sub>3</sub> material was found to be approximately 3.24μA. The time required to reach the steady state after the application of the 520ns light pulse was approximately 830μs.

(ii) Hydrogenated amorphous silicon

As with the a-As<sub>2</sub>Se<sub>3</sub> material the level of irradiance required to produce steady state photocurrent was found to decrease with an increase in applied electric field for the a-Si:H material. Due to the inferior photosensitivity of the a-Si:H material as previously shown,  $H_{\max}$  needed to be significantly higher in order to produce steady state photocurrent. For  $t_{\text{ph}}=360\text{ns}$  as used in the detectivity experiments, the maximum light intensity from the L2441 source was insufficient to drive the photocurrent into the steady state for the lowest electric field of  $0.66 \times 10^5 \text{ V/cm}$ . In order to reduce the level of irradiance required to drive the photocurrent into the steady state,  $t_{\text{ph}}$  was extended to 880ns which allowed  $H_{\max}$  to be in the range of  $693\text{mW/cm}^2$  to  $2.62\text{W/cm}^2$  for the range of electric field specified. The range of  $H_{\max}$  related to a range of  $E_{\text{in}}$  of approximately 54mJ to 25.5mJ thus leaving 46mJ to 74.5mJ for adjustment of the intensity of the issued light pulse.

The maximum available photocurrent from the 3mm dia Au contact on the a-Si:H material was also found to be approximately 3.24μA, but the time required to reach the steady state after the application of the 880ns light pulse was much longer (approximately 1.3ms) than for a-As<sub>2</sub>Se<sub>3</sub>.

The establishment of  $H_{\max}$  and the associated value of  $t_{\text{ph}}$  are important parameters when considering the OPT system. The establishment of steady state photocurrent not only dictates the maximum signal current that can be produced by the sample, but also serves as a datum signal for tomographic measurements as previously described. As demonstrated previously, the samples become essentially insensitive to changes in irradiance if the photocurrent is at, or close to the steady state. Since tomographic measurement relies upon variation in irradiance and therefore photocurrent to produce quantitative or qualitative data the peak photocurrent must be prevented from reaching the steady state. This was found to be most readily achieved by adjustment of the illumination period  $t_{\text{ph}}$ .

As observed in the detectivity experiments, both the a-As<sub>2</sub>Se<sub>3</sub> and a-Si:H materials exhibited an increase in responsivity with an increase in applied electric field. Figure 7.3 shows the responsivity vs. electric field for both materials. It can be seen that the a-As<sub>2</sub>Se<sub>3</sub> material is shown to exhibit greater responsivity over all electric fields than the a-Si:H material, again highlighting the a-As<sub>2</sub>Se<sub>3</sub> materials apparent superior photoconductivity. The results of the steady state investigation suggest that the a-As<sub>2</sub>Se<sub>3</sub> material is the more suitable material for OPT applications. The results further suggest, as with the detectivity results, that the electric field should be kept high in order to maximise responsivity and minimise the required levels of irradiance.

### 7.2.3 Establishment of maximum operating speed through the investigation of photoelectric fatigue.

#### (i) Amorphous arsenic triselenide.

The results of the investigation into the effects of fatigue observed in the a-As<sub>2</sub>Se<sub>3</sub> material showed the following:

1. For a fixed value of electric field, irradiance, and  $t_{ph}$ , the signal response was seen to deteriorate over time and that the rate of deterioration was dependant upon the flash repetition rate (FRR). The higher the FRR the higher the rate of degradation observed in the signal response.
2. The rate of decay was not constant but increased in magnitude as time proceeded and did not stabilise over the 30 minute test period.
3. The rate of decay was seen to increase with a decrease in applied electric field.
4. The dark current recorded between issued light pulses was seen to decay with time.
5. The observed effects of fatigue were transient in nature with the a-As<sub>2</sub>Se<sub>3</sub> material regaining its electrical properties after a short rest period at room temperature.

The dark current recorded 1ms prior to a light pulse being issued was seen to deteriorate over the 30 minute test period. The dark current decay was typically within the range of approximately 63% to 46% of its original value by the end of the 30 minute test period. As  $I_d$  is subtracted from  $I_s$  to determine the signal response (R), the decrease in  $I_d$  should result in an increase in R if no fatigue were present. From figure 6.8 it can be noted that no such increase in R is observable indicating that some fatigue is present in the signal response following the initial application of the light pulses.

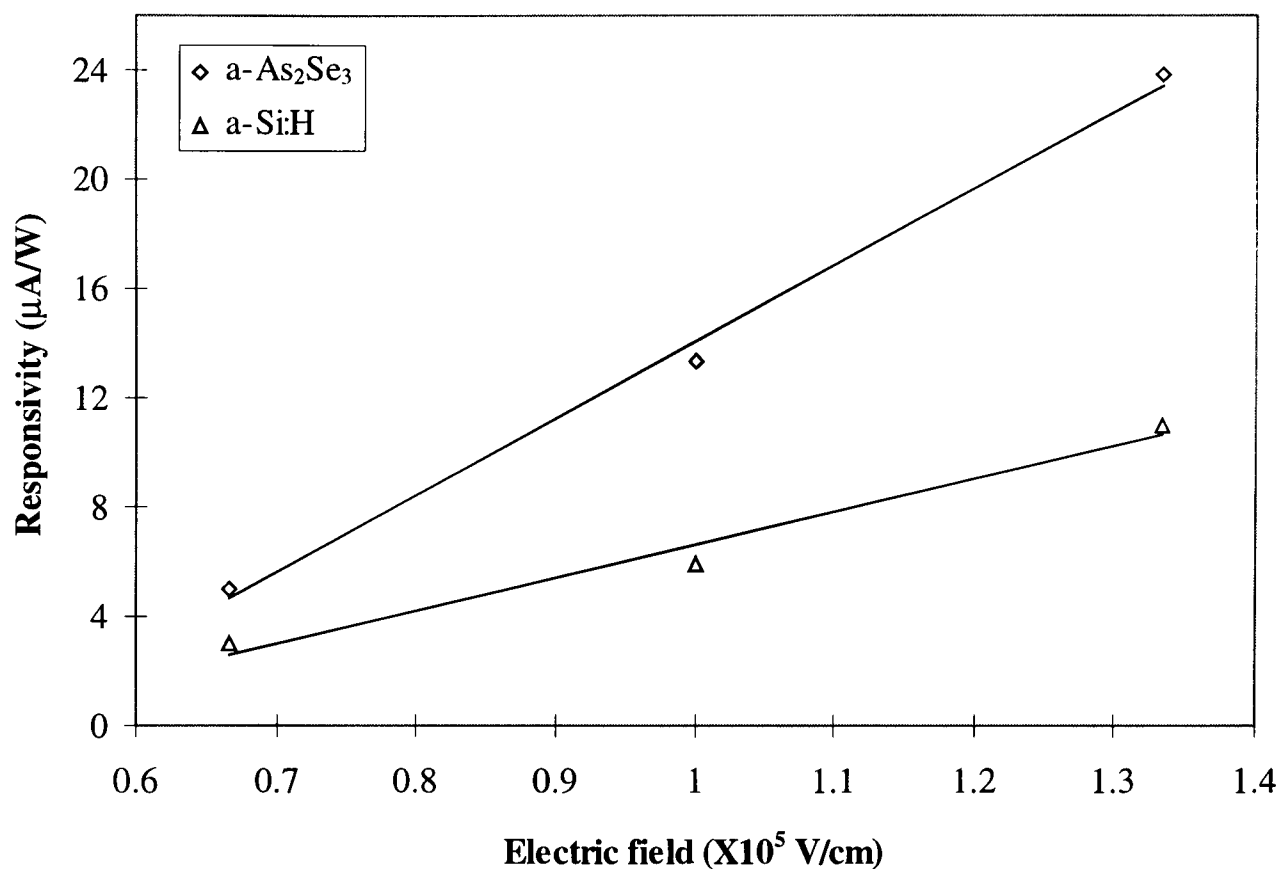


**Figure 7.3** Increase in responsivity due to increased electric field.

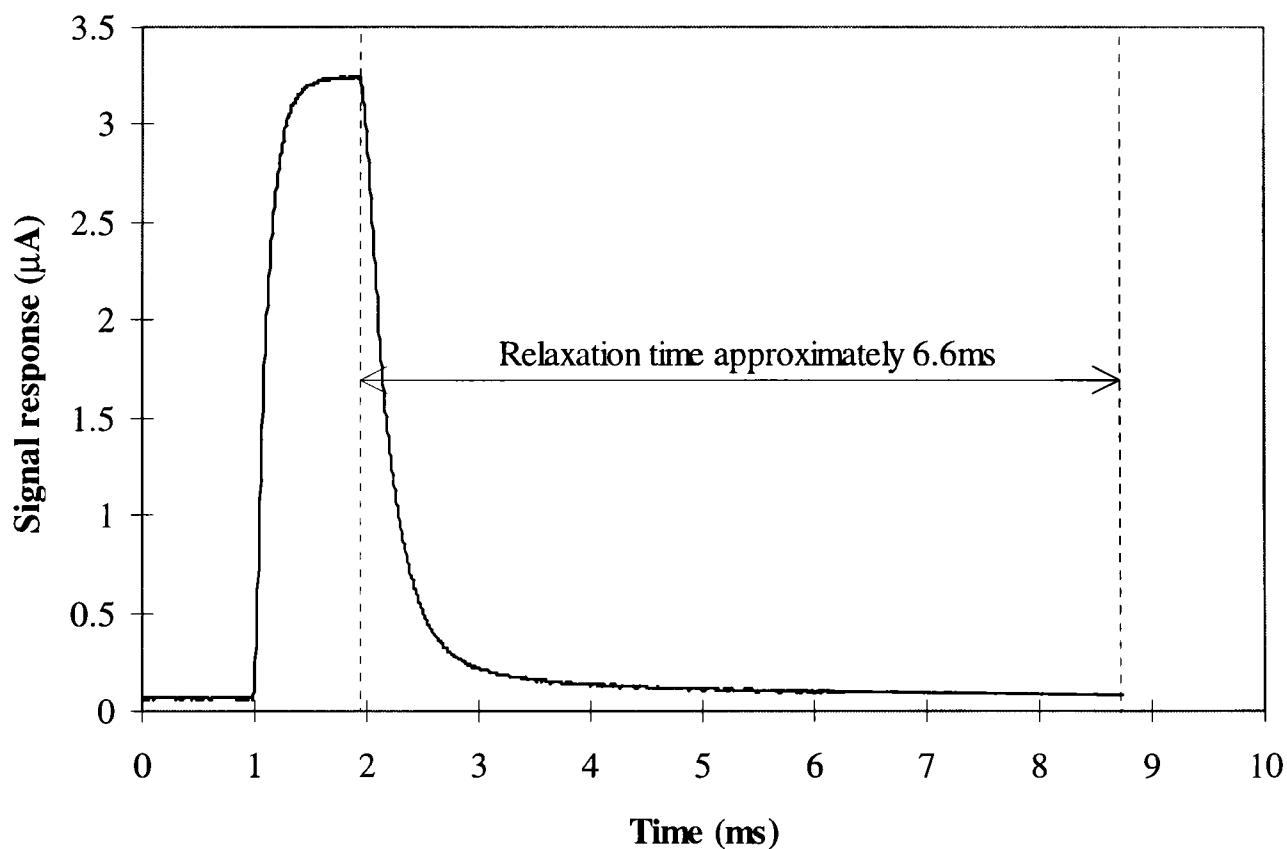


**Figure 7.4** Typical relaxation time in a-As<sub>2</sub>Se<sub>3</sub> after the steady state condition is reached.  $E=1.66 \times 10^5$  V/cm,  $t_{ph}=520$ ns, FRR=100Hz.

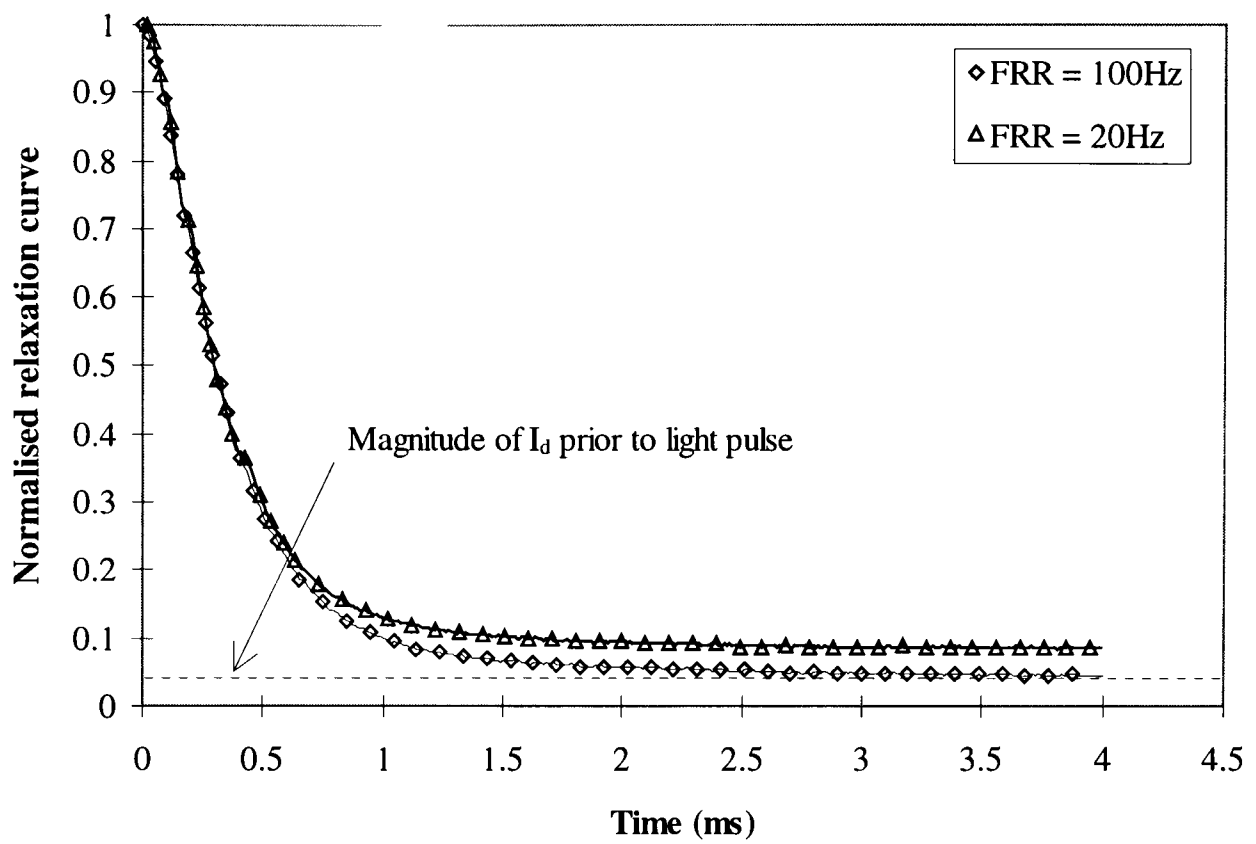
As mentioned previously, the rate of decay of R was seen to decrease with an increase in FRR. The maximum available FRR from the developed xenon flash unit was 100Hz, i.e. a light pulse was issued every 10ms. For a-As<sub>2</sub>Se<sub>3</sub>, light pulse half times of up to 520ns were employed. This resulted in an illumination period of approximately 520ns and a dark period of 9.48ms. The lowest FRR employed in the investigation was 20Hz giving a dark period of 49.48ms, thus the dark period was increased for a decrease in FRR. From the experimental current pulse data, it could be seen that R took typically 6.6ms<sup>†</sup> to relax back to its original magnitude prior to a light pulse being issued. Figure 7.4 shows a typical relaxation curve from the steady state. From the steady state experimentation previously conducted, we know that the time required for R to reach steady state conditions is approximately 830µs. This period added to the relaxation time yields a total time period for the current pulse of approximately 7.5ms. As stated previously, at the maximum FRR of 100Hz a light pulse is issued every 10ms, thus the total time required for a current pulse to be generated and decay back to its original magnitude is within the 10ms time period. If the time required for current pulse generation and relaxation was longer than the 10ms time period between light pulses, it would be expected that the value of I<sub>d</sub> which is calculated over a 1ms time period prior to each successive current pulse would increase as time proceeded. However, no such build up in I<sub>d</sub> was observed which indicated that the deterioration in R observed over the 30 minute test period for FRR's of greater than 20Hz was not caused by relaxation and timing constraints. However, a definite relationship between the FRR and the deterioration of R was observed. Figure 7.5 shows typical normalised relaxation curves taken arbitrarily at t=30mins for FRR's of 100Hz and 20Hz.

Figure 7.5 demonstrates that the rate of photocurrent decay from the peak signal response is faster for the higher FRR of 100Hz with the signal response reaching the value of I<sub>d</sub> prior to the light pulses being applied in approximately 4ms. The signal response at a FRR of 20Hz required approximately 6.5ms to reach the value of I<sub>d</sub> prior to the light pulse being issued. The shorter relaxation time for the FRR of 100Hz is indicative of enhanced conductivity. This increased conductivity is a possible explanation for the decay observed in the signal response at high FRR's as will be discussed further presently.

<sup>†</sup>The figure of 6.6ms was determined from observation of the relaxation curves of photogenerated current pulses recorded during tomographic experimentation.

The longest  $t_{ph}$  employed in the tomographic investigation in a-As<sub>2</sub>Se<sub>3</sub> was 520ns for steady state experimentation which meant that peak light intensity occurred at approximately 260ns. The time required for the signal response to reach steady state conditions was found to take approximately 830 $\mu$ s. This meant that the photocurrent was still increasing long after the termination of the light pulse. This observation could possibly be attributed to the phenomena of persistent photoconductivity, which can in itself be a valid xerographic imaging technique. A persistent photoconductivity image can be formed in the following manner which is essentially the reverse of traditional xerographic techniques. The photoconductive surface of the photoreceptor is illuminated in a desired pattern to form a latent image. During illumination, charge carriers are freed by the absorbed energy and are raised into the conduction band. Many of these electrons will be caught in shallow traps in the bulk of the layer and can remain in a state of near conduction after the illumination has terminated for a considerable period. Areas outside of the illumination pattern will remain non-conductive. The surface of the photoconductor is then charged by a corona device and the electric field established within the bulk of the layer facilitates the dissipation of the surface charge in the conductive regions whilst allowing the non-conductive regions to retain their charge in the dark whilst the latent image is transferred to another medium.

In the current system, a predetermined electric field is maintained within the a-As<sub>2</sub>Se<sub>3</sub> device for the duration of the test period. Light is passed through the semitransparent Au contact into the bulk of the device where charge generation takes place. The experimental results show that photocurrent continues to be produced long after the termination of the light pulse indicating that charge carriers are being released from trapping centres under the action of the applied electric field. The rate at which the charge carriers are being released from the traps i.e. the time required for the signal current to return to its original value prior to a light pulses being applied dictates the speed at which the system can be operated. The current study has shown that this relaxation time decreases for an increase in FRR. The only variable experimental parameter employed in the experiments was the FRR and the resulting dark periods (from 9.95ms at 100Hz to 49.5ms at 20Hz).



**Figure 7.5** Normalised relaxation curves due to varying FRR's.  $E=1.33 \times 10^5$  V/cm,  $H_e=225$  mW/cm<sup>2</sup>,  $t_{ph}=340$  ns.

At lower FRR's there is a longer dark period between issued light pulses. It may be argued that that the longer dark period allows more trapped charge carriers to be released by the action of the applied electric field, thus restoring conductivity prior to the application of the next light pulse. With the higher FRR's, a greater number of charge carriers will become trapped and then released by the electric field thus increasing conductivity prior to the application of the next light pulse. Such an increase in conductivity would lead to a decrease in the signal response as illustrated in figure 6.8. Past authors such as Schaffert (1975), Baxendale (1987), Wolverson and Phillips (1988), Shimakawa *et al* (1990), Abkowitz (1992), and Andriesh (1997) have reported fatigue in a-As<sub>2</sub>Se<sub>3</sub> caused by increased conductivity due to illumination.

#### Wolverson and Phillips 1988

Wolverson and Phillips (WP) sought to demonstrate decay in the photoconductivity of a-As<sub>2</sub>Se<sub>3</sub> under the effects of single pulse, repetitive pulse, and continuous light conditions. The a-As<sub>2</sub>Se<sub>3</sub> samples had coplanar Au electrodes separated by a 0.4mm gap upon their surface. The illumination source for the pulsed experimentation was a 725nm tuneable dye laser which was configured to give a light pulses of 10ns duration at a repetition rate of 2.7s for a period of approximately 4.5 minutes. The resulting photoconductivity of the a-As<sub>2</sub>Se<sub>3</sub> material was then recorded by a transient digitiser after the termination of the light pulse train. WP state that upon the issue of the first light pulse in the pulse train, charge becomes trapped within the bulk of the a-As<sub>2</sub>Se<sub>3</sub> sample. Remaining trapped charge from the initial light pulse then forms the boundary conditions for the next light pulse in the pulse train. At each application of a light pulse in the pulses train, the time scale of the experiment was reset to 0s, i.e. the time scale of the experiment was reset to the last light pulse applied. As the last light pulse in the pulse train was issued, the time scale of the experiment was again reset to 0s and the resulting photocurrent decay due to the release of the charge accumulated during the pulsed illumination period was recorded. The results of the investigation showed that the photocurrent decayed with time and that the rate of decay was dependant upon the repetition rate of the applied light pulse indicating a light history effect.

WP established the signal response by subtracting the value of dark current observed in a well dark rested a-As<sub>2</sub>Se<sub>3</sub> sample from the peak signal current recorded after the termination of the last light pulse to be issued in the pulse train. They did not report the condition of the dark current prior to each light pulse in the light pulse train. Additionally, WP reported the effect of the pulsed illumination period after the termination of the pulse train, but did not report on the condition of the photocurrent during the illumination period. In OPT light pulses are fired through the medium under test and the resulting photocurrents recorded to establish quantitative or qualitative data or a data set for imaging purposes. Thus it is of vital importance to monitor the condition of the photocurrent during the pulsed illumination period.

#### Shimakawa *et al* 1990

Shimakawa *et al* sought to demonstrate the detrimental effect of prolonged illumination upon the photoconductivity of a-As<sub>2</sub>Se<sub>3</sub>. The samples were 1.4µm thick and had Al electrodes placed 5mm apart on their surface. Visible light was provided from a tungsten halogen lamp configured to give an irradiance of 480mW/cm<sup>2</sup>. The authors state that during constant illumination (up to approximately 83minutes), the value of peak photocurrent decreased with time, and at extended time periods approached a saturation level. The sample was then allowed to rest in the dark for several hours and the illumination was reapplied. The peak photocurrent was found to have remained at the saturation level indicating that the photoconductivity of the a-As<sub>2</sub>Se<sub>3</sub> material had become 'frozen' due to the effects of the initial illumination. The sample was then annealed at 200°C for two hours and the test was re-run. The peak photocurrent was found to have returned to its original order of magnitude, i.e. the annealing process reversed the 'frozen' state induced by the initial illumination period.

Shimakawa *et al* attributed the decay of the photocurrent and the 'frozen' state to the illumination creating trapped charged metastable defects within the bulk of the a-As<sub>2</sub>Se<sub>3</sub> material. These defects were then stated as being the probable origin of an increased density of trapping centres which had been presumed to have led to the decrease in photocurrent. It was stated that the annealing process allows relaxation of the structure of the a-As<sub>2</sub>Se<sub>3</sub> material and thus the photogenerated metastable defects are reversible after annealing. In the present research, the degradation observed in the

magnitude of the photocurrent during the illumination period was not persistent. At the end of the 30 minute test period if the FRR was decreased to around 0.25Hz for example, the peak signal response was seen to start to recover and increase in magnitude with time, i.e. the degradation observed in the signal response was transient in nature. The absence of persistent degradation in the signal response was attributed to the fact that the light exposure times (520ns max) were very short compared to the exposure time employed by Shimakawa *et al* (up to 83 minutes). Additionally, the a-As<sub>2</sub>Se<sub>3</sub> material employed in the current research was 60μm thick which was exposed to a maximum irradiance of 319mW/cm<sup>2</sup> as opposed to the 1.4μm thick samples employed by Shimakawa *et al* which were exposed to a maximum irradiance of 480mW/cm<sup>2</sup>. The increased film thickness and reduced level of irradiance may have led to a decreased density of trapped charges due to the decreased depth of penetration of the issued light when compared to the system described by Shimakawa *et al*. Samples of a-As<sub>2</sub>Se<sub>3</sub> of varying thickness were not available to the research project and so this supposition could not be confirmed.

#### Abkowitz 1992

Abkowitz sought to clarify the effect of illumination on the light induced fatigue observed in various chalcogenide glasses by experimentation in both xerographic and electroded modes of operation. In the electroded mode of operation, continuous and pulsed visible light of varying duration and repetition rate was applied to the sample under test via a semitransparent contact on the sample surface (the contact material and geometry was not specified). An electric field was established in the sample by transient contact to a DC power supply. Initial experiments performed by Abkowitz were to determine if the chalcogenide material exhibited a light memory effect i.e. was the conductivity altered after the application of visible light. After exposure to illumination the sample was allowed to rest in the dark for a variable time period (from ms to several seconds). The results of this process showed that if the sample was charged after a 2s dark rest period after illumination (10mins), the conductivity of the material increased by more than an order of magnitude when compared to a sample that had been un-illuminated prior to being charged. This had a degrading effect upon the materials ability to retain the applied charge as has been observed in the current research with the deterioration of R over time.

Abkowitz then went on to ascertain the effect of the illumination period on the residual potential under increasing number of xerographic cycles. Abkowitz showed the level of residual potential encountered for exposure times from 1s to approximately 2.5 hours for a xerographic plate that had undergone 1 xerographic cycle and a xerographic plate that has undergone 100 xerographic cycles. The results clearly showed the residual potential for the xerographic plate that received 100 cycles was significantly higher than for the xerographic plate that received one cycle, and that the longer the exposure time, the higher the value of residual potential encountered. At long exposure times an increase of up to 200% was seen in the magnitude of residual potential for the xerographic plate that had undergone 100 cycles. Abkowitz attributed the increase in residual potential to an increase in the number of injected charge carriers becoming deeply trapped within the bulk of the device, i.e. for longer exposure times, a greater density of charge carriers were produced which then became deeply trapped and therefore increased the residual potential.

However, Abkowitz argued that for short light exposure times ( $\ll 1s$ ) the residual potential encountered for the xerographic plate that had undergone 100 cycles was comparable to a xerographic plate that had been completely dark rested and undergone no period of illumination. Thus for very short exposure times, no significant increase in residual potential was observable over multiple cycles. In the current research, the maximum  $t_{ph}$  employed into the investigation of fatigue in  $a\text{-As}_2\text{Se}_3$  was 520ns and no increase in residual potential as observable over the time scale of the experiment.

#### Andriesh 1997

Andriesh stated that the interaction of radiation with chalcogenide materials can lead to reversible and irreversible changes in the atomic and electronic structures of these materials, and that these changes can manifest themselves as mechanical, thermal, optical, or photoelectric changes. In agreement with the works described previously, Andriesh claimed that prolonged exposure to light causes a decrease in the photoconductivity in amorphous chalcogenides, and that the longer the exposure time the greater the degradation of photoconductivity. Andriesh employed pulsed visible light for a period of approximately 1.5mins (each light pulse being 2.7s in duration) to observe the nature of the resulting photocurrent pulses. Upon application of the first

light pulse, the photocurrent reached approximate steady state conditions. Upon the application of the second light pulse, the photocurrent was seen to reach the steady state condition at a faster rate than for the previous pulse indicating that conductivity had been enhanced. Upon comparison of the relaxation curves from the two experiments, it was reported that the time required for the relaxation curve due to the second light pulse to relax back to the level of current prior to the application of the initial light pulse, was shorter than for the first pulse. This demonstrated that as time proceeded the conductivity of the material was increasing. Andriesh's description of the shortening relaxation times due to successive illumination could relate to the shorter relaxation times observed in the current research as illustrated in figure 7.5.

Although characteristics of photoinduced fatigue such as degradation of signal response as a function of FRR has been demonstrated in the current study, the exact mechanism that causes the fatigue has not been established. All published works previously described with the exception of Andriesh (1997), investigated the photoconductivity after the termination of an illumination period and did not report the condition of the photocurrent during a pulsed illumination period as would be required for the investigation of the material for tomographic application. Although Andriesh employed an asynchronous light pulse, the 2.7s illumination period was significantly longer than the 520ns light pulse half times employed in the current study. An additional feature of the current study not employed by the workers described above, was the presence of a high electric field throughout the illumination period. The elucidation of the exact nature of the physical phenomena that led to the degradation of the signal response in the a-As<sub>2</sub>Se<sub>3</sub> material under pulsed illumination and constant electric field is beyond the scope of the current research project and is therefore suggested as further work.

The repetition rate at which light pulses can be issued dictates the speed of operation of any potential tomographic system. A maximum FRR of 20Hz was found to apply to the a-As<sub>2</sub>Se<sub>3</sub> material if degradation of the signal response was to be avoided. As OPT requires a minimum operating speed of 100Hz, the maximum FRR of 20Hz dictated that the a-As<sub>2</sub>Se<sub>3</sub> material was unsuitable for application in OPT systems and experimental investigation into the collection of quantitative and qualitative data was not performed for this material.

(ii) Hydrogenated amorphous silicon

The following observations were made during the investigation into the effects of photoinduced fatigue in a-Si:H.

1. For a fixed value of electric field, irradiance, and  $t_{ph}$ , the signal response seemed to deteriorate significantly in the first few minutes of operation after which time the signal response was stable.
2. The rate of deterioration was dependant upon the FRR. The higher the FRR the lower the rate of degradation observed in the signal response.
3. The dark current calculated 1ms prior to each successive light pulses was seen to increase with time and FRR.
4. The saturation level of the signal response could be set by adjustment of the applied electric field.
5. The effects of fatigue observed in the signal response seemed to be transient in nature.

Figure 6.22 shows the signal response for an electric field of  $0.66 \times 10^5$  V/cm under varying levels of FRR. The data points at  $t=0$  were recorded manually as a single pulse for reasons explained previously. Thus the data at  $t=0$  exhibits no fatigue and was approximately  $3.2 \mu\text{A}$  in magnitude for all FRR's. Upon application of the pulse train, the signal response was seen to deteriorate by approximately 32% to 37% of its original value within the first minute of operation. After this period the signal responses were seen to stabilise at a constant level. The magnitude at which the signal response stabilised was found to be dependant upon the FRR, and the magnitude of the signal response seemed to increase with an increase in FRR.

The dark current associated with the experimentation was seen to increase in magnitude over the 30 minute test period for all FRR's and that the higher the FRR the greater the increase in dark current. From the steady state experimentation described previously, it was noted that the time required for the signal current to reach approximate steady state conditions was approximately 1.1ms which was in response to a light pulse of 880ns half time with the peak light intensity occurring at approximately 440ns. As with the a-As<sub>2</sub>Se<sub>3</sub> material, the signal current appeared to

increase after the termination of the light pulse. The time required for the signal current to relax back to its original value prior to the application of the light pulse was found to be typically in the order of 9.8ms at a FRR of 100Hz. Thus a total time of approximately 11ms was required for the signal current to increase to its maximum value and relax back to its original value prior to the light pulse being issued. As the time interval between light pulses at 100Hz was 10ms, the signal current could not relax back to its original value prior to the light pulse being issued, and so the value of  $I_d$  calculated 1ms before the next light pulse in the pulse train issued increased in magnitude accordingly. The increase in dark current was therefore attributed to the fact that the signal response did not have sufficient time to relax back to its original value before a successive light pulse was applied, and so residual potential accumulated over the 30minute experimental period. The increase in dark current however, did not account for the large decrease in signal response observed over all FRR's.

Hydrogenated amorphous silicon is known to suffer from light induced degradation (LID) and this phenomena was first reported by Staebler and Wronski in 1977 who reported that significant changes in the dark conductivity and the photoconductivity were observable in a-Si films when subjected to long exposure of high intensity light. This was attributed to the creation of metastable defects which could be reversed by annealing at temperatures of greater than 150°C for a period of greater than 1 hour. The conclusions drawn from this work were that illumination with intense light leads to the creation of additional metastable states in amorphous silicon which influences its electronic and optical properties by decreasing the lifetime of excess generated carriers (Stutzmann *et al*, 1985). Guba (2000) states that LID has been the focus of extensive research over the last 20 years and that although it has generally been accepted that intense illumination results in the formation of metastable dangling bond defects, the exact nature of the defect generation is still a matter of conjecture. Guba explains that exposure to high intensity light can increase the density of neutral dangling bonds within the bulk layer of the a-Si:H material thus decreasing the photoconductivity. According to Guba, metastable defects can also be created by charge injection by the application of an electric field for example. Further causes of metastable defects are cited as impurities within the a-Si:H material and more recently that light exposure not only creates metastable defects, but actually changes the

structure due to the applied light altering the compressive stress of the material which results in expansion of the a-Si:H material.

Although it is difficult to draw firm conclusion as to the exact physical cause of degradation in a-Si:H, the following effects have been widely reported. (i) Photoconductivity seems to diminish over time when exposed to illumination. (ii) High intensity illumination for a short period causes a higher rate of degradation than lower intensity illumination at longer periods. (iii) Higher rates of degradation have been observed in thicker devices, the thicker the device, the higher the rate of degradation. (iv) The rate of degradation is not continuous but seen to reach a saturation level over time. (v) The photoconductivity may remain at the saturation level for extended periods of time, and that the photoconductivity can be restored to its original level prior to illumination by annealing.

From figure 6.22 it can be seen that in the current research the signal response decays very quickly in approximately the first minute to 2.5 minutes of the illumination period depending upon the FRR. The signal responses then reach a saturation level. Similar observations were made by Stutzmann *et al* in 1985.

#### Stutzmann *et al* 1985

Stutzmann *et al* report the time dependence of photocurrent when subjected to continuous light of ranging from  $1.7\text{mW/cm}^2$  to  $170\text{mW/cm}^2$  for a  $7\mu\text{m}$  thick a-Si:H sample. The illumination period was in the order of 90 minutes. The results showed that for light of  $1.7\text{mW/cm}^2$ , negligible degradation was observed in the photocurrent over the 90 minute exposure time. For light of  $17\text{mW/cm}^2$  the magnitude of the photocurrent had increased, and slight degradation of the photocurrent was observable. For light of  $170\text{mW/cm}^2$  however, a significant increase in photocurrent and degradation was observed. The initial photocurrent at  $t=0$  was approximately  $2.5\mu\text{A}$ . The photocurrent was seen to decay by 20% of its original value at  $t=2.5$  minutes and 50% of its original value at  $t=20$  minutes. The photocurrent was then seen to approximate a saturation state decaying to around 64% of the original level of photocurrent by the end of the 90 minute exposure time. Their results clearly showed that the rate of light induced degradation was dependant upon the intensity of the

light, and that the higher the light intensity the greater the rate of degradation. The authors attributed this phenomena to the fact that a greater density of dangling bond defects are created at higher light intensities leading to greater degradation observed in the photocurrent. Stutzmann *et al* state that at an exposure time of 90 minutes, light of  $50\text{mW/cm}^2$  yielded in the order of approximately  $1.3 \times 10^{12}$  dangling bond defects. Light of  $700\text{mW/cm}^2$  was stated as yielding in the order of  $7.5 \times 10^{12}$  dangling bond defects.

In the current research the photocurrent at a FRR of 100Hz for example, decayed by 20% of its original value in approximately 30s and decayed by approximately 30% of the original value to a saturation level after approximately 1 minute (extending to 2.5 minutes for lower FRR's). Thus the results show that the degradation observed in the current research was significantly faster that that as described by Stutzmann *et al*. The increase in the rate of degradation could be attributed to several possible causes.

1. The light employed in the fatigue experiments shown in figure 6.22 was  $693\text{mW/cm}^2$  which was significantly higher than the maximum  $170\text{mW/cm}^2$  employed by Stutzmann *et al*. An irradiance of  $693\text{mW/cm}^2$  was required in order to position the peak signal response just under the steady state for reasons previously described. Stutzmann *et al* demonstrated that degradation of the signal response occurred at a much faster rate for higher light intensities, thus the faster rate of degradation observed in the current research could possibly be due to the higher value of light intensity.
2. Guba (2000) states that increased degradation is observed in thicker a-Si:H devices. The a-Si:H device employed by Stutzmann *et al* was  $7\mu\text{m}$  in thickness, the a-Si:H device employed in the current research was  $27.1\mu\text{m}$ . Thus it is possible that the increased rate of degradation observed in the signal response was due to the increased thickness of the device. Samples of a-Si:H of varying thickness were not available to the research project and so this supposition could not be confirmed.
3. A fundamental difference of the illumination employed in the current research to that of Stutzmann *et al* is that the illumination is pulsed. Redfield and Bube (1996) state that pulsed illumination can be employed to accelerate the degradation process. The aim of this procedure was to allow experimental investigations of LID

to be carried out without the need for very long (up to several weeks) exposure times of continuous light. Rossi *et al* (1992) described an accelerated degradation test employing pulsed light from a xenon source.

### Rossi *et al* 1992

Rossi *et al* state that in order to ascertain the long term effects of LID, several techniques had been commonly employed previously to accelerate the rate at which the degradation occurred in order to speed up the experimental process. Such techniques included applying very high intensity constant illumination (up to  $14\text{W}/\text{cm}^2$ ), current injection, and electron irradiation. However, these techniques were stated as causing heating of the sample or creating irreversible defects. Rossi *et al* attempted to accelerate the degradation process by employing pulsed light from a xenon source. The light pulses were of approximately  $2\mu\text{s}$  duration with a repetition rate of 300Hz at  $100\text{mW}/\text{cm}^2$  and 30Hz at  $10\text{mW}/\text{cm}^2$ . The light from the xenon source was filtered by a ultra-violet filter and a infrared filter in order to simulate natural sunlight, i.e. visible light. Rossi *et al* initially sought to induce a 35% reduction in device efficiency due to LID by applying continuous light, pulsed light at 300Hz, and finally 30Hz. The sample was kept in an open circuit condition for all cases.

The results showed that for the same light intensity, a 35% reduction in device efficiency could be induced by the application of continuous light for a period of 30 hours. The same 35% reduction in efficiency could be induced in 20 minutes using pulsed illumination at 300Hz. Thus the use of pulsed illumination had resulted in the effects of LID being accelerated by a factor of 90. Rossi *et al* attribute the accelerated degradation to the pulsed light to metastable defects created by the recombination of localised electron-hole pairs. The high generation rate induced by pulsed illumination was stated as being able to maintain the recombination period for an extended period of time, thus leading to accelerated degradation.

As the current research employed pulsed illumination for tomographic purposes, a possible explanation of the rapid degradation observed in the signal response is that accelerated degradation had occurred due to the pulsed nature of the illumination. However, unlike Stutzmann *et al* and Rossi *et al* the level of degradation was not seen

to persist after the pulsed illumination period and the photocurrent could be seen to return to its original magnitude after a short rest period without the need for annealing. The difference between the current research and systems as described by Stutzmann *et al* and Rossi *et al* and others where the sample is held at the system ground or is open circuited, is that in order to produce suitable levels of photocurrent required for tomographic purposes, a high electric field is maintained across the a-Si:H sample constantly during the pulsed illumination period. A detailed analysis of the physical phenomena of LID due to pulsed light in the presence of a high electric field is outside of the scope of the current research and is therefore suggested as further work and is discussed further in chapter 8.

In terms of OPT, although degradation is observed in the signal response of the a-Si:H material over all FRR's and electric fields investigated, the degradation occurring at the required FRR for OPT (100Hz) occurs in approximately the first 60s of operation and then settles to a constant level with no further degradation observed over the 30 minute test period. The tomographic investigation has shown that the degradation is repeatable and the magnitude of the saturation level can be varied by the adjustment of the electric field as can be seen in figure 6.28. As will be discussed presently, experimentation employing tomographic prototypes has shown that once degradation in the signal response has ceased and the saturation level has been obtained, the a-Si:H material remains sensitive to changes in light intensity and therefore is suitable for tomographic application.

#### 7.2.4 Establishment of quantitative data.

The purpose of this experimental investigation was to determine if different levels of fluid could be accurately distinguished by the a-Si:H sensor at speeds required for OPT and after light induced fatigue of the material had terminated and stable level of signal response obtained. The experimental procedure employed the use of a single contact located centrally upon the sample as described previously. This configuration approximated a parallel beam projection system in that a single light source was trained upon a single contact. This single contact then formed a single view of a projection through the pipeline. Figure 6.34 shows the profile of the signal response through the entire cross section (44mm internal diameter) of the pipeline due to varying levels of water.

The results showed that the a-Si:H sensors was sensitive to changes in irradiance falling upon its surface after LID had taken place and at the required FRR of 100Hz. The results also showed there were various regions of sensitivity with 1mm changes in water level being detectable in the 0mm - 5mm range and 25mm to 44mm range. This meant that if a plug of air were to appear in the top 19mm of the pipeline, the position of the bottom of the plug could be accurately determined. If the bottom of the plug were to extend past the 19mm mark however, it would be known that a large plug of air for example had entered the sensing zone and that it extended into the bottom 25mm of the pipeline. However, unless the bottom edge extended in the bottom 5mm of the pipeline the bottom could not be accurately determined due to the 'flat' region observed in the signal response in the 5mm to 25m region of the pipeline. As stated previously, the results shown relate to a single view through the pipeline. Figure 7.6 shows the anticipated effect of taking a second view though the opposite side of the pipeline. The second view through the pipeline would provide the same regions of sensitivity as seen for the initial view. However, as the view was now looking from the other side of the pipeline the sensitive regions would interchange and the 20mm of 'flat' signal response would reduce to an anticipated 6mm. If multiple views were to be taken from equal distances around the perimeter of the pipeline it is believed that a 6mm diameter area would result in the centre of the pipeline which would be difficult to resolve.

As mentioned previously, the peak photocurrent due to an increase water level was higher in magnitude at each successive increase. This was due to the fact that the water within the pipeline was acting as a magnifying medium and the measured irradiance falling upon the light detection mechanism detailed in section 4.2.4 was seen to increase with an increase in water level. Thus rather than the light being attenuated by the fluid as it passed through the pipeline, the opposite was true. This was attributed to the fact that the angles of reflection/refraction of the light as it passed through the pipeline was altered by the changing water level, thus the amount of light received by the sensor varied accordingly. This variation in signal response due to magnification and not attenuation was not seen as significant. The peak signal response obtained for the various water levels have been shown to be repeatable over multiple test runs with the magnitude of the peak signal response being directly related to the level of water in the pipeline.

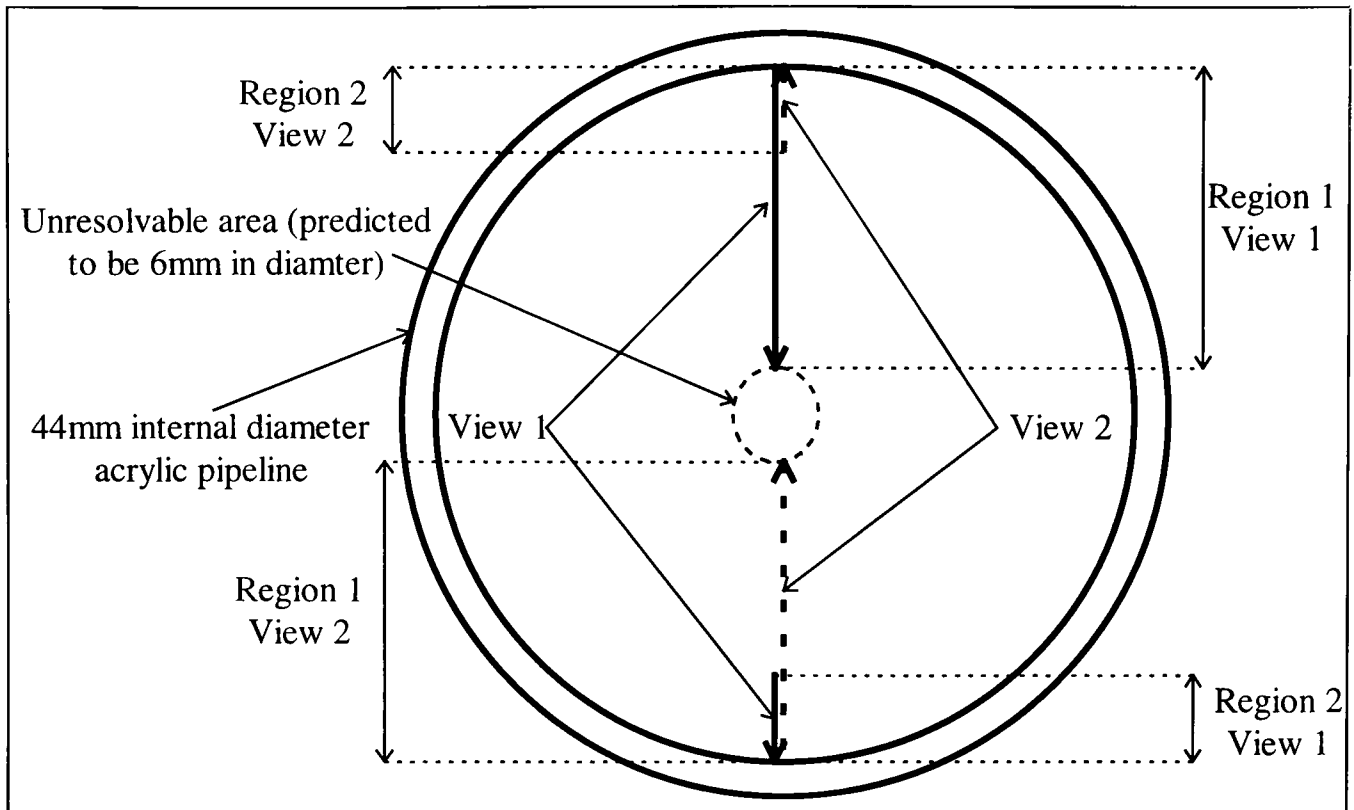


**Figure 7.6** Sketch of the regions of greatest sensitivity through pipeline diameter. Region 1 relates to the top 19mm of the pipeline, region 2 relates to the bottom 5mm of the pipeline.

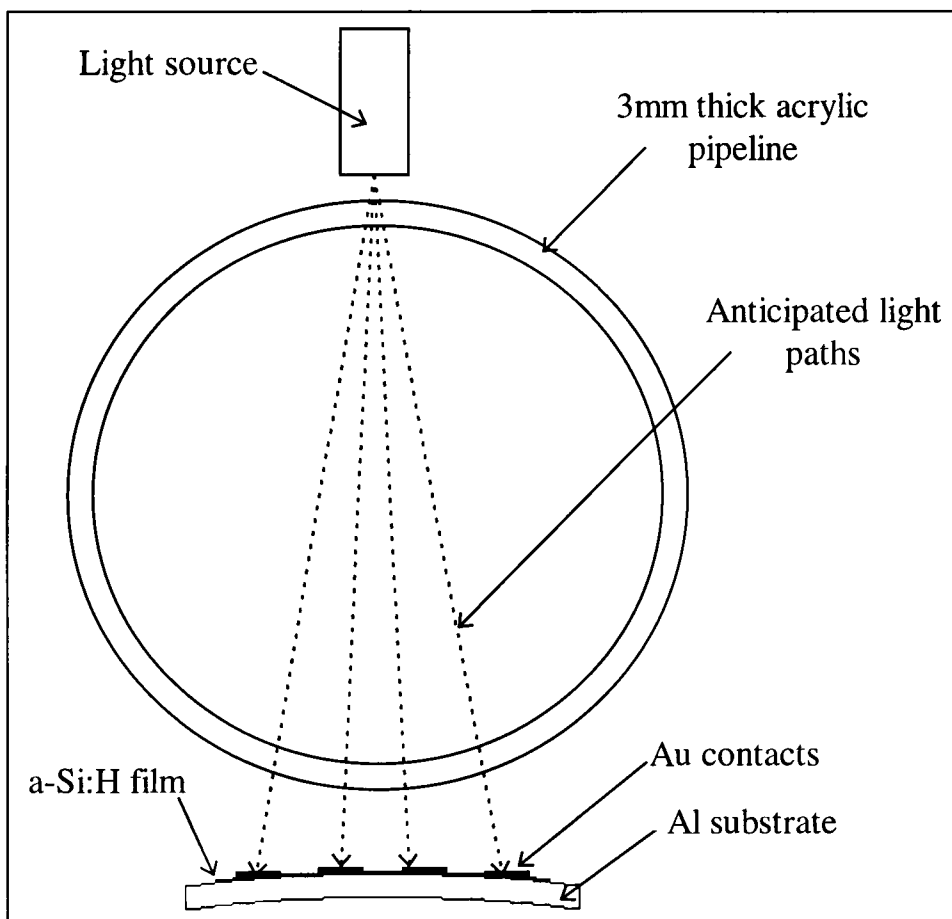


**Figure 7.7** Sketch of simplified light paths through the pipeline.

### 7.2.5 Establishment of qualitative data.

The aim of the qualitative investigation was to see if the a-Si:H sensor was sensitive enough to detect small changes in fluid colour within the pipeline thus indicating the a-Si:H material suitability for application in batch monitoring. Figure 6.36 shows the results of this investigation. It could be seen that the peak signal response was seen to decrease for an increase in fluid colour. Thus the light was being attenuated as it passed through the fluid mix. From figure 6.36, it could be seen that the sensitivity to changes in fluid colour was not constant but varied with fluid mix. It has been shown that maximum variance in changes of irradiance can be obtained by positioning the peak photocurrent just under the steady state condition. The variance in sensitivity observed as the fluid mix was increased, was attributed to the fact that the peak photocurrent at dense fluid mixes moved the peak signal response well away from the near steady state condition and into a region of insensitivity.

However, the variance in sensitivity observed over the range of fluid mix could be maximised by repositioning the peak signal response to just under the steady state condition for a given fluid mix. This procedure resulted in 0.5% changes in fluid colour to be accurately detected by the a-Si:H sensor over a 3% change in fluid mix. However, sensitivity decreased once more as the fluid mix increased beyond 3%. The sensitivity could be maximised once more by repositioning the peak photocurrent for the new level of fluid mix. This would mean that any potential tomographic system would have to have a means of changing the sensitivity of the signal response for a given range of fluid mix. This would be a very similar process to changing the voltage range on a voltmeter for example to coincide with a desired measurement. The peak signal current has shown to be adjustable by changing the intensity and duration of the issued light pulses. The developed xenon flash unit lends itself very well to this task where it has been shown that the intensity and duration of the light pulse can be easily set to a predetermined level by variation in discharge capacitance and input voltage.

### 7.2.6 Production of basic images.

#### (i) Bottom curvature of the pipeline.

The purpose of this investigation was to see if the a-Si:H sensor was sensitive enough to be able to determine variance in irradiance due to the insertion of a section of pipeline between the sensor and the light source, i.e. to determine if a range of signal response could be determined that resembled the curvature of the pipeline. The sensor arrangement was a single a-Si:H sample with sixteen  $2.5\text{mm}^2$  Au contacts spaced 1mm apart on its surface. This resulted in a 4 x 4 array. The illumination from the light source was applied in a cone beam projection manner with all 16 contacts being illuminated at the same time. The results showed that the signal response for the contact array did indeed produce a curved response as can be seen in figure 6.40. It was seen however, that the response was a positive going curve. This was attributed to the fact that due to the manner of cone beam projection, the length of the light paths through the pipeline to the sample surface varies. This differs from parallel beam projection in which the light paths from the source to the sensor are identical for every emitter/detector pair in the array. Figure 7.7 shows a sketch of the projection mechanism.

From figure 7.7 it can be seen that the middle two columns of contacts are physically closer to the bottom of the pipeline due to the curvature of the sample and the pipeline. The difference in height of the contacts upon the sample surface was estimated to be in the order of approximately 0.5mm and was deemed not to be significant when compared to the curvature of the pipeline itself. In order to ascertain if the a-Si:H sensor was sensitive to changes to light path length, i.e. distance from the light source to the sensor surface, a further experiment was performed. An a-Si:H sample with a single  $2.5\text{mm}^2$  contact located in the centre of the sample was positioned directly beneath the light source at a distance of 60mm (distance required for the insertion of the 44mm internal diameter pipeline). The light source was warmed up as previously described, and three current pulses were recorded at 15s intervals. The height of the light source was then increased by approximately 1mm and the test re-run. This process was repeated until the height of the light source had been increased from 60mm to 65mm. The results of this process can be seen in figure 7.8.

The results of the tests showed that the a-Si:H sensors were sensitive to changes of approximately 1mm in height from the light source to the sensor surface. The variance observed in the signal response could therefore be attributed to the 'fan out' of the light from the source and the curvature of the bottom of the pipeline. Multiple test runs were performed on each contact in the contact array and very good reproducibility of results was obtained. The magnitude of peak signal response is directly related to the amount of light falling upon the surface of the contact and the amount of light that falls upon the surface of the contact is in turn directly related to whatever is inserted between the light source and the sensor. Thus the variance in signal response encountered was deemed to be an accurate representation of the bottom of the pipeline.

#### (ii) Phantom object

The purpose of these series of tests was to see if an object placed on the bottom of the pipeline could be determined. The results of this process are shown in figure 6.42. Out of the sixteen contacts in the array, four were left uncovered, eight were left partially covered, and four were fully covered. As expected the results showed that the peak signal response decreased in relation to the amount of coverage of the contact by the phantom object. By the use of uncovered, partially covered, and fully covered contacts, it was demonstrated that the position of the phantom object relative to the bottom section of the pipeline previously determined, could be established by inspection of the peak signal response and comparing it to the peak signal response due to the bottom of the pipeline. However, an accurate image of the phantom object would require the use of multiple projections through the pipeline to determine its full geometry. This is discussed further in chapter 8.

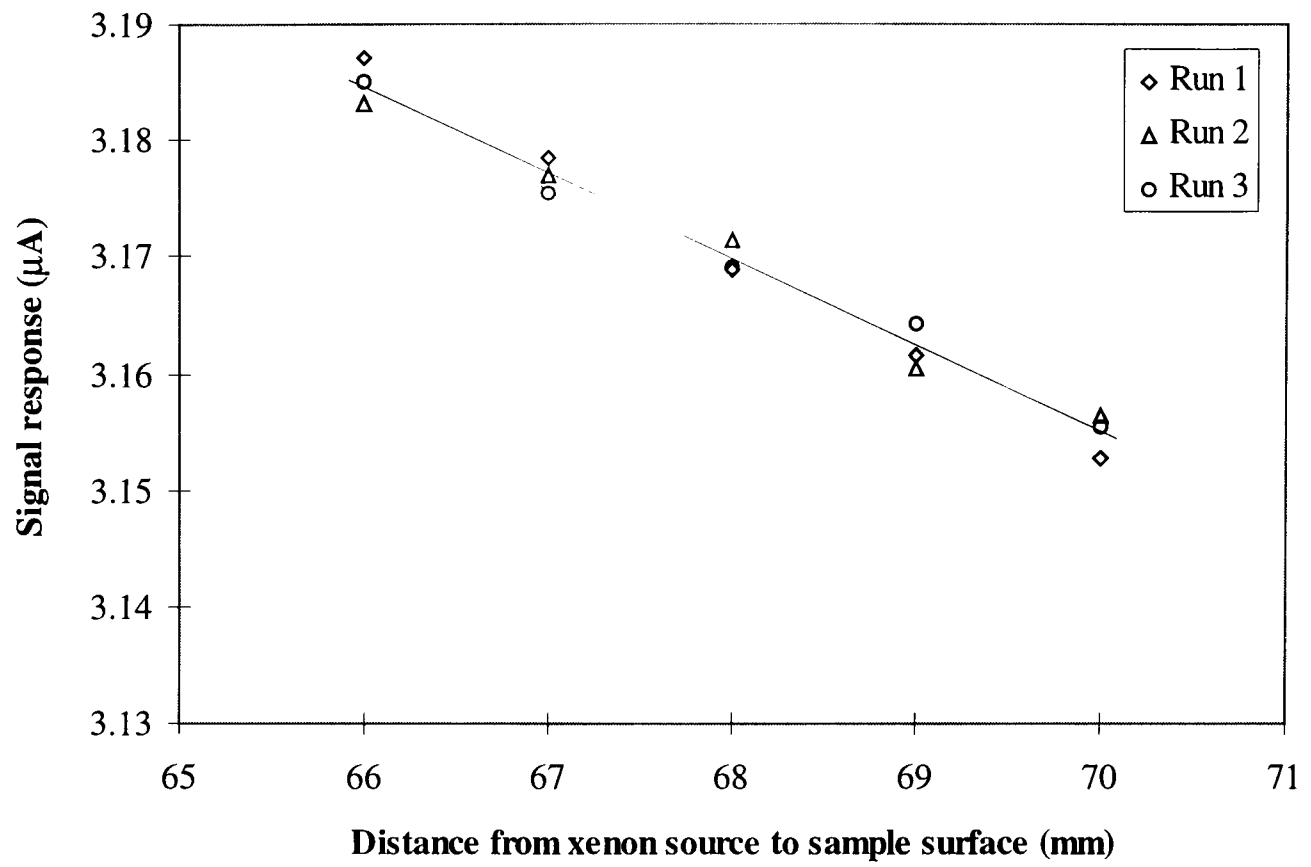


**Figure 7.8** Effect of altering distance of light source from sample surface.

## CHAPTER 8

### CONCLUSIONS AND SUGGESTIONS FOR FURTHER WORK

The aim of this chapter is to draw conclusion to the experimental findings reported in chapters 5 and 6 and also to suggest topics for further investigation.

#### 8.1 Amorphous arsenic triselenide

##### 8.1.1 Xerographic investigation

The xerographic investigation conducted upon the a-As<sub>2</sub>Se<sub>3</sub> device employed in this research, has shown that high charge acceptance in the order of 1080V giving a surface charge density of approximately  $1.7 \times 10^{-7}$  C/cm<sup>2</sup> was achievable indicating high dark resistivity. The rate of the dark decay in the a-As<sub>2</sub>Se<sub>3</sub> material was found to be field dependant, and half decay times of up to approximately 2.5 minutes were encountered. Residual potentials of approximately 20V or less were encountered for the material. All of these experimental measurements fall within the range of values that are considered to be suitable for xerographic application as has been stated previously in this thesis. Analysis of the dark discharge mechanism has concurred with other workers in that the dark discharge mechanism proceeds via a xerographic depletion discharge process. The overall conclusion of the xerographic investigation was that the a-As<sub>2</sub>Se<sub>3</sub> material employed in the current research exhibited all of the qualities that would be expected of a material for application in xerography. It was therefore concluded that the integrity of the a-As<sub>2</sub>Se<sub>3</sub> material had been established. Qualities such as high charge acceptance, high dark resistivity, greatly enhanced conductivity upon illumination, and low residual potentials are highly desirable in tomographic sensors. The xerographic investigation not only confirmed the integrity of the a-As<sub>2</sub>Se<sub>3</sub> material but also demonstrated that the a-As<sub>2</sub>Se<sub>3</sub> possessed the aforementioned qualities that would make a potential hard field optical sensor for OPT application.

##### 8.1.2 Tomographic investigation

The results of the tomographic investigation has shown that the a-As<sub>2</sub>Se<sub>3</sub> exhibited superior detectivity, responsivity, and speed of response when compared to the a-Si:H material, initially indicating that it was the more suitable of the two materials for tomographic application. However, an investigation into the effects of photoinduced

fatigue caused by pulsed illumination revealed that the a-As<sub>2</sub>Se<sub>3</sub> material could not be operated at FRR's of greater than 20Hz if degradation of the signal response was to be avoided. As OPT systems require a FRR of 100Hz or greater the a-As<sub>2</sub>Se<sub>3</sub> material was deemed unsuitable for application in OPT and was eliminated from further tomographic investigation.

## 8.2 Hydrogenated amorphous silicon

### 8.2.1 Xerographic investigation

The a-Si:H material was found to have high charge acceptance in the order of 655V which related to a surface charge density of  $2.15 \times 10^{-7} \text{ C/cm}^2$ . The rate of dark decay was again found to be field dependant and half decay times of up to approximately 30s were encountered in agreement with past workers as previously described. Residual potentials of approximately 20V were encountered in this material. Analysis of the dark discharge curves by the application of existing mathematical models developed to elucidate the nature of the discharge mechanism in a-Si:H, yielded comparable results to those published previously by other workers. As good comparison of results had been achieved, the integrity of the a-Si:H material employed in the current research had been confirmed.

### 8.2.2 Tomographic investigation

The results of the detectivity investigation showed that the a-Si:H material required an irradiance of between  $5.31 \text{ mW/cm}^2$  and  $28.32 \text{ mW/cm}^2$  depending upon the magnitude of the applied electric field in order to produce the smallest possible clean and repeatable photogenerated current pulse. The purpose of the detectivity experimentation was to determine the lowest light levels that the a-Si:H device could respond adequately to. Thus any potential imaging system would have to ensure that irradiance of at least  $H_{\min}$  (for a given electric field) would have to be incident upon the sensor surface after passing through whatever vessel and process was inserted between the light source and the a-Si:H sensor. Steady state experiments have shown that an irradiance of  $693 \text{ mW/cm}^2$  to  $2.62 \text{ W/cm}^2$ , again depending upon the applied electric field, is required to drive the signal response into approximate steady state conditions. The purpose of these series of tests was to establish the maximum incident irradiance ( $H_{\max}$ ) for the a-Si:H device. Light of a higher irradiance or longer duration would not produce a higher magnitude of signal response but would extend the time

that the signal response remained at the steady state condition. As has been demonstrated, if the signal response is allowed to remain in a steady state or near steady state condition, the a-Si:H device becomes virtually insensitive to changes in irradiance, thus rendering the device useless for tomographic measurements. A peak signal current positioning technique has been described that enables maximum sensitivity to irradiance to be established.  $H_{\max}$  is determined in order to establish the point at which the signal current reaches approximately steady state conditions. The signal response due to  $H_{\max}$  then serves as a 'template' for the positioning technique previously described.

$H_{\min}$  and  $H_{\max}$  therefore dictate the minimum and maximum light conditions for the a-Si:H device. The intensity of the issued light required to provide  $H_{\min}$  and  $H_{\max}$  after it has passed through a vessel and media is directly related to the type of vessel and media that is employed and is therefore highly application specific. In order to meet the requirement of portability in tomographic system design the light source employed needs to be adjustable so that  $H_{\min}$  and  $H_{\max}$  can be determined for a wide variety of pipeline dimension and media. The light source developed by the research project allows easy adjustment of the light intensity and duration and is therefore ideally suited for this purpose.

The responsivity of the a-Si:H device was found to be field dependant and was in the order of  $14.19\mu\text{A/W}$  to  $103\mu\text{A/W}$ . Plotted over a range of electric field, the responsivity showed a linear response over all levels of irradiance ( $3.45\text{mW/cm}^2$  to  $9.57\text{mW/cm}^2$ ) indicating that the Au contacts are ohmic. The responsivity was seen to increase with an increase in electric field. This suggested that the a-Si:H device be operated at a higher an electric field as possible in order to maximise the responsivity of the a-Si:H device to incident light. The electric field was increased to  $1.66 \times 10^5$  V/cm accordingly for further tomographic experimentation. In terms of system design the increased electric field would result in higher electrode potentials being required to establish the electric field. For the current a-Si:H device ( $27.1\mu\text{m}$ ) an electrode voltage of approximately 450V was required. Operator safety is a major concern when designing tomographic imaging systems and the electrode potentials employed in this study are officially classified as high voltage (I.E.E wiring regulations 16<sup>th</sup> edition

BS7671,1992) and can be potential lethal. Thus the design of any sensor array must meet all relevant health and safety considerations. An additional problem of using high electric fields is potential damage to the Au contacts or electrical breakdown of the a-Si:H material. No such problems were observed over the range of electric fields employed in this research.

A study as to the effects of pulsed illumination upon the a-Si:H device revealed that rapid degradation of the signal response was observable over approximately the first minute of operation at a FRR of 100Hz. The signal response was then seen to stabilise, the magnitude of the signal response being dictated by the applied electric field. It has been demonstrated that other workers have found that a-Si:H suffers from degradation in photoconductivity when exposed to extended periods of high intensity light. Many of these workers have found that the degradation in photoconductivity persists long after the illumination period has ceased and that the effect is reversible by annealing. In the current study, the effects photoinduced fatigue were found to be transient in nature, with the a-Si:H device regaining its original electrical properties prior to illumination after a short rest period at room temperature. A fundamental difference between the experimentation described by other workers and the current research, is that in order to produce sufficient magnitudes of photocurrent for tomographic purposes, a high electric field is maintained constantly throughout the pulsed illumination period. The exact nature of physical phenomena that causes the observed photoinduced fatigue under pulsed illumination and under constant high electric field is beyond the scope of the current research and is suggested for further work as is discussed presently.

In terms of tomographic application, the effects of the photoinduced fatigue were not deemed to be problematic other than the a-Si:H device would require a 60s pulsed illumination period prior to the commencement of the tomographic measurement. It has been shown that the intensity of the light issued from the light source can be selected in conjunction the magnitude of electric field to position the peak signal current to just under the steady state condition after the cessation of the effects of fatigue. Testing with tomographic prototypes demonstrated that the a-Si:H device was capable of producing qualitative and quantitative data in this condition. It has been shown that 1mm changes in water level and 0.5% changes in fluid colour contained

within a 50mm (external diameter) transparent acrylic pipeline could be accurately determined by the a-Si:H device at speeds required for OPT. Further testing by the use of a sensor array using a section of pipeline and a phantom object demonstrated that the a-Si:H device could be used for imaging purposes.

Hydrogenated amorphous silicon is sensitive to the entire visible spectrum, is mechanically and chemically stable, can be operated at high temperatures, and can be made into large area devices on a variety of substrates. Additionally, a-Si:H is cheap to manufacture, is non-toxic and can be readily discarded, and exhibits greater sensitivity to visible light than crystalline silicon. Our investigations have also shown that it can be operated at speeds required for OPT and can produce both qualitative and quantitative data for tomographic purposes. I therefore conclude that a-Si:H devices operated in the configurations stated within this thesis are suitable for application in OPT and can offer significant improvement in both tomographic measurement and system design over techniques currently employed, thus contributing to the advancement of OPT.

### 8.3 Suggestions for further work

#### 8.3.1 Effects of pulsed illumination

Although other workers have demonstrated that pulsed illumination can greatly accelerate the degradation process, published literature on the effects of pulsed illumination in a-Si:H under a constant high electric field proved elusive. It would therefore be useful to carry out a detailed study of the effects of pulsed illumination under high electric field in order to better understand the behaviour of the a-Si:H under these conditions with a view to improving the operation of any potential tomographic imaging system.

#### 8.3.2 Light source

The present light source has a maximum FRR of 100Hz which is suitable for OPT. However, the maximum speed at which the a-Si:H device could potentially be operated at could not be determined due to the 100Hz limitation of the current light source. It would therefore be interesting to develop a new light source that could supply much higher FRR's. This new light source could be used to further understand

the effects of pulsed illumination under constant high electric field as previously described.

### 8.3.3 Effects of elevated temperature

Due to the nature of OPT it is likely that any potential imaging system that is to be employed in OPT could be operated in high ambient temperatures due to heat generated by the process under test or plant in the vicinity of the imaging system. It is known that a-Si:H can be operated at temperatures of up to 250°C, and so could in theory be capable of being employed in extreme OPT conditions. However, it is not known how the a-Si:H device operated in the current configuration would behave at elevated temperatures. It would therefore be useful to investigate the a-Si:H devices ability to produce quantitative and qualitative data at elevated temperatures thus further exploring the OPT applications in which the a-Si:H device can be employed.

### 8.3.4 Tomographic rig

In order to be able to demonstrate the a-Si:H devices ability to produce near real time images or quantitative and qualitative data under on-line conditions, a further test rig needs to be constructed. It is envisaged that the rig would comprise of air and water pumps to produce air bubble and plug flow at various flow rates. It is also envisaged that the rig would need to be capable of pumping various liquids suspending semitransparent foreign objects such as small clear Perspex pellets for example to further demonstrate the a-Si:H devices imaging capabilities. An array of a-Si:H devices would need to be arranged around a transparent section of pipeline to form multiple views and projections in order that accurate 3D representations of the process under test could be established. The sensor array would need to be versatile in order that a wide variety of processes can be investigated, and also to allow various types of projection methods such as parallel beam, fan beam, and cone beam projection to be investigated. It is also envisaged that a transputer based computer system would be required to be developed in order to process the data from the sensor array.

### 8.3.4 Device design

a-Si:H can be made into very large area devices and on a wide variety of substrates including curved surfaces and flexible substrates. These properties are important to tomography because they allow great scope in the design and customisation of sensor

arrays when compared to the use of commercially available products. In order to allow greater customisation and therefore portability of the a-Si:H device, it would be useful to conduct a study as to the design of a-Si:H devices that could be simply constructed to form sensor arrays of various configuration. In the current study Au contacts of various size and configuration were sputtered onto the surface of the a-Si:H device. This process in itself is a very simple and effective means of producing customised sensor arrays and can offer considerable advantages over the use of commercial discrete components. However, this technique requires the purchase or access to a sputter coater.

Due to the small dimensions imposed on crystalline devices by difficulty in making them into large area devices, crystalline devices are commonly 'tiled' together to form large area devices for tomographic purposes. This however, can lead to poor resolution along the join lines. Whereas this could be seen as a major disadvantage in medical imaging system, it may not be significant in OPT. It is envisaged that this technique of 'tiling' devices together could be applied to a-Si:H devices to allow flexibility in array design. It is envisaged that a tomographic 'kit' comprising of single a-Si:H devices of various small size ( $<5\text{mm}^2$ ) and configuration that can be simply tiled together in flexible compartmented holding devices could be produced in conjunction with a versatile light source and image reconstruction software. This would allow simple but efficient tomographic systems to be constructed on site.

## REFERENCES

**Abkowitz M., Jansen F., and Melnyk A.R.,** 1985, Electrical behaviour of chemically modified amorphous Se studied by xerographic depletion discharge, *Philosophical magazine B*, Vol.51, No.4, 405-420.

**Abkowitz M.,** 1992, Light induced changes in the DOS of chalcogenide glasses studied by xerographic techniques, *Journal of Non-Crystalline Solids*, Vol. 141, 188-199.

**Amick J.A.,** 1959, *RCA review*, Vol.20, 770.

**Anderson E.E., Hartney M., and Weisfield R.,** 1998, An amorphous silicon imaging system for approved x-ray image capture in non-destructive evaluation, *Society for Photo-optical Instrumentation Engineers*, Vol.3399, 180-187.

**Andriesh A.M.,** 1997, Photoinduced phenomena in chalcogenide glass semiconductors, *In Physics and Applications of Non-Crystalline Semiconductors in Optoelectronics*, Kluwer Academic Publishers, 17-30.

**Apte R.B., Street R.A., Ready S.E., Jared D.A., and Moore A.M.,** 1998, Large area, low noise amorphous silicon imaging system, *Society of Photo-optical Instrumentation Engineers*, Vol.3301, 2-8.

**Bauer G. H., and Paasche S. M.,** 1987, Amorphous Si/SiC three layer structures for xerographic applications, *Journal of applied physics*, Vol.62, 268.

**Baxendale M.** 1987, *Xerographic spectroscopy and depletion discharge studies of a-Se, a-Se:Te alloys, a-As<sub>2</sub>Se<sub>3</sub>, and a-Si:H photoreceptors*, Thesis (PhD), Imperial College.

**Baxendale M., Biswas S., and Juhasz C.,** 1990, Xerographic dark discharge of a-Si:H(p) / a-Si:H(i) / aSi<sub>1-x</sub> C<sub>x</sub>:H photoreceptors: Hard copy and printing materials media and processes, *Society of Photo-optical Instrumentation Engineers*, Vol. 1253, 203- 211.

**Beck M.S., Compogrande E., Morris M, Richards R.A., and Waterfall R.C.,** 1993, *Tomographic technique for process design and operation*, Computational Mechanics Publications, UK.

**Beck M.S., Dyakowski T., and Williams R.A.,** 1999, Process tomography - the state of the art, *Transactions of the Institute of Measurement and Control*, Vol.20, No.4, 163-177.

**Beuthan J., Freyer R., Minet O., Tran Luu C., Hampel U., Naber R.D., and Müller G.,** 1996, Optical tomography of a rat brain, *Proceedings of SPIE The International Society for Optical Engineering*, Vol.2676, 91-102.

**Borsenburger P.M, and Wiess D.S.,** 1993, *Organic photoreceptors for imaging systems*, Marcel Dekker, New York.

**Borsenburger P.M., and Wiess D. S.,** 1998, *Organic photoreceptors for xerography*, Marcel Dekker, New York.

**Boudry J.M., and Antonuk L.E.,** 1996, Radiation damage of amorphous silicon, thin film, field effect transistors, *Medical Physics*, Vol.3, No5.

**Carlson C.F.,** 1942, US patent 2,297,691.

**Chan Y.C** 1983, *Xerographic properties of CdS and ZnO semiconductor powder resin binder layers*, Thesis (PhD), Imperial College.

**Chaouki J., Larachi F., and Dudukovic M.P.,** 1997, Non-invasive tomographic and velocimetric monitoring of multiphase flows, *Ind. Eng. Chem. Res.*, Vol.36, 4476-4503.

**Chubb J.N., and Malinverni P.** 1993, Comparative studies on methods of charge decay measurement, *Journal of Electrostatics*, Vol.30, 273-284.

**Cobine T.D.,** 1958, *Gaseous conductors: Theory and Engineering Applications*, Dover (New York), 254-255.

**Darton R.C., Thomas P.D., and Whalley P.B.,** 1995, *Optical tomography*, In *Frontiers in industrial tomography*, Scott.D.M., and Williams R.A., Eds., Engineering Foundation, New York.

**Dickin F.J., Williams R.A., and Beck M.S,** 1993, Determination of composition and motion of multi-component mixtures in vessels using electrical impedance tomography, *Chem. Eng. Sci.*, Vol.48, 1883.

**Dickin F.J., Zhao X.J., Abdullah M.Z., and Waterfall R.C.,** 1993, *Tomographic imaging of industrial process equipment using electrical impedance sensors*, In *Process tomography principles, techniques and applications*, Oxford Butterworth-Heinemann, 1995, 215-220.

**Donovan J.L.,** 1970, Xeroradiographic properties of amorphous selenium, *Journal of Applied Physics*, Vol.41, 2109-2114.

**Dugdale P., Green R.G., Hartley A.J., Jackson R.J., and Landauro J.,** 1991, *Tomographic imaging in industrial process equipment using optical sensor arrays*, In *Sensors Technologies and Systems*, IOP publishing Ltd., 227-232.

**Elliot S.R.,** 1992, *Physics of amorphous solids*, Longman, London.

**Fletcher, M. J.,** 1996, A review of optical inspection methods, *INSIGHT*, Vol.38., No.4, 270.

**Forsyth D.S., Kasap S.O., Wacker I., and Yannacopoulos S.,** 1994, Thermal fatigue of composites: ultrasonic and SEM evaluations, *Journal of Engineering Materials and Technology*, Vol.116, No.1, 113.

- Graeve T., Huang W., Alexander S.M., and Youming L.,** 1995, Amorphous silicon image sensor for x-ray applications, *Society of Photo-optical Instrumentation Engineers*, Vol.2415, 177 - 181.
- Graves M., Smith A., and Bachelor B.,** 1998, Approaches to foreign body detection in foods, *Trends in Food Science & Technology*, Vol.9, 21-27.
- Green R.G., Rahim R.A., Evans K., Dickin F.J., Naylor B.D., and Pridmore T.P.,** 1998, Concentration profiles in a gravity chute conveyor by optical tomography measurement, *Powder Technology*, Vol.95, 49-54.
- Gregory W., and Hertz H.M.,** 1989, Tuneable differential interferometer for optical tomography, *Applied Optics*, Vol.28, No.21, 4662-4667.
- Guba S.,** 2000, Multijunction solar cells and modules, *In Technology and applications of Amorphous silicon*, Street R.A Ed., Springer, NewYork, 253.
- Gundlach R.W., and Bergen R.F.** 1984, *Corona device*, European Patent Application 0,147,985.
- Hagihara H., and Okuda M.** 1995, *Xerographic apparatus with a detachable corona charger*, United States Patent, 5,576,820.
- Hamamatsu Photonics** 1995, *Super quiet xenon lamps*, Cat. No. TLSX1002E02.
- Hamamatsu Photonics** 1996, *Xenon flash lamps*, Cat. No. TLSX1008E03.
- Honlet M.,** 1998, Non destructive testing of complex materials and structures using optical techniques, *INSIGHT*, Vol. 40, No.3, 176.
- Huang S.M., Xie C.G., Thorn R., Snowden D., and Beck S.M.,** 1991, *Tomographic imaging of industrial process equipment design of capacitance sensing electronics for oil and gas based processes*, In *Sensors: Technology, systems and applications*, IOP publishing LTD, London, 197-202.
- Ing S.W., and Neyhart J. H.,** 1972, *Journal of applied physics*, Vol.43, 2670.
- Jenner R.P., and Vaezi-Nejad S.M.,** 1999, Development of a novel light source for the investigation of optical sensors, *Measurement and Control*, Vol.32, No.3, 75 - 78.
- Johansen R.E., Kasap S.O., Rowlands J., and Polischuk B.,** 1998, Metallic electrical contacts to stabilised amorphous selenium for use in X-ray image detectors, *Journal of Non-Crystalline Solids*, Vol. 270 - 230, 1360.
- Kakinuma H., and Wantanabe T.,** 1987, Dark discharge in hydrogenated amorphous silicon photoreceptors, *Journal of Applied Physics*, Vol. 62(5), 1837 - 1841.

- Kasap S.O., Baxendale M., and Juhasz C.**, 1987, Evidence for field assisted thermal emission of holes from deep mobility gap states in amorphous semiconductors from xerographic dark discharge measurements, *Journal of applied physics*, Vol.62, No.1, 171-173.
- Kasap S.O.**, 1989, Dark decay of electrostatic surface potential on dielectrics via bulk space charge build-up, *Journal of electrostatics*, Vol. 22, 69-90.
- Kasap S.O.**, 1991, *Photoreceptors: The selenium alloys*, in *Handbook of imaging materials*, Diamond A. S. Ed, Marcel Decker Pub, 329.
- Kasap S.O., Haugen C., Nerdoly M., and Rowlands J.A.**, 2000, Properties of a-Se for use in flat panel X-ray image detectors, *Journal of Non-Crystalline Solids*, Vol. 266-269, 1163-1167.
- Kaura T., and Srivastava V.K.** 1987, Surface potential decay in stretched and unstretched PVDF films, *Journal of Electrostatics*, Vol.15, 46.
- Keiss H.**, 1972, In *Current problems in electrophotography*, Berg W.F., and Hauffe K., Eds, de Gruyter, Berlin, 89.
- Keithley Instruments** 1984, *Low current measurements*, Application note 100.
- Lines D.**, 1998, Rapid inspection using integrated ultrasonic arrays, *INSIGHT*, Vol.40, No.8, 573-577.
- Li W., and Hoyle B.S.**, 1995, *Multiple active sensors in ultrasonic process tomography systems*, In *Frontiers in Industrial Process Tomography*, Engineering Foundation, New York.
- Lopushansky R.L., Light G.M., and Gupta N.K.**, 1998, Digital radiography of process piping, *Society of Photo-optical Instrumentation Engineers*, Vol.3398, 14-17.
- Melnyk, A, R.**, 1980, Hole emission defect states in amorphous  $As_2Se_3$ , *Journal of Non-Crystalline Solids*, Vol. 35/36, 837-842.
- Mooney W.J.**, 1991, *Optoelectronic Devices and Principles*, Prentice Hall, 62 - 67.
- Monroe Electronics Inc.** 1971, *Instruction manual for Isoprobe electrostatic voltmeter model 144*.
- Monroe Electronics Inc.** 1973, *Application note ES-01*.
- Monroe Electronics Inc.** 1985, *Application note ES-12*.
- Montrimas E., Tauraitiene S., and Tauraitis A.**, 1972, In *Current problems in electrophotography*, Berg W.F., and Hauffe K., Eds, de Gruyter, Berlin, 139.
- Mort J., and Pai D.M.**, 1975, *Photoconductivity and related phenomena*, Elsevier Scientific Publishing Company, New York, 6.

- Mort J.**, 1991, *Applications of amorphous silicon and related materials in electronic imaging*, in *Handbook of imaging materials*, Diamond A.S. Ed, Marcel Decker Pub, 448.
- Mott, N.F. and Davis E.A.**, 1979, *Electronic processes in non-crystalline materials (second edition)*, Clarendon Press, Oxford, England.
- Nakamura Z., Tsunekawa T., Ohtaki S., and Uchiyama T.**, 1977, *Electronic flash device with capacitor discharge cut off before full discharge*, US patent 4,012,665.
- Nakayama Y., Kita H., Takahashi T., Akita S., and Kawamura T.**, 1987, Dark decay of surface potential: measurement of the density of localised states on highly resistive amorphous silicon alloys', *Journal of Non-Crystalline Solids*, Vol. 97/98, 743-746.
- Neitzel U., Maack I., and Günther-Kohfahl S.**, 1994, Image quality of a digital chest radiography system based on a selenium detector, *Medical Physics*, Vol.21, No.4, 509-516.
- Pai D.M., and Springett B.E.**, 1993, Physics of electrophotography, *Reviews of Modern Physics*, Vol. 65, No.1, 163-211.
- Pai. D. M.**, 1997, Time of flight study of the compensation mechanism in a-Se alloys, *Journal of imaging science and technology*, Vol.41, No.2, 135.
- Pai D.M.**, 1998, *Proceedings of the fourth international congress on advances in non-impact printing technologies*, SPSE, Springfield Va. 46.
- Palma F.**, 2000, Multilayer colour detectors, *In Technology and applications of Amorphous silicon*, Street R.A Ed., Springer, New York, 309.
- Pillai P.K.C., Shroff N., and Tripathi A.K.**, 1983, Photoelectric properties of Michlers ketone effects of curing, *Journal of Electrostatics*, Vol. 10, 270.
- Popov I.A., Van Doorselaer G., Van Calster A., De Smet H., Callens F., and Boesman E.**, 1998, Prototype of 2D direct x-ray a-SiN:H sensor array, *Society of Photo-optical Instrumentation Engineers*, Vol. 3301, 126-130.
- Rahim R.A., Green R.G., Horbury N., Dickin F.J., Naylor B.D., and Pridmore T.P.**, 1996, Further development of a tomographic imaging system using optical fibres for pneumatic conveyors, *Measurement Science and Technology*, Vol.7, 419-422.
- Redfield D., and Bube R.H.**, 1996, *Photoinduced defects in semiconductors*, Cambridge University Press, England.
- Röntgen, W.C.**, 1896, On a new kind of rays, *Nature*.
- Rossi M.C., Brandt M.S., and Stutzmann M.**, 1992, Accelerated stability test for amorphous silicon solar cells, *Applied Physics letters*, Vol.60, No.14, 1709-1711.

**Rushing A.J.**, 1996, *Accurate dynamic control of the potential on the photoconductor surface using an up-datable look-up table*, US patent 5,523,831.

**Schaffert R.M.**, 1975, *Electrophotography*, Focal Press.

**Schien L.B.**, 1974, *Physics review B*, Vol.10, 3451.

**Shimakawa K., Inami S., and Elliot S.R.**, 1990, Reversible photoinduced change of photoconductivity in amorphous chalcogenide films, *Physical Review B*, Vol.42, No.18, 11 857 - 11 861.

**Staebler D.L. and Wronski C.R.**, 1977, *Applied Physics Letters*, Vol.31, 292.

**Stark W.** 1990, Surface potential homogeneity of corona charged FEP and PVDF electrets, *Journal of Electrostatics*, Vol. 25, 277-285.

**Stutzmann M., Jackson W.B., and Tsai C.C.**, 1985, Light induced metastable defects in hydrogenated amorphous silicon: a systematic study, *Physical Review B*, Vol.32, No.1, 23-47.

**Thomas P.D., Darton R.C., and Whalley P.B.**, 1998, Solving the structure of cellular foams by the use of optical tomography, *Ind. Eng. Chem. Res.*, Vol.37, 710-717.

**Vaezi-Nejad S.M.**, 1984, *Electrical properties of selenium based amorphous multilayer xerographic photoreceptors*, Thesis (PhD), Imperial College, 27.

**Vaezi-Nejad S.M., and Juhasz C.J.**, 1989, Characteristics of pin and wire corona devices for electrostatic charging, *International Journal of Electronics*, Vol.67, No.3, 437-446.

**Williams R.A., Atkinson K., Luke S.P., Barlow R.K., Dyer B.C., Smith J., and Manning M.**, 1995, Applications for tomographic technology in mining, minerals and food engineering, *Particle and Particle Systems Characterization*, Vol.12, 105-111.

**Williams R.A., and Beck M.S.** 1995, *Process tomography principles, techniques and applications*, Oxford Butterworth-Heinemann.

**Williams R.A., and Beck M.S.**, 1996, Process tomography: a European innovation and its applications, *Measurement Science and Technology*, Vol.7, 215-224.

**Withers P.M.**, 1996, Ultrasonic, acoustic and optical techniques for the non invasive detection of fouling in food processing equipment, *Trends in Food Science & Technology*, Vol.7, 293-298.

**Wolverson D., and Phillips R.T.**, 1988, The decay of photoconductivity in a-As<sub>2</sub>Se<sub>3</sub> following repetitive pulses excitation, *Philosophical Magazine B*, Vol.7, No.5., 635-637.

**Xie C.G., Huang S.M., Holye B.S., and Beck MS.,** 1991, *Tomographic imaging of industrial process equipment: development of system model and image reconstruction algorithm for capacitive tomography*, In *Sensors: Technology, systems and applications*, IOP publishing LTD, London, 203-208.

**Yaffe M.J., and Rowlands J.A.,** 1997, X-ray detectors for digital radiography, *Phys. Med. Biol.*, Vol. 42, 33.

**Yatsuzuka K., Mizuno Y., and Asano K.** 1994, Electrification phenomena of pure water droplets dripping and sliding on a polymer surface, *Journal of Electrostatics*, Vol.32, 157-171.

**Zhao W., and Rowlands J.A.,** 1992, A large area solid state detector for radiology using amorphous selenium, *Society of Photo-optical Instrumentation Engineers-medical imaging VI: instrumentation*, Vol.1651, 134 -143.

**APPENDIX 1****Core MATLAB program**

```

cd d:\ports; %change to home directory containing .m file
clc; %clear the screen
clear; %clear old variables from the workspace
k=menu('CHOOSE REQUIRED OPTION','Create a New File','Load .mat File','Excel','*.mat Directory Listing','*.xls Directory Listing','Matlab Workspace','DOS Prompt','Exit Matlab');
%main menu
if k==1; % if option 1 do the following
dos('d:\ports\collect4'); %run C data aquisition file called collect_3 as DOS shell
[fid,message]=fopen('d:\ports\test','r'); %open the C file called test which contains the collected data,
% and return a file identifier and error message
[a,count]=fscanf(fid,'%f'); %read infinite characters from the file pointed to by the fid
% and assign the data to the variable a and the number of data points collected
sample_no=[1:count]; %assign the number of samples collected (denoted by count)
%to a 1 column array using transpose
Data_file=[sample_no,a]; %assign a two column array to Data_file
plot(a) %Plot the variable
grid;
title('Data Collection','fontsize',17);
xlabel('Sample Number','fontsize',16);
ylabel('Magnitude','fontsize',16);
pause
close; %close the figure window
fclose(fid); %close the file
cd d:\ports\matfile; %directory in which .mat files will be saved
[filename,pathname]=uiputfile('*.mat','save as'); %automatically display save as menu and return
%the entered file and path name
Date_Time=fix(clock); %add the current time and date to the file before it is saved
eval(['save',[pathname, filename]],a); %save the variable a to the entered file and pathname
%eval is used in order to be able to use [filename,pathname]
v=menu('CHOOSE REQUIRED OPTION','Save as .dat File','Matlab Workspace','Quit Matlab');
%menu to prompt for user to save the current data file
if v==1;
eval(['load',[pathname, filename]]); %load the current .mat file
cd d:\ports\datfile; %change to the directory that contains the data files
save tempname.dat Data_file -ascii; %save the two column Data_file as a ascii file (.dat)
! d:\msoffice\excel\excel.exe
%execute DOS command to launch Excel
cd d:\ports; %return to home directory
end
if v==2
cd d:\ports
end
end
if k==2
cd d:\ports\matfile;
[filename,pathname]=uigetfile('*.mat','open');%automatically display open menu
eval(['load',[pathname, filename]]);%load the file relating to the entered filename and pathname
b=menu('ENTER .mat LOAD OPTION','Load Time/Date','Load Variable','Return to Main Menu','Matlab Workspace','Exit Matlab');
if b==1
disp([filename,' Was Compiled on:']);%display message with loaded filename
Date_Time%display the saved time and date to the screen
disp('Press Any Key To Continue')
pause;

```

```

b=menu('ENTER .mat LOAD OPTION','Load Time/Date','Load Variable','Return To Main
Menu','Matlab Workspace','Exit Matlab');
%return to previous menu
end
if b==2
clc;
disp([filename]);%display the loaded filename on the screen
Data_file=[sample_no,a]%load the saved sample numbers and data to the Matlab workspace
end
if b==3
collects%return to main menu
end
if b==5
quit
end
cd d:\ports;
end
if k==3
!d:\msoffice\excel\excel.exe
go to DOS command and load Excel
collects %return to main menu
end
if k==4
cd d:\ports\matfile;
disp('D:\PORTS\MATFILE\*.mat');%display message
dir d:\ports\matfile\*.mat %change directory to directory containing .mat files
disp('Press Any Key To Continue');
pause;
cd d:\ports;%return to home directory
collects %return to main menu
end
if k==5
cd d:\ports\datfile; %change to directory containing xls files
disp('D:\PORTS\DATFILE\*.xls');
dir d:\ports\datfile\*.xls %list all .xls files
disp('Press Any Key To Continue');
pause;
collects %return to main menu
end
if k==6
cd d:\ports
end
if k==7
!
%goes to DOS prompt
collects %returns to main menu
end
if k==8
quit %terminate Matlab
end

```

**APPENDIX 2****Turbo C control program listing**

```

#include<stdio.h>      /*use standard input/output*/
#include<graphics.h>  /*use graphics*/
#include<conio.h>     /*use console input/output*/
#include<dos.h>       /*use dos functions*/
#include<time.h> /*use timing functions*/
#include<stdlib.h>    /*use standard library*/

#define CWR 0x207      /*defines control word register*/
#define PRINTER_PORT 0X378 /*data outputted via printer port base address*/
#define STATUS_PORT 0X379 /*data inputted via status port, base address +1*/
#define PORT_A 0X204    /*address of port A on 8255a*/
#define PORT_B 0X205    /*address of port B on 8255a*/
#define PORT_C 0X206    /*address of port C on 8255a*/
#define INTERFACE_CARD_SETUP 0X09A /*set up mode for 8255a*/

main() /*start of main program*/
{
int mode; /*defines as a integer*/
int modeoption;
int gdriver=DETECT, gmode, x_max, y_max; /*initialises graphics system*/
initgraph(&gdriver, &gmode, "\\tc");
cleardevice(); /*clears screen*/
title(); /*name of procedure*/
cleardevice();
modetype();
cleardevice();
while(!kbhit()); /*continue until keypress*/
} /*end of main program*/

title() /*start of title procedure*/
{
setbkcolor(BLUE); /*sets background colour*/
setcolor(LIGHTGREEN); /*sets foreground colour*/
rectangle(160,190,460,270); /*draws a rectangle, top left point, bottom right point*/
rectangle(161,191,459,269);
rectangle(159,189,461,271);
floodfill(240,210,LIGHTGREEN); /*fills rectangle with colour, coordinates inside rectangle*/
setcolor(RED);
outtextxy(205,205,"SAMPLE TRANSPORT MECHANISM");
outtextxy(215,225,"90 DEGREE STEPPER MOTOR");
outtextxy(245,235,"CONTROL PROGRAM");

do
{
outtextxy(207,255,"PRESS ANY KEY TO CONTINUE"); /*displays flashing
message*/

delay(6000);
setcolor(WHITE);
outtextxy(207,255,"PRESS ANY KEY TO CONTINUE");
delay(6000);
setcolor(DARKGRAY);
}
while(!kbhit());
getch(); /*terminates obtained character from keypress*/

```

```

modetype()      /*start of mode required menu*/
{
int modeoption;
setbkcolor(BLUE);
setcolor(LIGHTGREEN);
rectangle(160,180,460,275);
rectangle(161,181,459,274);
rectangle(159,179,461,276);
floodfill(240,210,LIGHTGREEN);
setcolor(RED);
outtextxy(205,196,"ENTER DESIRED STEPPING MODE:");
outtextxy(180,216,"1:");
setcolor(DARKGRAY);
outtextxy(205,216,"ONESHOT");
setcolor(RED);
outtextxy(180,231,"2:");
setcolor(DARKGRAY);
outtextxy(205,231,"NORMAL SPIN");
setcolor(RED);
outtextxy(180,246,"3:");
setcolor(DARKGRAY);
outtextxy(205,246,"REVVED SPIN");
setcolor(RED);
outtextxy(180,260,"4:");
setcolor(DARKGRAY);
outtextxy(205,260,"EXIT");
gotoxy(55,13);
flushall();                          /*flushes out old data of stream*/
scanf("%d",&modeoption);              /*reads an integer and assigns the value to modeoption*/
    if(modeoption==1) oneshot();       /*if value is 1 jump to procedure oneshot*/
    else
    if(modeoption==2) normal();
    else
    if(modeoption==3) revvedspin();
    else
    if(modeoption==4) abort();         /*terminates programme*/
    else
    {
    setcolor(LIGHTGREEN);
    outtextxy(195,155,"ENTER NUMBER OF MODE REQUIRED");
    sound(700);
    delay(2000);
    nosound();
    modetype();      /*jumps to start of mode menu until correct data is entered*/
    }
}

oneshot()
{
int mode_pos_neg;
cleardevice();
setbkcolor(BLUE);
setcolor(LIGHTGREEN);
rectangle(160,180,480,275);
rectangle(161,181,479,274);
rectangle(159,179,481,276);
floodfill(240,210,LIGHTGREEN);
setcolor(RED);
outtextxy(175,200,"ENTER POLARITY OF APPLIED CHARGE:");

```

```

outtextxy(190,220,"1:");
setcolor(DARKGRAY);
outtextxy(200,220," POSITIVE POTENTIAL");
setcolor(RED);
outtextxy(190,240,"2:");
setcolor(DARKGRAY);
outtextxy(200,240," NEGATIVE POTENTIAL");
setcolor(RED);
outtextxy(190,260,"3:");
setcolor(DARKGRAY);
outtextxy(200,260," EXIT");
gotoxy(56,13);
flushall();
scanf("%d",&mode_pos_neg);

        if(mode_pos_neg==1) oneshot_pos();
        else
        if(mode_pos_neg==2) oneshot_neg();
        else
        if(mode_pos_neg==3) abort();
}

oneshot_pos()
{
int a;
int osnoc;
int ostdsc;
int input_word;
int CONVERSION_HIGH_BYTE_LOW_MSB_VALID;
int START_CONVERSION_BYTE_LOW_MSB_VALID;
int BYTE_HIGH_LSB_VALID;
int BUSY_MASK;
int END_OF_CONVERSION;
int first_byte;
int second_byte;
int final_first_byte;
int final_second_byte;
int busy;
float final_voltage;
float final_voltage_x200V;
long int sample_rate;

cleardevice();
setbkcolor(BLUE);
setcolor(LIGHTGREEN);
rectangle(110,25,520,111);
rectangle(111,26,519,112);
rectangle(109,24,521,113);
floodfill(165,80,LIGHTGREEN);
setcolor(RED);
outtextxy(260,38,"ONESHOT MODE");
outtextxy(130,55,"ENTER NUMBER OF CYCLES REQUIRED :");
gotoxy(51,4);
flushall();
scanf("%4d",&osnoc);
while ((osnoc>=1000)||(osnoc<1)||(osnoc==1266)) /*while outside limits display error message and
rescan data*/
{
        setcolor(LIGHTGREEN);

```

```

        outtextxy(115,140,"YOU ARE OUTSIDE LIMITS OR HAVE ENTERED
        CHARACTERS");
        outtextxy(195,150,"( ACCEPTABLE RANGE 1-1000 )");
        sound(700);
        delay(2000);
        nosound();
        gotoxy(51,4);
        flushall();
        scanf("%4d",&osnoc);
    }
setcolor(BLUE);
outtextxy(115,140,"YOU ARE OUTSIDE LIMITS OR HAVE ENTERED CHARACTERS");
outtextxy(195,150,"( ACCEPTABLE RANGE 1-1000 )");
setcolor(RED);
outtextxy(130,70,"ENTER TIME DELAY AT SCOROTRON(s):");
gotoxy(51,5);
flushall();
scanf("%5d",&ostdsc);
while ((ostdsc<1)||ostdsc>3600)||ostdsc==1266) /*time delay from 1 second to 1 hour*/
    {
        setcolor(LIGHTGREEN);
        outtextxy(115,140,"YOU ARE OUTSIDE LIMITS OR HAVE ENTERED
        CHARACTERS");
        outtextxy(195,150,"( ACCEPTABLE RANGE 1 - 3600 SECS)");
        sound(700);
        delay(2000);
        nosound();
        gotoxy(51,5);
        flushall();
        scanf("%5d",&ostdsc);
    }
setcolor(BLUE);
outtextxy(115,140,"YOU ARE OUTSIDE LIMITS OR HAVE ENTERED CHARACTERS");
outtextxy(195,150,"( ACCEPTABLE RANGE 1 3600 SECS)");
setcolor(RED);
outtextxy(130,85,"ENTER SAMPLING RATE(ms)      :");
setcolor(DARKGRAY);
outtextxy(130,95,"Note 10,000 = 1 second");
setcolor(RED);
gotoxy(51,6);
flushall();
scanf("%12d",&sample_rate);
while ((sample_rate<1)||sample_rate>10000000000)||sample_rate==1266) /*time delay is from 1
sec to 1 hour*/
    {
        setcolor(LIGHTGREEN);
        outtextxy(115,140,"YOU ARE OUTSIDE LIMITS OR HAVE ENTERED CHARACTERS");
        outtextxy(190,150,"( ACCEPTABLE RANGE 30 MINUTES MAX )");
        sound(700);
        delay(2000);
        nosound();
        gotoxy(51,6);
        flushall();
        scanf("%12d",&sample_rate);
    }
setcolor(BLUE);
outtextxy(115,140,"YOU ARE OUTSIDE LIMITS OR HAVE ENTERED CHARACTERS");
outtextxy(190,150,"( ACCEPTABLE RANGE 1 3600 SECS )");
setbkcolor(BLUE);
setcolor(LIGHTGREEN);

```

```

rectangle(110,120,520,191);
rectangle(111,121,519,192);
rectangle(109,119,521,193);
floodfill(265,150,LIGHTGREEN);
setcolor(RED);
outtextxy(240,133,"POSITION OF SAMPLE");
setcolor(DARKGRAY);
outtextxy(160,155,"SCOROTRON CHARGER");
outtextxy(360,155,"XENON FLASH");

do
    {
        /*routine for energizing motor and moving the sample*/
        a=inportb(STATUS_PORT); /*input a byte from the status port and assign it
                                to a*/
        if (a&32)scorotron_graphic(); /*if bit 5 display scorotron position graphic*/
        sleep(ostdsc); /*delay at scorotron charger secs*/
        outportb(PRINTER_PORT,0X09); /*move sample to measuring station*/
        timestart(); /*get current system time*/
        do
            {
                a=inportb(STATUS_PORT);
            }
            while(!(a&8)); /*scans status port until time stop goes high*/
            if(a&8)timestop(); /*if bit 3 get time at end of run*/
            if(a&64) xenon_graphic(); /*if bit 6, display xenon position graphic*/
            /*energise coil behind measuring station to keep sample in position*/
            outportb(PRINTER_PORT,0X0C);
            delay(300);
            outportb(PRINTER_PORT,0X09);
            do
                {
                    FILE *fp;
                    if ((fp=fopen("test","wb"))==NULL)
                        {
                            printf("Error could not open new file\n");
                            exit(1);
                        }
                    CONVERSION_HIGH_BYTE_LOW_MSB_VALID=0X04;
                    START_CONVERSION_BYTE_LOW_MSB_VALID=0X00;
                    BYTE_HIGH_LSB_VALID=0X06;
                    BUSY_MASK=0X14;
                    outport(CWR,INTERFACE_CARD_SETUP);
                    outportb(PORT_C,CONVERSION_HIGH_BYTE_LOW_MSB_VALID);
                    do
                        {
                            outportb(PORT_C,CONVERSION_HIGH_BYTE_LOW_MSB_VALID);
                            outportb(PORT_C,START_CONVERSION_BYTE_LOW_MSB_VALID);
                            outportb(PORT_C,CONVERSION_HIGH_BYTE_LOW_MSB_VALID);
                            /*do
                                {
                                    END_OF_CONVERSION=inportb(PORT_C);
                                    busy=END_OF_CONVERSION&BUSY_MASK;
                                }
                                while(busy=0X00);*/
                            first_byte=inportb(PORT_A);
                            final_first_byte=first_byte<<4;
                            outportb(PORT_C,BYTE_HIGH_LSB_VALID);
                            second_byte=inportb(PORT_B);
                            final_second_byte=final_first_bytelsecond_byte;
                            final_voltage=final_second_byte*4.884161164e-3;

```

```

        final_voltage_x200V=final_voltage*200;
        fprintf(fp,"%4.3f\n",final_voltage_x200V);
        setbkcolor(BLUE);
        setcolor(LIGHTGREEN);
        rectangle(110,200,200,226);
        rectangle(111,201,199,227);
        rectangle(109,199,201,228);
        floodfill(130,210,LIGHTGREEN);
        setcolor(RED);
        outtextxy(117,211,"ADC OUTPUT");
        gotoxy(27,14);
        fprintf(stdout,"%2.3f",final_voltage);
        gotoxy(34,14);
        printf("V");
        setbkcolor(BLUE);
        setcolor(LIGHTGREEN);
        rectangle(110,235,456,261);
        rectangle(111,236,455,262);
        rectangle(109,234,457,263);
        floodfill(130,250,LIGHTGREEN);
        setcolor(RED);
        outtextxy(117,245,"COMPENSATED ELECTROSTATIC VOLTMETER
        OUTPUT");
        gotoxy(59,16);
        fprintf(stdout,"%4.3f",final_voltage_x200V);
        gotoxy(68,16);
        printf("V");
        delay(sample_rate);
    }
    while(!kbhit());
    fclose(fp);
}

while(!kbhit());
outportb(PRINTER_PORT,0X03); /*move back to scorotron*/
delay(300);
outportb(PRINTER_PORT,0X06);
scorotron_graphic();          /*display scorotron position graphic*/
osnoc--;                      /*decrement number of cycles required by one*/
setbkcolor(BLUE);
setcolor(LIGHTGREEN);
rectangle(110,329,360,350);
rectangle(111,330,359,351);
rectangle(109,328,361,352);
floodfill(170,340,LIGHTGREEN);
setcolor(RED);
outtextxy(117,338,"NUMBER OF CYCLES REMAINING");
gotoxy(47,22);
printf("%4d",osnoc);
setcolor(DARKGRAY);
}
while(osnoc>0);                /*continue until required number of cycles has expired*/
sleep(3);
cleardevice();
setcolor(LIGHTGREEN);
rectangle(160,205,470,220);
rectangle(161,206,469,219);
rectangle(159,204,471,221);
floodfill(165,215,LIGHTGREEN);
setcolor(RED);

```

```

outtextxy(245,210,"SEQUENCE COMPLETE");
sound(700);
delay(2000);
nosound();
delay(600000);
cleardevice();
modetype();
}

oneshot_neg()
{
int a;
int osnoc;
int ostdsc;
int input_word;
int CONVERSION_HIGH_BYTE_LOW_MSB_VALID;
int START_CONVERSION_BYTE_LOW_MSB_VALID;
int BYTE_HIGH_LSB_VALID;
int BUSY_MASK;
int MASK_FIRST_BYTE;
int END_OF_CONVERSION;
int first_byte;
int second_byte;
int final_first_byte;
int final_second_byte;
int busy;
float final_voltage;
float final_voltage_x200V;
long int sample_rate;

cleardevice();
setbkcolor(BLUE);
setcolor(LIGHTGREEN);
rectangle(110,25,520,111);
rectangle(111,26,519,112);
rectangle(109,24,521,113);
floodfill(165,80,LIGHTGREEN);
setcolor(RED);
outtextxy(260,38,"ONESHOT MODE");
outtextxy(130,55,"ENTER NUMBER OF CYCLES REQUIRED :");
gotoxy(51,4);
flushall();
scanf("%4d",&osnoc);
while ((osnoc>=1000)||osnoc<1)||osnoc==1266) /*while outside limits display error message and
rescan data*/
    {
        setcolor(LIGHTGREEN);
        outtextxy(115,140,"YOU ARE OUTSIDE LIMITS OR HAVE ENTERED
CHARACTERS");
        outtextxy(195,150,"( ACCEPTABLE RANGE 1-1000 )");
        sound(700);
        delay(2000);
        nosound();
        gotoxy(51,4);
        flushall();
        scanf("%4d",&osnoc);
    }
setcolor(BLUE);
outtextxy(115,140,"YOU ARE OUTSIDE LIMITS OR HAVE ENTERED CHARACTERS");
outtextxy(195,150,"( ACCEPTABLE RANGE 1-1000 )");

```

```

setcolor(RED);
outtextxy(130,70,"ENTER TIME DELAY AT SCOROTRON(s):");
gotoxy(51,5);
flushall();
scanf("%5d",&ostdsc);
while ((ostdsc<1)||ostdsc>3600)||ostdsc==1266) /*time delay from 1 second to 1 hour*/
    {
        setcolor(LIGHTGREEN);
        outtextxy(115,140,"YOU ARE OUTSIDE LIMITS OR HAVE ENTERED
        CHARACTERS");
        outtextxy(195,150,"( ACCEPTABLE RANGE 1 - 3600 SECS)");
        sound(700);
        delay(2000);
        nosound();
        gotoxy(51,5);
        flushall();
        scanf("%5d",&ostdsc);
    }
setcolor(BLUE);
outtextxy(115,140,"YOU ARE OUTSIDE LIMITS OR HAVE ENTERED CHARACTERS");
outtextxy(195,150,"( ACCEPTABLE RANGE 1 - 3600 SECS)");
setcolor(RED);
outtextxy(130,85,"ENTER SAMPLING RATE(ms)      :");
setcolor(DARKGRAY);
outtextxy(130,95,"Note 10,000 = 1 second");
setcolor(RED);
gotoxy(51,6);
flushall();
scanf("%12d",&sample_rate);
while ((sample_rate<1)||sample_rate>10000000000)||sample_rate==1266) /*time delay is from 1
sec to 1 hour*/
    {
        setcolor(LIGHTGREEN);
        outtextxy(115,140,"YOU ARE OUTSIDE LIMITS OR HAVE ENTERED CHARACTERS");
        outtextxy(190,150,"( ACCEPTABLE RANGE 30 MINUTES MAX )");
        sound(700);
        delay(2000);
        nosound();
        gotoxy(51,6);
        flushall();
        scanf("%12d",&sample_rate);
    }
setcolor(BLUE);
outtextxy(115,140,"YOU ARE OUTSIDE LIMITS OR HAVE ENTERED CHARACTERS");
outtextxy(190,150,"( ACCEPTABLE RANGE 1 3600 SECS )");
setbkcolor(BLUE);
setcolor(LIGHTGREEN);
rectangle(110,120,520,191);
rectangle(111,121,519,192);
rectangle(109,119,521,193);
floodfill(265,150,LIGHTGREEN);
setcolor(RED);
outtextxy(240,133,"POSITION OF SAMPLE");
setcolor(DARKGRAY);
outtextxy(160,155,"SCOROTRON CHARGER");
outtextxy(360,155,"XENON FLASH");
do
    {
        a=inportb(STATUS_PORT); /*routine for energizing motor and moving the sample*/
                                /*input a byte from the status port and assign it
                                to a*/
    }

```

```

if (a&32)scorotron_graphic();      /*if bit 5 display scorotron position graphic*/
sleep(ostdsc);                    /*delay at scorotron charger secs*/
outportb(PRINTER_PORT,0X09); /*move sample to measuring station*/
timestart();                      /*get current system time*/
do
{
a=inportb(STATUS_PORT);
}
while(!(a&8));                    /*scans status port until time stop goes high*/
if(a&8)timestop();                /*if bit 3 get time at end of run*/
if(a&64) xenon_graphic();        /*if bit 6, display xenon position graphic*/
outportb(PRINTER_PORT,0X0C); /*energise coil behind measuring station to keep
sample in position*/
do
{
FILE *fp;
if ((fp=fopen("test","wb"))==NULL)
{
printf("Error could not open new file\n");
exit(1);
}
CONVERSION_HIGH_BYTE_LOW_MSB_VALID=0X05;
START_CONVERSION_BYTE_LOW_MSB_VALID=0X01;
BYTE_HIGH_LSB_VALID=0X07;
BUSY_MASK=0X15;
MASK_FIRST_BYTE=0XFFFFFF00;
outport(CWR,INTERFACE_CARD_SETUP);
outportb(PORT_C,CONVERSION_HIGH_BYTE_LOW_MSB_VALID);
do
{
delay(1);
outportb(PORT_C,START_CONVERSION_BYTE_LOW_MSB_VALID);
delay(1);
outportb(PORT_C,CONVERSION_HIGH_BYTE_LOW_MSB_VALID);
do
{
END_OF_CONVERSION=inportb(PORT_C);
busy=END_OF_CONVERSION&BUSY_MASK;
}
while(busy=0X00);
first_byte=inportb(PORT_A);
final_first_byte=((first_byte<<4)+MASK_FIRST_BYTE);
outportb(PORT_C,BYTE_HIGH_LSB_VALID);
second_byte=inportb(PORT_B);
final_second_byte=final_first_bytelsecond_byte;
final_voltage=((final_second_byte*4.884161164e-3)+0X0A);
final_voltage_x200V=final_voltage*200;
fprintf(fp,"%4.3f\n",final_voltage_x200V);
setbkcolor(BLUE);
setcolor(LIGHTGREEN);
rectangle(110,200,200,226);
rectangle(111,201,199,227);
rectangle(109,199,201,228);
floodfill(130,210,LIGHTGREEN);
setcolor(RED);
outtextxy(117,211,"ADC OUTPUT");
gotoxy(27,14);
fprintf(stdout,"%2.3f",final_voltage);
gotoxy(34,14);
printf("V");
}

```

```

        setbkcolor(BLUE);
        setcolor(LIGHTGREEN);
        rectangle(110,235,456,261);
        rectangle(111,236,455,262);
        rectangle(109,234,457,263);
        floodfill(130,250,LIGHTGREEN);
        setcolor(RED);
        outtextxy(117,245,"COMPENSATED ELECTROSTATIC VOLTMETER
        OUTPUT");
        gotoxy(59,16);
        fprintf(stdout,"%4.3f",final_voltage_x200V);
        gotoxy(68,16);
        printf("V");
        delay(sample_rate);
    }
    while(!kbhit());
    fclose(fp);
}
while(!kbhit());
outportb(PRINTER_PORT,0X03); /*move back to scorotron*/
delay(300);
outportb(PRINTER_PORT,0X06);
scorotron_graphic(); /*display scorotron position graphic*/
osnoc--; /*decrement number of cycles required by one*/
setbkcolor(BLUE);
setcolor(LIGHTGREEN);
rectangle(110,329,360,350);
rectangle(111,330,359,351);
rectangle(109,328,361,352);
floodfill(170,340,LIGHTGREEN);
setcolor(RED);
outtextxy(117,338,"NUMBER OF CYCLES REMAINING");
gotoxy(47,22);
printf("%4d",osnoc);
setcolor(DARKGRAY);
}
while(osnoc>0); /*continue until required number of cycles has expired*/
sleep(3);
cleardevice();
setcolor(LIGHTGREEN);
rectangle(160,205,470,220);
rectangle(161,206,469,219);
rectangle(159,204,471,221);
floodfill(165,215,LIGHTGREEN);
setcolor(RED);
outtextxy(245,210,"SEQUENCE COMPLETE");
sound(700);
delay(2000);
nosound();
delay(600000);
cleardevice();
modetype();
}

normal()
{
int nsnoc;
int nstd;
cleardevice();
setbkcolor(BLUE);

```

```

setcolor(LIGHTGREEN);
rectangle(160,125,470,185);
rectangle(161,126,469,184);
rectangle(159,124,471,186);
floodfill(165,180,LIGHTGREEN);
setcolor(RED);
outtextxy(250,132,"NORMAL SPIN MODE");
outtextxy(170,149,"ENTER NUMBER OF CYCLES REQUIRED:");
gotoxy(54,10);
flushall();
scanf("%4d",&nsnoc);
while ((nsnoc>1000)||(nsnoc<1))/*while outside limits display error message and rescan data*/
    {
        setcolor(LIGHTGREEN);
        outtextxy(115,100,"YOU ARE OUTSIDE LIMITS OR HAVE ENTERED
        CHARACTERS");
        outtextxy(175,110,"( ACCEPTABLE RANGE 1-1000 CYCLES )");
        sound(700);
        delay(2000);
        nosound();
        gotoxy(54,10);
        flushall();
        scanf("%4d",&nsnoc);
    }
setcolor(BLUE);
outtextxy(115,100,"YOU ARE OUTSIDE LIMITS OR HAVE ENTERED CHARACTERS");
outtextxy(175,110,"( ACCEPTABLE RANGE 1-1000 CYCLES )");
setbkcolor(BLUE);
setcolor(RED);
outtextxy(170,165,"PULSE TIME DELAY REQUIRED (ms) :");
gotoxy(54,11);
flushall();
scanf("%5d",&nstd);
while ((nstd<1000)||(nstd>30000)||(nstd==1266)) /*1266 = characters*/
    {
        setcolor(LIGHTGREEN);
        outtextxy(115,100,"YOU ARE OUTSIDE LIMITS OR HAVE ENTERED
        CHARACTERS");
        outtextxy(170,110,"( ACCEPTABLE RANGE 1000 - 30000 ms )");
        sound(700);
        delay(2000);
        nosound();
        gotoxy(54,11);
        flushall();
        scanf("%5d",&nstd);
    }
setcolor(BLUE);
outtextxy(115,100,"YOU ARE OUTSIDE LIMITS OR HAVE ENTERED CHARACTERS");
outtextxy(170,110,"( ACCEPTABLE RANGE 1000 - 30000 ms )");
setbkcolor(BLUE);
setcolor(LIGHTGREEN);
rectangle(160,100,470,160);
rectangle(161,101,469,159);
rectangle(159,99,471,161);
floodfill(165,125,LIGHTGREEN);
setcolor(RED);
outtextxy(240,210,"POSITION OF SAMPLE");
outtextxy(190,230,"CORONA CHARGER");
outtextxy(340,230,"XENON FLASH");
do

```

```

    {
        /*routine for energizing motor*/
        setcolor(DARKGRAY);
        outtextxy(212,243,"ÛÛÛÛÛÛÛÛÛÛ");
        outtextxy(212,248,"ÛÛÛÛÛÛÛÛÛÛ");
        outportb(PRINTER_PORT,0X03); /*address of first coil*/
        delay(nstd);
        setcolor(WHITE);
        outtextxy(212,243,"ÛÛÛÛÛÛÛÛÛÛ");
        outtextxy(212,248,"ÛÛÛÛÛÛÛÛÛÛ");
        setcolor(DARKGRAY);
        outtextxy(353,243,"ÛÛÛÛÛÛÛÛÛÛ");
        outtextxy(353,248,"ÛÛÛÛÛÛÛÛÛÛ");
        outportb(PRINTER_PORT,0X06); /*address of first coil*/
        delay(nstd);
        setcolor(WHITE);
        outtextxy(353,243,"ÛÛÛÛÛÛÛÛÛÛ");
        outtextxy(353,248,"ÛÛÛÛÛÛÛÛÛÛ");
        outportb(PRINTER_PORT,0X0C); /*address of first coil*/
        delay(nstd);
        outportb(PRINTER_PORT,0X09); /*address of first coil*/
        delay(nstd);
        setcolor(DARKGRAY);
        outtextxy(212,243,"ÛÛÛÛÛÛÛÛÛÛ");
        outtextxy(212,248,"ÛÛÛÛÛÛÛÛÛÛ");
        setcolor(WHITE);
        outtextxy(353,243,"ÛÛÛÛÛÛÛÛÛÛ");
        outtextxy(353,248,"ÛÛÛÛÛÛÛÛÛÛ");
        nsnoc--; /*decrement number of cycles required by one*/
        setbkcolor(BLUE);
        setcolor(LIGHTGREEN);
        rectangle(160,278,470,310);
        rectangle(161,279,469,309);
        rectangle(159,277,471,311);
        floodfill(170,304,LIGHTGREEN);
        setcolor(RED);
        outtextxy(170,291,"NUMBER OF CYCLES REMAINING  :");
        gotoxy(54,19);
        printf("%4d",nsnoc);
    }
    while(nsnoc>0);
    delay(30000);
cleardevice();
setcolor(LIGHTGREEN);
rectangle(160,205,470,220);
rectangle(161,206,469,219);
rectangle(159,204,471,221);
floodfill(165,215,LIGHTGREEN);
setcolor(RED);
outtextxy(245,210,"SEQUENCE COMPLETE");
sound(700);
delay(2000);
nosound();
delay(600000);
cleardevice();
modetype();
}

revvedspin()
{
int rsnoc;

```

```

int rstd;
int initialtd;
initialtd=2400;
cleardevice();
setbkcolor(BLUE);
setcolor(LIGHTGREEN);
rectangle(160,125,470,215);
rectangle(161,126,469,214);
rectangle(159,124,471,216);
floodfill(165,180,LIGHTGREEN);
setcolor(RED);
outtextxy(250,132,"REVVED SPIN MODE");
outtextxy(170,149,"ENTER NUMBER OF CYCLES REQUIRED:");
gotoxy(54,10);
flushall();
scanf("%5d",&rsnoc);
while ((rsnoc >10000)||rsnoc <1)||rsnoc==1266)
    {
        setcolor(LIGHTGREEN);
        outtextxy(115,100,"YOU ARE OUTSIDE LIMITS OR HAVE ENTERED
        CHARACTERS");
        outtextxy(180,110,"( ACCEPTABLE RANGE 1 10000 )");
        sound(700);
        delay(2000);
        nosound();
        gotoxy(54,10);
        flushall();
        scanf("%5d",&rsnoc);
    }
setcolor(BLUE);
outtextxy(115,100,"YOU ARE OUTSIDE LIMITS OR HAVE ENTERED CHARACTERS");
outtextxy(180,110,"( ACCEPTABLE RANGE 1 10000 )");
setbkcolor(BLUE);
setcolor(RED);
outtextxy(170,165,"PULSE TIME DELAY REQ (>=500ms) :");
gotoxy(54,11);
flushall();
scanf("%5d",&rstd);
while ((rstd<500)||rstd>10000)||rstd==1266)    /*1266 = characters*/
    {
        setcolor(LIGHTGREEN);
        outtextxy(115,100,"YOU ARE OUTSIDE LIMITS OR HAVE ENTERED
        CHARACTERS");
        outtextxy(170,110,"( ACCEPTABLE RANGE 500 - 10000 ms )");
        sound(700);
        delay(2000);
        nosound();
        gotoxy(54,11);
        flushall();
        scanf("%5d",&rstd);
    }
setcolor(RED);
outtextxy(170,197,"NUMBER OF CYCLES REMAINING  :");
gotoxy(54,13);
printf("%5d",rsnoc);
setcolor(BLUE);
outtextxy(115,100,"YOU ARE OUTSIDE LIMITS OR HAVE ENTERED CHARACTERS");
outtextxy(170,110,"( ACCEPTABLE RANGE 500 - 10000 ms )");
setcolor(RED);
do

```

```

    {
    outportb(PRINTER_PORT,0X09);
    delay(initialtd);
    outportb(PRINTER_PORT,0X03);
    delay(initialtd);
    outportb(PRINTER_PORT,0X06);
    delay(initialtd);
    outportb(PRINTER_PORT,0X0C);
    delay(initialtd);
    initialtd -=10;
    }
    while(initialtd>rstd);
do
    {
    outportb(PRINTER_PORT,0X09);
    delay(rstd);
    outportb(PRINTER_PORT,0X03);
    delay(rstd);
    outportb(PRINTER_PORT,0X06);
    delay(rstd);
    outportb(PRINTER_PORT,0X0C);
    delay(rstd);
    rsnoc--;
    outtextxy(170,197,"NUMBER OF CYCLES REMAINING  :");
    gotoxy(54,13);
    printf("%5d",rsnoc);
    }
    while(rsnoc>0);
delay(30000);
cleardevice();
setcolor(LIGHTGREEN);
rectangle(160,205,470,220);
rectangle(161,206,469,219);
rectangle(159,204,471,221);
floodfill(165,215,LIGHTGREEN);
setcolor(RED);
outtextxy(245,210,"SEQUENCE COMPLETE");
sound(700);
delay(2000);
nosound();
delay(600000);
cleardevice();
modetype();
}
timestart()
{
struct time start;
gettime(&start);
setbkcolor(BLUE);
setcolor(LIGHTGREEN);
rectangle(110,270,286,290);
rectangle(111,271,285,291);
rectangle(109,269,287,292);
floodfill(130,280,LIGHTGREEN);
setcolor(RED);
outtextxy(117,277,"TIME AT START OF RUN");
gotoxy(38,18);
printf("%2d %2d %2d %2d\n",start.ti_hour,start.ti_min,start.ti_sec,start.ti_hund);
}

```

```

timestop()
{
struct time stop;
gettime(&stop);
setbkcolor(BLUE);
setcolor(LIGHTGREEN);
rectangle(110,300,286,320);
rectangle(111,301,285,321);
rectangle(109,299,287,322);
floodfill(130,310,LIGHTGREEN);
setcolor(RED);
outtextxy(117,307,"TIME AT END OF RUN");
gotoxy(38,20);
printf("%02d %02d %02d %02d\n",stop.ti_hour,stop.ti_min,stop.ti_sec,stop.ti_hund);
}

xenon_graphic()
{
    setcolor(WHITE);
    outtextxy(195,170,"████████");
    outtextxy(195,175,"████████");
    setcolor(DARKGRAY);
    outtextxy(375,170,"████████");
    outtextxy(375,175,"████████");
}

scorotron_graphic()
{
    setcolor(DARKGRAY);
    outtextxy(195,170,"████████");
    outtextxy(195,175,"████████");
    setcolor(WHITE);
    outtextxy(375,170,"████████");
    outtextxy(375,175,"████████");
}

```

### **APPENDIX 3**

#### **Establishment of optimum PSSS and electrostatic voltmeter calibration**

##### **(i) Establishment of optimum probe to sample surface spacing**

The probe to sample surface spacing (PSSS) is an important parameter as it can determine the static accuracy of the electrostatic voltmeter and also act as a protection mechanism against destructive electrical arcing. In theory, as the electrostatic voltmeter employs a field nulling technique, the PSSS should be irrelevant as long as the same potential exists on both the probe and the sample under test. In this circumstance the electric field between them would be 0V. However, in practice error signals due to undesirable capacitive coupling and electrical noise can affect the charge measurement in that offsets can occur if the PSSS is varied. Monroe Electronic Inc. (1973) state a special zeroing technique to allow the PSSS to be varied without offsets in the electrostatic voltmeter output being encountered. However, the measuring system can still be prone to error from electrical noise for large values of PSSS. Figure AP3.1 was compiled from manufacturers data (Monroe Electronics Inc., 1971) and shows how the percentage error of the electrostatic voltmeter varies with PSSS. It was seen that the system error increased as the PSSS was increased, this suggested that ideally the PSSS spacing should be as small as possible.

However, due to the potentially high surface potential required for the xerographic investigations, the possibility of electrical arcing had to be considered. If the PSSS was small and the potential upon the sample under test was high, dielectric breakdown of the air separating the probe head and the sample surface may occur which could result in a destructive electrical arc entering the transparent probe. Figure AP3.2 was compiled from manufactures data (Monroe Electronics Inc., 1985) and shows the minimum PSSS required over a range of surface potentials if electrical arcing is to be avoided. It was seen that at the maximum range of the probe (2kV) a minimum PSSS of 2mm was required if electrical arcing was to be prevented. For charge acceptance measurements where the surface potential was unknown, the potential limiting grid within the scorotron charger was set to 2kV in order to prevent surface charges of >2kV coming into contact with the probe. The PSSS was set at 2mm accordingly for charge acceptance measurements. For experimentation where the surface potential is

of a predetermined level, it would be possible to decrease the PSSS in order to improve system accuracy. However, figure AP3.1 suggested that any improvement in system error by reduction of the PSSS would be negligible and so the PSSS was fixed at 2mm for all experimentation.

(ii) Calibration procedure for Monroe model 144 electrostatic voltmeter

For accuracy of results it was essential that the electrostatic voltmeter was properly calibrated. The attenuation network of the model 144 is a temperature compensated carbon film network which can drift with age (Monroe Electronics Inc., 1971). The calibration procedure was conducted in-situ inside the light tight enclosure with a brass test plate replacing the sample holder and sample. The brass test plate was positioned at the same location and height as the sample and was positioned directly under the transparent probe and the PSSS was set to 2mm. A 1mm thick sheet of rubber was used to insulate the brass test plate from the rotating sample support arm. A power cable was attached directly to the brass test plate in order that predetermined potential could be applied. A Brandenburg model 2475R stabilised HV power supply was used to supply the potentials to the brass test plate. A Solartron 7510 digital voltmeter with an accuracy of 0.001% was used to set the potential on the brass test plate, and monitor the output from the electrostatic voltmeter.

The potential on the brass test plate was initially set to the system ground and the Solartron 7510 was used to check that the test plate potential was <1mV. The zero control on the model 144 was then set to 0V accordingly. A positive potential of +200V was then applied to the brass test plate and the output calibration of the model 144 was adjusted until the output displayed upon the Solartron 7510 DVM was 1V. The potential upon the brass test plate was then increased in 100V increments and the output recorded up until a potential of +1kV. The results of the calibration process are shown in figure AP3.3 and table AP3.1. The results shown in table AP3.1 showed that the accuracy of the electrostatic voltmeter was decreasing as the surface potential was increasing and a maximum difference of 3.5V was encountered between the potential applied to the test plate and the output of the electrostatic voltmeter (x200).

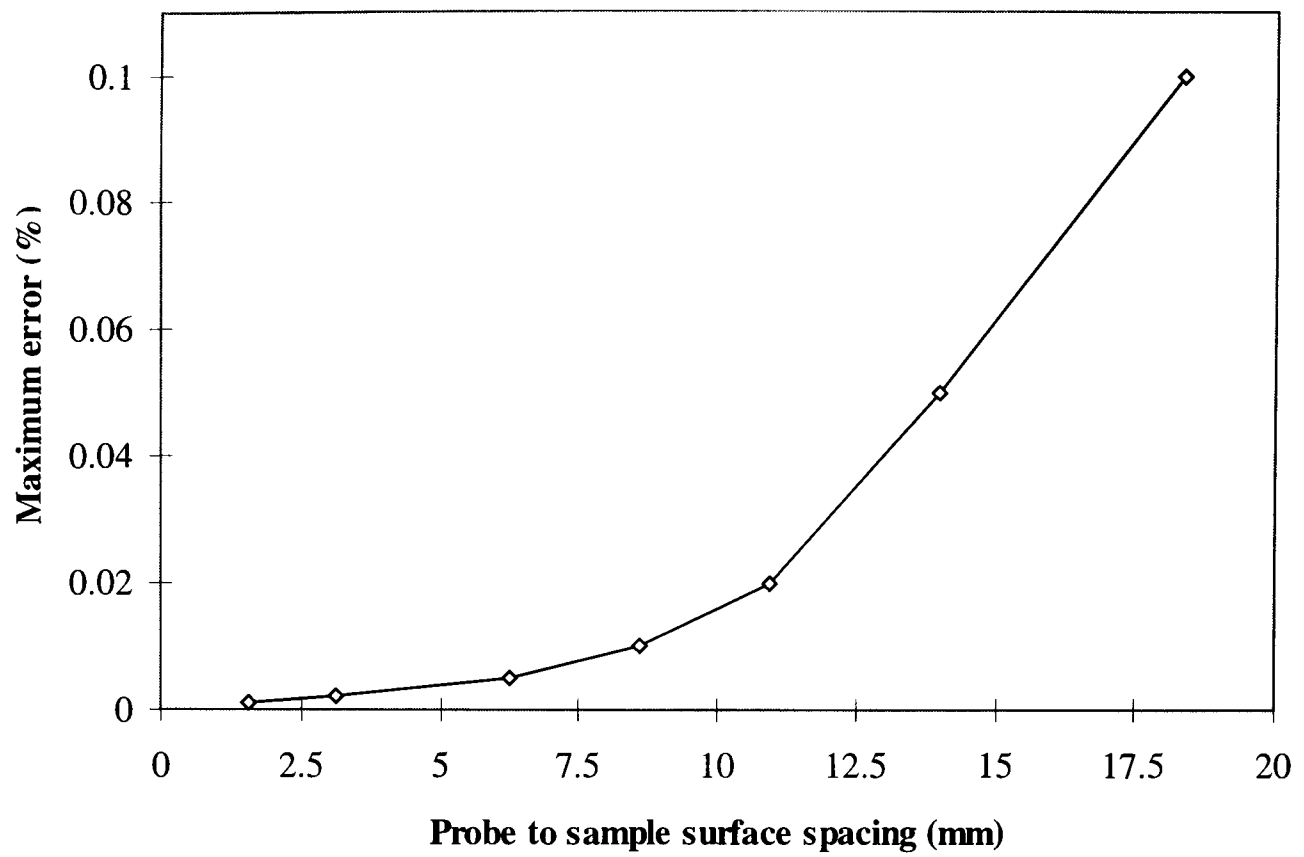


**Figure AP3.1 Graph showing effect of altering PSSS on system error**

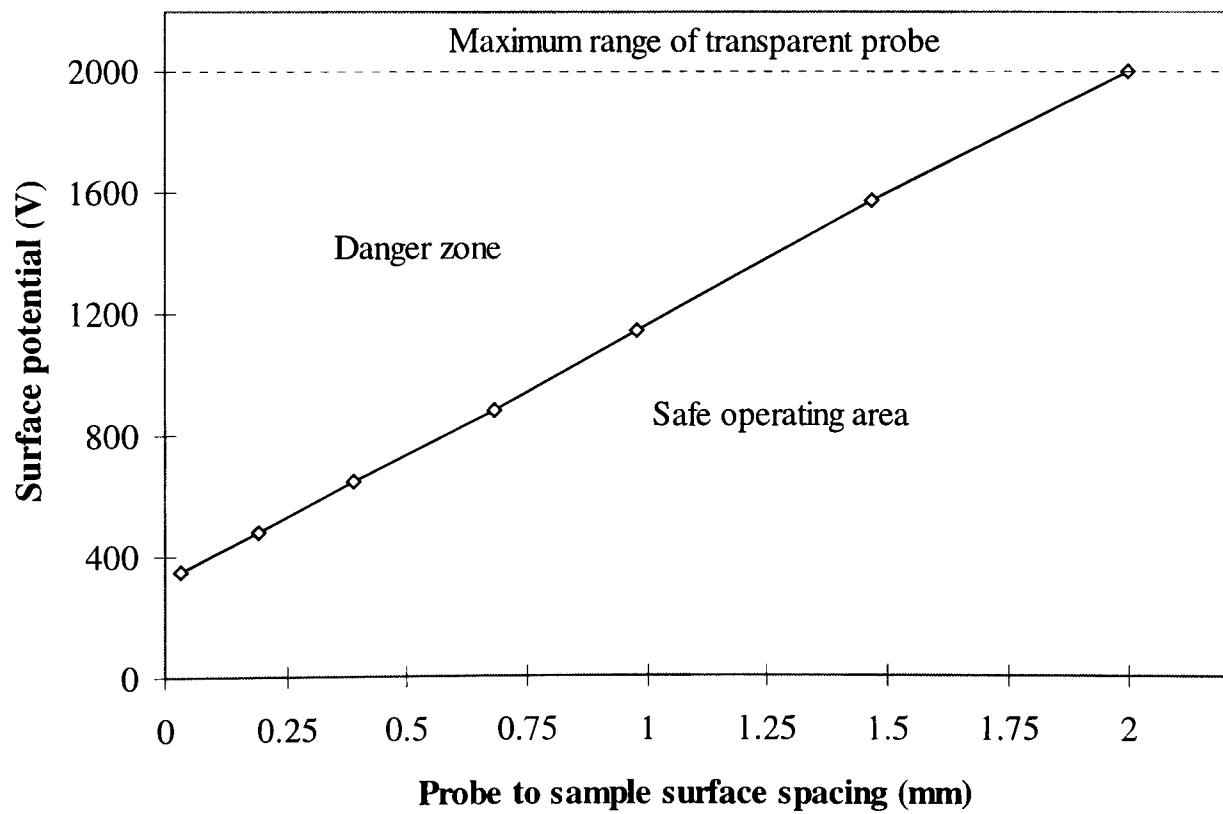


**Figure AP3.2 Graph showing safe operating PSSS for applied surface potential**

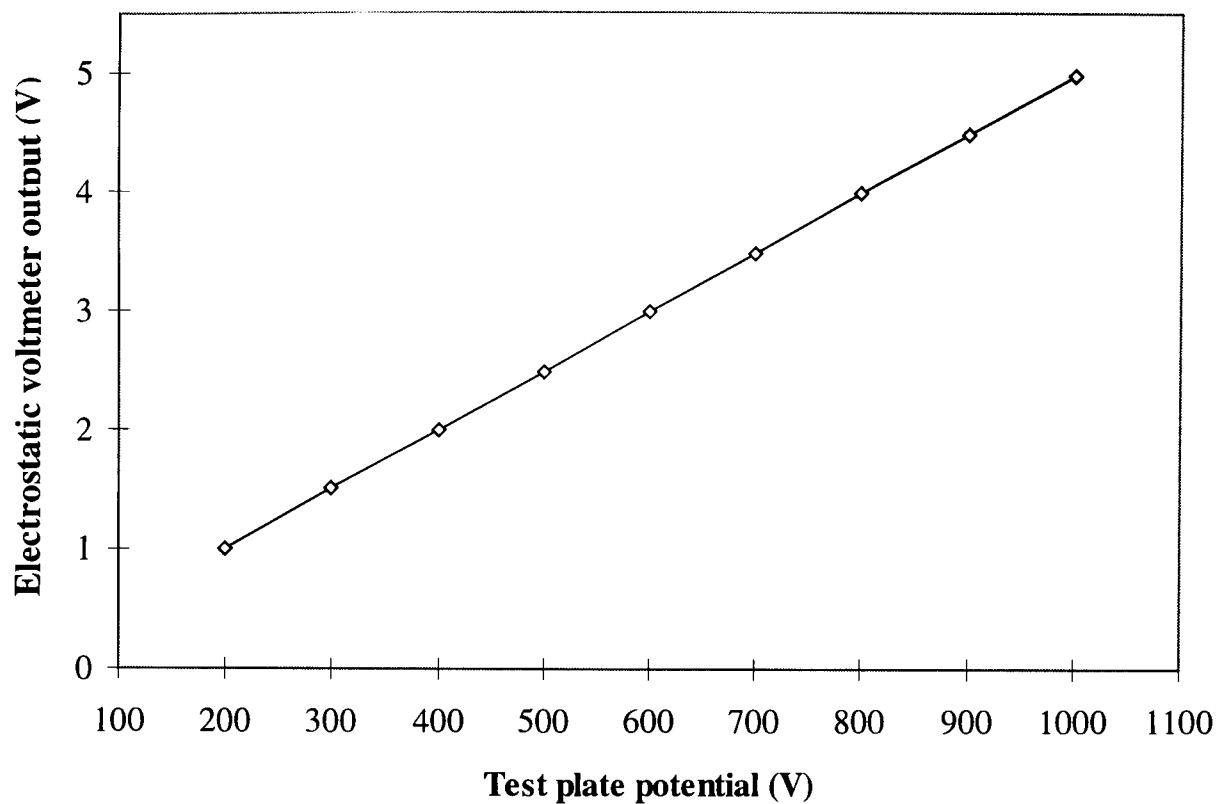


**Figure AP3.3 Calibration results of Monroe model 144 electrostatic voltmeter.**

Test plate potential (V)	Ideal o/p (V)	Measured o/p (V)	Error (mV)	Measured o/p (x200) (V)	Error (x200) (V)	Error (%)
200	1	1	0	200	0	0
300	1.5	1.49	0.3	299.94	0.06	0.02
400	2	1.99	8.7	398.26	1.74	0.43
500	2.5	2.48	10.1	497.98	2.02	0.40
600	3	2.98	10.7	597.86	2.14	0.35
700	3.5	3.48	14	697.2	2.8	0.4
800	4	3.98	14	797.2	2.8	0.35
900	4.5	4.48	16	896.8	3.2	0.35
1000	5	4.98	17.5	996.5	3.5	0.35

**Table AP3.1 Test data for calibration of electrostatic voltmeter.**

**APPENDIX 4****MATLAB analysis programs**

```

(i) Program for the analysis of the discharge mechanism in a-As2Se3
%curve fitting routine and
%determination of depletion time
load run_94.mat;
format short
complete_time=sample_no*0.5;
complete_data=a;
w=polyfit(complete_time,complete_data,3);
new_time_interpolation=(0.5:0.1:220.5);
q=polyval(w,new_time_interpolation);
plot(new_time_interpolation,q,'r')
xlabel('Time(s)');
ylabel('Surface potential(V)')
title('Run_72, sample_29, ASSEICF95');
grid
pause
dv=diff(q);
dt=diff(new_time_interpolation);
dvdt_complete_data=dv./dt;
complete_time_diff=0.5:0.1:220.4;
plot(complete_time_diff,abs(dvdt_complete_data),'r');
axis([10,150,0,6]);
xlabel('Time(s)')
ylabel('|dv/dt|(Vs^-1)');
title('Run_72, sample 29, ASSEICF95');
grid
pause
plot(log(complete_time_diff),log(abs(dvdt_complete_data)), 'r')
axis([2,4.5,0,1.7]);
xlabel('ln Time(s)');
ylabel('ln |dv/dt|(Vs^-1)');
grid
pause
hold on
time_zone_1=complete_time_diff(80:length(complete_time_diff)-1860);
data_time_zone_1=dvdt_complete_data(80:length(dvdt_complete_data)-1860);
data_time_zone_1=abs(data_time_zone_1);
log_time_zone_1=log(time_zone_1);
log_data_time_zone_1=log(data_time_zone_1);
c_time_zone_1=polyfit(log_time_zone_1,log_data_time_zone_1,1);
a_time_zone_1=exp(c_time_zone_1(2))
b_time_zone_1=c_time_zone_1(1)
y_time_zone_1=a_time_zone_1*time_zone_1.^b_time_zone_1;
plot(log(time_zone_1),log(y_time_zone_1),'g')
p_time_zone_1=b_time_zone_1+1
constant_a_tz_1=a_time_zone_1/((-6e-3^2/(2*10.8*8.85e-14))*p_time_zone_1)
time_zone_2=complete_time_diff(540:length(complete_time_diff)-1150);
data_time_zone_2=dvdt_complete_data(540:length(dvdt_complete_data)-1150);
data_time_zone_2=abs(data_time_zone_2);
log_time_zone_2=log(time_zone_2);
log_data_time_zone_2=log(data_time_zone_2);
c_time_zone_2=polyfit(log_time_zone_2,log_data_time_zone_2,1);
a_time_zone_2=exp(c_time_zone_2(2))
b_time_zone_2=c_time_zone_2(1)

```

```

y_time_zone_2=a_time_zone_2*time_zone_2.^b_time_zone_2;
plot(log(time_zone_2),log(y_time_zone_2),'g')
p_time_zone_2=-b_time_zone_2-1
constant_a_tz_2=(-(10.8*8.85e-14)/(2*a_time_zone_2))*(416.131/6e-3)^2*p_time_zone_2
pause
hold off
close
time_zone_1_ab=(0:0.1:48.47)';
dvdt_ab_1= a_time_zone_1*time_zone_1_ab.^b_time_zone_1;
plot(time_zone_1_ab,dvdt_ab_1,'r')
hold on
time_zone_2_ab=(48.47:0.1:220.5)';
dvdt_ab_2= a_time_zone_2*time_zone_2_ab.^b_time_zone_2;
plot(time_zone_2_ab,dvdt_ab_2,'r')
xlabel('Time (s)');
ylabel('|dV/dt| (V/s^-1)')
grid
pause
hold off
close
plot(log(time_zone_1_ab),log(dvdt_ab_1),'r')
hold on
plot(log(time_zone_2_ab),log(dvdt_ab_2),'r')
grid
xlabel('ln Time (s)');
ylabel('ln |dV/dt| (V/s^-1)')
pause
hold off
close
%routine to deconvolute currents using Abkowitz model
%calculation of theoretical dV/dt
x_deconv_1=[0;43.2];
y_deconv_1=[log(416.130);log(208.065)];
w=polyfit(x_deconv_1,y_deconv_1,1);
x_deconv_new=(0:0.01:43.2)';
q_deconv_1=polyval(w,x_deconv_new);
c_deconv_zone_1=polyfit(x_deconv_new,q_deconv_1,1);
a_deconv_zone_1=exp(c_deconv_zone_1(2))
b_deconv_zone_1=c_deconv_zone_1(1)
y_deconv_zone_1=a_deconv_zone_1*x_deconv_new.^b_deconv_zone_1;
dvdt_deconv=a_deconv_zone_1*x_deconv_new.^b_deconv_zone_1;
plot(x_deconv_new,log(dvdt_deconv),'g')
hold on
time_zone_1_new=(0:0.01:48.47)';
dvdt_time_zone_1_new=a_time_zone_1*time_zone_1_new.^b_time_zone_1;
plot(time_zone_1_new,dvdt_time_zone_1_new,'r')
grid
xlabel('Time (s)')
ylabel('|dV/dt| (V/s^-1)')
legend('g','Abkowitz model thermal generation only','r','Abkowitz model thermal generation and surface injection')
pause
hold off
close

```

(ii) program to establish discharge mechanism in a-Si:H

```

load run_99.mat;
format short
complete_time=sample_no*0.5;
complete_data=a;
w=polyfit(complete_time,complete_data,3);
new_time_interpolation=(0.5:0.1:168)';
q=polyval(w,new_time_interpolation);
plot(new_time_interpolation,q,'r')
axis([0 170 0 450])
xlabel('Time(s)');
ylabel('Surface potential(V)')
grid
pause
close
dv=diff(q);
dt=diff(new_time_interpolation);
dvdt_complete_data=dv./dt;
complete_time_diff=0.5:0.1:167.9;
plot(complete_time_diff,abs(dvdt_complete_data),'r');
axis([0 150 0 15])
grid
xlabel('Time (s)')
ylabel('|dV/dt| (V/s^-1)')
pause
close
semilogy((complete_time_diff),(abs(dvdt_complete_data)), 'r')
axis([0 150 0.2 30])
xlabel('Time (s)')
ylabel('ln |dV/dt| (V/s^-1)')
grid
pause
close
loglog((complete_time_diff),(abs(dvdt_complete_data)), 'r')
axis([0 150 0.1 30])
grid
xlabel('Time (s)')
ylabel('|dV/dt| (V/s^-1)')
hold on
time_zone_1=complete_time_diff(1:length(complete_time_diff)-1580);
data_time_zone_1=dvdt_complete_data(1:length(dvdt_complete_data)-1580);
data_time_zone_1=abs(data_time_zone_1);
log_time_zone_1=log(time_zone_1);
log_data_time_zone_1=log(data_time_zone_1);
c_time_zone_1=polyfit(log_time_zone_1,log_data_time_zone_1,1);
a_time_zone_1=exp(c_time_zone_1(2))
b_time_zone_1=c_time_zone_1(1)
y_time_zone_1=a_time_zone_1*time_zone_1.^b_time_zone_1;
p_time_zone_1=b_time_zone_1+1
plot((time_zone_1),(y_time_zone_1),'g')
time_zone_2=complete_time_diff(400:length(complete_time_diff)-250);
data_time_zone_2=dvdt_complete_data(400:length(dvdt_complete_data)-250);
data_time_zone_2=abs(data_time_zone_2);
log_time_zone_2=log(time_zone_2);
log_data_time_zone_2=log(data_time_zone_2);
c_time_zone_2=polyfit(log_time_zone_2,log_data_time_zone_2,1);
a_time_zone_2=exp(c_time_zone_2(2))
b_time_zone_2=c_time_zone_2(1)
y_time_zone_2=a_time_zone_2*time_zone_2.^b_time_zone_2;
p_time_zone_2=-b_time_zone_2-1

```

```

plot((time_zone_2),(y_time_zone_2),'g')
pause
close
clc
inv_l=1/2.71e-3;
electric_field=q/2.71e-3;
sqrt_electric_field=sqrt(electric_field);
difference=(sqrt_electric_field(1:length(sqrt_electric_field)-1)));
plot(difference',log(inv_l*(abs(dvdt_complete_data))))
grid
ylabel('L^-1 * |dV/dt| (V/s^-1/cm^-1)')
xlabel('E^1/2(V/cm^-1)')
axis([75,350,4.5,9])
hold on
difference_scaled=(sqrt_electric_field(180:(length(sqrt_electric_field)-1)-0));
dvdt_complete_data_scaled=dvdt_complete_data(180:length(dvdt_complete_data)-0);
w2=polyfit(difference_scaled',log(inv_l*(abs(dvdt_complete_data_scaled))),1);
q2=polyval(w2,difference_scaled');
plot(difference_scaled',q2,'r')
[x1,y1]=ginput(1);
[x2,y2]=ginput(1);
slope=(y1-y2)/(x1-x2);
Beta=slope^2
bpf_insert=(slope^2*1.602177338e-19)^2;
Dielectric_const_PF=1.602177338e-19^3/(pi*8.85e-14*bpf_insert)
Dielectric_const_S=1.602177338e-19^3/(4*pi*8.85e-14*bpf_insert)
Diff_PF=10-Dielectric_const_PF
Diff_S=10-Dielectric_const_S
hold off
close

```

**APPENDIX 5****MATLAB program for the production of 3D images**

```

x=[1 1 1 1;2 2 2 2;3 3 3 3;4 4 4 4];
x=rot90(x);
y=[1 2 3 4;1 2 3 4;1 2 3 4;1 2 3 4];
y=rot90(y);
y=rot90(y);
y=rot90(y);
[x_grid,y_grid]=meshgrid(x,y);
z=[3.014,2.306,2.422,3.029;
  2.336,1.817,1.797,2.366;
  2.295,1.843,1.8675,2.393;
  3.02,2.155,2.383,3.011];
xi=interp5(x,6);
yi=interp5(y,6);
zi=interp5(z,6);
colormap(gray);
mesh(xi,yi,-zi);
axis([0 4.5 0 4.5 -3.3 -1.78]);
grid
xlabel('Column number');
ylabel('Row number');
zlabel('Mean signal response X10^-6A')
hold on
errbar3(1,1,-3.014,-0.01153,-0.01153);
errbar3(1,2,-2.336,-0.035144,-0.035144);
errbar3(1,3,-2.295,-0.03392,-0.03392);
errbar3(1,4,-3.02,-0.01062,-0.01062);
errbar3(2,1,-2.306,0.02423,0.02423);
errbar3(2,2,-1.817,0.03617,0.03617);
errbar3(2,3,-1.843,0.03414,0.03414);
errbar3(2,4,-2.155,0.02441,0.02441);
errbar3(3,1,-2.422,0.02317,0.02317);
errbar3(3,2,-1.797,0.03723,0.03723);
errbar3(3,3,-1.8675,0.03505,0.03505);
errbar3(3,4,-2.383,0.02648,0.02648);
errbar3(4,1,-3.023,0.00934,0.00934);
errbar3(4,2,-2.366,0.01346,0.01346);
errbar3(4,3,-2.393,0.01196,0.01196);
errbar3(4,4,-3.0161,0.01088,0.01088);
x=[1 1 1 1;2 2 2 2;3 3 3 3;4 4 4 4];
x=rot90(x);
y=[1 2 3 4;1 2 3 4;1 2 3 4;1 2 3 4];
y=rot90(y);
y=rot90(y);
y=rot90(y);
[x_grid,y_grid]=meshgrid(x,y);
z=[3.0075,3.088,3.08,3.029;
  3.005,3.0754,3.0831,3.027;
  3.0097,3.0793,3.0764,3.0202;
  3.02,3.0818,3.0841,3.0114];
xi=interp5(x,3);
yi=interp5(y,3);
zi=interp5(z,3);
mesh(xi,yi,-zi);
errbar3(1,1,-3.0075,0.01153,0.01153);
errbar3(1,2,-3.005,0.0111,0.0111);

```

```
errbar3(1,3,-3.0097,0.00924,0.00924);  
errbar3(1,4,-3.02,0.01062,0.01062);  
errbar3(2,1,-3.088,0.0123,0.0123);  
errbar3(2,2,-3.0754,0.0127,0.0127);  
errbar3(2,3,-3.0793,0.00856,0.00856);  
errbar3(2,4,-3.0818,0.00833,0.00833);  
errbar3(3,1,-3.08,0.00977,0.00977);  
errbar3(3,2,-3.0831,0.0118,0.0118);  
errbar3(3,3,-3.0764,0.01035,0.01035);  
errbar3(3,4,-3.0841,0.00897,0.00897);  
errbar3(4,1,-3.029,0.00734,0.00734);  
errbar3(4,2,-3.027,0.01021,0.01021);  
errbar3(4,3,-3.0202,0.00869,0.00869);  
errbar3(4,4,-3.0114,0.00982,0.00982);  
mmview3d  
pause  
hold off
```

**APPENDIX 6****Published paper**

This paper was the most recent in a series of papers to be published concerning the research project. The paper 'Application of amorphous semiconductors for optical tomography' was published in the refereed journal 'Measurement and Control', Vol.33, No.6, July 2000, pages 175-180.

# Application of amorphous semi-conductors for optical tomography

**R P Jenner, BEng(Hons), AMIEE, & S M Vaezi-Nejad,**

BSc, MSc, DIC, PhD, CEng, FInstMC, MIEE,

*Electronics Research Group,*

*Advanced Instrumentation and Control Research Centre,*

*Medway School of Engineering, University of Greenwich.*

## Introduction

Photoconductivity measurements were performed in both xerographic and electroded modes by the use of a purpose-built xenon flash unit<sup>1</sup>. The experimental system developed is an integral part of an on-going PhD programme<sup>2</sup> on the application of amorphous semiconductors as sensors for optical process tomography (OPT). Control of the laboratory apparatus and the collection of data is fully automated, and the laboratory apparatus<sup>3,4</sup> conforms to all relevant health and safety regulations concerning working with high voltages.

Extensive software has been written for the data handling, data management, data display and numerical analysis of the experimental data. The advantages of amorphous semiconductors for OPT are briefly discussed in the first section. The subsequent two sections contain an overview of the developed experimental apparatus and a brief description of amorphous semiconductor materials' ability to produce

qualitative and quantitative data for imaging or control signal generation.

## Advantages of amorphous semiconductors

Significant advances in tomographic imaging over recent years have led to highly accurate and efficient tomographic imaging systems. However, such systems that rely upon ionising radiation can be very expensive and complex and can pose a risk to operator safety due, for example, to radiation found in x-ray imaging systems or to very-high-intensity light found in systems that employ lasers as the illumination source. Thus there is currently great demand in the process industries for economical, accurate, fast, easy to use, portable, and safe tomographic imaging systems. The authors believe that tomographic imaging systems that employ amorphous semiconductors as sensing elements can help to fulfil the process industries' requirements.

The term amorphous can be defined

as 'random'. Amorphous materials can be insulators or semiconductors, and at very low temperatures they can also become superconductors<sup>5,6</sup> in which periodicity is absent. Our past investigations have shown that amorphous semiconductors have the fol-

lowing main advantages that make them particularly attractive for use in OPT systems.

(a) OPT systems utilise visible light as the illumination source.

(b) Amorphous semiconductors are mechanically and chemically stable.

(c) Amorphous semiconductors can be made into large-area devices. For example, amorphous selenium-based flat panels used in medical x-ray imaging systems have been made into single devices as large as 29.2 x 40.6cm<sup>2</sup> that can image the entire thoracic region.

Amorphous selenium (a-Se) is a chalcogenide glass which has been used extensively in the xerographic industries. A requirement of xerographic photoreceptors, as with OPT, is that they are sensitive to the entire visible spectrum. The sensitivity of a-Se in the red region can be improved by the addition of tellurium (Te) to the a-Se film. The addition of arsenic (As) to the a-Se film can also improve stability and increase the film's sensitivity in the red region of the visible spectrum.

Amorphous selenium also suffers from problems of structural instability which could make it unsuitable for tomographic imaging systems. It can crystallise at temperatures above 100°C which means that the a-Se film becomes very highly conductive and any applied electrostatic charge dissipates at a rapid rate. The introduction of As not only increases the sensitivity of the a-Se film, it can also retard the crystallisation rate if the quantity of As is sufficient.

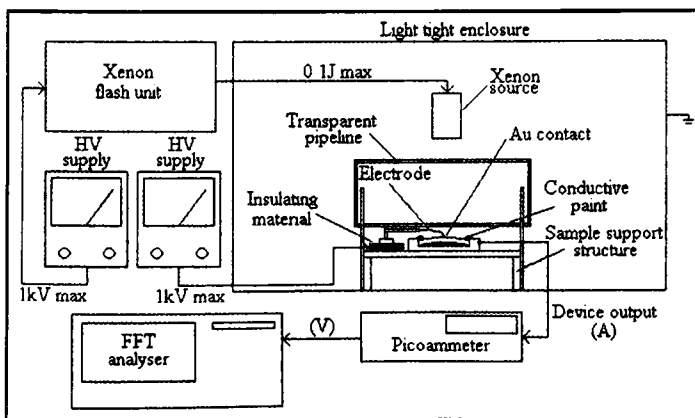


Figure 1: Basic block diagram for experimentation in the electroded mode of operation.

Selenium alloys comprising 40% As and 60% a-Se are termed amorphous arsenic triselenide (a-As<sub>2</sub>Se<sub>3</sub>), are sensitive to the entire visible spectrum and are more mechanically and chemically durable than a-Se alloys which contain much smaller amounts (<1%) of As<sup>8</sup>. The addition of a small amount of Cl (~30 ppm) improves the speed of response by increasing the mobility of holes as free-charge carriers in a-As<sub>2</sub>Se<sub>3</sub> films.

The high electrical resistivity in hydrogenated amorphous silicon (a-Si:H) films (~10<sup>13</sup> Ω/cm) and its high photosensitivity make this semiconductor material also attractive as a sensor for OPT.

## Experimental investigations

In the initial stages of the current research, the electrical properties of various amorphous semiconductors including a-Se, a-As<sub>2</sub>Se<sub>3</sub>, a-SeTe, a-Si and a-Si:H were measured and compared using xerographic experimental techniques. Based upon the results of this investigation, a-As<sub>2</sub>Se<sub>3</sub> and a-Si:H were selected for further investigation. The computer-controlled experimental apparatus (CCEA) was designed to allow experimentation in the xerographic mode of operation to be performed, in which the free surface of the sample is electrostatically charged by a scorotron charger and the resulting decay curves are recorded and analysed.

All tomographic experimentation reported here was performed in the electroded mode of operation whereby semi-transparent gold (Au) contacts of a few angstroms thickness were sputtered onto the surface of the materials under test. A single 100 μm diameter electrode was connected to the Au film in order to make electrical contact with the device so that a pre-defined electric field (E) could be applied to the material under test. Pulses of visible light were then applied through a transparent tomographic prototype to the sensor surface and the resulting photocurrent was monitored and recorded.

A brief description of the experimental system is included in the fol-

lowing sub-section. Our preliminary investigations have identified the suitability of a-As<sub>2</sub>Se<sub>3</sub> and a-Si:H as sensors for OPT based upon the following main criteria.

## Signal response

The signal response,  $R(\lambda)$ , of the materials can be defined as the difference in magnitude of the dark current ( $I_d$ ) and the peak output current ( $I_s$ ) when the Au film is illuminated with visible light having a higher energy than the band gap of the material under test<sup>9</sup>. The magnitude of  $R(\lambda)$  (measured in volts or current) was dependent upon the material under test, the size of Au contact, the applied electric field, the radiant power of the light incident upon the Au contact, the duration of the incident light, and the light pulse repetition rate. As light pulses are passed through the tomographic prototype, the radiant power of the light incident upon the Au contact varies due to the action of the tomographic prototype and the media contained within that prototype. As a result there is a variation in the magnitude of  $R(\lambda)$ . It is the variance in  $R(\lambda)$  resulting from the action of the tomographic prototype and media that provides quantitative and qualitative data for image representation or media analysis or data for process control purposes.

## Responsivity

The responsivity of the material (measured in A/W) is the ratio of  $I(s)$  to the radiant power of incident light. The measurement of responsivity could be the determining factor in selecting materials for OPT applications. For example, if a particular material were exhibiting superior responsivity under set experimental conditions, the following advantages could ensue.

(1) Due to the superior responsivity of the material, an increase in  $I_s$  would be detected, leading to an improved signal-to-noise ratio (SNR).

(2) The enhanced responsivity may lead to the detection of smaller changes in incident light, thus improving the efficiency of the system.

(3) In application terms, the superior

responsivity could also allow the distance between the light source and detector to be increased, thus allowing larger-diameter pipelines and vessels and also denser mediums to be monitored.

(4) In terms of operator safety, the superior responsivity of the material allows the electric field and light intensity applied to the device to be reduced.

(5) Finally, the active area of the Au contact could be reduced, thus improving the resolution of the system.

## Speed of response

The speed of response is defined as the time required for the current to go from  $I_d$  to  $I_s$  after illumination has occurred,  $t(I_s)$ , or the time required for the current to return to its original value prior to the illumination period,  $t(I_d)$ <sup>9</sup>. The speed of response of a material is a very important parameter as it determines the maximum operating frequency of the tomographic system.

In the current research we are particularly interested in  $t(I_s)$  as the variance in  $I_s$  and therefore  $R(\lambda)$ , is used for image representation or media analysis. Once we have established and recorded  $R(\lambda)$ , no further information from the current pulse is required for tomographic purposes, and the Au contact is switched to the ground state to remove remaining current as quickly as possible. Thus  $t(I_s)$  is the dominant factor in establishing the system's maximum speed of operation and it is desirable that  $t(I_s)$  is as short as possible.

## Dark current

Dark current ( $I_d$ ) can be defined as the amount of current that flows through the device in the dark and can be considered as noise. If the device were an ideal insulator in the dark, no current would flow in the dark and  $I_s$  would be the true value of detected photocurrent when the sample surface was illuminated. However, as the devices are not ideal and current can be injected by the Au contact, the value of  $I_d$  must be subtracted from  $I_s$  to determine  $R(\lambda)$ . Dark current is problematic in that it reduces the resolution of the measuring system and limits the smallest value of  $I_s$  that can

be accurately detected. It is therefore desirable that  $I_d$  be as small and as stable as possible.

## Repetitive tomographic cycling

If the a-As<sub>2</sub>Se<sub>3</sub> and a-Si:H devices are to find application as sensors for OPT, they must be capable of producing repeatable values of  $R(\lambda)$  over extended periods of time at operating speeds required for OPT applications (100Hz minimum<sup>10</sup>). The sensor is said to be fatigued when it can no longer maintain its electrical properties and light-induced degradation (LID) is observed in the signal response. The amount of fatigue experienced by the device depends upon the material under test, the electric field, the intensity of the incident light, and the repetition rate of the illumination pulses ( $L_{rep}$ ).

$L_{rep}$  is an important parameter in that if it is greater than the time required for the material to regain its original value of resistance prior to a light pulse being issued,  $I_s$  degenerates and therefore  $R(\lambda)$  cannot be maintained over extended periods of time. The CCEA allows the measurement of  $I_s$ ,  $R(\lambda)$ ,  $I_d$  and fatigue in order to establish the suitability of materials for OPT applications.

## Experimental apparatus

The description of the CCEA, its associated characteristics and performance will be discussed in terms of the electroded mode of operation. The samples were cut to be 20mm<sup>2</sup> pieces, and a 2mm wide strip of semiconductor material was removed from all sides of each sample to allow electrical contact to the conductive substrate to be made. All experimentation was performed within a purpose-built light-tight enclosure which was conductive and kept at the system ground to prevent any internal build-up of unwanted electrostatic charge. All components within the enclosure were also kept at the system ground for the same reason.

In the electroded mode of operation we were concerned with observing how the samples behaved under OPT conditions. These have semi-transparent

ent Au contacts of various dimensions and configurations sputtered onto their surface. Each Au contact can be considered as a single pixel of information. The sample was placed in a purpose-built holder, which in turn sat on a sample support structure. A base made from insulating material was fixed to the floor of the light-tight enclosure and locating holes were positioned around the base perimeter. Matched locating pins on the sample support structure ensured that if the sample needed to be removed from the system, it was always returned to exactly the same position. The sample holder was machined from conductive material with a recess into which the sample was placed. Electrically conductive paint was then applied from the conductive sample holder to the exposed portion of the sample substrate. A low-noise shielded cable was then attached to the sample holder which formed the device output.

A 100 $\mu$ m electrode was then attached to a power supply terminal on the sample holder. An insulating device was used to isolate the power supply from the sample holder. The other end of the electrode was then attached to the Au contact by electrically conductive paint. A stabilised HV power supply was used to supply voltages of up to 1kV to the sample. In this manner, predetermined levels of electric field could be induced in the sample under test. A support plate was attached to each end of the sample support structure, holding a tomographic prototype in position directly over the sample. The tomographic prototypes comprised transparent acrylic pipe sealed at both ends. A screw cap at one end of the pipe allowed the insertion of various media. The support plates suspended the pipe so that the centre of the pipe was directly aligned with the centre of the sample. They were interchangeable so that pipelines of various dimensions could be employed in the system.

The two most common types of light projection in OPT are fan-beam and parallel-beam projection. With fan-beam projection a single light source is used to flood an array of

sensors with light simultaneously. This has the advantage that fewer light sources are required, but the disadvantage that the light-path through the media to the array of sensors is not the same, which can result in complex sensor array configurations and image reconstruction algorithms.

With parallel-beam projection, every sensor in an array requires its own light source. The light sources and the sensors are arranged so that the light-paths through the media are the same for all sensors. This has the advantage in that reconstruction algorithms previously developed for medical tomography can be readily employed. The disadvantage is that multiple light sources are required.

In the current research, both types of projection have been investigated. For fan-beam projection, the tomographic prototype was left transparent for its entire length. But for parallel-beam projection the inside of the tomographic prototype was painted matt black, with a small transparent window left to columnise the light as it passed through the prototype and media to the sensor.

The xenon light source was positioned directly above the tomographic prototype in direct alignment with the centre of the pipeline and sample. The height of the light source can be adjusted for various pipeline dimensions. When experimentation was to be performed, the Au contact was switched to the system ground and the xenon source was pulsed at 100Hz for 15 minutes in order to bring the xenon gas up to maximum working temperature. The intensity of the light was dependent upon the input energy to the source, the distance between the source electrodes, and the pressure of the xenon gas. The xenon source was also run at 100Hz for 15 minutes to ensure that the gas pressure was at its maximum and thus the light intensity was at its peak and at its most stable. The light was then removed and a predetermined electric field was established in the sample via the HV supply and electrode.

Once the electric field had been established, dark current started to flow through the sample. This dark

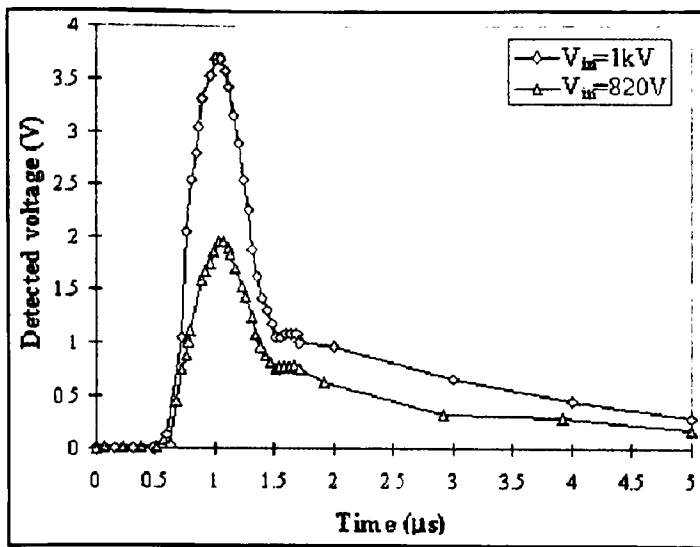


Figure 2: Graph showing change in light intensity whilst maintaining pulse duration.

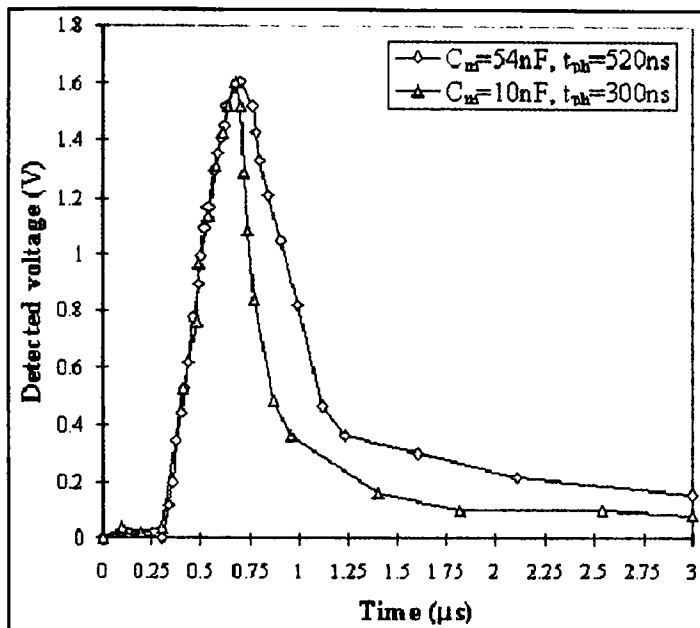


Figure 3: Graph showing change in pulse duration whilst maintaining light intensity.

current interfered with the tomographic measurement in that it reduced the resolution of the measuring system. Both the dark ( $I_d$ ) and photocurrents ( $I_s$ ) were measured using a picoammeter. The picoammeter was then switched to the relative mode which nullified any existing value of  $I_d$  and allowed maximum measurement resolution. Light of user-defined intensity, duration and repetition rate was then applied to the tomographic prototype, through the media, and onto the sample surface. The resulting photocurrent was measured with the picoammeter which provided a continuous inverted analogue output.

This output was then taken to a personal fast Fourier transform (FFT) analyser and converted to a digital

photo-diode. The photodiode, mounted in a replica of the sample support structure, was fixed on the support structure at the exact height and position of the sample surface. When a light pulse was to be recorded, the sample was removed from the system and the replica support structure was inserted. Again locating pins ensured that the structure always went into the system in the correct position. Before tomographic experimentation, the photodiode was inserted into the system and the xenon source was brought up to maximum working temperature as previously described. The desired light pulse intensity and duration were then set and the light pulse was recorded using a 100MHz digital storage oscilloscope.

signal. The time dependence of the data was continuously displayed upon the FFT analyser screen, and the FFT analyser was set to store the data automatically at user-defined intervals direct to a 3.5-inch disk. The data was then transferred to a PC where statistical analysis using the MATLAB software package was performed.

The light source used for the PID and tomographic experiments, described in a previous paper<sup>1</sup>, and Figures 2 and 3 demonstrate how the light intensity and duration can be altered by the developed light source. The intensity and duration of incident light that fell upon the sample surface was detected by a Hamamatsu S1722-02 PIN fast

### Experimental results and discussion

The current investigation was concerned with establishing the suitability of a-As<sub>2</sub>Se<sub>3</sub> and a-Si:H as hard field sensors for OPT, i.e. were the materials capable of producing accurate and repeatable quantitative and qualitative data for various media contained within tomographic prototypes at high speed for extended operational periods?

#### Quantitative data

In determining the selected materials' ability to establish quantitative data, experimentation focused primarily on tomographic prototypes containing various levels of water. The aim was to determine if the selected materials were sensitive enough to distinguish accurately between various levels of water contained within the tomographic prototypes. The experimentation would indicate the materials' suitability for application in fluid level/volume detection and for the imaging of air bubble/plug flow.

Initial experimentation was concerned with establishing if the samples could accurately detect the limits of the tomographic prototype, i.e. distinguish between a prototype full of water ( $R_{full}$ ) and an empty one ( $R_{empty}$ ). This involved establishing  $R(\lambda)$  over a 30 minute period under varying conditions of electric field, light intensity, light pulse duration and light pulse repetition rate to establish the maximum gap ( $R_{diff}$ ) that could be detected between the full and empty prototypes. The establishment of  $R_{diff}$ , which dictated the resolution of the tomographic prototype, was found to be in the order of  $1.332\mu A$  for the a-Si:H material and  $0.885\mu A$  for the a-As<sub>2</sub>Se<sub>3</sub>.

Once the optimum value of  $R_{diff}$  had been established and shown to be repeatable, water of a pre-determined level (measured from the bottom internal surface of the pipeline) was added to the tomographic prototype. Using the same experimental conditions to establish  $R_{diff}$ ,  $R(\lambda)$  was again monitored for a half-hour period and recorded. This process continued until

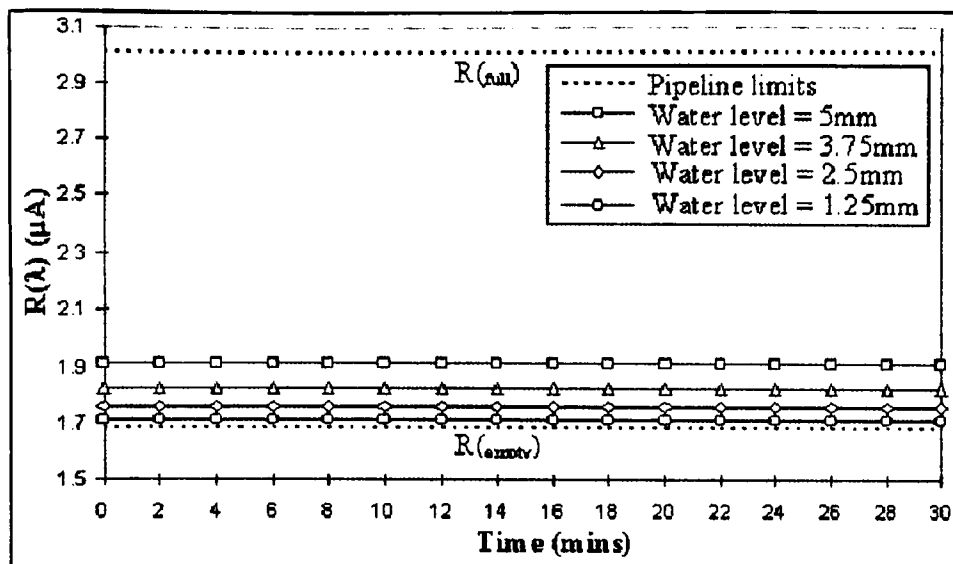


Figure 4: Graph showing signal response due to 1.25mm changes in water level contained within the first 5mm of the pipeline for the a-Si:H material. Dashed lines refer to the pipeline limits, i.e. the signal response due to a pipeline full of water and an empty pipeline.

the whole diameter of the tomographic prototype had been resolved. The water level was continually adjusted until the smallest detectable change in water level was established.

Figure 4 shows an example of this process with  $R_{full}$  and  $R_{empty}$  for a 44mm tomographic prototype (internal diameter) and the change in  $R(\lambda)$  due to a 1.25mm change in water level in the first 5mm of the pipeline. Data shown relates to the mean values of  $R_{full}$ ,  $R_{empty}$  and  $R(\lambda)$  averaged over several 30-minute test periods for the a-Si:H material. It could be seen that 1.25mm changes in water level were wholly distinguishable from one another and were the smallest changes in water level found to be determinable if crossover between the standard deviations observed in  $R(\lambda)$  due to the changes in water level were to be avoided.

### Qualitative data

Experimentation was also carried out to see if the a-As<sub>2</sub>Se<sub>3</sub> and a-Si:H materials were sensitive to changes in fluid concentration contained within the tomographic prototype. This would establish the their suitability for applications in the quality control of fluids contained within pipelines or vessels, and in the detection of foreign objects within those fluids. Further application may be found in the detection or imaging of semi-transparent foodstuffs such as vegetables<sup>11</sup>.

This investigation was carried out by completely filling the tomographic prototype with water mixed with a coloured concentrate at various levels of concentration, and monitoring  $R(\lambda)$  over a half-hour period. The maximum photocurrent was  $R_{full}$ , i.e. the pipeline was full of water with 0% concentrate added. Experimentation then proceeded by changing the volume of concentrate in the water.

Figure 5 shows the effect of altering the concentration of the fluid in 0.5% increments. It can be clearly seen that the magnitude of  $R(\lambda)$  reduced as the fluid concentration was increased. Thus the incident light falling upon the sample was attenuated as it passed through the tomographic prototype by the level of fluid concentration. The attenuation provided by the changing colour of the fluid produced the variance in  $R(\lambda)$  required for the collection of qualitative data.

The level of concentration was altered until the fluid became so dense that the incident light upon the sample surface had insufficient radiant power to produce a clean and repeatable signal. This

procedure then set the maximum level of concentration ( $R_{min} \approx 82.5\%$ ) that could be employed in the tomographic prototype.

### Speed of response

Data relating to the speed of response of the a-As<sub>2</sub>Se<sub>3</sub> and a-Si:H samples was derived from the current pulses recorded when  $R(\lambda)$  was monitored. For tomographic purposes, the speed at which the samples reached  $R(\lambda)$  is a very important parameter when the maximum operating speed of any potential imaging system is to be considered.

The time for  $I_s$  to reach 63% of  $R(\lambda)$  was denoted by  $\tau_{response}(rise)$ , and the time for  $I_s$  to decay from  $R(\lambda)$  to 37% of  $R(\lambda)$  was denoted by  $\tau_{response}(fall)$ . These response times denote how quickly the samples respond to the incident light falling on the sample surface. The time required for  $I_s$  to rise from 10% to 90% of  $R(\lambda)$  was termed the rise time ( $\tau_{rise}$ ), and that for  $I_s$  to fall from 90% to 10% of  $R(\lambda)$  was termed the fall time ( $\tau_{fall}$ ). The rise time was one of the most important parameters when establishing the maximum operating speed of the system.

Figure 6 shows two current pulses recorded at  $t=15$  minutes for 10% and 50% fluid mixtures. The experimental parameters were set to prevent  $I_s$  and therefore  $R(\lambda)$  from reaching steady-state conditions in order to establish maximum variance in  $R(\lambda)$ . We are exploiting the variance in  $R(\lambda)$ , due to attenuation of the issued light as it passes through the tomographic proto-

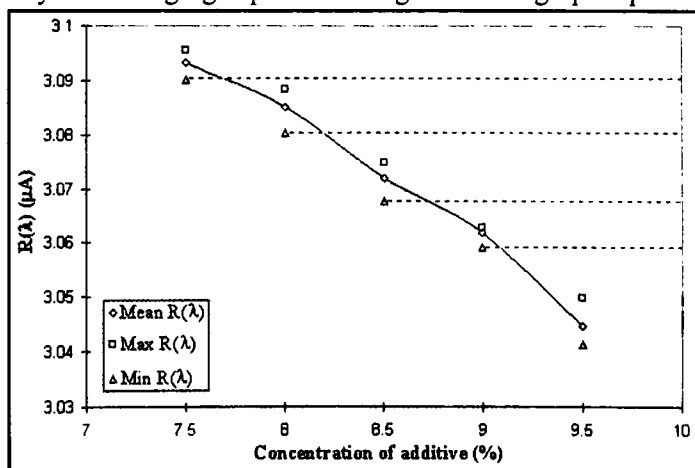


Figure 5: Graph showing changes in photocurrent due to 0.5% changes in fluid concentration. (Error bars show average standard deviation monitored over a 30-minute test period.)

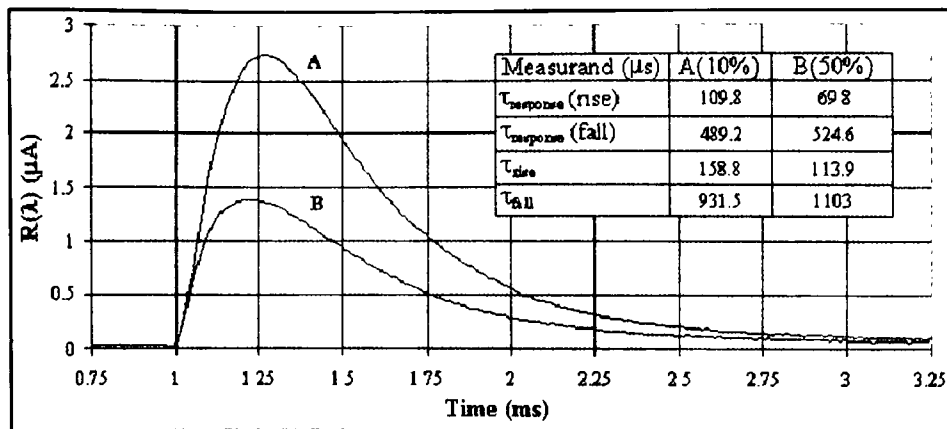


Figure 6: Graph showing change in response and rise-time due to a 40% change in fluid concentration.

type and media to the sample surface, to produce quantitative and qualitative data. Thus once  $R(\lambda)$  had been determined and recorded, no further information was required from the current pulse and the Au contact could be switched to ground via a high-speed switching mechanism<sup>12</sup> which can switch high-voltage supplies to ground in  $<1\mu\text{s}$ .

The removal of current after  $R(\lambda)$  has been recorded can greatly increase the time at which a successive light pulse can be issued. The rise and response times of the two current pulses are dependent upon the concentration of the fluid mixture, with  $\tau_{\text{rise}}=109.8\mu\text{s}$  for the 10% concentration and  $69.8\mu\text{s}$  for the 50% concentration, which demonstrates that the speed at which the system can be operated is highly application specific.

## Conclusions

A computer-controlled experimental system has been described for the investigation of a- semiconductor devices as image sensors. Of the various

devices employed in the current investigations, a- $\text{As}_2\text{Se}_3$  and a-Si:H have been identified as the most suitable for OPT applications. The measurements reported show that both materials are suitable for tomographic purposes. Our preliminary investigations show that repeatable quantitative and qualitative data can be obtained from the samples under test, confirming their suitability for OPT applications.

## References

- Jenner RP & Vaezi-Nejad SM: Development of a novel light source for the investigation of optical sensors, *Measurement+Control*, vol.32, pp.75-78, 1999.
- Jenner RP: The first year of a PhD project: a personal view, *Measurement+Control*, vol.30, no.6, 1997.
- Vaezi-Nejad SM & Jenner RP: Principles and application of advanced transient photoconductivity techniques, *IEEE Instrumentation & Measurement Tech'gy Conf Procs*, Ottawa, vol.2, p.942, 1997.
- Jenner RP & Vaezi-Nejad SM: Development of instrumentation for a novel computer controlled experimental appara-

tus, *Procs of 2nd Int'l Conf on Planned Maintenance, Reliability & Control*, Univ of Oxford, p.109, 1998.

- Mott NF & Davis EA: *Electronic processes in non-crystalline materials*, Clarendon Press, 1979.
- Elliot SR: *Physics of amorphous solids*, Longman Press, 1992.
- Apte RB, Street RA, Ready SE, Jared DA & Moore AM: Large area, low noise amorphous silicon imaging system, *Soc of Photo-optical Instrumentation Eng'rs*, vol.3301, pp.2-8, 1998.
- Kasap SO: Photoreceptors: the selenium alloys, *Handbook of imaging materials*, AS Diamond (ed), Marcel Decker Pub, p.329, 1991.
- Joshi NV: *Photoconductivity: art, science and technology*, Marcel Decker, New York, 1990.
- Williams RA & Beck MS: *Process tomography: principles, techniques and applications*, Oxford Butterworth-Heinemann, pp.5-6, 1995.
- Williams RA, Atkinson K, Luke SP, Barlow RK, Dyer BC, Smith J & Manning M: Applications for tomographic technology in mining, minerals and food engineering, *Particle & Particle Systems Characterization*, vol.12, pp.105-111, 1995.
- Pisarkiewicz T & Kuta S: A measurement set-up for photoconductivity decay experiments, *Measurement Science & Tech'gy*, vol.9, pp.1007-1009, 1997.

## Acknowledgement

Dr S M Vaezi-Nejad wishes to acknowledge the award of a Royal Society grant and a Fellowship of Engineering international travel grant. These enabled the author to attend an international conference in Canada and establish collaborative research programmes with the University of Saskatchewan.

# Instrument Engineer's Yearbook

**Entry forms for next year's edition are now available from the Publications Department.**

If you would like your company to be listed, please contact the Publications Department.  
**Deadline for entries is 18th August 2000**

